

# USE OF MICROWAVE TECHNIQUES IN MEDICAL DIAGNOSTICS AND THERAPY

Mabrouka Haiba .A. Ehtaiba



A thesis submitted to Cardiff University  
for the degree of Doctor of Philosophy

April 2017

## **DECLARATION**

This work has not previously been accepted in substance for any degree and is not concurrently submitted in candidature for any degree.

Signed..... (candidate) Date.....

### **Statement 1**

This thesis is being submitted in partial fulfilment of the requirements for the degree of PhD.

Signed..... (candidate) Date.....

### **Statement 2**

This thesis is the result of my own independent work/investigation, except where otherwise stated. Other sources are acknowledged by explicit references.

Signed..... (candidate) Date.....

### **Statement 3**

I hereby give consent for my thesis, if accepted, to be available for photocopying and for inter-library loan, and for the title and summary to be made available to outside organisations.

Signed..... (candidate) Date.....

# ABSTRACT

The main original contribution in this thesis is the novel application of microwave open-ended coaxial probes in the characterisation of the electrical properties of normal and cancer tissues, and their use for cancer therapy.

In terms of the cancer diagnosis part, this thesis shows the design, analysis and realization of new open-ended microwave sensors with a needle aperture to assess their sensitivity and usefulness for microwave characterizations of materials. These needle-type sensors are capable of penetrating easily into semi-solid and multilayered material. This is very important in cancer diagnosis since they permit non-destructive measurement, with the advantage of using them as medical needles that have higher sensitivity at low frequencies than the usual flat aperture probes. Moreover, the sensors have been developed to measure properties of normal and cancer tissues for early cancer detection applications.

In terms of the cancer treatment part, a novel non-thermal microwave irradiation technique has been adapted and developed for complete annihilation of cancer cells with a limited peak temperature of 42°C and short treatment time of 5 minutes.

# ACKNOWLEDGEMENTS

First and foremost, I thank the Almighty Allah for showering his infinite bounties and grace upon me, which has given me the strength, patience and knowledge to continue and finish my research work.

I would like to offer my most sincere thanks to my supervisor, Professor Adrian Porch for the opportunity to work with such an exciting field. I am grateful for his counsel and he has my lasting admiration. I must also thank him for all suggestions, explanations, and improvements in the writing of this thesis. There are no words to express my thanks towards him.

I am very grateful to my co-supervisor Professor Johannes Benedikt. His advice, technical expertise and encouragement helped me many times in the work of this thesis I also appreciate all the hours we spent together during the various experiments we conducted together. I would like to thank Dr. Xin Yang and Dr. Jonathan Lees for supporting.

I acknowledge the financial support of Libyan government. Thank you also to my friends and colleagues whose enlightening conversation has informed and enthused.

This research would not be possible without the help of many people. I wish to express my gratitude to them all for their contributions. Many thanks to the technicians in the electrical/electronic workshop, mechanical workshop, and IT group in the School of Engineering for their help and cooperation. Mr. A. Rankmore, I owe him a big thanks. He helped me during my research.

My thanks go to Dr. Florian Siebzehnrubl and his team at the Cardiff School of European Cancer Stem Cell Research Institute who have encouraged collaboration and have allowed my research to flourish.

My thanks go to Professor Wen Jiang and his team, especially Tracey Martin and Sioned Owen, at Henry Wellcome Building of cancer research, for their assistance in providing the cancerous samples and the biological analysis of these results in terms of therapy part.

This work would not have been possible without the love and patience from my brother Ali, and my friend Fatma, who I depended upon for support during the most challenging part of my research. They have always provided balanced insight and pulled me back to reality to ensure my completion of this degree.

I would like to give my deepest thanks to my precious mother, my brothers, sisters and my sister's husband, Ali, whose unfaltering support and encouragement have been invaluable.

The following experimental work was not conducted by the author:

- The microscopic images and determining the viability of the cells was carried out by Dr. Florian Siebzehnrubl from European Cancer Stem Cell Research Institute, Cardiff University, who is an expert within this field.
- Preparation of the cancer cells, processing the cells after radiation, the microscopic images, determining the viability of the cells, and cancer cells analysis were carried out by Dr. Tracey Martin and Dr. Sioned Owen, at Henry Wellcome Building of Cancer Research, Cardiff University.
- The circuit design of the handheld diagnostic tool for future skin cancer trials was developed by Mr. Michael Casbon from the School of Engineering, Cardiff University.

# PUBLICATIONS

**Mabrouka Haiba .A. Ehtaiba**, Xin Yang, Johannes Benedikt, and Adrian Porch, “Needle-Type Microwave Coaxial Sensor for Dielectric Characterization,” *Submitted to IEEE Transactionson Microwave Theory and Techniques*, under review.

**Mabrouka Haiba .A. Ehtaiba**, Xin Yang, Johannes Benedikt, and Adrian Porch, “Non-invasive Breast Cancer Diagnostic Tool Using Microwave Needle Probes,” *Submitted to IEEE Transactions on Biomedical Engineering*, under review.

## CONTENTS

<b>1 INTRODUCTION &amp; THESIS SUMMARY</b> .....	<b>1</b>
1.1 Sensing of cancerous and normal tissues.....	1
1.2 Microwave non-destructive techniques (NDT) .....	2
1.2.1 Advantages of NDT.....	3
1.3 Thesis scope.....	4
1.4 Thesis outline.....	4
<b>2 MICROWAVE MEASUREMENT TECHNIQUES</b> .....	<b>7</b>
2.1 Resonant techniques .....	7
2.1.1 Limitations of resonant techniques.....	7
2.2 Non-resonant techniques .....	8
2.2.1 Transmission line method (Waveguide).....	9
2.2.2 Free space method .....	9
2.2.3 Coaxial probe method .....	10
2.3 The choice of microwave techniques for this research.....	12
2.4 Flat open-ended coaxial sensor theory .....	13
2.4.1 Effect of flange .....	15
2.5 Modelling of the open-ended coaxial probe .....	16
2.5.1 Capacitive model.....	17
2.5.2 Radiation model or antenna model.....	17
2.5.3 Virtual line model.....	18
2.5.4 Rational function model .....	19
2.6 Errors and calibration .....	20
<b>3 NEEDLE-TYPE MICROWAVE COAXIAL SENSOR FOR DIELECTRIC CHARACTERIZATION</b> .....	<b>21</b>
3.1 General introduction .....	21
3.2 Principles, theory and simulation .....	23
3.2.1 Analytical analysis .....	23
3.2.2 Numerical analysis .....	29
3.3 Experiment.....	46
3.3.1 Probe design and feasibility analysis.....	46

3.4 Experimental set-up .....	47
3.5 Results and Discussion .....	55
<b>4 BREAST CANCER DIAGNOSTIC TOOL USING A MICROWAVE NEEDLE PROBE .....</b>	<b>58</b>
4.1 Microwave cancer diagnostic techniques .....	59
4.1.1 Microwave thermography .....	59
4.1.2 Microwave tomographic techniques.....	61
4.2 Biological tissue structure and composition .....	62
4.2.1 Polarisation and relaxation theory .....	64
4.3 Breast cancer diagnostic tool using microwave needle probes .....	67
4.3.1 Dielectric Properties of Tissue .....	69
4.3.2 Hydration and salinity effects on biological tissue .....	70
4.3.3 Needle-type probe measurement system .....	73
4.3.4 Examination of the sensing volume .....	74
4.4 Simulation results .....	76
4.5 Experimental results .....	76
4.6 Discussion.....	78
<b>5 MICROWAVE NON-THERMAL IRRADIATION FOR CANCER THERAPY .....</b>	<b>87</b>
5.1 Literature Review .....	89
5.1.1 Cancer Treatment Techniques.....	90
5.1.2 Comparison of Ablation Techniques.....	93
5.1.3 Microwave Ablation – Previous Studies .....	95
5.1.4 Microwave Ablation – Theory .....	96
5.2 Probe modelling in COMSOL .....	97
5.3 Simulation results .....	101
<b>6 EXPERIMENTAL SETUP FOR MICROWAVE IRRADIATION OF CANCER CELLS.....</b>	<b>106</b>
6.1 System overview.....	106
6.1.1 Signal Generator .....	107
6.1.2 High Power Amplifier .....	108
6.1.3 Circulator.....	111
6.1.4 Directional Coupler .....	112
6.1.5 Open-ended coaxial applicator .....	114
6.2 System Calibration.....	114
6.2.1 Electromagnetic Radiation Meter .....	117
6.3 Measurements and Instrumentations .....	117
6.3.1 Peripheral Hardware .....	118
6.3.2 Software.....	119
<b>7 EXPERIMENTS AND RESULTS FOR MICROWAVE IRRADIATION OF CANCER CELLS .....</b>	<b>124</b>
7.1 Equipment Calibration and Preliminary Measurement at 5.8 GHz.....	124
7.2 Methodology.....	124
7.2.1 Lab Study 1 – RG402 applicator - Flat aperture .....	127
7.2.2 Lab Study 2 – RG402 applicator - Flat aperture .....	129

7.2.3 Results of Study 1 and Study 2 .....	130
7.2.4 Study 3 – RG405 applicator – <i>in vivo</i> liver tissues .....	138
7.2.5 Study 4 – Use of Electric Cell-Substrate Impedance Sensing (ECIS) technique .....	140
7.3 Discussion.....	161
<b>8 CONCLUSIONS AND FUTURE WORK .....</b>	<b>165</b>
8.1 Conclusions.....	165
8.1.1 Cancer detection .....	165
8.1.2 Cancer treatment.....	166
8.2 Recommendations for Further Work .....	168
8.1 Microwave Handheld Skin Diagnostic Tool for clinic trail .....	168
<b>APPENDIX I.....</b>	<b>173</b>
<b>BIBLIOGRAPHY .....</b>	<b>177</b>

# LIST OF FIGURES

Figure 2.1: Transmission Line (Waveguide) Method [6].	9
Figure 2.2: Free Space Measurement Method [9].	10
Figure 2.3: Coaxial Probe Method [11].	10
Figure 2.4: Fabrication of coaxial probe with elliptic aperture. (a) Coaxial open end with a bevel angle and (b) bevel section view of a coaxial line.	11
Figure 2.5: Electric field lines for an open-ended coaxial probe [22].	13
Figure 2.6: The Agilent High Temperature Dielectric Probe [24].	14
Figure 2.7: Two types of open-ended coaxial probes. (a) Probe without flange and (b) probe with flange.	15
Figure 3.1: Cross section of the elliptic coaxial line.	25
Figure 3.2: A pattern of tetrahedral mesh of probe aperture.	36
Figure 3.3: Electric field distribution around the probe aperture, at 0.1 GHz, a) $\varphi = 0^\circ$ , b) $\varphi = 80^\circ$ with air sample. $a = 0.255$ mm, $b = 0.84$ mm, and $l = 20$ mm.	37
Figure 3.4: Typical response of power reflection of open-ended coaxial sensor with and without sample (in this case, a water), 0.1 - 3 GHz.	38
Figure 3.5: Simulated reflection coefficient of different probe aperture models with real permittivity sample, a) the magnitude, b) the phase at 0.1 and 1 GHz.	39
Figure 3.6: (a) Simulated comparison of the amplitude of the reflection coefficient for $\varphi = 0^\circ$ and $80^\circ$ with several values of the dielectric constant. (b) Simulated comparison of the $ S_{11} $ for air and hexane.	41
Figure 3.7: Simulated reflection coefficient of probe aperture $\varphi = 0^\circ$ & $80^\circ$ models with distance through two layers with $\epsilon' = 1$ and 3, a) the magnitude, b) the phase at 0.1 GHz.	41
Figure 3.8: Simulated reflection coefficient of needle probes with aperture angles $\varphi = 0^\circ$ and $22.5^\circ$ , plotted as a function of distance between two layers	

with $\epsilon' = 1$ and 10, a) the magnitude, b) the phase at 3 GHz. ....	41
Figure 3.9: Simulated reflection coefficient with distance through two layers with $\epsilon' = 1$ , and $\epsilon' = 3, 10, 100$ , a) the magnitude, b) the phase at 3 GHz.....	42
Figure 3.10: Diagram describes the two layers with interface region that presents 0mm distance.....	42
Figure 3.11: Simulated reflection coefficient of probe aperture with $\varphi = 0^\circ$ with distance through two layers with $\epsilon' = 1$ and $\epsilon^* = 76.7273 - i11.1869$ , a) the magnitude, b) the phase at 3 GHz. ....	43
Figure 3.12: Simulated magnitude of reflection coefficient for probe aperture with $\varphi = 0^\circ$ with distance through two layers with fat and muscle tissues, at 0.1, 0.3, 1, and 3 GHz. ....	43
Figure 3.13: Simulated phase of reflection coefficient for probe aperture with $\varphi = 0^\circ$ with distance through two layers with phantom of fat and muscle human tissues, a) at 0.1 and 1 GHz, b) at 0.3 and 3 GHz. ....	43
Figure 3.14: Simulated magnitude of reflection coefficient of probe aperture $\varphi = 22.5^\circ$ models with distance through two layers with fat and muscle tissues, at 0.1, 0.3, 1 and 3 GHz. ....	44
Figure 3.15: Simulated phase of reflection coefficient of probe aperture $\varphi = 22.5^\circ$ models with distance through two layers with phantom of fat and muscle human tissues, a) at 0.1 and 1 GHz, b) at 0.3 & 3 GHz. ....	44
Figure 3.16: Simulated reflection coefficient of probe aperture $\varphi = 80^\circ$ models with distance through two layers with phantom of fat and muscle human tissues , a) the magnitude, b) the phase at 0.1 and 1 GHz. ....	44
Figure 3.17: The Simulated magnitude reflection coefficient of probe aperture $\varphi = 0^\circ$ , $\varphi = 22.5^\circ$ and $\varphi = 80^\circ$ models with distance through two layers with phantom of fat and muscle human tissues , a) 0.1GHz, b) 1 GHz. ....	45
Figure 3.18: The Simulated phase reflection coefficient of probe aperture $\varphi = 0^\circ$ , $\varphi = 22.5^\circ$ and $\varphi = 80^\circ$ models with distance through two layers with phantom of fat and muscle human tissues , a)	

0.1GHz, b) 1 GHz. ....	45
Figure 3.19: Open-ended coaxial probes with different apertures. ....	47
Figure 3.20: The side sectional view and front sectional view. ....	47
Figure 3.21: Photograph of the microwave sensors. ....	48
Figure 3.22: Photograph of measurement set-up connected to microwave performance network analyser (PNA). ....	49
Figure 3.23: 2× T-LSM050A motorized stages. ....	50
Figure 3.24: Simulated (dashed line) and measured (solid line) relative complex reflection coefficients resulting by different probe apertures at 0.1 to 3 GHz of, a) Water, b) Methanol, c) Acetone, d) Ethanol, and e) Chloroform. .....	52
Figure 3.25: Simulated (orange line) and measured (blue line) , a- $ S_{11} $ , b- Phase at probe aperture $\varphi = 0^\circ$ , $\varphi = 22.5^\circ$ , $\varphi = 45^\circ$ , and $\varphi = 80^\circ$ with distance sweep through two layers of air and beef fat, at 0.1 GHz. ....	53
Figure 3.26: Simulated (orange line) and measured (blue line) c- $ S_{11} $ , d- Phase at probe aperture $\varphi = 0^\circ$ , $\varphi = 22.5^\circ$ , $\varphi = 45^\circ$ , and $\varphi = 80^\circ$ with distance sweep through two layers of air and beef fat, at 1 GHz. ....	54
Figure 3.27: Plot of the $ S_{11} $ of the relative complex reflection coefficient as a function of permittivity, a- $ S_{11} $ of open-ended probe at 0.1, 0.3, 1, and 3 GHz, b- $ S_{11} $ of $\varphi = 0^\circ$ , and $\varphi = 80^\circ$ , at 0.1 GHz. Plot of the phase of the relative complex reflection coefficient as a function of permittivity, c- phase of open-ended probe at 0.1, 0.3, 1, and 3 GHz, d- phase of $\varphi = 0^\circ$ , and $\varphi =$ $80^\circ$ , at 0.1 GHz. ....	57
Figure 4.1: The relative dielectric constant versus frequency for normal and malignant breast tissue [94]. ....	61
Figure 4.2: Dispersion regions in tissues depending on frequency [107]. ....	63
Figure 4.3: Electric polarization in a dielectric [112]. ....	64
Figure 4.4: Debye dispersion of water at 20 °C [33]. ....	66
Figure 4.5: Photograph of the microwave needle sensors injected into breast cancer sample. ....	69
Figure 4.6: Simulated (dashed line) and measured (solid line) relative complex reflection coefficients resulting for different probe apertures at 0.1 to 3 GHz of rat breast cancer tissues. ....	76

Figure 4.7: Frequency dependence of dielectric loss factor ( $\epsilon''$ ) of pure water and different saline concentrations in the frequency range 50 MHz to 3 GHz, measured by our needle probes. ....	77
Figure 4.8: Simulated and measured relative complex reflection coefficient resulting by different probe apertures at 0.1 to 3 GHz of rat breast normal and cancer tissues by needle probes. ....	78
Figure 4.9: Measured normal saline (dashed line) and breast cancer (solid line) relative complex reflection coefficients resulting by different probe apertures at 0.1 to 3 GHz. ....	79
Figure 4.10: Measured relative complex reflection coefficient of normal saline, using needle probes of varying angles, from 50 MHz to 3 GHz. ....	80
Figure 4.11: The variation of (a) the relative permittivity, and (b) the conductivity of normal and cancer tissues between 100 MHz and 3GHz measured using our needle probes compared with values from the literature. ....	83
Figure 4.12: The variation of, (a) the dielectric constant ( $\epsilon'$ ), and (b)- the dielectric loss factor ( $\epsilon''$ ), of saline solution between 50 MHz and 3GHz for a $\varphi = 0^\circ$ probe compared with simulation and calculated values. ....	85
Figure 5.1: Schematic of minimally-invasive liver tumor RF ablation procedure. The ablation catheter is inserted through a small incision and steered into the tumor under ultrasound imaging guidance[171] .....	92
Figure 5.2: A diagram illustrating the impact an electric field has upon polar molecules [179]. ....	93
Figure 5.3: Sequential CT images obtained during RF vs MW ablation in <i>in vivo</i> porcine lungs. Note the larger ablation zones (arrows) at each time point in the microwave panel [175]. ....	94
Figure 5.4: Labelled diagram of the RG402 microwave probe and sample as generated by COMSOL. ....	99
Figure 5.5: The mesh generated by COMSOL. ....	100
Figure 5.6: The solved model for 10W of radiation delivered into a water sample as generated by COMSOL. ....	100
Figure 5.7: The electric field distribution at different power levels. a) 10W, b) 30W & c) 50W. ....	102
Figure 5.8: The geometry, a), and results of a simulation, b), at 50W for water in the	

sample container.....	103
Figure 5.9: Electric field distribution of sample container filled with water and air at 50W.....	104
Figure 5.10: Simulated model of the cancerous sample in the container to be used experimentally, a) the geometry of the container, b) electric field at 10W, c) electric field at 30W & d) electric field at 50W.....	104
Figure 6.1: Schematic of the high power microwave system from source to probe (applicator).....	106
Figure 6.2: Simple diagram of class A amplifier circuit [190].	108
Figure 6.3: Example gain compression plot, in this case the P1dBm level is set at 20dBm output [193].	110
Figure 6.4: Photograph of used circulator.....	112
Figure 6.5: Four port directional coupler diagram [195].	113
Figure 6.6: Photograph of used directional coupler.....	113
Figure 6.7: Photograph of used RG402 open-ended coaxial applicator. ....	114
Figure 6.8: Diagram of forward signal calibration process.....	115
Figure 6.9: Diagram of reflection signal calibration process.....	115
Figure 6.10: Cascade coupler setup for measuring Rx and Tx. ....	116
Figure 6.11: HF meter.....	117
Figure 6.12: Agilent U2021XA Power Meter with USB connection. ....	118
Figure 6.13: J-type thermocouple insulated with glass.....	119
Figure 6.14: Flowchart of power meter's configuration in LabVIEW.....	120
Figure 6.15: Block diagram of power meter's configurations in LabVIEW.....	120
Figure 6.16: Flowchart of main measurement VI in LabVIEW. ....	122
Figure 6.17: Main panel of the main measurement VI in LabVIEW. ....	123
Figure 7.1: Dimensions for container used in preliminary experiment. ....	124
Figure 7.2: Pulse signal with different duty cycles.....	126
Figure 7.3: Different duty cycle and delivered power effects with temperature on a water sample.....	127
Figure 7.4: (a) Dimensions of each well. (b) Showing the 96-F-bottom wells that are used for cell insertion. ....	128
Figure 7.5: Microscopic view of the cancer cells at 5x optical zoom (a) before heating (b) immediately after heating & (c) 24 hours after heating in a water bath at 40°C, with no microwave irradiation.....	130

Figure 7.6: Microscopic view of the cancer cells at 10x optical zoom (a) before heating (b) immediately after heating and (c) 24 hours after heating in a water bath at 40°C, with no microwave irradiation. ....	131
Figure 7.7: Microscopic view of the cancer cells at 5x optical zoom (a) before heating (b) immediately after heating & (c) 24 hours after heating in a water bath at 50°C, with no microwave irradiation. ....	131
Figure 7.8: Microscopic view of the cancer cells at 10x optical zoom (a) before heating (b) immediately after heating and (c) 24 hours after heating in a water bath at 50°C , with no microwave irradiation. ....	131
Figure 7.9: Microscopic view of the cancer cells at 5x optical zoom (a) before radiation (b) after radiation (c) 24 hours after radiation.....	132
Figure 7.10: Microscopic view of the cancer cells at 10x optical zoom (a) before radiation (b) after radiation (c) 24 hours after radiation. ....	132
Figure 7.11: Temperature of the sample and $S_{11}$ for 30 W microwave pulse radiation with 5% duty cycle.....	132
Figure 7.12: Microscopic view on the cancer cells at 5x optical zoom (a) before radiation (b) after radiation (c) 24 hours after radiation. ....	133
Figure 7.13: Microscopic view on the cancer cells at 10x optical zoom (a) before radiation (b) after radiation (c) 24 hours after radiation. ....	133
Figure 7.14: Temperature of the sample and the $S_{11}$ for 30 W microwave pulse radiation with 5% duty cycles. ....	133
Figure 7.15: Microscopic view of the cancer cells at 5x optical zoom (a) before radiation (b) after radiation (c) 24 hours after radiation. ....	134
Figure 7.16: Microscopic view of the cancer cells at 10x optical zoom (a) before radiation (b) after radiation(c) 24 hours after radiation ....	134
Figure 7.17: Temperature of the sample and $S_{11}$ for 40 W microwave pulse radiation with 5% duty cycles. ....	134
Figure 7.18: Microscopic view of the cancer cells at 5x optical zoom (a) before radiation (b) after radiation (c) 24 hours after radiation. ....	135
Figure 7.19: Microscopic view on the cancer cells at 10x optical zoom (a) before radiation (b) after radiation (c) 24 hours after radiation. ....	135
Figure 7.20: Temperature of the sample and $S_{11}$ for 40 W microwave pulse radiation with 5% duty cycles. ....	135
Figure 7.21: System set up measurement.....	138

Figure 7.22: a) Liver - Control Area a b) Liver - Microwave a.....	139
Figure 7.23: a) Liver - Control Area b b) Liver - Microwave b.....	139
Figure 7.24: Two fiber optic thermometry probes, (a) STF Probe. (b) MicroProbe.....	140
Figure 7.25: Incubation chamber at 37 °C. ....	141
Figure 7.26: Small metal piece for temperature probe movement control. ....	141
Figure 7.27: a) The Countess™ II FL Automated Cell Counter. b) C-Chip Disposable Hemocytometer .....	142
Figure 7.28: Microscopic view of the cancer cells after 24Hrs.a) Non radiated - Healthy cancer cells (No.8), b) First exposure- cancer cells (No.6).....	144
Figure 7.29: Temperature of the sample and $S_{11}$ for 50 W microwave pulse radiation with 5% duty cycles, for 180 s exposure. ....	144
Figure 7.30: ECIS measurements.....	145
Figure 7.31: Cells medium refresh after 24 hrs.....	145
Figure 7.32: Microscopic view of the cancer cells for microwave thermal and non- thermal effects. a) Temperature – 42°C - (DEAD) b) Temperature – 60°C (DEAD) .....	148
Figure 7.33: New RG402 pointed applicator with 2 mm distance from the outer conductor end. ....	149
Figure 7.34: Effect on distribution of membrane associated proteins. (a) Staining of the control cells, (b) Staining of cells for 50W, 15 minute microwave exposure. ....	152
Figure 7.35: Changes in protein expression after non-thermal irradiation. ....	153
Figure 7.36: standard 6 well culture plate. ....	154
Figure 7.37: large diameter pointed probe. ....	154
Figure 7.38: Pointed RG402 probe for exploring the importance of cell contact.....	155
Figure 7.39: Different exposure regimes on suspensions of cancer cells. ....	157
Figure 7.40: Pointed RG405 probe, with double-ended RG405 for calibration procedures. ....	158
Figure 7.41: Zooming in of the pointed RG405 tip. ....	158
Figure 7.42: Microscope view for well – (a) of three exposure zones as demonstrated in Table 7-12 . ....	158
Figure 7.43: Microscope view for well – (b) of four exposure zones. Zones 1, 2, and 3 divided to two images due to the small view field of the microscope. ....	159

Figure 7.44: Microscope view for well – (c) of two exposure zones. Zones 1 and 2 divided to two images due to the small view field of the microscope. ....	160
Figure 7.45: The lipid bilayer arrangement in a cell membrane [211]. .....	162
Figure 8.1: Prototype Microwave Handheld Skin Diagnostic Tool for clinic trial.....	169
Figure 8.2: Three proposed cylindrical cavities with ability of separated electric and magnetic response for non-thermal cancer characterization applications.....	170

# **CHAPTER 1 INTRODUCTION & THESIS SUMMARY**

This thesis focuses on microwave sensor technologies in cancer diagnostic and therapeutic applications. The contributions are intended to provide innovative solutions in this highly exciting and evolving field, where microwave-based sensor systems provide value through complementing and replacing existing technologies or even enabling novel sensing solutions.

A new study arising from this research is based on a needle-type microwave coaxial sensor as a diagnostic device that is certified, analysed, and ready to be used to investigate suspected cases of cancer in real environments, which achieves high resolution at a low microwave frequency range of 0.1 to 3 GHz.

Another new comprehensive study from this research, based on a novel microwave sensor technique is developed that has been proved to be successful in treating cancerous cells utilising microwave irradiation without a strong thermal effect. This technique shows a proof of concept non-thermal microwave treatment with unique features in terms of pulsing and frequency. Various experimental results are outlined, including investigation of the non-thermal mechanisms of interaction of actively grown cancer tissues with high power pulsed microwave irradiation.

The current efforts in our development, and prototyping, are fully analysed in both diagnosis and therapy systems, which include underlying sensor principles, microwave technologies and infrastructure, as well as hardware and validation procedures.

## **1.1 Sensing of cancerous and normal tissues**

In the last decades, a great number of researchers have contributed to the study of the interactions between biological matter and electromagnetic fields. Many investigated

the dielectric properties of living matter. Some others analysed the differences between a cancerous agglomerate of cells and normal tissues. Huge steps have been made and many techniques have been developed, including experimental methods and simulations to derive the properties of these tissues.

## **1.2 Microwave non-destructive techniques (NDT)**

Microwave non-destructive techniques have a long history dating since the early 1950's [1]. Microwave signals penetrate inside dielectric (i.e. electrically insulating, or low loss) media easily. The depth of penetration is dictated by the loss factor of the dielectric material (i.e. its ability to absorb microwave energy) and the frequency of operation. Measurements can be conducted via a contact or non-contact fashion, while operating on one side of a material or using its both sides (reflection or transmission techniques, respectively). Microwave NDT techniques are sensitive to geometrical and dimensional variations of a medium or the presence of defects within the medium. Polarization properties of microwave signals can be used to increase measurement sensitivity to defects of a certain orientation, such as cracks or surface scratches on solid samples [2]. It is not necessarily true that because microwave signals have wavelengths in the centimeter range, the resolution obtained using these signals cannot be better than a large fraction of the operating wavelength. Microwave NDT techniques have shown measurement resolutions of a few microns at 10 GHz (i.e. wavelength of 3 cm in free space). If resolution, in a given application, is considered to be the smallest spatial distance between two defects so that they can be individually detected, then near-field microwave and millimeter wave techniques have provided resolutions of better than a tenth of a wavelength. It has also been shown that an increase in frequency does not necessarily render better measurement resolution in all cases. Also, at around 12 GHz fatigue cracks on metal surfaces with widths in the range of a few microns have been detected [2]. In addition, spatial resolution is a function of the microwave sensor used (e.g. open-ended coaxial lines, open-ended waveguides, cavity resonators, etc.) [2]. Taking the example of an open-ended coaxial probe, since a coaxial transmission line is a TEM structure, its cross sectional dimensions are not wavelength limited so its spatial resolution as a probe is limited only by its miniaturisation, most importantly the radius of curvature of its central conductor.

### **1.2.1 Advantages of NDT**

Microwave techniques are based on the interaction of radiated electromagnetic energy with material media. However, there are other techniques that utilize the same principle as microwaves for NDT purposes such as, optical frequencies (including infrared and ultraviolet), X-rays, and gamma rays; all of these can be classes as “electromagnetic” NDT. It is obvious that, although the underlying principles of basic materials interactions are the same, the scope of the possible applications, the equipment and technology used, and the associated costs and implications for the patient in healthcare applications, may be quite different.

In a majority of microwave NDT applications where detection is the primary objective, there is very little, if any need for complicated post signal processing. Capability of providing real-time information makes these techniques suitable for online medical applications [2]. The operator need not be a microwave expert to conduct microwave NDT measurements once a system has become operational. Since the required operating power for most NDT applications (excluding microwave heating sources) are in the few milliwatts range, and the majority of these techniques are conducted in near-field with a high degree of frequency selectivity, they do not cause any Electromagnetic interference (EMI) and neither are they affected by EMI. There are no environmental hazards associated with these techniques. Furthermore, microwave signals do not penetrate conductors thicker than a few microns, that can be used to contain high power microwave fields. One of the most attractive aspects of microwave NDT techniques is the availability of many different probes/sensors. Some of these may render better results than others for a specific application. In addition, optimization of system parameters for obtaining more sensitive results makes microwave NDT techniques very powerful.

Once the underlying theoretical foundations of the interaction of microwaves with a given medium is understood and modelled, one may develop an electromagnetic model to predict the outcome of a measurement in order to optimize it for obtaining the highest possible measurement sensitivity

### **1.3 Thesis scope**

The accurate contrast measurement between cancer and normal tissue is still challenging in cancer diagnosis. Although many techniques for cancer sensors have been presented, there are several problems that still need to be solved. The work in this thesis addresses some of these problems in microwave cancer sensor design. The problems addressed can be summarized as: resolution, size, cost, simplicity, real time measurements.

The proposed sensors in this research are suitable to characterize material and cancer tissues in both diagnosis and treatment applications. Then, on the basis of previous works in this field, and the same sensors are applied as a simple and quick technique to both diagnose and treat cancerous tissue.

### **1.4 Thesis outline**

In the following chapters, some aspects of the dielectric properties of cancerous and normal tissues are discussed and some new developments and measurements are presented.

**Chapter 2** – This starts with a review of existing microwave techniques for characterizing the dielectric permittivity of the material to find out the most accurate and suitable method for the application interest of this research. This is followed by focussed discussion on the open-ended coaxial probe technique and a review of the literature has been carried out to adequately understand the theoretical models to aid its analysis.

**Chapter 3** – This describes the novel coaxial needle sensors, with ellipsoidal apertures, which have been developed for characterizing materials at microwave frequencies, with focus on enhancing the sensitivity at lower microwave frequencies (0.1 to 3 GHz). The theory of the open-ended coaxial sensor perturbation and its analytical and numerical analysis by using FEM are concisely presented. Then, the probe design and its feasibility analysis are described. Experimental set-up and methods are highlighted. Simulated and experimental results are presented and discussed, with conclusions.

**Chapter 4** – This reviews the existing microwave cancer diagnosis techniques, followed by a discussion of the new non-invasive technology with high spatial resolution at low frequency based on complex permittivity measurement of normal and cancerous tissues using needle-type coaxial probes. The new data are compared with the theoretical model, and with data from the literature.

**Chapter 5** – A novel cancer treatment has been developed to identify a new means of destroying cancerous tissue through the use of non-thermal microwave radiation, with the following features:

- Minimally invasive, reduced trauma, reduced treatment times.
- Utilisation of modern microwave equipment and control to deliver high power, high frequency and pulsed signals with temperature control.

The key concept is to distinguish between heating effects and radiation effects in contributing towards cell necrosis. A comprehensive review of currently microwave cancer treatment techniques is given, that assesses the various treatment options of cancer, with a particular focus on ablation methods. Then, a comparison of ablation techniques is conducted, considering the advantages of each. A number of models using COMSOL Multiphysics software are presented for open-ended probes, analysing their ability to deliver power.

**Chapter 6** – The experimental setup utilised to generate both the high-power pulsed and continuous wave microwave radiation is explored in detail. A LabVIEW programme has been written to control, measure and record of a range of parameters including temperature, reflection coefficient  $S_{11}$  and dissipated power. This will be helpful for on-line analysis of irradiation during cancer treatment.

**Chapter 7** – Numerous experiments and comprehensive data tables, microscopic images results on both live cancer cells in suspensions and in tissues by applying the non-thermal microwave irradiation technique are presented, a topic which has not been discussed before in the literature. Continued research and development of the technique are presented, aimed for providing tools for better management of those factors important for treatment efficiency.

**Chapter 8** – Finally, this chapter draws together all of the general conclusions of the techniques and data presented in chapters 3-7, together with some suggestions and recommendations for future research.

## **CHAPTER 2 MICROWAVE MEASUREMENT TECHNIQUES**

In this chapter, the methods of measuring dielectric mechanisms at microwave frequencies are outlined and a justification of the use of a broadband open-ended coaxial probe is presented.

Measurement of material properties at microwave frequencies has existed for a very long time, dating as far back as the 1940's with numerous methods that are generally divided into resonant and non-resonant techniques. The particular measurement methods used in cancer detection and treatment sector are described here with their principles and limitations.

### **2.1 Resonant techniques**

Resonant techniques involve a shifting in the resonant frequency and the change in absorption characteristics of a tuned resonator, due to the insertion of a sample of material. This is achieved by reflecting EM waves within a structure and attempting to measure the phase velocity and decay through shifts in wavelength (hence frequency) and the power at resonance. Examples of structures used include resonant cavities (by the cavity perturbation technique), dielectric and microstrip type ring resonators [3].

#### **2.1.1 Limitations of resonant techniques**

The problem which is common to all resonant techniques is that measurements are all conducted at one resonant frequency of the structure (or, in a smaller number of cases,

at a small number of discrete harmonic frequencies). The dielectric properties of samples containing water have a large dependence on frequency, generally modelled using the Debye model (explained in chapter 4), and also very high losses in the microwave spectrum, which may be troublesome with a resonator that is centre frequency dependent. This is due to the limited number of measurement points across the resonant bandwidth in the frequency domain. Also, though their sensitivity of resonant methods may be high, high permittivity materials, especially with high loss, are actually harder to measure since the principle of operation involves dampening a resonator, and lossy materials may destroy the initial resonance. Therefore high sensitivity is only attained with small sample volumes. On other hand, non-resonant methods using the coaxial probe, coplanar waveguide and transmission lines in general are capable of providing continuous measurements over a wide frequency spectrum, but have a much lower sensitivity.

## **2.2 Non-resonant techniques**

A non-resonant technique can measure over a broad range of frequencies, which is a primarily important aspect for this research. The operation principle for these methods is to categorize the material by sending a wave into a structure and determining the reflection and/or transmission coefficients that are caused by changes in characteristics impedance and wave velocity [4]. These give information about the interaction of the EM fields with the material, and allow broadband determination of complex relative permittivity and permeability. A one port measurement of reflection from a structure such as an open-ended coaxial probe allows only the measurement of complex permittivity, since there are only two measurement variables, namely, the amplitude and phase of  $S_{11}$ . These methods involve building the sample into a transmission line or reflection structure by either placing the sample within a region of high field density, terminating a line with the sample, or building a microwave structure out of the sample itself. Among various non-resonant techniques, some of the most popular and most important methods for dielectric measurements are briefly discussed here. However, the open-ended coaxial line has been chosen for use in this research, owing to its flexibility and applicability as a needle type probe for tissue studies.

### 2.2.1 Transmission line method (Waveguide)

This is another common method in which a material sample is put inside the centre of enclosed transmission line, as shown in Figure 2.1. Both reflection and transmission coefficients are measured. It has higher accuracy and more sensitivity than the coaxial line but, if based on a waveguide sample cell, it has a narrower frequency range than for a coaxial probe [5]. Sample preparation is relatively difficult, and thus more time consuming, because the sample must cover entire cross-section area of the line, with no air gaps that completely gives inaccurate measurements; therefore, it must be in slab (for rectangular waveguide) or annular geometry (for circular waveguide) [6].

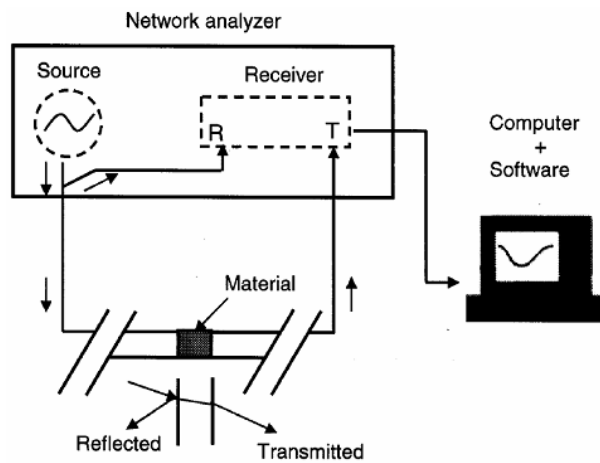


Figure 2.1: Transmission Line (Waveguide) Method [6].

### 2.2.2 Free space method

This technique is non-contacting and non-destructive, typically used at higher frequency, although it can be used with low frequency but it has a practical sample size limitation. In the free-space technique the large, flat samples of homogeneous (i.e. uniform without irregularities) solid material are required to measure the dielectric characteristics. The material is placed between two horn antennas to focus microwave energy on it, for measurement of S parameters in conjunction with vector network analyzer [7]. The advantage of using the free-space measurement technique is to get reflection and transmission coefficients with no physical contact to sample, which is best for thin flat materials [8], as illustrated in Figure 2.2.

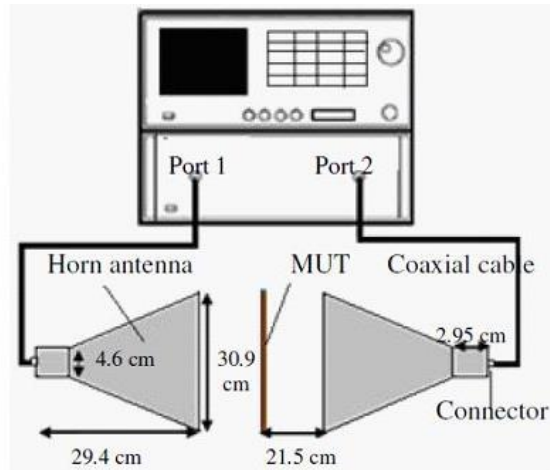


Figure 2.2: Free Space Measurement Method [9].

### 2.2.3 Coaxial probe method

Open-ended coaxial sensors have found a prominent place in a wide realm of material characterization and applications. This is the one of the most convenient and frequently used techniques to measure lossy materials (e.g. biological tissues) at high frequencies. Commonly it is known as the coaxial probe, coaxial-line probe or open-ended coaxial line method [10]. It is a simple, broadband (TEM) transmission line which, with a vector network analyzer (VNA) used to measure complex reflection coefficient  $S_{11}$ . There is no lower frequency range for the method and the upper frequency range is determined by the generation of non-TEM coaxial modes. For example, when using SMA or 3.5 mm connectors, the upper cut-off frequencies are about 18 and 26.5 GHz, respectively. The aperture (i.e. the open end of the coaxial) of the coaxial probe is used to sense the reflected signal (phase and magnitude) from the target material. For flat surfaces, the probe touches the sample and for liquids it is immersed into sample, as presented in Figure 2.3. It is a very simple method and permits dielectric measurements over broad frequency range.

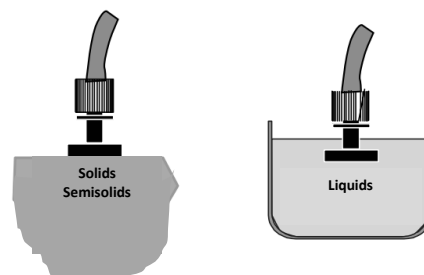


Figure 2.3: Coaxial Probe Method [11].

The large and shape-specific samples requirement within waveguide approaches is eliminated in the coplanar and coaxial probe methods [12]; where for the coaxial probe the sample size needs only be a few times the aperture diameter. Although large bandwidths can be measured using a flat aperture open-ended probe, these measurements require intimate sample contact and are thus used mostly for liquids or soft samples [13].

Cancer and normal cells which are analysed in chapters 4 of this thesis, for example, have been characterized here using the open-ended coaxial probe approach from 0.1 to 3 GHz to obtain both real and imaginary parts of the complex dielectric permittivity. In addition, the same approach has been used at discrete frequencies of 2.2 GHz and 5.8 GHz to treat cancer cells.

In 1992, Yansheng and Fadhel [14] introduced different open-ended elliptical apertures, so called needle-type coaxial probes [15], for measurement of microwave permittivity of methanol and demonstrated increased sensitivity in the low microwave frequency range from 2 to 4 GHz as shown in Figure 2.4. The reason for examining this probe in more detail in this thesis is to improve the sensitivity (and resolution) of measurements and to facilitate *in vivo* measurements of biological tissues. This study was shown that open-ended elliptical coaxial probes (bevelled probes) can be successfully used in wideband dielectric constant measurements with the advantages of increasing sensitivity and can easily be applied to gels and living tissues, and in general for biological applications both for measurements and microwave radiation treatment [16].

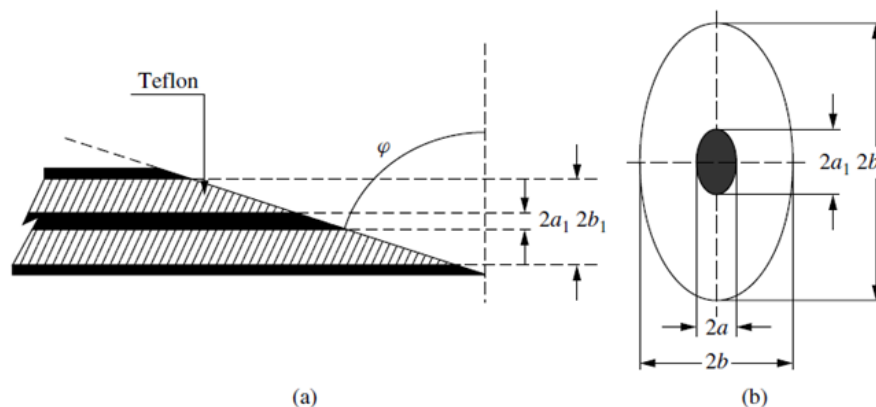


Figure 2.4: Fabrication of coaxial probe with elliptic aperture. (a) Coaxial open end with a bevel angle and (b) bevel section view of a coaxial line. Modified from [14].

The key advantages of the needle (i.e. bevelled) aperture probe over the standard (flat) aperture probe are:

- 1- As the bevel angle increases (i.e. sensing area increases), the measurement sensitivity increases. It is found that in the case  $\phi = 45^\circ$ , an improvement of 40% may be achieved in comparison with the standard probe, and 90% in the case  $\phi = 60^\circ$ .
- 2- The bevel probe is suitable for *in vivo* measurements of biological tissues. The permittivity of tissues *in vivo* is often different from that *in vitro* [17]. The needle-like probe shape makes it easier to insert it into living tissues.

### **2.3 The choice of microwave techniques for this research**

In general, the choice of technique depends on many factors such as the frequency of interest ( $f$ ), the expected value of complex permittivity ( $\epsilon_r^*$ ), the required measurement accuracy, the material properties (i.e., homogeneous, isotropic), the material form (i.e., liquid, powder, solid, film), sample size restrictions, destructive or non-destructive, contacting or non-contacting and temperature.

The information presented in the previous section was considered when choosing the optimum technique that is appropriate for the aims of this thesis. In many cases it is possible to use modelling prior to measurements to provide the optimum performance. In this thesis, emphasis on using open-ended coaxial probe technique for measurements of the dielectric properties of cancer and normal tissues is presented. Our focus on them arises from their current importance in medical applications. The main merits of the developed probe technique are ease of use and fabrication simplicity. Additionally, for an open-ended coaxial probe, one can simply inject into human tissues. High sensitivity is paramount in this research since it is to be used in the diagnosis of cancer tissues, to see if microwaves can achieve high contrast between cancerous and healthy tissue. This thesis will also try and make the most of the open-ended coaxial probe by evaluating its potential using a myriad of different aperture geometries.

Two recent comprehensive publications on RF and microwave dielectric measurements can be recommended as a general background. They are the Good Practice Guide [18] and a report that deals specifically with lossy liquids [19]. A recent review in [20] is also recommended. An introduction to the theory of dielectric relaxation and its measurement is provided by [21].

## 2.4 Flat open-ended coaxial sensor theory

As seen in Figure 2.5, the coaxial probe has electrical field lines both inside the probe and a fringing field at its end. The probe is nothing more than a center conductor surrounded by a dielectric material and an outer conductor, basically an open-ended coaxial line.

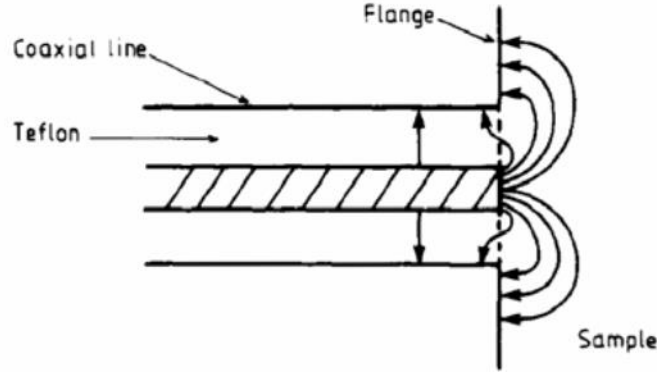


Figure 2.5: Electric field lines for an open-ended coaxial probe [22].

When a signal is transmitted to the probe's end, the sample is seen as a load. The fringing field interacts with the sample, where it displaces the ions and charge carriers. This energy causes a reflection coefficient at the aperture plane,  $\Gamma(\omega, \epsilon)$ , that is measured as  $S_{11}$  by a vector network analyser (VNA) at the measurement calibration plane.

$\Gamma(\omega, \epsilon)$  is a complex value, dependent on the permittivity of the sample and the angular frequency at which the reflection was measured. With  $\Gamma(\omega, \epsilon)$  known, the characteristic admittance of the load may be calculated by (2.1).

$$Y_L(\omega, \epsilon) = Y_o \frac{1 - \Gamma(\omega, \epsilon)}{1 + \Gamma(\omega, \epsilon)} \quad (2.1)$$

where  $Y_o$  is the probe's characteristic admittance. With  $Y_L(\omega, \epsilon)$  calculated, permittivity may be found from the equation (2.2) by using an appropriate iterative process [23]. This is most easily done using a computer.

$$Y_L(\omega, \epsilon) = j\omega C_1 + jA\omega^3 \epsilon^2 + B\omega^4 \epsilon^{2.5} \quad (2.2)$$

where A and B are the constants dependent on the frequency and dimensions of the aperture.

The principal method of measuring permittivity is with an Agilent Dielectric Probe Kit [24] as seen in Figure 2.6. The kit consists of an open-ended coaxial probe, calibrating standards, and a computer interface. A calibrated probe needs to be in full contact with the sample; no air may exist between the sample and the probe to obtain accurate permittivity values. Once the measurement is triggered, (2.1) and (2.2) are used to calculate permittivity.

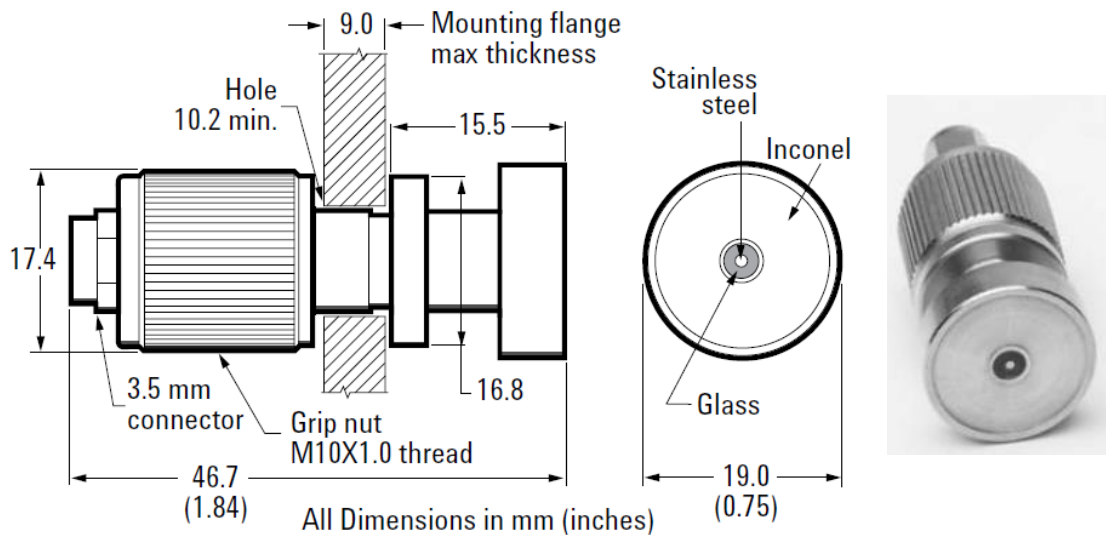


Figure 2.6: The Agilent High Temperature Dielectric Probe [24].

The probe is usually fixed into a broader flange, so that its capacitance is easier to model and to ensure the repeatability of sample loading [3, 25]. The fields at the probe end fringe into the sample and change as they come into contact with the material [11]. This method assumes the sample to be non-magnetic, isotropic and homogenous and to have a flat surface (i.e.  $\varphi = 0^\circ$ ) if it is a solid. Also the sample must be thick enough, “semi-infinite”, much larger than the diameter of the aperture of the open-ended coaxial line, because this method assumes that interactions of the electromagnetic field with the non-contacting boundaries of the sample are not sensed by the probe. The open-ended coaxial probe has been studied, analysed, and used by many authors [26-28] for microwave permittivity measurements with its tip immersed or contact in the sample under test [25].

### 2.4.1 Effect of flange

Improvements for complex permittivity measurement are achieved with short, open-ended coaxial probes by adding a finite conducting flange at the probe's aperture and by utilizing a more accurate aperture formulation [29]. A comparison of the measured permittivity by using two kinds of open-ended coaxial probe (i.e. a probe without a flange and a probe with flange) has shown that a conductor flange with a diameter of about 10 times the outer diameter of the probe significantly improves the performance of the probe because the flange model more closely represents the model of an infinite ground plane. The two probes described by (2.3) for the probe without flange and (2.4) for the probe with flange [29].

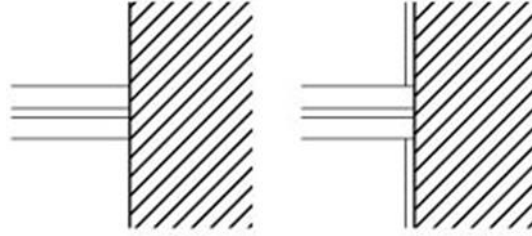


Figure 2.7: Two types of open-ended coaxial probes. (a) Probe without flange and (b) probe with flange.

$$Y_L = \frac{j2\omega I_1}{[\ln(b/a)]^2} \epsilon - \frac{j\omega^3 \mu_0 I_2}{[\ln b/a]^2} \epsilon^2 + \frac{\pi\omega^4 \mu_0^{3/2}}{12} \left[ \frac{b^2 - a^2}{\ln(b/a)} \right]^2 \epsilon^{5/2} \quad (2.3)$$

$$Y_L = \epsilon_r + \zeta \epsilon_r^2 \quad (2.4)$$

where  $\omega$  is the operating angular frequency and  $a$  and  $b$  are the inner and outer radii of the coaxial probe, respectively.  $I_1$  and  $I_2$  are integration constants dependent on the geometry of the probe's aperture. In 1999, David *et al.* developed a stain less steel open-ended coaxial probe to measure the complex permittivity of solid dielectric materials at elevated temperatures up to 1000°C and over a broad frequency range [30].

In biological applications, open-ended coaxial lines have been used as sensors for *in vivo* and *in vitro* measurements of the dielectric properties of biological substances [25, 26, 31, 32]. In several biomedical applications, it is necessary to know the dielectric properties of specific human tissues at microwave frequencies, particularly for hyperthermia treatments. These biological tissues are essentially constituted of water, free ions like Na<sup>+</sup>, K<sup>+</sup>, Ca<sup>++</sup>, Cl<sup>-</sup>, and great variety of proteins. This composition makes the dielectric properties of the tissues similar to those of saline solutions [33].

These kinds of solutions are characterized by a large dielectric loss factor at low frequencies (less than 3 GHz) owing to ionic conductivity [34].

In the last few years, there has been a growing interest toward the development of methodologies for non-invasive electromagnetic diagnostics based on dielectric spectroscopy, particularly operating in the microwave frequency bands. Dielectric spectroscopy has been used for a number of quality control purposes; for example, measurements of the complex dielectric permittivity,  $\epsilon^*(f)$ , have been used for [35]. A non-destructive broad-band permittivity measurement method used open-ended coaxial lines as impedance sensors which were terminated by a semi-infinite medium.

The commonly used technique to obtain the complex dielectric permittivity ( $\epsilon^*$ ) consists of measuring the complex reflection coefficient ( $\Gamma^*$ ) using a network analyser, with phase calibrated to the aperture plane. Afterwards, the complex permittivity ( $\epsilon^*$ ) is obtained through a model that gives the complex admittance of the probe's tip as a function of the dielectric permittivity of the surrounding medium, which is considered semi-infinite.

A certain number of these models exist in the literature. Comparative experimental studies are available in the open literature to assess the precision of these models, when measurements are made on high loss media such as saline solutions or biological tissues. One of the main goals of this research is to fabricate needle type, open ended coaxial probes with different end angles and assess the robustness in sensitivity of each probe for low and high loss materials, use a range of frequencies. Consequently, a judicious choice of the kind of open-ended coaxial probe can be made when measurements of biological tissues are required for diagnostic and treatment purposes.

## **2.5 Modelling of the open-ended coaxial probe**

Four models have been considered for open ended coaxial probe: the capacitive model [26] and [27], the antenna model [36], the virtual line model [37], and the rational function model [38-40].

### 2.5.1 Capacitive model

The equivalent circuit of this model consists of two capacitances connected in parallel. The first one,  $C(\varepsilon_r)$ , is related to the dielectric properties of the sample while the other,  $C_f$ , is the fringe field capacitance independent of these properties. When a dielectric sample with complex relative permittivity is connected to the probe, the equivalent capacitance will be changed and therefore the reflection coefficient is given by (2.5):

$$S_{11}^* = S_{11} e^{j\varphi} = \frac{1 - j\omega Z_0 [C(\varepsilon_r) + C_f]}{1 + j\omega Z_0 [C(\varepsilon_r) + C_f]} \quad (2.5)$$

where  $C(\varepsilon_r) = \varepsilon C_0$ ,  $C_0$  is the capacitance of the air-filled parallel plate capacitor,  $\omega$  is the measurement angular frequency ( $\omega = 2\pi f$ ) and  $Z_0$  is the characteristic impedance of coaxial line. The complex relative permittivity is given by (2.6):

$$\varepsilon_r = \frac{1 - S_{11}^*}{j\omega Z_0 C_0 (1 + S_{11}^*)} - \frac{C_f}{C_0} \quad (2.6)$$

The parameters  $C_f$  and  $C_0$  must be obtained to calculate  $\varepsilon_r$ . Calibration of the open-ended probe with a standard sample with known dielectric permittivity at the aperture plane can be used to derive  $C_f$  and  $C_0$  [3, 34].

### 2.5.2 Radiation model or antenna model

The coaxial probe is considered as a radiation source [3]. The equivalent circuit consists of two capacitors ( $C_1, \varepsilon_r C_2$ ) and a conductance ( $G$ ), all these elements being connected in parallel. The capacitance  $C_1$  is independent of the sample and results from the fringe field inside the air-filled coaxial line. The capacitance  $\varepsilon_r C_2$  is due to presence of the sample and is dependent on the permittivity of the material under test. The conductance  $G$  is the radiation conductance and representing the power radiated from the end of the line [3, 25, 41]. The normalized admittance is given by (2.7):

$$\frac{Y}{Y_0} = j\omega C_1 Z_0 + j\omega \varepsilon_r C_2 + Z_0 G(\omega, \varepsilon_r) \quad (2.7)$$

where  $Y_0$  and  $Z_0$  are the characteristic admittance and impedance of the line respectively,  $\varepsilon_r$  is the complex permittivity and  $\omega$  the angular frequency. For an electrically small antenna it is found that [31, 42]:

$$G(\omega, \varepsilon_r) = \varepsilon_r^{5/2} G(\omega, \varepsilon_0) \quad (2.8)$$

$$\frac{Y}{Y_0} = j\omega C_1 Z_0 + j\omega \varepsilon_r C_2 + \varepsilon_r^{5/2} G(\omega, \varepsilon_0) \quad (2.9)$$

The admittance can be expressed as (2.10):

$$\frac{Y}{Y_0} = K_1 + K_2 \varepsilon_r + K_3 \varepsilon_r^{5/2} \quad (2.10)$$

The factors  $K_1$ ,  $K_2$  and  $K_3$  are all complex and they can be obtained by using three known media in the calibration procedure. A more accurate model is [32].

$$\frac{Y}{Y_0} = K_1 + K_2 \varepsilon_r + K_3 \varepsilon_r^2 + K_4 \varepsilon_r^{5/2} \quad (2.11)$$

where the frequency dependence of  $C_1$  has been considered. Another approximation is [43]:

$$\frac{Y}{Y_0} = K_1 \varepsilon_r + K_2 \varepsilon_r^2 + K_3 \varepsilon_r^{5/2} \quad (2.12)$$

Using quasi-static analysis, an approximation for very low frequency is [43]:

$$\frac{Y}{Y_0} = K_1 \varepsilon_r + K_2 \varepsilon_r^2 \quad (2.13)$$

For all models, determination of parameters  $K_i$  is achieved by the calibration procedure.

### 2.5.3 Virtual line model

The sample of the material under test where the probe is terminated can be modelled as a virtual part of the transmission line. The transmission line consists of a part of physical line with length  $D$  and a part of virtual line with length  $L$ , which models the material under test [3, 37]

The complex permittivity of the sample related to the measured  $S_{11m}$  is:

$$\varepsilon_d = \frac{-jc\sqrt{\varepsilon_t} \frac{1 - S_{11m}e^{2j\beta tD}}{1 + S_{11m}e^{2j\beta tD}} \cot\left(\frac{2\pi fL\sqrt{\varepsilon_t}}{c}\right)}{2\pi fL} \quad (2.14)$$

where  $f$  is the measurement frequency and  $c$  is the light speed,  $S_{11m}$  is the complex reflection coefficient measured at the reference plane before the physical line (at the

analyzer port),  $\beta_t$  is the propagation constant in the coaxial cable feeding the aperture and  $\varepsilon_t$  is the permittivity of the material inside the physical coaxial line.

The values  $D$  and  $L$  can be found by calibration using two well-known dielectric calibration materials such as deionized water and air.

#### 2.5.4 Rational function model

In the rational function model, the coaxial probe is immersed in the material under test. The energy storage in the near-field region, the evanescent mode of the probe and the radiation effects have to be considered [3, 38, 40]. The admittance of the probe is given by (2.15):

$$\frac{Y}{Y_0} = \frac{\sum_{n=1}^4 \sum_{p=1}^8 a_{np} (\sqrt{\varepsilon_r})^p (j\omega a)^n}{1 + \sum_{m=1}^4 \sum_{q=1}^8 \beta_{mq} (\sqrt{\varepsilon_r})^q (j\omega a)^m} \quad (2.15)$$

$Y$  is the admittance at the end of the coaxial probe,  $Y_0$  is the characteristic admittance of the coaxial probe,  $\varepsilon_r$  is the complex relative permittivity of the sample of the material,  $a_{np}$  and  $\beta_{mq}$  are the coefficients of the model, and  $a$  is the inner diameter of the coaxial probe.

To obtain the complex permittivity of the sample from measured complex admittance values referred at the end of the probe the inverse problem has to be solved [38].

$$\sum_{i=0}^8 (b_i - Y c_i) (\sqrt{\varepsilon_r})^i = 0 \quad (2.16)$$

$$b_p = \sum_{m=1}^4 a_{mp} (j\omega a)^m \quad (p = 1, 2 \dots 8) \quad (2.17)$$

$$b_0 = 0 \quad (2.18)$$

$$c_q = \sum_{m=1}^8 \beta_{mq} (j\omega a)^m \quad (q = 1, 2 \dots 8) \quad (2.19)$$

$$c_0 = 1 + \sum_{m=1}^8 \beta_{m0} (j\omega a)^m \quad (2.20)$$

In this model, there is no need for calibration parameters and the model parameters  $a_{np}$  and  $\beta_{mq}$  have been established and optimized [34].

The virtual line model provides the best results for measurements of permittivity, while the results obtained with the antenna model are also accurate except at low frequencies [34]. In practice, the capacitive model is the easiest to use and has presents good results in the literature.

## **2.6 Errors and calibration**

Measurements using network analyzers may have three kinds of errors, systematic, random and drift. Random errors are unpredictable and they can be removed by making several measurements and taking the average values. Drift errors are due to the change of working conditions and require a stable environment in terms of temperature and humidity to be eliminated. Systematic errors mainly include directivity, match, cross talk and frequency response. All these errors are due to imperfections in the measurement systems and most of them do not vary with time. They can be characterized through a calibration procedure and mathematically removed during the process of measurement.

Calibration is a process which computes the systematic errors from measurements on known reference standards. When subsequent measurements are made, the effects of systematic errors are mathematically eliminated. There are two kinds of error corrections that can be made, response and vector corrections. Response calibration is simple to perform but corrects only a few of the systematic error terms. Vector-error calibration can account for all major sources of systematic errors, but needs more calibration standards and also requires that the network analyzer can measure both phase data and magnitude [3]. With further calibrations, drift errors can be removed. Once the network analyzer is calibrated the drift, stability, and repeatability errors will degrade the system performance and notice wrong measurement with known materials for example air. This usually means that the system will need to be recalibrated at some interval depending on the system usage, environment and required accuracy. Further information on RF and microwave measurements, on coaxial line and waveguide, and on metrological terms such as S-parameters in the frequency domain etc. can be found in [18] and in texts such as [44].

## **CHAPTER 3 NEEDLE-TYPE MICROWAVE COAXIAL SENSOR FOR DIELECTRIC CHARACTERIZATION**

### **3.1 General introduction**

Arising from the need for the measurement of dielectric contrast between the relative permittivity of cancer tissues and normal tissues at microwave frequencies, novel needle-type microwave coaxial sensors have been developed for characterizing material properties, of healthy and cancerous tissues in particular. This study focuses on the modelling of the sensors in order to optimise their design in terms of the angle, operating frequency, and feasibility. The performance of the sensors was initially simulated and verified in EMPro (*Electromagnetic Professional*) software and then experiments on some liquids and tissue samples were taken. Significant contrasts between various samples have been registered both in the simulations and experiments, with good agreement between them. It is hoped to use these sensors to detect tissue lesions as cancerous or non-cancerous, benign or malignant, within a non-destructive, real-time system that will reduce the need for excision and biopsy.

The technique is based on measured reflection coefficients using a vector network analyser, in which the operating frequency and probe aperture geometry depend on the dielectric properties of sample under test. An open-ended coaxial cable with different cut angles is adopted for the design of the sensors (i.e.,  $\varphi = 0^\circ$ ,  $\varphi = 22.5^\circ$ ,  $\varphi = 45^\circ$ ,  $\varphi = 67.5^\circ$  and  $\varphi = 80^\circ$  degrees). These sensors are practically easy to fabricate and to use, making them suitable for use on humans. Several types of samples are tested to verify sensor performance over the frequency range 0.1 to 3 GHz. Flat aperture probes cannot penetrate tissue when made from semi-rigid cables, unlike that for the needle

probe. A major electrical difference between the two structures is that the needle-type sensor has a much larger sensing region, which is ellipsoidal. The radiated energy density is greatest near the aperture and decreases monotonically in the radial direction. Therefore, as with the open-ended coaxial probe, materials closer to the aperture have more impact on the sensed reflection values.

This chapter presents a new technique of predicting the reflection coefficient of a microwave sensor for different samples using the finite element method (FEM). Comparison results between measured and calculated reflection coefficient were found to be in good agreement, with magnitude and phase errors of less than 5%.

Among several methods, microwave sensors have now found wide use in many applications based on the use of contrast in dielectric properties between different materials. This gives assurance of early detection and the practical usefulness of the developed system. Whereas flat aperture coaxial sensors are not capable of penetrating easily into semi-solid and multilayered material (i.e. a stratified medium), elliptical aperture sensors developed recently permit non-destructive measurement of such materials, with the advantage of using them as medical needles that have higher sensitivity at low frequencies than the flat aperture probes.

To achieve high accuracy and sensitivity at lower microwave frequencies (for example, the 0.1 to 3 GHz range used here), the aperture of the sensors should have a large sensing area. The use of a sharp needle maximizes this sensing area whilst keeping the diameter of the coaxial cable small. The large sensing area means that the sample covering factor will be high (i.e., a high fraction of the electric field energy will be exposed to the sample), so the sensor will be more sensitive to the presence of the sample. High sensing area can be accomplished using needle-type apertures with high cut angles ( $\varphi$ ), but this also necessitates large sample size.

A previous study by Yansheng [15] involved different open-ended elliptical apertures for measurement of microwave permittivity of methanol and demonstrated increased sensitivity in the low microwave frequency range 2 to 4 GHz. However, the precise and complete investigation of the effects of the apertures' angles and sensing areas on microwave permittivity measurement does not appear to have been published elsewhere to date. A systematic study for the case of different open-ended elliptical aperture coaxial lines with low range frequencies and various permittivity is presented here, with

the aim of achieving greater sensitivity for measurement in the 0.1 to 3 GHz range. A different elliptical aperture model of the open-ended coaxial probes is designed that have been used to relate the coaxial line end impedance to the complex permittivity of the material under test for calculating the reflection coefficient. The properties of an elliptical aperture coaxial probe are investigated with a numerical modelling technique based on finite element method in radio and microwave frequencies. The method has been implemented in EMPro software [45] for a three-dimensional geometry.

### **3.2 Principles, theory and simulation**

An open-ended of probe is immersed into the material to be tested. Then, the waves scattered from the sensor aperture would penetrate into the target sample which entirely covers the aperture area of probe. The electromagnetic field distribution in the vicinity of the aperture is determined theoretically, on the basis of aperture theory and boundary matching of the field components which are results of the solution to a boundary value problem. A solution of the scattering from the flat open end of a coaxial line in contact with a lossy dielectric was presented by Mosig *et al.*[46]. The formal analysis solution of the boundary-value problem was introduced by King *et al* [47] for the case of an elliptic coaxial line filled with isotropic dielectric material. The dielectric properties of the material determine the measured quantities such as complex reflection coefficient at the aperture. A theoretical study was carried out, considering the electromagnetic field near the aperture. Imposing the continuity of the tangential field components yields a dyadic Green's equation, which is solved by numerical techniques. One obtains in this way, generally with the help of a computer, a relationship linking the reflection coefficient with the material permittivity. This approach was first applied to rectangular waveguide probes [48] [49] [50] and then to azimuthally independent modes in circular waveguide [46].

#### **3.2.1 Analytical analysis**

The optimization of the performance of open-ended coaxial microwave sensor requires the knowledge of the propagation characteristics and field distributions and their dependence on the fabrication parameters. In terms of the flat open-ended aperture, the

coaxial sensor is assumed to be uniform along its longitudinal  $z$  axis. The electromagnetic fields at the frequency  $\omega$  and with time dependence have the form:

$$\mathcal{H}(x, y, z, t) = H(x, y)e^{j(\omega t - \beta z)} \quad (3.1)$$

$$\mathcal{E}(x, y, z, t) = E(x, y)e^{j(\omega t - \beta z)} \quad (3.2)$$

where,  $\beta$  is the propagation constant in the positive  $z$  direction.

In the material, electromagnetic fields are radiated, due to both the dominant *TEM* mode and the higher order *TM* modes within the plane of the aperture. We assume that the coaxial line is excited in its principal transverse electromagnetic (TEM) mode. At higher frequencies, TM modes are propagated with a cut-off frequency determined by the inner and outer radii of the coaxial line. These TM modes are allowed by the field boundary conditions and are comprised of Bessel and Neumann functions, the latter allowed since the axis is not included in the field region. In the frequency range up to 3 GHz, higher order modes are strongly evanescent (i.e. well below their cut-off frequencies). However, they will be excited at discontinuities in the coaxial line (e.g. at the open circuit termination), and so are included in some of the coaxial aperture models [51].

At first, the radiation from an open-ended elliptical aperture coaxial line, as primarily used in this research, is examined. The cross section of this coaxial line is shown in Figure 3.1. The semi-major and semi-minor axes of the ellipses which characterize the dimensions of the outer and inner conductors of the coaxial line are  $a_1, a_o, b_1$  and,  $b_o$  respectively. The radiated magnetic field of the outside space region is related to the tangential electric field of the aperture  $E_\rho(\rho', \phi')$  as follows [52]:

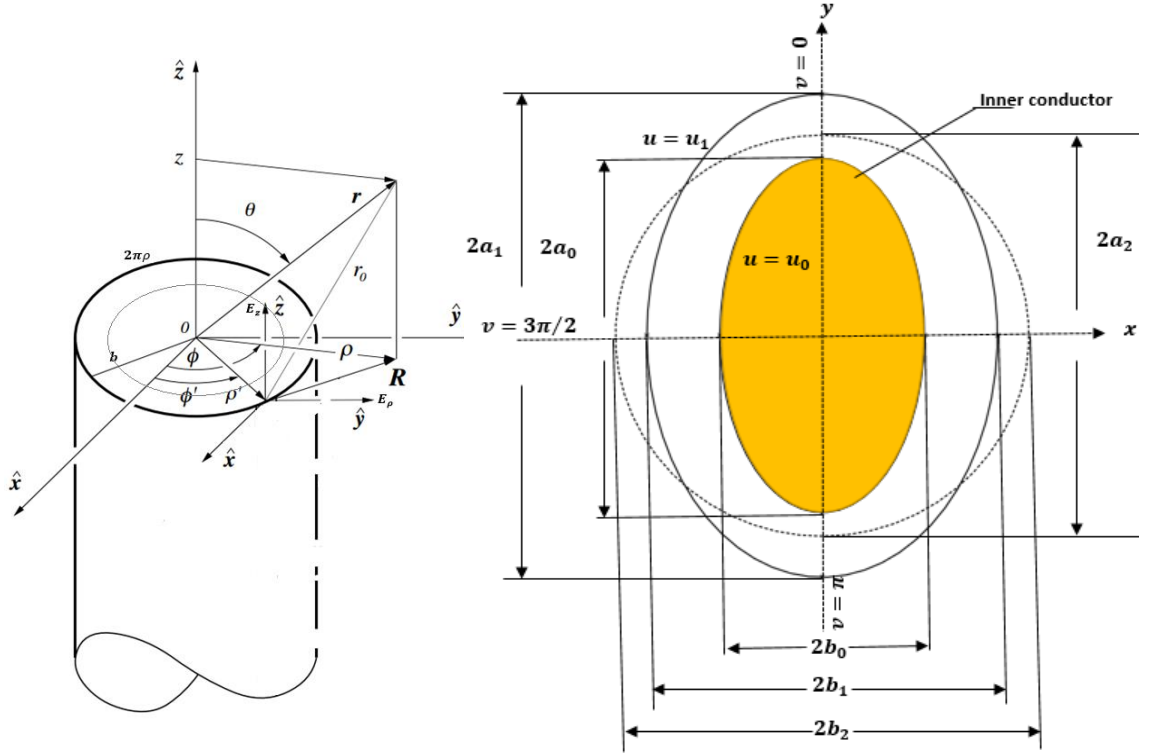


Figure 3.1: Cross section of the elliptic coaxial line.

$$dH = \frac{i}{2\pi\omega\mu_0} E_\rho(\rho', \phi') (\nabla\nabla. + k^2) \frac{e^{jkr}}{r} (i_{\rho'} \times i_z) \rho' d\rho' d\phi' \quad (3.3)$$

where

$$r = [\rho^2 + \rho'^2 - 2\rho\rho' \cos(\phi - \phi') + z^2]^{1/2}, \quad k = \frac{2\pi}{\lambda_0} \sqrt{\epsilon\mu} \quad (3.4)$$

and  $(\rho', \phi')$  are the transverse coordinates of the source point within the aperture, and  $r$  is the distance from source to observer.  $i_{\rho'} \times i_z = -i_{\phi'}$ , the resulting unit vector has components in  $\rho$  and  $\phi$  directions in the unprimed coordinates.  $E_\rho(\rho', \phi') = E_\rho(\rho')$ , is taken to be the principal mode of the coaxial line, and exhibits no variations in the  $\phi'$  direction [47] [52]. The operator  $(\nabla\nabla.)$  involves differentiations with respect to unprimed coordinates. Thus (3.3) can be integrated with respect to  $\phi'$ , the resulting expression having only a  $\phi$  component, and is independent of  $\phi$ . The operator  $\nabla = i_\phi \partial/\partial\phi$  is zero, and the term proportional to  $(\nabla\nabla.)$  is consequently zero. The magnetic field of the free space region is therefore related to  $E_\rho(\rho')$  as:

$$H_\phi(\rho, z) = \frac{k^2}{2\pi i \omega \mu_0} \int_a^b E_\rho(\rho') \rho' d\rho' \int_0^{2\pi} \frac{e^{jkr}}{r} \cos \psi d\psi \quad (3.5)$$

where  $\psi = \phi - \phi'$ ,  $a$  and  $b$  are the radius of inner conductor and the outer conductor respectively. The last integral can be expressed in terms of Bessel functions [53] and evaluating the  $\phi$  integral gives:

$$H_\phi(\rho, z) = -i\omega\varepsilon_0 \int_a^b E_\rho(\rho') \rho' d\rho' \cdot \int_0^\infty \frac{\exp[-(\zeta^2 - k^2)^{1/2}|z|] J_1(\zeta\rho) J_1(\zeta\rho') \zeta d\zeta}{(\zeta^2 - k^2)^{1/2}} \quad (3.6)$$

where  $\arg(\zeta^2 - k^2)^{1/2} = 0$  and  $-\pi/2$  for  $\zeta > k$  and  $\zeta < k$ , respectively. The  $\phi$  symmetrical magnetic fields of the coaxial line are expressed as [54]:

$$H_\phi(\rho, z) = \frac{A_0}{\rho} (e^{ik_i z} - R_0 e^{-ik_i z}) + \sum_{n=1}^{\infty} A_n R_n(\rho) \exp(\gamma_n z) \quad (3.7)$$

or

$$H_\phi(\rho, z) = A_0 H_{\phi 0} (e^{ik_i z} - R_0 e^{-ik_i z}) + \sum_{n=1}^{\infty} A_n R_n(\rho) \exp(\gamma_n z) \quad (3.8)$$

where  $H_{\phi 0}$  denotes the magnetic field of the principal mode with  $A_0$  as its coefficient, and  $A_n R_n(\rho)$  describes the fields of higher order modes at the probe aperture. The propagation factor of mode  $n$  is given by:

$$\gamma_n = i(k_i^2 - \lambda_n^2)^{1/2}, \operatorname{Re} \gamma_n \leq 0 \quad (3.9)$$

where  $k_i = \omega(\mu_0 \varepsilon_i)^{1/2}$ , and  $R_0$  is the reflection coefficient of the principal (*TEM*) mode. The radial function  $R_n(\rho)$  is defined by:

$$R_n(\rho) = N_n [J_1(\lambda_n \rho) Y_0(\lambda_n a) - J_0(\lambda_n a) Y_1(\lambda_n \rho)] \quad (3.10)$$

where  $J_m(x)$  is the Bessel function of the first kind and  $Y_m(x)$  is the Bessel function of the second kind of order  $m$ . The eigenvalues  $\lambda_n$  are computed from [55]:

$$Y_0(\lambda_n a) J_0(\lambda_n b) = J_0(\lambda_n a) - Y_0(\lambda_n b) \quad (3.11)$$

and the normalizing factor  $N_n$  is defined by:

$$N_n^{-1} = \frac{(2)^{1/2}}{\pi \lambda_n} \left[ \frac{J_0^2(\lambda_n a)}{J_0^2(\lambda_n b)} - 1 \right]^{1/2} \quad (3.12)$$

The radial electric field component  $E_\rho$  is computed from (3.7):

$$i\omega\varepsilon E_\rho(\rho, z) = \frac{\partial}{\partial z} H_\phi(\rho, z) \quad (3.13)$$

The amplitudes  $A_n$  are related to the aperture field at  $z = 0$ ;  $E_\rho(\rho, 0) = E_\rho(\rho)$ . Multiplying  $E_\rho(\rho, 0)$ , as computed from (3.13), with  $R_n(\rho)\rho d\rho$  and integrating from  $\rho = a$  to  $b$  gives:

$$A_n = \frac{i\omega\varepsilon_t \int_a^b E_\rho(\rho) R_n(\rho) \rho d\rho}{\lambda_n} \quad (3.14)$$

Multiplying  $E_\rho(\rho, 0)$  with  $d\rho$  and integrating from  $\rho = a$  to  $b$  gives:

$$A_0 = \frac{\omega\varepsilon_t}{k_i} \frac{\int_a^b E_{\rho 0}(\rho) d\rho}{[1 + R_0] \log(b/a)} \quad (3.15)$$

In our measurements, very small sensors are utilized and the dimensions of the probes are generally much smaller than the wavelength. Therefore, all the higher order TM modes in the calculation may be neglected in order to simplify the problem [56]. Then, the electric field  $E_{\rho 0}$  is taken to be the principal mode of the coaxial line and hence all terms containing  $A_n$  are equal to zero. It should be remarked also that the effect of the higher modes may be calculated by using the method, similar to that mentioned in [55], although the computation will be very complicated. The calculation was simplified by King *et al.* [47], however, is too lengthy to go into here. The propagation factors (3.9) will be equal to [55]:

$$\gamma_0 = j\beta_0 = j\sqrt{\varepsilon_c}(\omega/c_0) \quad n = 0 \text{ (propagated)} \quad (3.16)$$

$$\gamma_n = \alpha_n = \sqrt{\lambda_n^2 - \varepsilon_c(\omega/c_0)^2} \quad n > 0 \text{ (evanescent)} \quad (3.17)$$

The principle mode is TEM here, which is always propagated, onto which will be superposed TM modes at higher frequencies, as their cut-off frequencies allow as given below from references [47] [57].

$$H_{\phi 0}(\rho, \phi) \sim \frac{A}{\sqrt{\cosh^2 u - \cos^2 v}} = \frac{A}{\sqrt{\rho^2 - \phi^2}} \quad (3.18)$$

$$E_{\rho 0}(\rho, \phi) \sim H_{\phi 0}(\rho, \phi) \sqrt{\frac{\mu_t}{\varepsilon_t}} \quad (3.19)$$

where  $\cosh u = \rho$  and  $\cos v = \phi$  and  $A$  is the amplitude of the magnetic field to be determined.

When the field distribution around the probe aperture has been computed, the reflection coefficient is derived. This reflection coefficient originates from transmission-line theory and is defined in terms of a transmitted and reflected electric field which is formulated in terms of complex-valued, frequency dependent matrices. The device dealt with here is one port device.

In terms of an elliptical aperture, in practice, the fabrication of an elliptic coaxial line is quite intricate, and a simple method to obtain the elliptic configuration such a needle is to bevel the open-end of a circular coaxial line [58] [59], as shown in Figure 3.1. The resulting aperture may be considered as a transition from circular to elliptic and the radiation aperture becomes elliptic as well. Although the cross-section of the open-ended circular coaxial probe with bevel angle  $\varphi$  is elliptic, the inner and outer ellipses of the aperture of the probe do not coincide simultaneously with the commonly used elliptic coordinates [57]. To simplify the calculation, an assumption is made to lightly deform the outer ellipse so as to make it coincide with the elliptic coordinates [57] of the inner ellipse. The equal area principle, used to make the areas of the ellipses before and after deformation equal to each other, is used, i.e.:

$$a_2 b_2 = a_1 b_1 = a_1^2 \cos \varphi \quad (3.20)$$

where  $a_1, b_1$ , and  $a_2, b_2$ , are the major and minor semi-axis of the outer ellipse before and after deformation, respectively. For elliptic coordinates, from [57] it was found that:

$$C^2 = a_2^2 - b_2^2 = a_0^2 - b_0^2 = a_0^2 \sin^2 \varphi \quad (3.21)$$

Therefore,

$$C = a_0 \sin \varphi \quad (3.22)$$

Equations (3.20) and (3.22) are solved for  $a_2$ , and they give:

$$a_2 = \sqrt{\frac{C^2 + \sqrt{C^4 + 4a_1^4 \cos^2 \varphi}}{2}} \quad (3.23)$$

and so  $b_2$  then can be found easily.

### 3.2.1.1 Experimental considerations for coaxial sensor and sample

The dimensions of the coaxial line and the upper operation frequency are selected to permit propagation of the dominant *TEM* mode only. As a result, only this mode can be used to excite the line and carry out the measurements. The discontinuity appearing at the plane of the aperture (i.e.  $z = L$  specified for the mathematical derivation) excites a reflected *TEM* wave, which propagates back along the line, and a number of higher order modes, which are all evanescent as a result of the line dimensions and, therefore, decay rapidly along the line. The incident *TEM* mode has no angular variation of the fields as previously mentioned (i.e. it is independent of  $\phi$ ); the line and aperture are completely axially symmetrical for the flat aperture sensor. As a result, the higher order modes excited at the discontinuity can only be *TM* modes. In terms of the dimensions of object tested, they must be sufficiently large for the field to have decayed to negligible amplitude on the far sides, as in practice, fields decay fairly rapidly in the material away from the aperture according to transmission-line theory.

### 3.2.2 Numerical analysis

As the range of guiding structures becomes more complicated, the need for numerical analysis becomes greater and more demanding. The main objective of a numerical method is to solve a Partial Differential Equation (PDE) or Integral Equation on a discrete set of points of the solution domain, called discretisation. Unfortunately, the analytical solutions are not accurate owing to the assumption of homogeneity in those formulations, such as the use of an approximated approach to solve the singularity point in the equations [51] [60]. Several computational techniques have been developed to solve electromagnetic related problems not amenable to analytical or exact solutions. The most common techniques include the finite element method (FEM), the method of moment (MoM), and the finite difference time domain (FDTD). FEM is particularly advantageous for electromagnetic field problems, because of its applicability to waveguides with complex and arbitrary shape and material discontinuity, arbitrary refractive index profile, and even anisotropy [61] [62]. Recently, the finite element method has become a powerful tool throughout engineering applications for its flexibility and versatility, being used in complicated geometries, heat transfer, fluid flow, semiconductor, and electromagnetic problems where analytical solutions cannot

be obtained. Gabriel [63] showed that the finite element technique is well suited to the study of the fringing fields of coaxial probes. For the above reasons, the FEM method was chosen to analyse the electromagnetic field distribution around the sensor aperture by using EMPro simulator.

### 3.2.2.1 Finite element formulation

Finite element formulations are usually established via a variational or a Galerkin (method of moments or weighted residuals) approach. The latter is more flexible but when it is possible, it is advantageous to take a variational approach, especially when one global parameter (like propagation constant) is required [64].

The two-dimensional scalar FEM was introduced by Gajda [65] to solve Laplace's equation indirectly in the rotationally symmetric region of air-filled open-ended coaxial line. In addition, the capacitance expression obtained from scalar FEM is only satisfied at lower frequency. The vector FEM in High Frequency Structure Simulator (HFSS) was used by [66] to investigate the commercial coaxial probe but restricted to reflection properties of air. In this thesis, the application of FEM in Electromagnetic Professional simulator (EMPro) was extended to the determination of reflection coefficient of air and different samples by using flat and different needle-type open-ended probes.

#### 3.2.2.1.1 Finite element analysis of open-ended coaxial probe

An open-ended coaxial probe consists of inner and outer conductors, with radii  $a$  and  $b$ , respectively as shown in Figure 3.1. For any TM or TE wave, the partial difference equation (PDE) formulation is given by:

$$\vec{\nabla} \times \left( \frac{1}{\varepsilon} \vec{\nabla} \times \vec{H} \right) - k_o^2 \mu \vec{H} = 0 \quad (3.24)$$

$$\nabla \times \left( \frac{1}{\mu_r} \nabla \times E(x, y, z) \right) - k_o^2 \varepsilon E = 0 \quad (3.25)$$

where  $\varepsilon = \varepsilon_o \varepsilon_r$  is the permittivity of material. For open coaxial line, magnitude field  $\vec{H}$  is a function of  $\rho$  and  $z$ , but independent of  $\phi$ , thus:

$$-\frac{\partial}{\partial \rho} \left( \frac{1}{\varepsilon \rho} \frac{\partial}{\partial \rho} (\rho H_\phi) \right) - \frac{1}{\varepsilon} \frac{\partial^2}{\partial z^2} H_\phi - \mu k_o^2 H_\phi = 0 \quad (3.26)$$

The first order of differential argument in (3.26) can be represented by electric field components [51]:

$$-j\omega E_z = -\frac{1}{\varepsilon} \frac{\rho}{\partial \rho} (\rho H_\phi) \quad (3.27)$$

$$-j\omega E_\rho = -\frac{1}{\varepsilon} \frac{\partial}{\partial z} (H_\phi) \quad (3.28)$$

To avoid singularities at the axis ( $\rho = 0$ ) of rotation, a dependent variable  $U$  has been inserted, defined as the angular component of the magnetic field divided by the radial space coordinate  $\rho$ .

$$U = \frac{H_\phi}{\rho} \quad (3.29)$$

Substituting this into (3.26) leads to:

$$-\frac{\partial}{\partial \rho} \left( \frac{\rho}{\varepsilon} \frac{\partial U}{\partial \rho} + \frac{2U}{\varepsilon} \right) - \frac{\rho}{\varepsilon} \frac{\partial^2 U}{\partial z^2} - \rho \mu k_o^2 U = 0 \quad (3.30)$$

The potential  $k^{\text{th}}$ , is approximated by trial function  $U^{(k)}$  with constant coefficients in each element of the discretization process, such that [67] [68] :

$$U^{(k)} = \sum_{j=1}^N U_j^{(k)} \alpha_j \quad (3.31)$$

where  $U_j^{(k)}$  are the potentials at vertex  $j$ , which remain to be determined,  $\alpha_j$  are the real-valued linear interpolation functions (as shape functions of coordinates  $\rho$  and  $z$ ).  $N$  represents the number of nodes, which is defining the  $k^{\text{th}}$  element.

Using the weighted residual techniques, the (3.31) is substituted into the governing equation (3.30), whereby multiplying the result by  $\alpha_i$  and integrating over the area of the element, gives:

$$\sum_{j=1}^N U_j^{(k)} \iint_{(k)} \left[ -\frac{\partial}{\partial \rho} \left( \frac{\rho}{\varepsilon} \frac{\partial \alpha_j}{\partial \rho} + \frac{2\alpha_j}{\varepsilon} \right) - \frac{\rho}{\varepsilon} \frac{\partial^2 \alpha_j}{\partial z^2} - \rho \mu k_o^2 \alpha_j \right] \alpha_i d\rho dz = 0 \quad (3.32)$$

Equation (3.32) was simplified to yield from [68]:

$$= \oint_{(k)} j\omega E_{tan}^{(k)} \alpha_i dl \quad (3.33)$$

where  $l$  is the path of integration, that follows the perimeter of  $k^{th}$  element in a counter clockwise direction. The fields were integrated to get an average for the whole sensor boundary; therefore, the field needs to be multiplied by  $2\pi\rho$  while integrating. Finally, Galerkin's principle for nodal finite elements is implemented in FEM for transformation of (3.33) to equivalent systems of algebraic equations.

### 3.2.2.1.2 Boundary conditions

The azimuthal magnetic field in a coaxial line is assumed to be that of a *TEM* wave,

$$H_\phi = \frac{1}{\rho} e^{-jk_oz} \quad (3.34)$$

Equation (3.34) is applied to the excitation boundary of the coaxial line with the phase factor,  $e^{-jk_oz}$  assumed equal to 1. One of the open-ended coaxial probes used in this thesis has an inner radius,  $a = 0.255$  mm and an outer radius,  $b = 0.84$  mm. The inner of the coaxial line is made of copper, surrounded by PTFE or Teflon ( $\epsilon_r = 2.05$ ) as a dielectric, while the external medium of the coaxial aperture probe is air ( $\epsilon_r = 1$ ) or a lossy material. All conductors of coaxial probe are assumed perfect electric conductor (PEC). Consequently, the continuity boundary conditions for tangential component of the electric field are applied and imposed at a border of conductors.

$$\hat{n} \times \vec{E} = 0 \quad (3.35)$$

At the outer boundary, the continuity boundary condition (PEC) sets the tangential component of the electric field,  $E_z$  to zero. Generally, the low reflecting or so-called radiation boundary is based on the difference between the total field and the field of the incident wave. For coaxial antenna or radiator, the relationship between  $\vec{H}$  and  $\vec{E}$  at the scattering region is expressed as [68]:

$$\vec{H} = \frac{\hat{e}_z \times \vec{E}}{\eta} \quad (3.36)$$

The unit vector  $\hat{e}_z$  points in the direction of propagation, while  $\eta$  is the complex intrinsic impedance of the medium.

$$\eta = \sqrt{\frac{j\omega\mu}{\sigma + j\omega\varepsilon}} \quad (3.37)$$

where  $\sigma$  is conductivity of the medium. Hence (3.36) becomes:

$$\hat{e}_z \times \sqrt{\varepsilon} \vec{E} = -2\sqrt{\mu} H_{oz} + \sqrt{\mu} H_z \quad (3.38)$$

$$\approx -\sqrt{\mu} H_\phi \quad (3.39)$$

where  $E_{tan} = \hat{e}_z \times \vec{E}$  and  $\sigma = 0$  for the lossless material. Substituting (3.29) into (3.39), yields:

$$E_{\rho-tan} = -\left(\sqrt{\mu/\varepsilon}\right) \rho \frac{H_\phi}{\rho} \quad (3.40)$$

$$= -\left(\sqrt{\mu/\varepsilon}\right) \rho U \quad (3.41)$$

Subsequently, the trial function (3.31) is substituted for  $U$  and the integral on right-hand side of (3.33) is written as:

$$\oint_{(k)} E_{tan}^{(k)} \alpha_i dl = - \oint_{(k)} \left[ \left(\sqrt{\mu/\varepsilon}\right)^{(k)} \sum_{j=1}^N U_j^{(k)} \alpha_j \right] \alpha_i dl \quad (3.42)$$

$$= - \sum_{j=1}^N U_j^{(k)} \oint_{(k)} \alpha_j \left[ \left(\sqrt{\mu/\varepsilon}\right)^{(k)} \right] \alpha_i dl \quad (3.43)$$

The axial symmetry boundary condition is along the z-axis. At the symmetry axis, the tangential part of the magnetic field may vanish and the meridional fields must satisfy the conditions.

$$E_\rho = 0 \quad (3.44)$$

$$\frac{\partial E_z}{\partial \rho} = 0 \quad (3.45)$$

An electromagnetic wave having its direction of propagation along the coaxial cable is introduced, imposing port type boundary conditions on the one end of the cylinder that models the coaxial probe. On the input port an excitation wave is imposed having an

incident power of 1mW, for example, for diagnosis part. In order to compute the scattering parameters the following relations in terms of power have been used:

$$S_{11} = \sqrt{\frac{\text{Power reflected}}{\text{Power incident}}} \quad (3.46)$$

The magnetic field,  $H_\phi$  at each radius point on the excitation boundary can be written in terms of reflection coefficient,  $S_{11}$

$$H_\phi = H_{\phi_{in}}(1 - S_{11}) \quad (3.47)$$

$$= \frac{1}{\rho}(1 - S_{11}) \quad (3.48)$$

where  $H_{\phi_{in}}$  is the incident magnetic field on the excitation boundary. From (3.47), the reflection coefficient,  $\Gamma$  ( or  $S_{11}$  ) can be deduced as :

$$S_{11} = \frac{H_{\phi_{in}} - H_\phi}{H_{\phi_{in}}} \quad (3.49)$$

The aperture reflection coefficient,  $S_{11A}$  at  $z = l$  plane (aperture probe) with respect to  $S_{11}$  at  $z = 0$  (excitation plane) is defined as:

$$S_{11A} = S_{11}e^{2jk_c l} \quad (3.50)$$

where  $k_c$  is the propagation constant of the coaxial probe.  $l$  is equal to 20 mm as illustrated in Figure 3.19.

### 3.2.2.1.3 FEM Simulator of EMPro

EMPro is a generic finite element method solver based on custom partial differential equations (PDE). The FEM Simulator within EMPro provides a complete solution for electromagnetic simulation of arbitrarily-shaped and passive three-dimensional structures. The basic solving procedure in EMPro includes geometric modelling, physical modelling, mesh generation, FEM matrix assembly, matrix solving and post processing. A mesh is a pattern of tetrahedra that is applied to a design in order to discretize the design into small elements as in Figure 3.2. The basic mesh needs refining particularly in the regions of high field gradient. Thereafter, the mesh generator works

out the numbering and coordinates of each node and the geometry of each element for the given order. A simulation setting up by specifying the parameters of a frequency plan, such as the frequency range of the simulation, the sweep type (i.e. Adaptive, Logarithmic, Linear or Single sweep), and in addition, selection of the solution method (i.e. direct or iterative method). When the setup is complete, the simulation can be run. The simulation process uses the mesh pattern, and the electric fields in the design are calculated. S-parameters are then computed based on the electric fields. If the adaptive frequency sample sweep type is chosen, fast and accurate simulation is generated, based on a rational fit model. The following wave equation is solved by EMPro to calculate the full 3D field solution [45]:

$$\nabla \times \left( \frac{1}{\mu_r} \nabla \times E(x, y, z) \right) - k_o^2 \epsilon_{rc} E = 0 \quad (3.51)$$

where  $\mu_r$  is the complex relative permeability,  $\epsilon_{rc}$  is the complex relative permittivity,  $E(x, y, z)$  is a complex vector representing an oscillating electric field and  $k_o$  is the free space phase constant ( $k_o^2 = \omega^2 \mu_o \epsilon_o$ ).

The geometry of the measurement system is symmetrical with respect to the centre axis of the probe. For excitation, a wave with unit amplitude at broadband frequencies (0.1 to 3 GHz) is applied between the inner- and outer-conductor of the probe. The incident wave which propagates to the probe surface was made by exciting  $E_\rho$  and  $H_\phi$  on the line of length  $L = 20 \text{ mm}$ .

The three dimensional electromagnetic structures of the open-ended flat and elliptical-aperture coaxial probe shown in Figure 3.2 are considered. The results computed by EMPro software are illustrated in the next section for different materials.

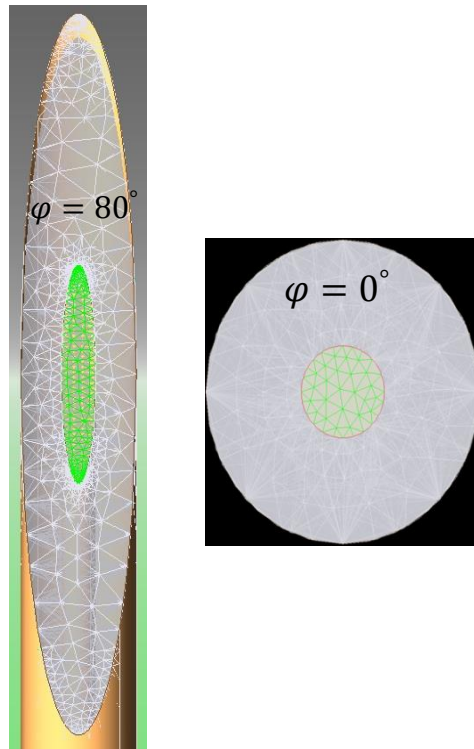


Figure 3.2: A pattern of tetrahedral mesh of probe aperture.

#### 3.2.2.1.4 Simulation performance

The EMPro runtime is essentially dependent on the refined mesh number, in addition to computer resources. The simulation was implemented using EMPro (2013.07) on a PC with a 3.50 GHz Intel(R) Core™ i7-3770K, 4 Cores, 8 Logical processors. Different configurations were simulated using EMPro software in advance of probe fabrication. The main objective of these simulations was to find an optimum set of conditions for each probe which could be used in the performance analysis of the probes with unknown permittivity values. Previously, many sensor types based on the reflection coefficient have been fabricated, which are highly sensitive to the presence of the dielectric properties of the high-permittivity liquids or human tissue [26, 69]. However, these sensors have limited accuracy, particularly with low permittivity values [70]. For example, a flanged coaxial probe with larger dimensions radiating into a material was presented in [71]. This was used for achieving high sensitivity to measure materials with a low dielectric constant at low microwave frequencies, since no distinction can be made between the phase and amplitude characteristics of the reflection coefficient for different values of the dielectric constant with probes of small dimensions. It is thus

clearly proven that a probe with larger dimensions drastically improves measurement accuracy for low permittivity materials at frequencies up to 1.5 GHz.

### 3.2.2.1.5 Electromagnetic field distribution around the aperture

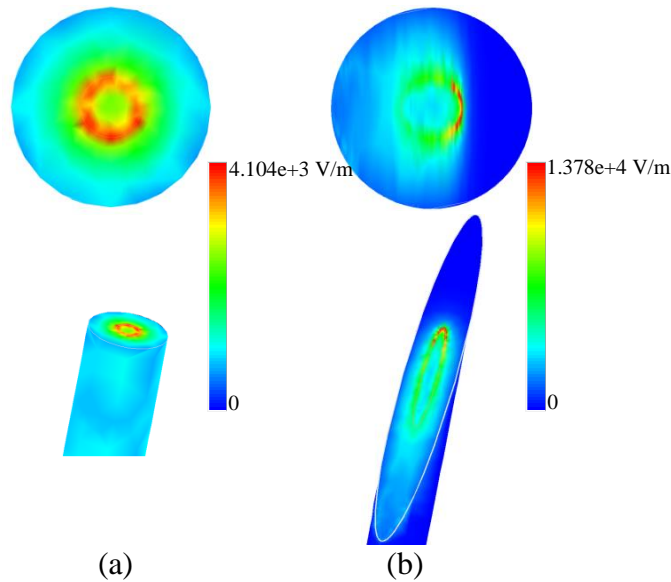


Figure 3.3: Electric field distribution around the probe aperture, at 0.1 GHz, a)  $\phi = 0^\circ$ , b)  $\phi = 80^\circ$  with air sample. **a = 0.255 mm, b = 0.84 mm, and l = 20 mm.**

Results are given in Figure 3.3 (a) and Figure 3.3 (b) using EMPro. Figure 3.3 (a) shows the simulated electric field map in the aperture plane of an open-ended, flat ( $\phi=0^\circ$ ) coaxial probe. The same technique was used to generate the same plots for different elliptical apertures, an example of which is shown in Figure 3.3 (b). The field distribution around the probe surface has been computed to derive the reflection coefficient. The electric fields concentrate on the edge of the inner conductor. Judging from the probe structure, field concentration at the outer edge of the inner conductor is high, so mesh cells should be made finer in this region to compute the field distribution accurately; for example, 12401 and 15575 tetrahedra are needed for flat and needle-type aperture probes, respectively, as illustrated in Figure 3.2. The fringe fields of the probe aperture are perturbed by the introduction of small material samples. The dielectric samples are placed in front of the aperture, a region of high electric field. This generally leads to an increased phase and reduced magnitude of the reflection coefficient that can be related to the complex relative permittivity of the material under test. Figure 3.4 shows schematically the changes in complex reflection coefficient when it is terminated with a lossy sample, which covers the aperture with no gap (in this case water as an

illustration).

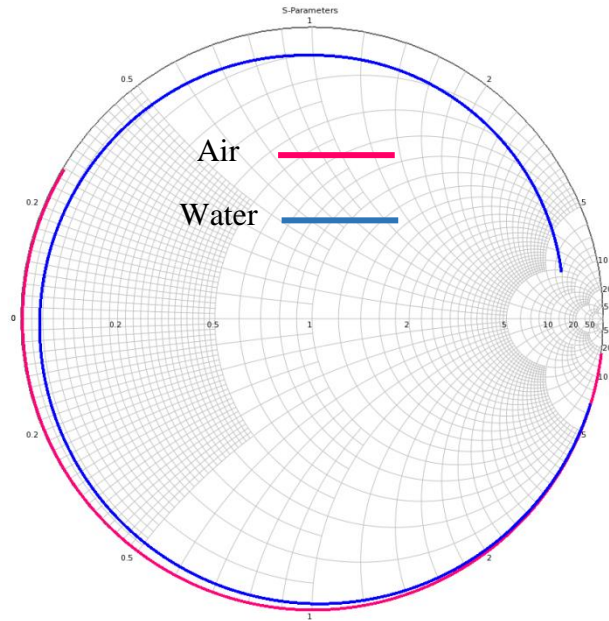


Figure 3.4: Typical response of power reflection of open-ended coaxial sensor with and without sample (in this case, a water), 0.1 - 3 GHz.

### 3.2.2.1.6 The analysis of probes with lossless and lossy media

In order to study the performance of the sensors and test their sensitivity at low microwave frequencies, simulation of various probe aperture shapes with known permittivity was analysed. Each probe was modelled over a variety of frequencies, while the sample permittivity,  $\epsilon_m$ , was varied from 1 to 100 in each case to simulate the range of dielectric parameters that could be encountered by the frequency. A lossless medium is one whose dielectric constant is purely real.

In Figure 3.5 the medium in contact with the probe was assumed to have a real permittivity ( $\epsilon' = \text{constant}, \epsilon'' = 0$ ). The reflection coefficient plotted as a function of  $\epsilon'$  is illustrated for different probe apertures at 0.1 and 1 GHz. From the results of both frequencies, the values obtained for the magnitude and phase of the reflection coefficient with varying real permittivity validate the theory for the open-ended coaxial probe outlined in the previous section. As a result of increasing the cut angle of the aperture, (i.e. an increased sensing area), subsequently, the sensitivity noticeably becomes enhanced, as indicated in Table 3-1 and Table 3-2. In order to set a value of  $\epsilon_m$  for the sensitivity test, examination of the results in Figure 3.5 suggests  $\epsilon_m$  should be greater than or equal to 3.

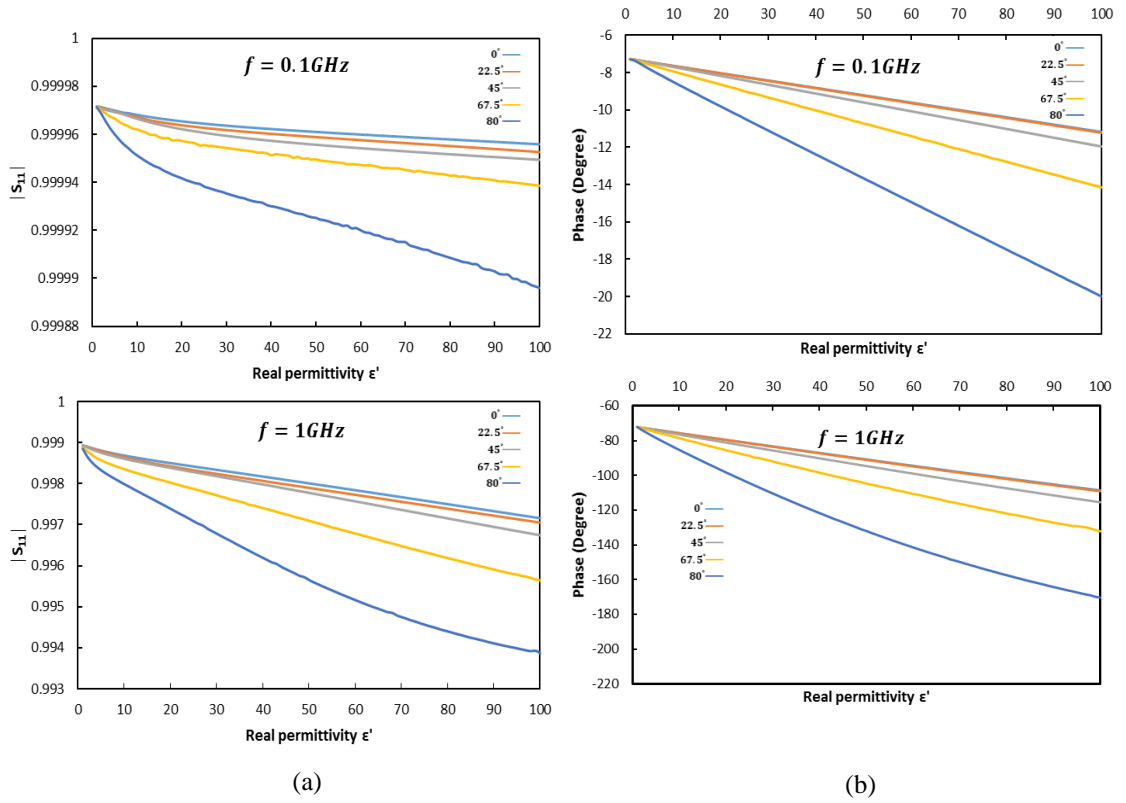


Figure 3.5: Simulated reflection coefficient of different probe aperture models with real permittivity sample, a) the magnitude, b) the phase at 0.1 and 1 GHz.

The sensitivity is higher at higher frequency  $f$  owing to a greater value of  $\frac{d|S_{11}|}{df}$  as shown in Table 3-1 and Table 3-2 when frequency increases by ratio of 10.

Table 3-1 Relative sensitivity (%) of probes at 0.1GHz to  $\varphi = 0^\circ$  in case of real permittivity.

0.1GHz								
$\epsilon_m$	$\varphi = 22.5^\circ$		$\varphi = 45^\circ$		$\varphi = 67.5^\circ$		$\varphi = 80^\circ$	
	$ S_{11} $	Phase	$ S_{11} $	Phase	$ S_{11} $	Phase	$ S_{11} $	Phase
	%	%	%	%	%	%	%	%
<b>3</b>	0.000028	0.02	0.000062	0.02	0.000215	0.75	0.000544	2.07
<b>10</b>	0.000089	0.09	0.00016	0.8	0.00061	3.86	0.0017	11.23
<b>50</b>	0.00022	0.27	0.000535	4.17	0.00114	16.5	0.0036	48.24
<b>100</b>	0.00033	0.4	0.000646	6.98	0.0017	26.55	0.00599	78.86

Table 3-2 Relative sensitivity (%) of probes at 1GHz to  $\varphi = 0^\circ$  in case of real permittivity.

		<b>1GHz</b>							
		$\varphi = 22.5^\circ$		$\varphi = 45^\circ$		$\varphi = 67.5^\circ$		$\varphi = 80^\circ$	
$\epsilon_m$	$ S_{11} $	<i>Phase</i>	$ S_{11} $	<i>Phase</i>	$ S_{11} $	<i>Phase</i>	$ S_{11} $	<i>Phase</i>	
	%	%	%	%	%	%	%	%	
<b>3</b>	0.00063	0.04	0.0032	0.3	0.02	0.92	0.03	3.38	
<b>10</b>	0.00414	0.11	0.01	1.1	0.03	3.82	0.07	12.75	
<b>50</b>	0.01	0.33	0.02	4.23	0.09	15.32	0.24	45.44	
<b>100</b>	0.015	0.49	0.04	6.33	0.15	21.76	0.33	56.87	

### 3.2.2.1.7 Probes sensitivity examination by the EMPro

A three-dimensional geometry of the bevelled coaxial probes was implemented in EMPro for detailed examination of the ability to distinguish the contrast of dielectric properties between different layers. The sensitivity test as a function of microwave frequency, cut angle of probe aperture and permittivity is accomplished numerically.

#### - As a function of aperture cut angle $\varphi$ , sample permittivity

The results of Figure 3.6 (a) and (b) were obtained by simulations using  $\varphi = 0^\circ$  and  $\varphi = 80^\circ$  probes. There is an obvious greater contrast in  $|S_{11}|$  with dielectric constant when using the  $\varphi = 80^\circ$  probe. The contrast with air is distinct even for materials with low dielectric constants such as hexane ( $\epsilon_r = 1.89$ ), as illustrated in Figure 3.6 (b). Additionally, Figure 3.7, Figure 3.8, and Figure 3.9 show the effects of aperture angle, frequency and lossless medium on sensitivity measurements as the sensor is inserted and move forward from air to material (i.e. two layers), and 0 mm distance is the interface region between the two layers as illustrated in Figure 3.10.

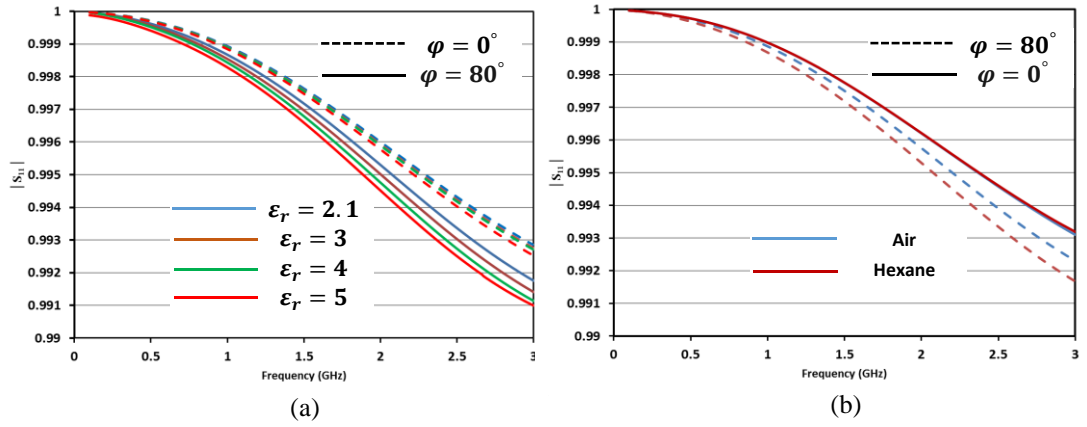


Figure 3.6: (a) Simulated comparison of the amplitude of the reflection coefficient for  $\varphi = 0^\circ$  and  $80^\circ$  with several values of the dielectric constant. (b) Simulated comparison of the  $|S_{11}|$  for air and hexane.

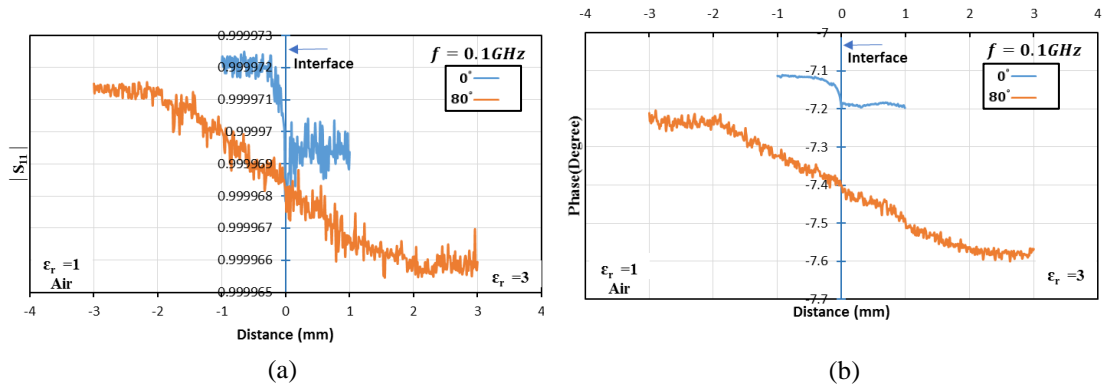


Figure 3.7: Simulated reflection coefficient of probe aperture  $\varphi = 0^\circ$  &  $80^\circ$  models with distance through two layers with  $\epsilon' = 1$  and  $3$ , a) the magnitude, b) the phase at  $0.1 \text{ GHz}$ .

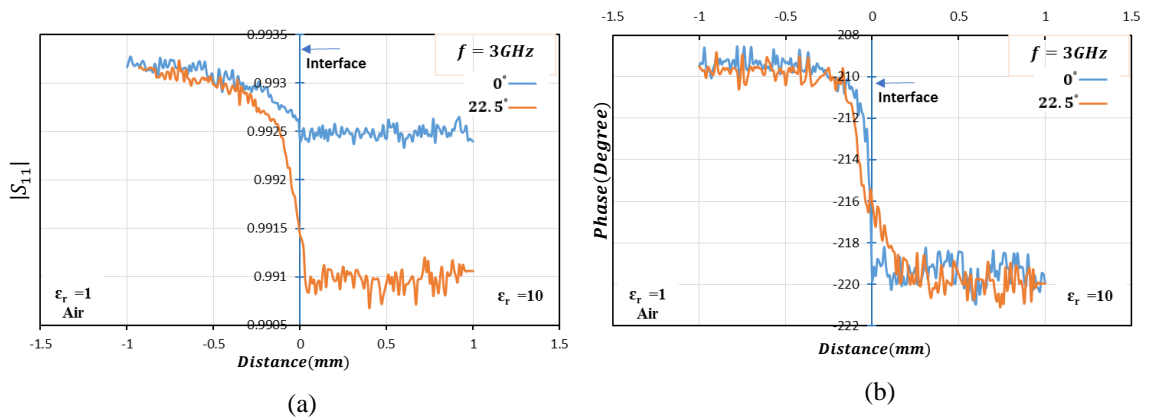


Figure 3.8: Simulated reflection coefficient of needle probes with aperture angles  $\varphi = 0^\circ$  and  $22.5^\circ$ , plotted as a function of distance between two layers with  $\epsilon' = 1$  and  $10$ , a) the magnitude, b) the phase at  $3 \text{ GHz}$ .

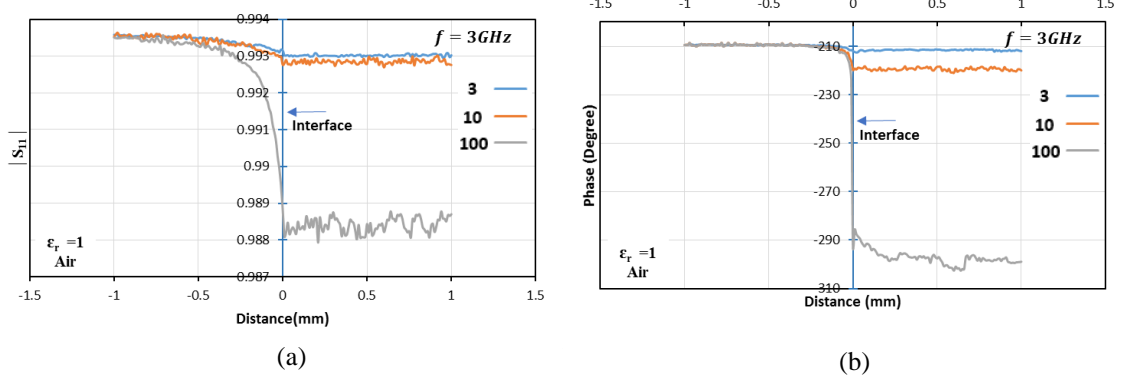


Figure 3.9: Simulated reflection coefficient with distance through two layers with  $\epsilon' = 1$ , and  $\epsilon' = 3, 10, 100$ , a) the magnitude, b) the phase at 3 GHz.

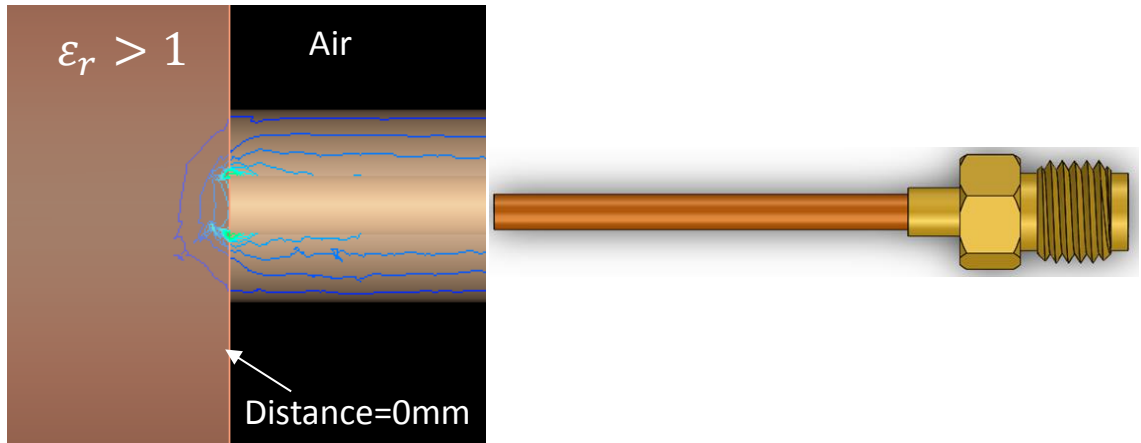


Figure 3.10: Diagram describes the two layers with interface region that presents 0mm distance.

A solution of the scattering from the open end of a coaxial line in contact with a lossy dielectric was presented by Mosig *et al.* [55]. In case of lossy media ( $\epsilon'' \neq 0$ ). If the electric field  $E$  is expressed as the gradient of a scalar potential  $\nabla\phi$ :

$$E = -\nabla\phi \quad (3.52)$$

then for the case of a harmonic field, Ampère's Law will be:

$$\nabla \times H = -(\sigma + j\epsilon * \omega) \nabla\phi \quad (3.53)$$

Here  $H$  is the magnetic field,  $\sigma$  the conductivity,  $\epsilon$  the permittivity and  $\omega$  is the angular frequency. Taking the divergence of the above equation gives:

$$(\sigma + j\epsilon\omega) \nabla^2\phi = 0 \quad (3.54)$$

which can be solved using finite element techniques to define the electric field penetration. In Figure 3.11 the medium in contact with the probe was assumed to be lossy with  $\epsilon' = 76.7$  and  $\epsilon'' = 11.18$ .

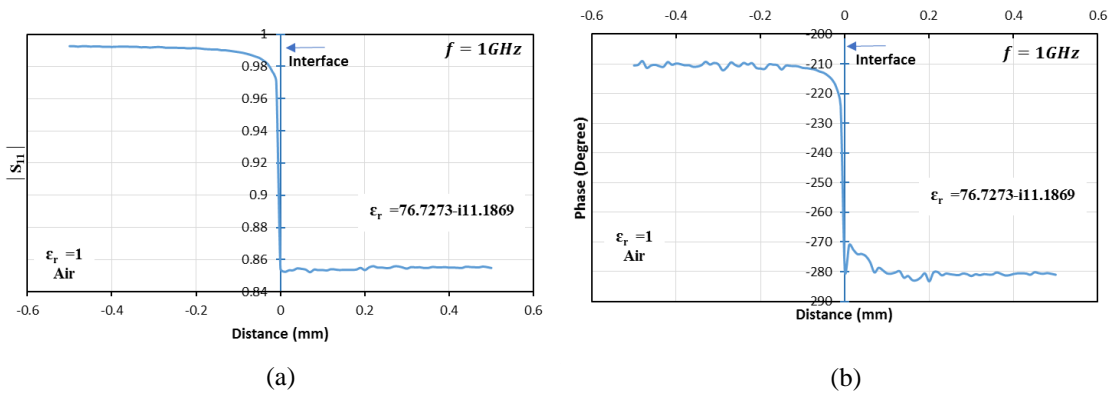


Figure 3.11: Simulated reflection coefficient of probe aperture with  $\varphi = 0^\circ$  with distance through two layers with  $\epsilon' = 1$  and  $\epsilon^* = 76.7273 - i11.1869$ , a) the magnitude, b) the phase at 3 GHz.

### – Human tissue phantom

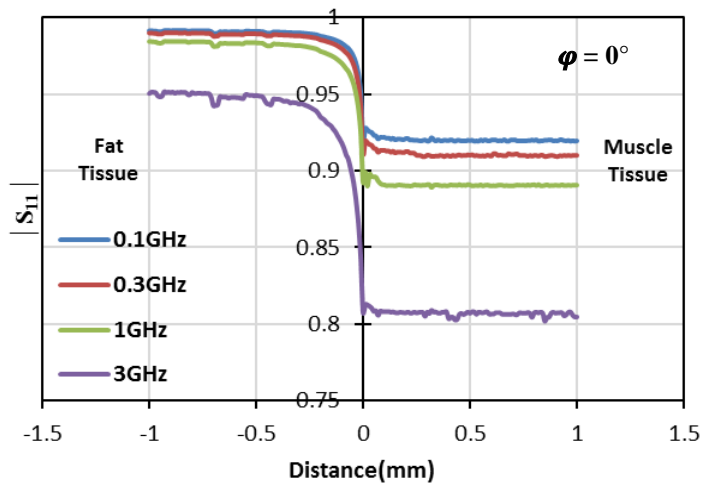


Figure 3.12: Simulated magnitude of reflection coefficient for probe aperture with  $\varphi = 0^\circ$  with distance through two layers with fat and muscle tissues, at 0.1, 0.3, 1, and 3 GHz.

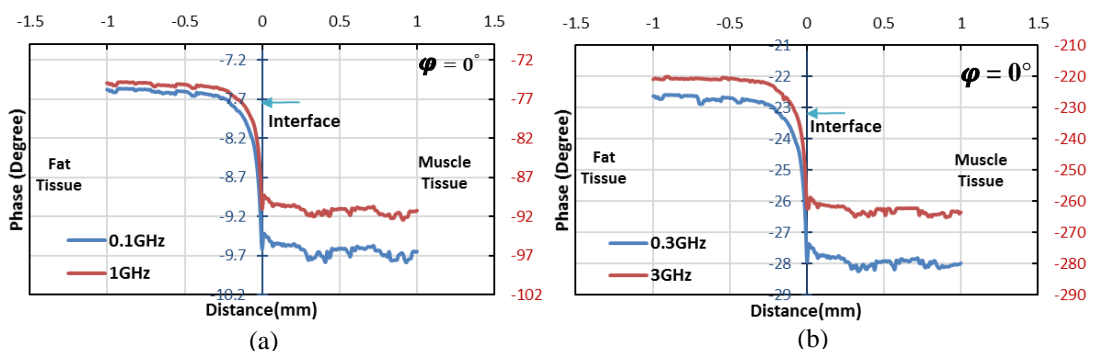


Figure 3.13: Simulated phase of reflection coefficient for probe aperture with  $\varphi = 0^\circ$  with distance through two layers with **phantom of fat and muscle human tissues**, a) at 0.1 and 1 GHz, b) at 0.3 and 3 GHz.

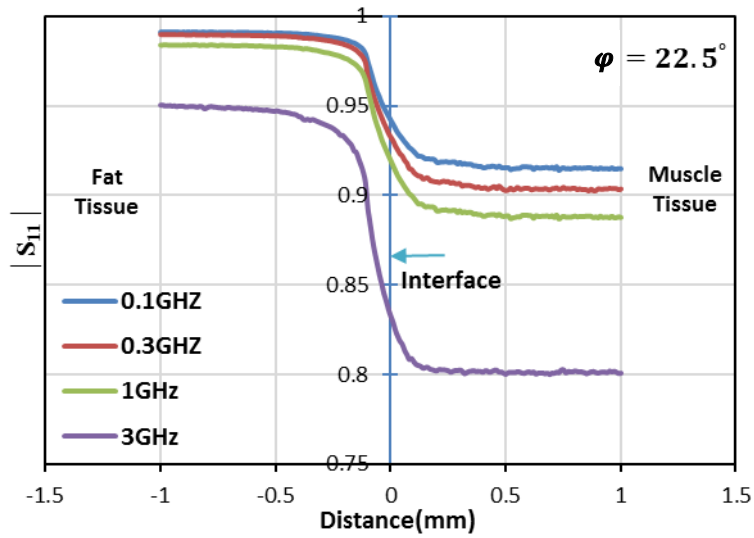


Figure 3.14: Simulated magnitude of reflection coefficient of probe aperture  $\varphi = 22.5^\circ$  models with distance through two layers with fat and muscle tissues, at 0.1, 0.3, 1 and 3 GHz.

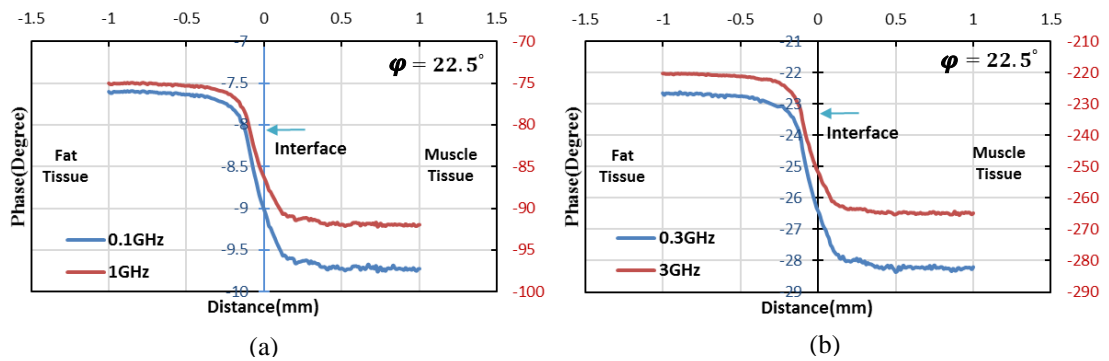


Figure 3.15: Simulated phase of reflection coefficient of probe aperture  $\varphi = 22.5^\circ$  models with distance through two layers with phantom of fat and muscle human tissues, a) at 0.1 and 1 GHz, b) at 0.3 & 3 GHz.

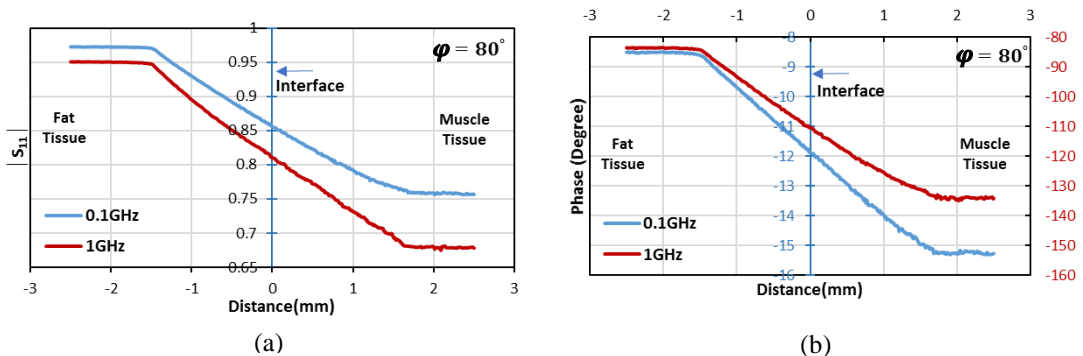


Figure 3.16: Simulated reflection coefficient of probe aperture  $\varphi = 80^\circ$  models with distance through two layers with phantom of fat and muscle human tissues, a) the magnitude, b) the phase at 0.1 and 1 GHz.

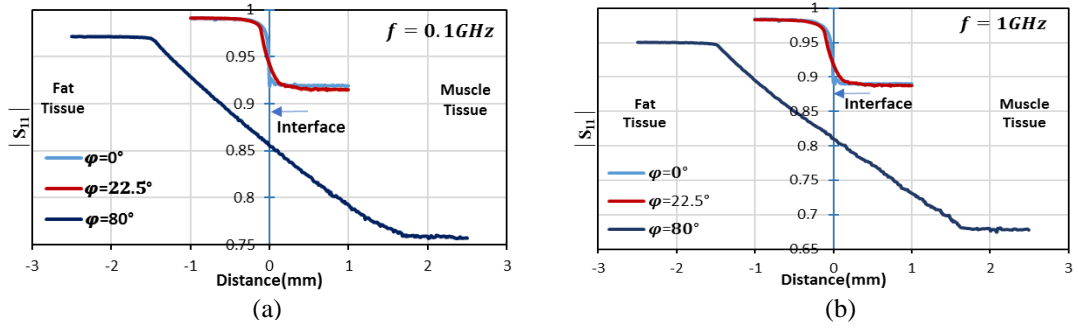


Figure 3.17: The Simulated magnitude reflection coefficient of probe aperture  $\varphi = 0^\circ$ ,  $\varphi = 22.5^\circ$  and  $\varphi = 80^\circ$  models with distance through two layers with phantom of fat and muscle human tissues, a) 0.1GHz, b) 1 GHz.

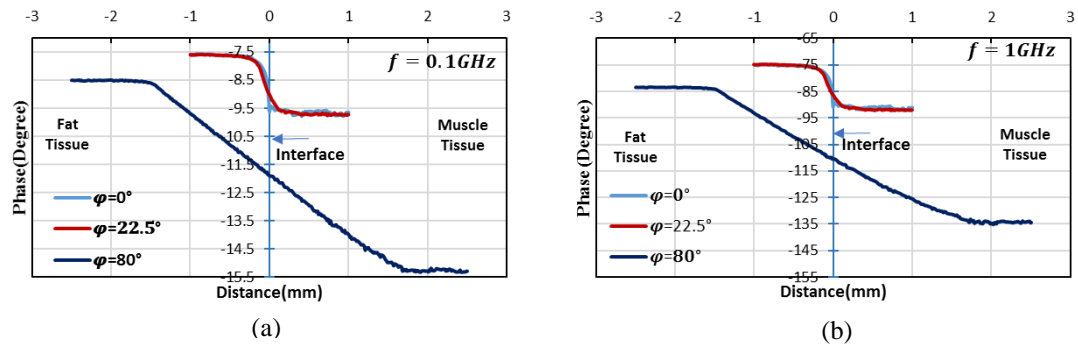


Figure 3.18: The Simulated phase reflection coefficient of probe aperture  $\varphi = 0^\circ$ ,  $\varphi = 22.5^\circ$  and  $\varphi = 80^\circ$  models with distance through two layers with phantom of fat and muscle human tissues, a) 0.1GHz, b) 1 GHz.

Table 3-3 Relative sensitivity percentage of  $\varphi = 0^\circ$ , at 0.3, 1, and 3GHz.

<b><math>\varphi = 0^\circ, f = 0.1 \text{ GHz as reference}</math></b>						
<b><math>f(\text{GHz})</math></b>	<b><math>f = 0.3\text{GHz}</math></b>		<b><math>f = 1\text{GHz}</math></b>		<b><math>f = 3\text{GHz}</math></b>	
	<b><math> S_{11} </math></b>	<b>Phase</b>	<b><math> S_{11} </math></b>	<b>Phase</b>	<b><math> S_{11} </math></b>	<b>Phase</b>
	%	%	%	%	%	%
<b>Fat</b>	0.13	198.28	0.71	887.69	4.06	2838.74
<b>Muscle</b>	0.92	190.41	2.92	846.66	12.21	2629.01

Table 3-4 Sensitivity percentage of  $\varphi = 22.5^\circ$ , at 0.3, 1, and 3GHz.

<b><math>\varphi = 22.5^\circ, f = 0.1 \text{ GHz as reference}</math></b>						
<b><math>f(\text{GHz})</math></b>	<b><math>f = 0.3\text{GHz}</math></b>		<b><math>f = 1\text{GHz}</math></b>		<b><math>f = 3\text{GHz}</math></b>	
	<b><math> S_{11} </math></b>	<b>Phase</b>	<b><math> S_{11} </math></b>	<b>Phase</b>	<b><math> S_{11} </math></b>	<b>Phase</b>
	%	%	%	%	%	%
<b>Fat</b>	0.17	198.22	0.72	887.5	4.19	2839.83
<b>Muscle</b>	1.08	189.28	2.99	845.03	12.33	2615.32

Table 3-5 Sensitivity percentage of  $\varphi = 80^\circ$ , at 1GHz.

$\varphi = 80^\circ$ , $f = 0.1 \text{ GHz as reference}$		
$f = 1\text{GHz}$		
$f(\text{GHz})$	$ S_{11} $ %	<i>Phase</i> %
<i>Fat</i>	2.23	881.24
<i>Muscle</i>	2.06	789.43

### 3.3 Experiment

#### 3.3.1 Probe design and feasibility analysis

In this method, the sample is placed against an aperture of the sensor and its reflection coefficient is simply measured. The complex permittivity of the material is then calculated using an equivalent admittance model of the coaxial sensor [72]. The schematic diagram of the needle-type open ended coaxial sensors used in the experiments is shown in Figure 3.19. Critical studies of open ended coaxial sensor have been discussed by Grant [69] . However, his paper did not thoroughly discuss the electric field distribution inside the coaxial line.

##### - Configuration and dimensions coaxial sensor

In this thesis, an open-ended coaxial probe has been constructed from a semirigid  $50 \Omega$  coaxial cable (RG405), which is available commercially, and fabricated to measure the reflection coefficient. Figure 3.20 shows the side sectional view of the fabricated coaxial probes. The aperture of coaxial probe has an inner diameter  $2a = 0.51 \text{ mm}$ , dielectric (Teflon) diameter  $2b = 1.68 \text{ mm}$  and outer conductor diameter  $2.21 \text{ mm}$ . The side sectional view shows the cut angle  $\varphi$  and length  $L = 20 \text{ mm}$  semi-rigid coaxial cable equipped with a female-type SMA plug connector. The permittivity of the cable section was taken to be 2.05. Typically, the coaxial cable was machined flat and polished to form an open surface end. Then, four different elliptical cut apertures with  $22.5^\circ$ ,  $45^\circ$ ,  $67.5^\circ$  and  $80^\circ$  degrees were fabricated to resemble the sharp end of a needle, as shown in Figure 3.19.

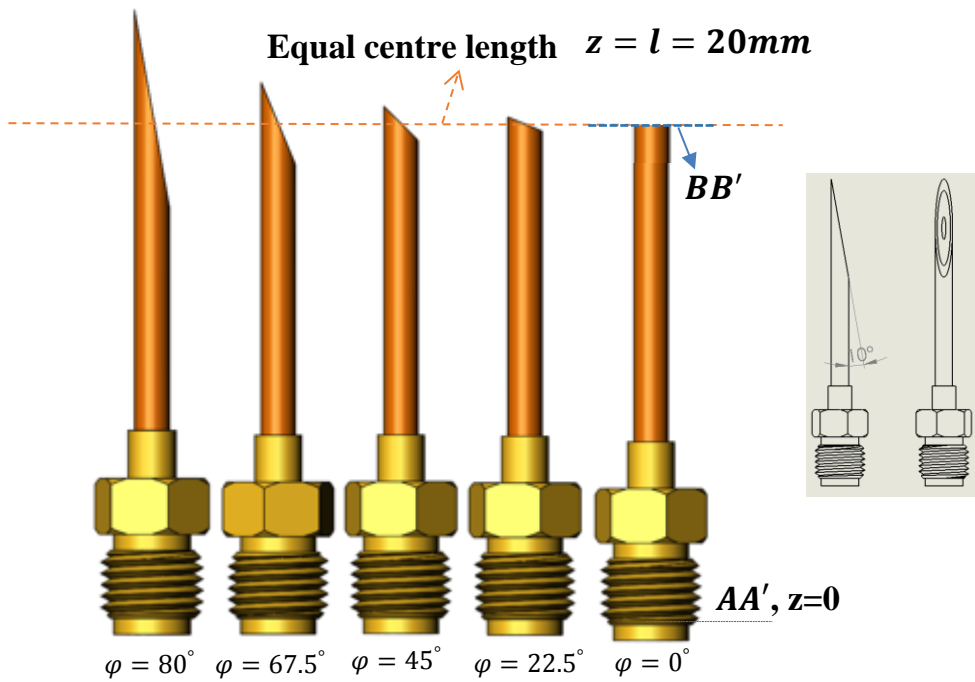


Figure 3.19: Open-ended coaxial probes with different apertures.

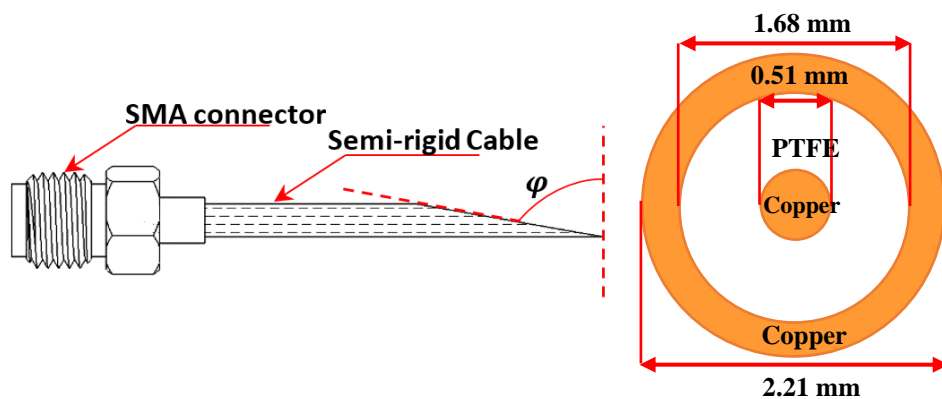


Figure 3.20: The side sectional view and front sectional view.

### 3.4 Experimental set-up

The experimental setup that was used during the research is shown in Figure 3.21 and Figure 3.22. It comprises five needle-type coaxial probes, with different ending angles,  $0^\circ$  (flat),  $22.5^\circ$ ,  $45^\circ$ ,  $67.5^\circ$ , and  $80^\circ$ . An Agilent PNA-L network analyser (N5232A) incorporating its own scattering parameter test set with frequency range between 300

KHz and 20 GHz, was used for measuring both amplitude and phase of  $S_{11}$ . A computer running a bespoke Labview program was used to control the measurements. The frequency range of the measurements was 100 MHz – 3 GHz with a 3 MHz step (1000 points). The calibration of the network analyser was done by the standard Agilent 85052D calibration kit using the SOLT technique to the plane of the SMA connector, as shown by the dashed line at the SMA connector in Figure 3.22. The measurement system used here to measure the reflection of various dielectric materials consisted of two different parts. The first part is used to measure the complex relative reflection coefficient of different samples with the use of probes of different aperture shapes, and to compare with the results obtained by simulation.



Figure 3.21: Photograph of the microwave sensors.

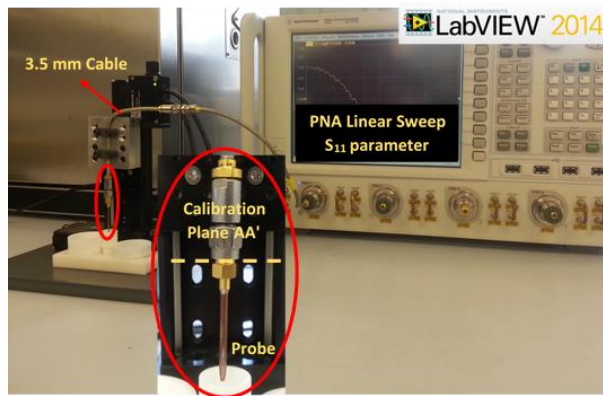


Figure 3.22: Photograph of measurement set-up connected to microwave performance network analyser (PNA).

The second part aims to examine the sensitivity of each aperture to stratified layers. Consequently, the effects of the cut angle of the elliptical aperture have been studied and reported numerically and experimentally. In this measurement setup,  $2 \times$  T-LSM050A motorized stages shown in Figure 3.23, with 50 mm travel per axis, were utilized. The two stages can be bolted together in whatever configuration is required. In this research purpose, they were configured as an XZ system. Adapter plates for fixing the sensor and horizontal platform for a sample's holder were machined. The resolution of these stages is  $0.048 \mu\text{m}$  and repeatability is  $< 1 \mu\text{m}$ , which is more than acceptable for our application. Both stages can be controlled simultaneously by the Labview program. In addition, a specific holder was customized for the measurement of a selected sample. The customized holder was made from a PTFE material with different sizes which were mounted on nylon platform. The probe has a movable platform which was mounted on a very precise stand, as shown in Figure 3.22. A sample was placed into a holder at the centre of the platform. The sample was placed on a nylon platform, and moved forward to the aperture of the coaxial probe by using a thumb screw, or is controlled automatically by the stage. The cut angle surface of the probe was used as a probe guide to ensure that the probe aperture was fully immersed in the sample.

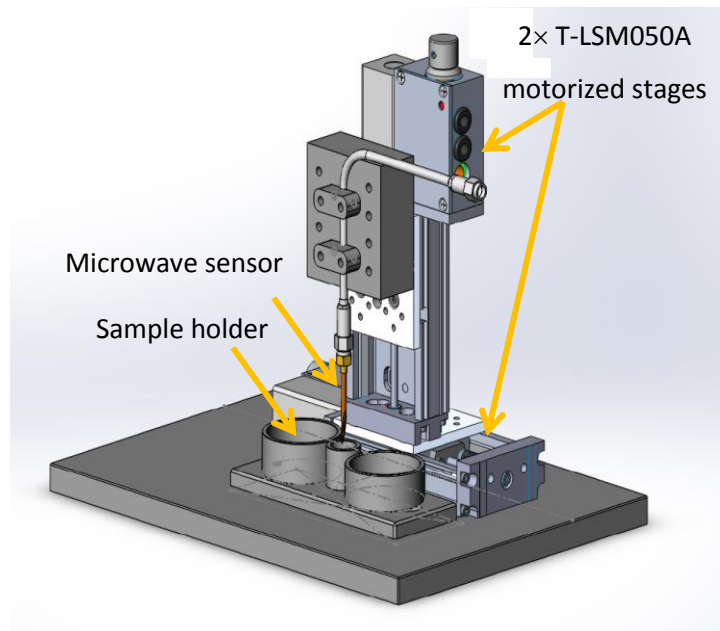


Figure 3.23: 2× T-LSM050A motorized stages.

– **Reflection coefficient measurement with constant distance**

In this section, the complex reflection coefficients of water, methanol, acetone, ethanol, and chloroform are presented experimentally over the frequency range of 0.1 to 3 GHz by using the flat and different needle-type coaxial probes. Then, air measurements were taken for each probe and followed by the probe immersed fully in each liquid. Each sample was immersed and measured three separate times with standard deviations across the samples obtained at each measured frequency. The stimulus had a 1000 point linear sweep between 0.1–3 GHz, an IF Bandwidth of 1kHz, input power of 0 dBm and 32 times averaging. Consequently, the random systematic errors associated with the reflection coefficient are very low. The sample was left on the probe tip to settle for 2 minutes with averaging restarted prior to the measurement. For the careful measurement of the reflection coefficient of samples, it was noticed that the probe should not move at all during the measurement and the position of the probe also should be the same for different samples.

Figure 3.24 shows in sequence the relative complex reflection coefficient at the aperture for water, methanol, acetone, ethanol, and chloroform. Those results show a good match between simulated and measurement results. In each case the experiment should follow a systematic procedure that will enhance the reproducibility of the results. This may be outlined as follows: The calibration process was carried out after the network analyzer had an initial warm up period of approximately an hour. The measurements were repeated three times with three different probes which have same aperture angle, for each probe using the same procedures. Several runs for each probe with the same sample were taken to allow the deviation of results to be examined. The measurement in all figures incorporate a systematic error due to multiple reflections by the uncalibrated probe connector, the effects of which cause the measured reflection coefficient to oscillate about the actual value, this effect becoming more apparent at high frequencies.

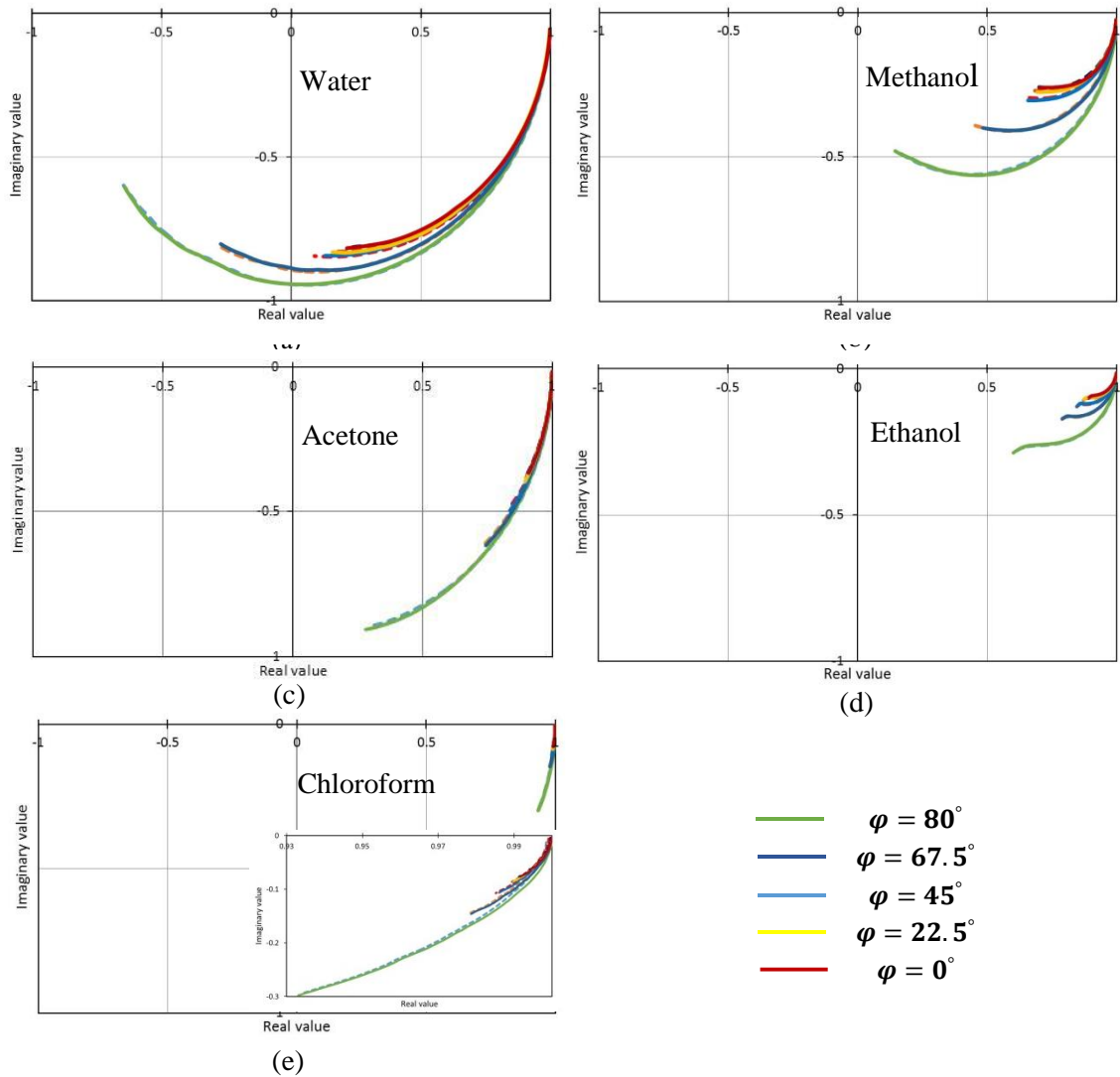


Figure 3.24: Simulated (dashed line) and measured (solid line) relative complex reflection coefficients resulting by different probe apertures at 0.1 to 3 GHz of, a) Water, b) Methanol, c) Acetone, d) Ethanol, and e) Chloroform.

– **Reflection coefficient of two layers with distance sweep**

In order to test the relative merits of each probe, experiment and simulation distance sweeps of 10  $\mu\text{m}$  steps were performed with air as the first layer followed by beef fat as the second layer, considered to have a very low permittivity.

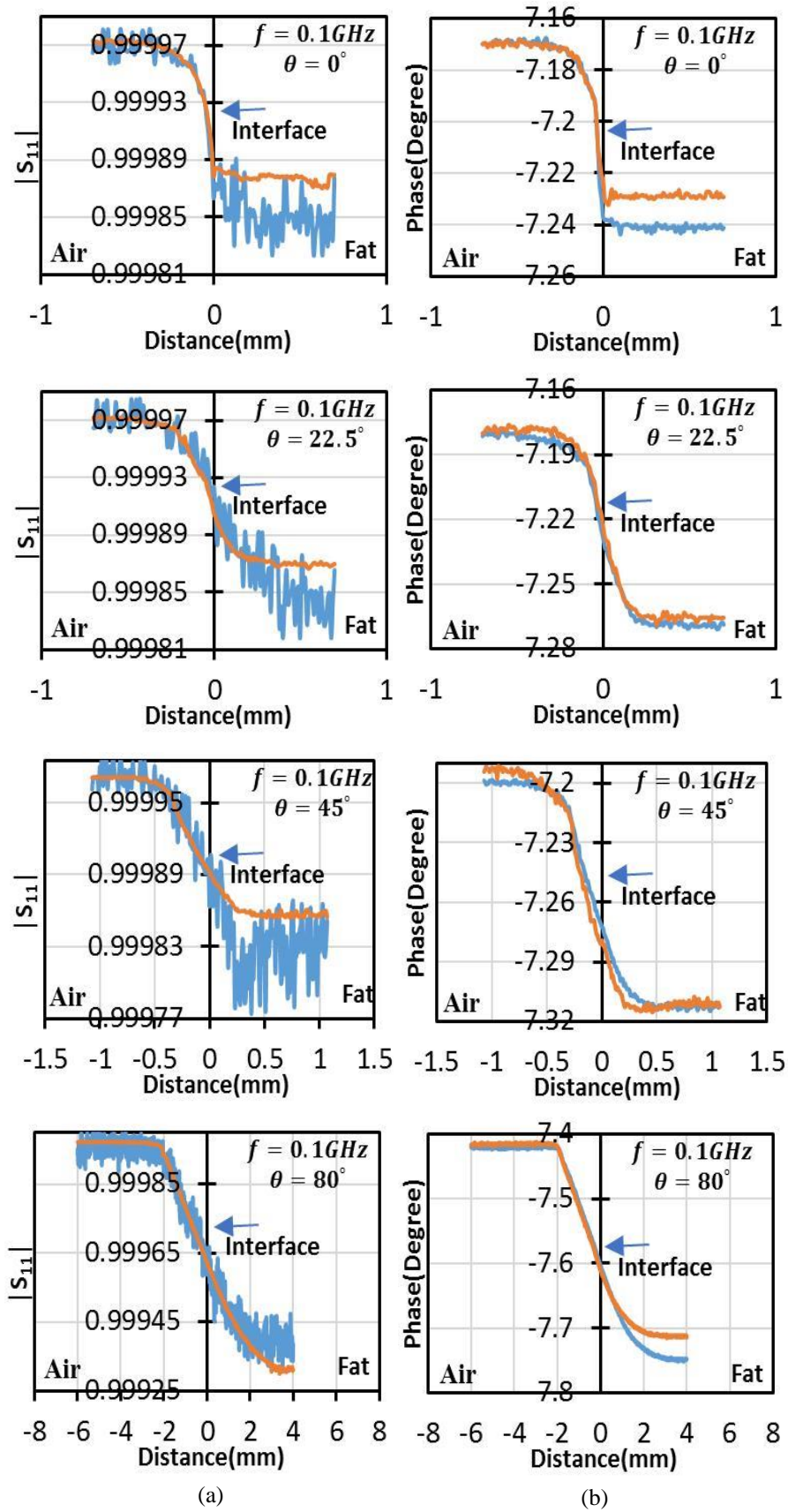


Figure 3.25: Simulated (orange line) and measured (blue line), a-  $|S_{11}|$ , b- Phase at probe aperture  $\varphi = 0^\circ$ ,  $\varphi = 22.5^\circ$ ,  $\varphi = 45^\circ$ , and  $\varphi = 80^\circ$  with distance sweep through two layers of air and beef fat, at 0.1 GHz.

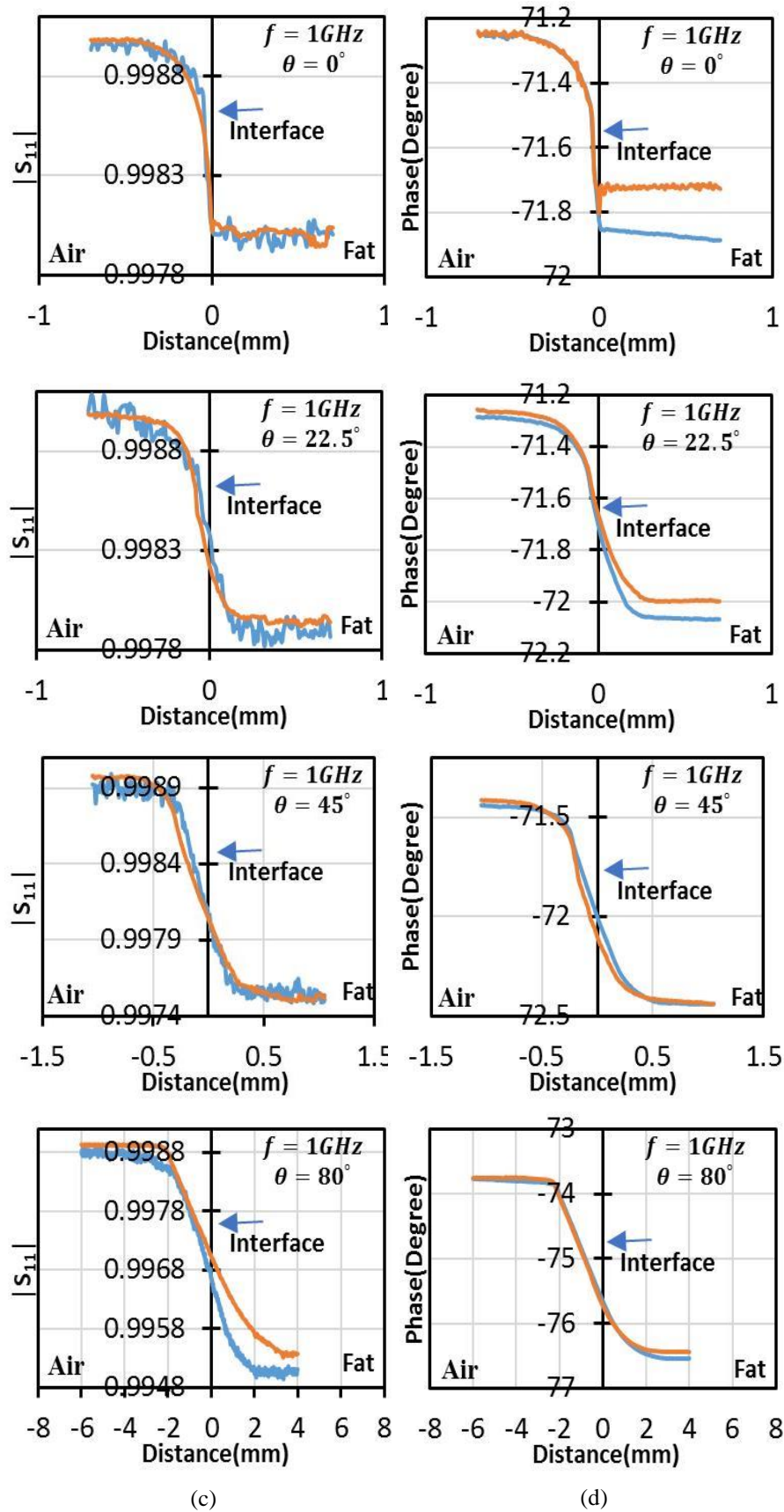


Figure 3.26: Simulated (orange line) and measured (blue line) c-  $|S_{11}|$ , d- Phase at probe aperture  $\phi = 0^\circ$ ,  $\phi = 22.5^\circ$ ,  $\phi = 45^\circ$ , and  $\phi = 80^\circ$  with distance sweep through two layers of air and beef fat, at 1 GHz.

### 3.5 Results and Discussion

The open end of the coaxial line was terminated by different samples with different values of complex permittivity and relaxation times, in line with those used in the simulations. Thus, the fringing field (over the sensing area  $\approx \pi b^2$ ) [73] from the coaxial probe aperture was sufficiently covered by the sample. This can be applied based on the principle that the different signals are reflected from the terminal surface of the sample at the coaxial aperture. Figure 3.6 (a) suggests that  $|S_{11}|$  varies with the microwave frequency and real permittivity for all probes over frequency range 0.1 to 3 GHz. Furthermore, the results assure the validity of improved sensitivity for the needle-type, open-ended coaxial probe and have sufficient accuracy for the measurement of low permittivity materials such as hexane at low microwave frequencies.

Figure 3.24 shows the comparison between relative complex reflection coefficients of different samples predicted by FEM with the measured data. The values of complex reflection coefficient given in Figure 3.24 are normalized to the free-space complex reflection coefficient  $S_{11\text{air}}$  to eliminate the additional phase change due to the electrical length of the probe itself. There are small differences in the values of reflection coefficient from the simulation and measurement results, but are mainly caused by the measurement uncertainties of the dimensions of the sensor aperture in terms of flatness, some very small air bubbles in the liquid samples, the problem in the calibration of the tip of the probe and the relative permittivity of the material, as well as fluctuations in the ambient temperature. Fluctuations in the  $|S_{11}|$  and phase were less than 5% of their average value.

As the complex permittivity decreases, the relative complex reflection coefficient increases subsequently. The complex reflection coefficient curves obtained from the needle probes are very interesting for all samples. The liquid materials that were tested in this research have all been studied previously and their dielectric behaviour is well documented. Values of the Debye parameters for these solvents at an ambient temperature of 25 °C were taken from [74-76]. For methanol, the sensitivity in  $|S_{11}|$  and phase parts of the relative complex reflection coefficient becomes significant as the aperture angle and frequency increases gradually in comparison with flat probe, as shown in Figure 3.27. It can be seen that the flat aperture probe exhibits lower sensitivity to the sample permittivity than the needle aperture probes. This contrast is far

greater when the angle of the aperture,  $\varphi$ , is stepped from  $0^\circ$  to  $80^\circ$ .

The numerical and experimental variations in the magnitude,  $|S_{11}|$  and the phase of the reflection coefficient with distance sweep, moving from an air layer to beef fat layer, for 0.1, 1, and 3GHz microwave frequencies and varying aperture angles are illustrated respectively in Figure 3.25 and Figure 3.26. These findings clarify the obvious contrast for both  $|S_{11}|$  and phase between the air and beef fat with comparison with the predicted results. As the cut angle increases the sensitivity increases dramatically for both magnitude and phase. The numerical results revealed that the  $|S_{11}|$  and phase of reflection coefficient are assumed to be constant as long as the probe sensing area was totally covered by the sample. Slight fluctuations can be observed in the numerical modelling which were mainly caused by the variations in the mesh density within critical areas for the simulation, e.g. at the surface of the centre conductor.

The measured data of  $|S_{11}|$  are less precise than for phase when measuring low loss materials. It is also observed that the data for  $|S_{11}|$  are less sensitive to the change of permittivity at low frequency than the phase. Obviously,  $|S_{11}|$ , is not quite a suitable parameter to monitor the contrast at 0.1GHz with small cut angle based on these measurements. In contrast, the sensitivity in phase, with respect to permittivity, is quite high for all the frequencies. Therefore, it is suggested that the phase of reflection coefficient is the most flexible and reliable parameter at low frequency, permittivity, and aperture angle. In general, as probes become more needle-like, the magnitude and phase decrease significantly and as result the sensitivity increases since the sensing area increases distinctly for  $\varphi=80^\circ$ . Finally, the results proclaim the success of this approach by showing measurements performed on liquids of known dielectric properties.

#### - **The modelling analysis of a probe with an internal discontinuity**

It is important to mention that there was a discrepancy between the experimental values and the FEM values that have obtained from EMPro of the reflection coefficient for  $\varphi = 0^\circ$ . The difference is around 8% in the case of the 0.1GHz while 3GHz is slightly higher. This may be explained in two ways. Firstly the simulation is run under absolutely perfect conditions. That is, the dimensions of the probe constructed may drift due to the errors introduced in the manufacture by both man and machine. Secondly the probe measured is vulnerable to experimental wear and tear which cannot be accounted for in the EMPro model. This error can be influenced by scratches on the face of the

probe or the Teflon. However, without taking these details into account the magnitude and phase of the reflection coefficient calculated deviates from the experimental less than 8%. The discrepancy in the FEM results can be accounted for by the SMA connector. Also the same situation exists that was discovered in the analysis of the needle probes, that is there must be a small fringing effect, at the internal discontinuity with the fabricated probe. To calibrate the modelled probe with the fabricated one, a small length of 1mm was added to the original length of 20 mm of the modelling probe, with slightly different characteristic impedance of  $51\Omega$  to emulate the effect of a slight mismatch due to the SMA connector. In addition, three probes from each probe were fabricated to minimize such error resulting through the fabrication process.

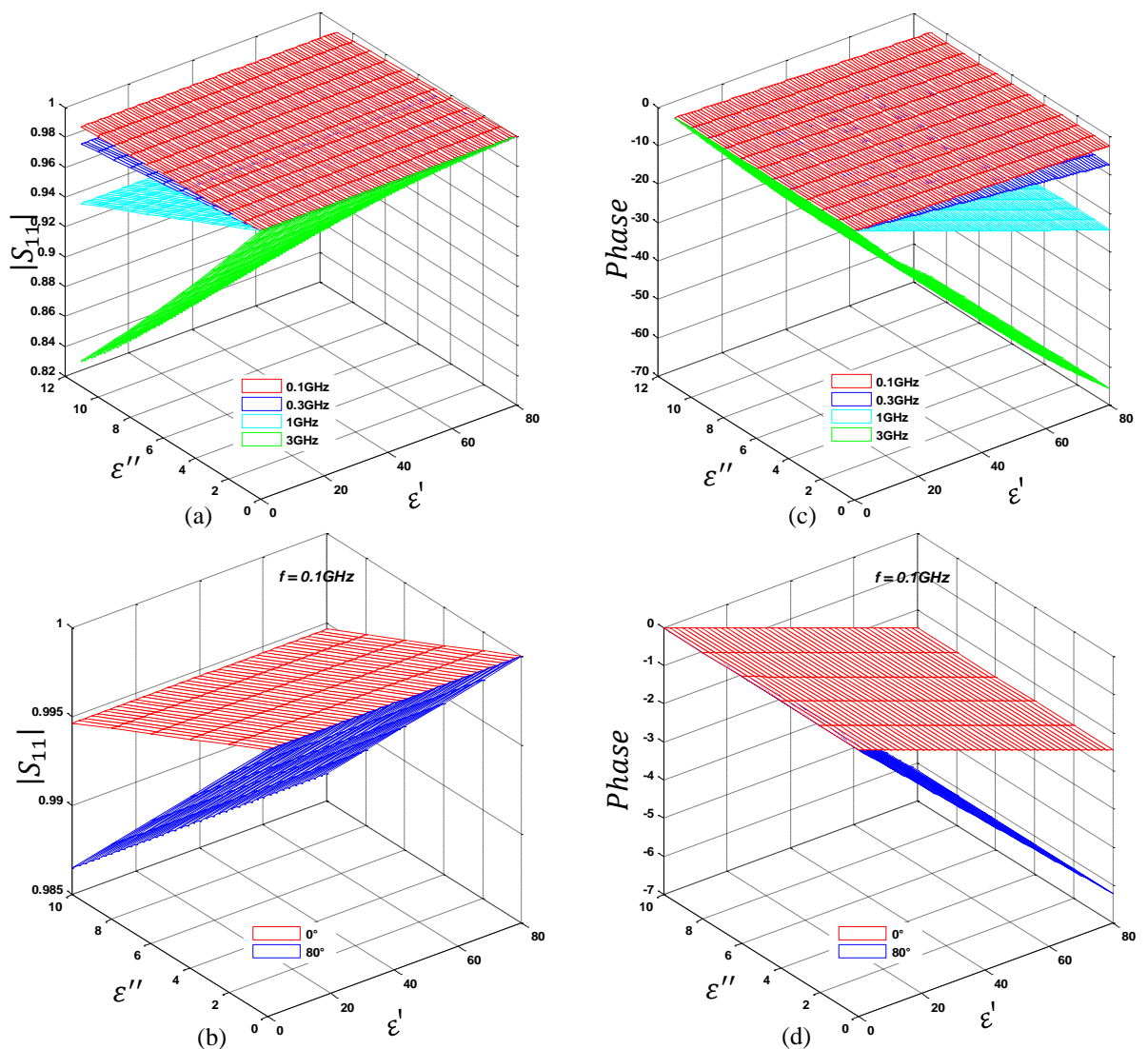


Figure 3.27: Plot of the  $|S_{11}|$  of the relative complex reflection coefficient as a function of permittivity, a-  $|S_{11}|$  of open-ended probe at 0.1, 0.3, 1, and 3 GHz, b-  $|S_{11}|$  of  $\phi = 0^\circ$ , and  $\phi = 80^\circ$ , at 0.1 GHz. Plot of the phase of the relative complex reflection coefficient as a function of permittivity, c- phase of open-ended probe at 0.1, 0.3, 1, and 3 GHz, d- phase of  $\phi = 0^\circ$ , and  $\phi = 80^\circ$ , at 0.1 GHz.

## **CHAPTER 4 BREAST CANCER DIAGNOSTIC TOOL USING A MICROWAVE NEEDLE PROBE**

It is argued here that unless one has a sound and clear understanding of the fundamental steps in the interaction of microwaves with various tissues and a thorough understanding of how to manipulate various microwave sensors for measurements purposes, the so-called ‘tinkering’ with microwave sensors may not render acceptable results.

The use of the microwave electromagnetic wave bands to explore material properties needs the understanding of materials’ dielectric and conducting properties [77]. For biological tissues, there is a wide spectrum of information such as relaxation processes and orientational polarization of the molecules, all of which contribute to the tissue’s complex dielectric function and its variation with frequency and temperature.

Dielectric properties of normal and cancer tissues have been investigated using a needle-type microwave sensor. The objectives of this study are to investigate the optimum needle-type sensor as a function of contrast between normal and cancer tissues, and to show that microwave technology produces high sensitivity comparing with those produced by other technologies.

Recently, many studies show the potential of microwaves as diagnostic tools for early stages of cancer disease and associated with the property contrast with normal tissues.

In this chapter, the results of a study of the dielectric properties of various cancer and normal tissues as a function of microwave frequency and aperture angle were discussed. To perform this task, first we studied the dielectric properties of cancer tissue namely: breast cancer. Subsequently, the ability of microwaves to detect, and the role of frequency in this detection is presented.

## **4.1 Microwave cancer diagnostic techniques**

The main attractions of microwaves in the diagnosis of tumours are the innocuous nature of this type of energy at low levels, the relatively low cost of even complex microwave systems compared to the computer-assisted tomography (CAT) and magnetic resonance imaging (MRI), and the distinctly different permittivity of tumour tissue compared to normal tissue. An additional feature is the availability of a relatively wide range of frequencies. Thus, multi-frequency systems can be developed; as well, the frequency of a given system can be tailored to the application.

A general objective of microwave diagnostic applications is to use the difference between the permittivity of diseased tissue and healthy host tissue to detect abnormality and its location. The aim has been to develop a microwave method that is competitive with existing diagnostic techniques, such as CAT, MRI, or mammography. In addition to active microwave systems to detect tumours, passive microwave radiometry has been explored for this purpose [78, 79]. The principle of operation relies on an increased tumour temperature compared with healthy breast tissue. Microwave systems offer an advantage over infrared methods, as they penetrate much deeper.

In addition to radiation, another important use of microwave energy in medicine is for the thermal ablation of tissue. In this application, microwave energy is used to create localised dielectric heating (diathermy) resulting in controlled destruction of tissue; this will be discussed in more detail in Chapter 5.

Microwave ablation also provides desiccation of tissue without the excessive charring and nerve damage associated with RF ablation. Various applications include treatment of large tumours or removal of unwanted tissue masses, for example liver tumours, lung tumours and prostate ablation. Microwaves can also be used to coagulate bleeding in highly vascular organs such as the liver and spleen. Finally, using microwave technology in medicine has provided a solution for getting information about many diseases, especially for detection of malignant tumours inside a human body.

### **4.1.1 Microwave thermography**

Microwave thermography is a technique which allows estimation of internal body temperatures from measurement of the natural thermal radiation emitted by body tissues

[80]. This technique has a number of potentially important medical applications for the detection, diagnosis and treatment monitoring of diseases which produce regional or localised temperature changes in the body's normal temperature distribution. For instance, initial studies of its clinical application have included osteo-articular diseases, vascular disorders, diseases of the acute abdomen, and cancers in the breast, thyroid and brain [81], [82], [83], [84], [85]. Microwave thermography, in contrast to other thermographic imaging techniques, detects electromagnetic radiation which has penetrated medically useful distances, of the order of several centimetres, through body tissues, thus allowing a passive, non-invasive measurement of subcutaneous temperatures [86], [87]. For example, microwave thermography systems operate at frequencies of 3 — 3.5GHz, and allow a reasonable penetration depth (about 0.8cm in muscle, and about 5cm in fat), and reasonable lateral spatial resolution (about 0.7 to 2cm near the antenna) [33].

#### **4.1.1.1 Microwave thermography in breast disease**

A promising application of microwave thermography is in the detection of early (asymptotic) breast cancer. A very large number of women develop breast cancer at some point throughout their lives. Despite widespread publicity about self-examination, it is unusual for women to present with lesions at a curable stage: most women are diagnosed with symptomatic breast cancer, too late to have any chance of being cured. The only real hope in these circumstances lies in regular screening of women at risk [88].

There is clearly a need for new screening methods such as microwave thermography to provide aid in clinical diagnosis. Microwave thermography should be particularly useful when used in younger women who are more likely to have dense glandular tissue in which detection of lesions by mammography is difficult; and also as a preliminary screening method to identify high risk women who may then be given mammography. This would reduce the number of women exposed to X-rays and the risk associated with this.

Breast cancer detection is one of the important applications of microwaves in biomedicine. It has been demonstrated that there exists an obvious contrast between the relative permittivity of malignant breast tissues and normal breast tissues at microwave frequencies [89] as shown in Figure 4.1. Also, Chung-Kwang Chou *et al.* recognized

that tumours have different dielectric properties that vary from those of normal tissue [90].

Several studies of the electromagnetic dielectric properties of biological tissues at microwave frequencies have shown that the dielectric constant contrast between malignant and benign breast tissues is adequate to advise microwaves as a useful diagnostic tool for early stage breast cancer detection [1, 91-93].

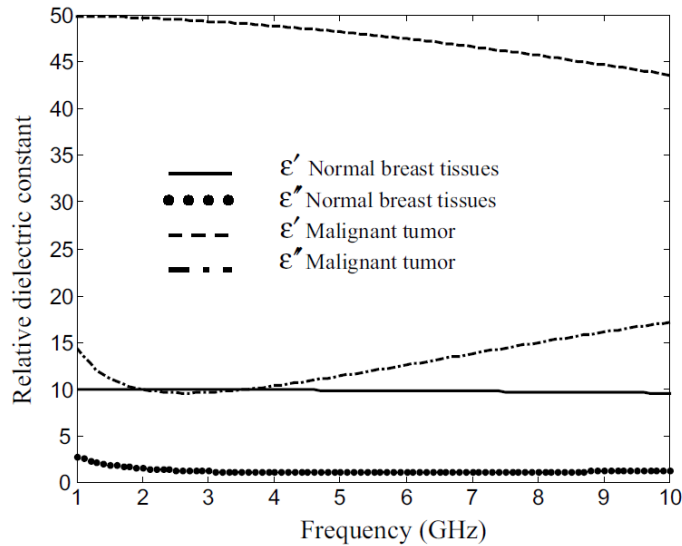


Figure 4.1: The relative dielectric constant versus frequency for normal and malignant breast tissue [94].

Thus, in order to permit the design and predict the range and safety of a microwave hyperthermia treatment system, biophysical data, including high frequency relative permittivity and electrical conductivity, are needed. It is extremely important that values and ranges for normal and pathological tissues are established [95], [96], [97], [98].

#### 4.1.2 Microwave tomographic techniques

Microwave tomography is another area in which knowledge of the dielectric properties of tissues is essential. This is an active imaging technique for temperature or dielectric measurement using an inverse scattering reconstruction. The tissue region of interest is illuminated by a known microwave source, and the microwave field scattered by the tissue is measured; this potentially allows a reconstruction of the dielectric structure of the illuminated tissue. Equipment has been developed at 3GHz and at 2.45GHz, [99], [100], [101], [102]. In order to understand local field variations in the tomographic reconstruction, a good knowledge is needed of the microwave properties of tissues and

their temperature variation [100]. One possible area of expansion with tomographic techniques is detection of breast cancer. If carcinomas within an individual exhibit dielectric properties sufficiently different from normal tissues in the same individual, it may be possible to detect them by dielectric retrieval. Knowledge of the dielectric properties of breast cancers would be essential for this field of application.

## **4.2 Biological tissue structure and composition**

Biological tissue is a complex mixture of water, ions, membranes, and macromolecules of a wide range of shapes and sizes. The main component of biological materials is water, accordingly; tissue electrical parameters can be divided into two groups: high water content, including muscle, blood, and organs; and low water content, including fat and bone [103, 104]. These two groups are generally referred to as the muscle or the fat tissue cases. The biological materials have complicated electrical response and do not behave like simple mixtures of components. Significant effort has been developed into determining the permittivity values for various tissue types. The relative dielectric constants of these tissues have been extensively researched, and various mathematical models have been developed [92].

The mechanisms of the interaction are quite understood, the theory underpinned by experimental data and forming part of a well-established classical theory of bioelectrical phenomena. This phenomenon is seen in Figure 4.2, where the generalized curves have four distinct regions of decreasing dielectric constant, called  $\alpha$ -dispersion,  $\beta$ -dispersion,  $\delta$ -dispersion, and  $\gamma$ -dispersion [104-107]. The main aspects of the dielectric spectrum of a biological tissue are described as follows [1]:

- The dielectric properties of tissues are highly frequency and temperature dependent.
- The relative permittivity of a tissue may reach values of up to  $10^6$  or  $10^7$  at frequencies below 100 Hz.
- It decreases at high frequencies [108] in three main steps known as the  $\alpha$ ,  $\beta$  and  $\gamma$  dispersions.
- The  $\gamma$  dispersion, in the gigahertz region, is caused by the polarization and relaxation of water molecules [109].

- The  $\beta$  dispersion, in the hundreds of kilohertz region, is mainly caused by the polarization of cellular membranes which act as barriers to the flow of ions between the intra and extra cellular media. Other contributions to the  $\beta$  dispersion come from the polarization of protein and other organic macromolecules.
- The low frequency  $\alpha$  dispersion, which is up to KHz, is associated with ionic diffusion processes at the site of the cellular membrane.

The frequency dependence of the complex permittivity in the  $\gamma$  dispersion region can be expressed as:

$$\varepsilon^*(\omega) = \varepsilon_\infty + \frac{\varepsilon_s - \varepsilon_\infty}{1 + (j\omega\tau)^{1-\alpha}} + \frac{\sigma_i}{j\omega\varepsilon_0} \quad (4.1)$$

The previous equation is the well-known Cole-Cole expression in which  $\varepsilon_\infty$  is the permittivity at  $\omega\tau \gg 1$ , and  $\varepsilon_s$  the permittivity at  $\omega\tau \ll 1$  and  $\alpha$  is a parameter describing some broadening of the dispersion;  $\sigma_i$  is the conductivity caused by ionic drift and to the lower frequency polarisation mechanisms.  $\tau$  is the relaxation time.

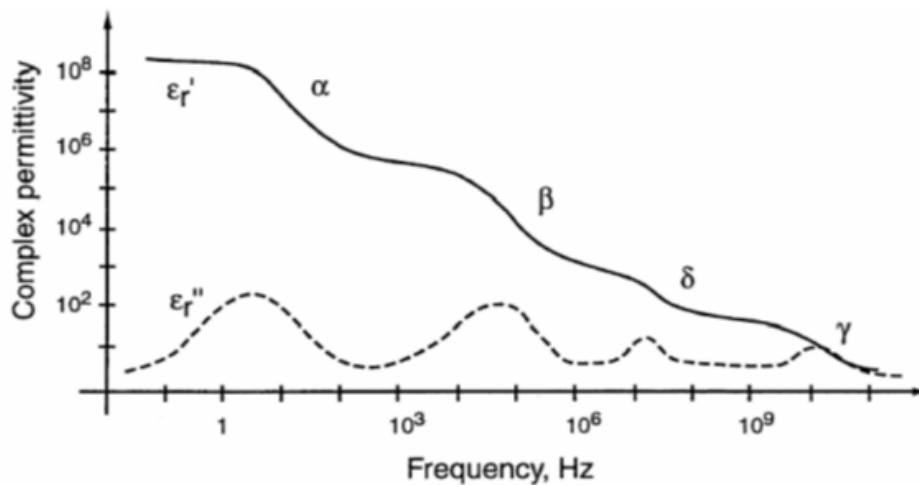


Figure 4.2: Dispersion regions in tissues depending on frequency [107].

The basic building block of all tissues is the cell, specialised for each different type of tissue to perform specific functions. The cell is made up of a mass of protoplasm, containing proteins, polysaccharides, nucleic acids and lipids, bound by a delicate membrane. Molecules of the protoplasm are suspended in water, known as intracellular water, which comprises about 75% of the mass of most living cells. The cells themselves are suspended in an aqueous environment, made up mainly of interstitial (or intercellular) water. In the human body intracellular water comprises 67% of its total

water content, interstitial water 25%. The remaining 8% is contained in plasma (extracellular water). A delicate balance exists between the constituents of these three types of fluid. They vary in ionic composition but plasma and interstitial may be treated as being 0.9% sodium chloride solution. Intracellular water has a very different ionic profile having a high concentration of potassium ions among others [110].

#### 4.2.1 Polarisation and relaxation theory

When tissues are subjected to high-frequency electromagnetic radiation, the polarization process, which is caused by the physical displacement of charge and takes time to develop, may exhibit a definite tendency to lag the applied field due to the extreme rapidity of the applied oscillation as shown in Figure 4.3. This difference in phase is generally referred to as relaxation [111]. This relaxation process generally becomes apparent when the applied field gives rise to a polarisation which lags behind the field and which relaxes at about the same rate as the field alternates.

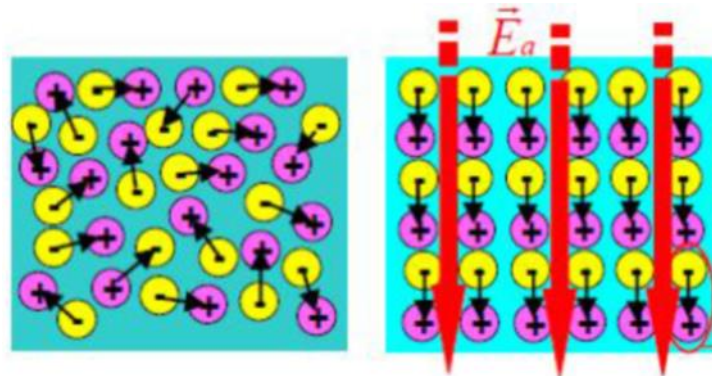


Figure 4.3: Electric polarization in a dielectric [112].

When an electric field is applied on a specific material, the complete polarization effect can be summarized in four distinct processes as follows:

- (a) Electronic polarization, which consists of the small displacement of the electrons relative to the nucleus. This process is extremely rapid, requiring on the order to  $10^{-15}$  seconds to reach equilibrium.
- (b) Atomic polarization, which entire atoms may each experience a small displacement with respect to each other. This is only a very small effect, requiring an approximately time of  $10^{-12}$  to  $10^{-14}$  seconds to reach equilibrium.

- (c) Ionic crystals may exhibit a small amount of polarisation, due to displacement of the lattice ions, requiring a time of about  $10^{-12}$  seconds to reach equilibrium.
- (d) The polarisation resulting from the orientation of permanent dipoles may have various equilibrium times to align themselves with the field depending on the state of the material. For small molecules of low viscosity, the time is from  $10^{-10}$  to  $10^{-11}$  seconds, for heavy viscous liquids it increases to about  $10^{-6}$  seconds, and on the order of minutes for some solids. Since the period of a microwave oscillation is on the order of  $10^{-10}$  seconds, a liquid dielectric, under the influence of microwave radiation, will show an appreciable effect resulting from permanent dipole polarization. This kind of polarization occurs at microwave frequency, and biological materials usually contain permanent dipoles and so potentially possess all three types of polarizability [113]. However, only orientational polarisation is important at microwave frequencies: the other effects occur at much higher frequencies of imposed field. Space-charge polarisation, which is not a dipolar effect, is also important at microwave frequencies, in particular at interfaces within a heterogeneous material. These will be discussed in more detail in the next two sections.

Debye [114] developed the original theory showing the functional relationship for the complex dielectric constant, permanent dipole moment, and relaxation time (i.e. a measure of molecules and dipoles mobility) [115]. There is a relationship between polarization and permittivity. In the presence of an electric field, as the permittivity increases, the ability of the material to polarize increases accordingly. Hence, permittivity is a measure of the amount of dipole moment density induced by an electric field [116]. Therefore, it effects the reflection of the electromagnetic waves at the interfaces and the attenuation of wave energy within materials.

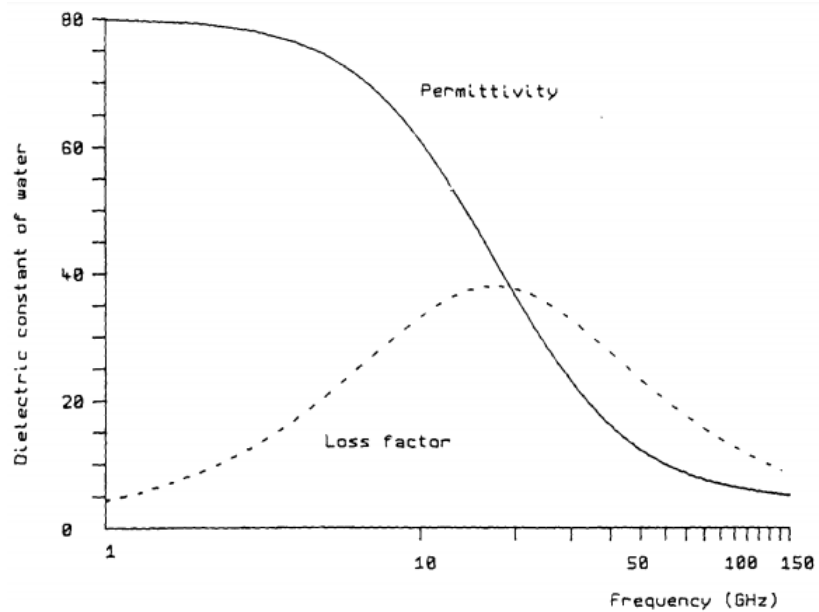


Figure 4.4: Debye dispersion of water at 20 °C [33].

#### - The permittivity of water tissue

The relative permittivity data of tissues were measured by many references and fitted by many models. Hurt presented multiterm Debye dispersion expressions which fit the relative permittivity data of muscle fibres, transverse and parallel to the applied electrical field from 10 Hz to 100 GHz [108]. Hurt's study showed that the permittivity of transverse muscle differs from that of parallel muscle only for frequencies below  $\approx 1$  MHz. Data and interaction mechanisms have been discussed in detail by Schwan [105], Johnson and Guy [117], and Geddes [118]. Other references on the interaction of alternating electrical fields with matter are Grant *et al.*[119], Presman [120], Schwan and Foster [121], Foster *et al.*[122], Stuchly [123], and Schwan [124]. Also, the dielectric constant and conductivity of actual muscle tissue at 37 °C can be obtained from the literature [90].

In 1977, Schwan and Foster reviewed the Dielectric permittivity and conductivity data for tissue over the frequency range of 0.1-10 GHz. This study demonstrated that the conductivity of muscle increases quadratically with frequency above 1 GHz, which suggested a Debye relaxation for tissue water centred at 20 GHz at room temperature. First, the high frequency dielectric properties of muscle predict that the tissue water exhibits a Debye dipolar absorption centred at 20 GHz at room temperature, identical to that of pure water as shown in Figure 4.4. Second, the increase in tissue conductivity

above 1 GHz in muscle, skin, and liver, corresponds to a free water content of roughly 70% of the tissue weight, comparable to the known water content of these tissues [125].

The most important reason of studying the biological effects of electromagnetic fields and measuring the physiological parameters is to extend the area of diagnosis and treatment in the biomedical field [111]. It is necessary to understand the dielectric properties of individual biological tissues. H. P. Schwan was a primary researcher involved in developing this understanding [126]. Today, Schwan's work is still broadly cited, and his understanding of biological permittivity helped pave the way for more sophisticated microwave biomedical fields, such as hyperthermia treatments and microwave thermography, which are effective methods for treating tumours.

### **4.3 Breast cancer diagnostic tool using microwave needle probes**

A new non-invasive technology utilizing microwave diagnostics with high spatial resolution at low frequency based on complex permittivity measurement of normal and cancerous tissues has been proposed using a needle-type coaxial probe (i.e. RG405 probe, which is about the same size as one of the standard hypodermic needle sizes ). An associated measuring system has been tested by simulation and experiment in chapter 3, to be used for distinguishing normal and cancerous breast rat tissues. Simulation results using EMPro software are provided here and demonstrated the potential of microwave needle-type sensors for breast cancer diagnostics. Since the extracted tissues were very thin they were measured experimentally using probes of end angles  $\varphi = 0^\circ$  and  $22.5^\circ$ . Dielectric properties of breast tissues were measured over the frequency range of 0.1 to 3 GHz. The contrast sensitivity of the reflection coefficient is found to increase with end angle. For example, compared with  $\varphi = 0^\circ$ , simulations for  $\varphi = 80^\circ$  at the low frequency end (0.1 GHz) show that the magnitude increases by 13.8% and the phase increases by 163%.

Microwave imaging has been recently developed as a time domain method for cancer diagnostics [127]. Imaging of the cancerous region relies on a high contrast in complex permittivity at microwave frequencies between cancerous and normal tissue, probed using ultra-wide band antennas which are compact in size and have low cross polarization characteristics [128]. In contrast to microwave imaging techniques,

microwave diagnosis utilizing an open-ended coaxial probe relies on frequency domain measurements of complex permittivity to characterize potentially cancerous tissue. The development of open-ended coaxial dielectric probes during the last two decades has facilitated the routine measurement of high frequency (i.e. >100 MHz) tissue dielectric properties in the case of human [26, 129] and animal studies [31, 130].

A flat open-ended coaxial probe technique from 0.5-30 GHz was utilized in reference [131] and reported noticeable differences in the conductivity and relative permittivity of cancerous and metastasized breast tissue relative to normal healthy breast tissue. Other extensive experimental tests have been done for examining the difference in complex permittivity between cancerous and non-cancerous breast tissue with flat open-ended coaxial probes [132-134]. After examining 319 samples from 196 patients over the range 0.5-20 GHz, the results show that large variations exist in the relative permittivity and conductivity when examining healthy breast tissue by itself [134]. This variation is due to the breast tissue non-homogeneity, since some portions contain more adipose tissue (low water content, low  $\epsilon_r$ ) while other portions contain larger amounts of fibroconnective and glandular tissues (high water content, high  $\epsilon_r$ ) [134]. As reported in [134], there is only a 10% difference in complex permittivity on average between high water content healthy tissue and cancerous tissue, making it almost difficult to distinguish between them.

These published results were produced through the use of flat open-ended coaxial probes with low spatial resolution. Although these instruments are generally considered to be the gold standard for characterizing electromagnetic properties of tissues because the tools can be validated against homogeneous samples of materials with known dielectric properties, this method has the disadvantage of its low sensitivity at low frequency and permittivity. This study introduces non-invasive, small diameter needle coaxial probes which offer higher sensitivity for an immediately distinguishing between normal and cancerous tissues. In fact, relatively few studies have reported on the use of the technique, aside from some liquid characterization [135]. The technique proposed here utilizes a microwave needle-type probe where multiple measurements at low microwave frequency are used in making the final decision on whether or not the tissue under test is cancerous as presented in Figure 4.5. The electrical properties of the breast tissues were calculated using the measured data from the needle probes when fitted with the Debye model. This study presents a comprehensive study of the dielectric properties

of normal and cancerous breast tissues, with comparison of our tissue data with previous studies.

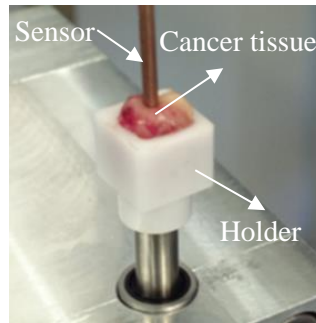


Figure 4.5: Photograph of the microwave needle sensors injected into breast cancer sample.

### 4.3.1 Dielectric Properties of Tissue

Experimental data in the literature consistently show that the permittivity and conductivity of cancerous breast tissue are significantly greater than those for normal tissue [136, 137]. In fact, such a trend was first distinguished by Fricke and Morse [138] for the permittivity and by Foster and Schepps [139] for the conductivity. The conductivities of malignant mammary samples are typically in the range of 0.8 – 1.4 S/m, while those of normal tissue are between 0.1 – 0.2 S/m at a frequency of 100 MHz [129], [140], [141]. In addition, Hazlewood *et al.* [142] summarized that malignant tissues present elevated relaxation times when compared to normal tissues, pointing out that a significant increase in the motional freedom of water has occurred. The dielectric results may also relate to the observation that the water content and sodium concentration in tumour cells is higher than in normal cells [143]. The origins of this are likely to be the increased hydration associated with the rapid metabolism of cancer cells and the surrounding angiogenic vasculature [144], [145] and also that cancer cells have reduced membrane potentials [146], [147] and an altered ability to absorb positive ions [148].

Several previous studies of the dielectric properties of normal and cancerous breast tissue have been undertaken and a comprehensive review of the individual findings is presented in [149]. As results, dielectric measurements may usefully complement such studies as those summarized here and provide new insights to develop a fast and accurate technique to diagnose cancer in non-invasive manner. Several studies of the electromagnetic dielectric properties of biological tissues at microwave frequencies

have shown that the dielectric constant contrast between malignant, benign and normal breast tissues is adequate to use microwaves as a useful diagnostic tool for early stage breast cancer detection as shown in Figure 4.1. For example, Chaudhary *et al.* [141] measured the dielectric properties of normal and malignant breast tissue between 3 MHz and 3 GHz. Joines *et al.* [140] measured the dielectric properties of various types of normal and malignant tissue from 50 to 900 MHz. Surowiec *et al.* [129] measured the relative permittivity of infiltrating breast carcinoma and the surrounding tissue at frequencies between 20 kHz and 100 MHz using an automatic network analyser and an end-of-line capacitor sensor. This study examines in detail the observed dielectric properties of cancerous and normal tissues at microwave frequencies. In order to put these into context, the properties of water and physiological saline are first discussed in the next section.

### 4.3.2 Hydration and salinity effects on biological tissue

The result of the interaction between the microwave electric field and biological tissues in general is oscillation of the itinerant polar water molecules and ions (from dissolved ionic salts). Therefore, the static dielectric constant and the relaxation time are reduced and an ionic conductance is introduced. For a pure liquid, the Debye model [114] describes the frequency-dependent dielectric properties, as presented in :

$$\varepsilon^* = \varepsilon_\infty + \frac{\varepsilon_s - \varepsilon_\infty}{1 + \omega^2\tau^2} - j \frac{(\varepsilon_s - \varepsilon_\infty)\omega\tau}{1 + \omega^2\tau^2} \quad (4.2)$$

In this equation  $\varepsilon_\infty$  and  $\varepsilon_s$  are the limiting high frequency and low-frequency permittivity values which were calculated by Hasted [150]. In case of the biological tissues, introducing an ionic conductance requires the addition of an extra term on the right hand of the equation for  $\varepsilon''$ , so that:

$$\varepsilon'' = \varepsilon_d'' + \varepsilon_\sigma'' \quad (4.3)$$

where

$$\varepsilon_d'' = \frac{\varepsilon_s - \varepsilon_\infty}{1 + \omega^2\tau^2} \omega\tau, \quad \varepsilon_\sigma'' = \frac{\sigma}{\varepsilon_0\omega} \quad (4.4)$$

and the subscripts “*d*” and “*σ*” stand for contributions due to dipole rotation (e.g. alignment of dipolar molecules) and ionic conduction (e.g. movement of charge

carriers) [151], respectively;  $\sigma$  is the ionic conductivity in S/m of a material which is proportionally related to the total dielectric loss factor of materials [152], [153],  $\omega$  is the angular frequency in rad/s, and  $\epsilon_0$  is the permittivity of free space or vacuum (see ref. [154] for a detailed discussion of this equation).

The ionic conductivity plays a major role at lower frequencies (e.g., <200 MHz), whereas both ionic conductivity and dipole rotation of free water play a combined role at microwave frequencies, the ionic conductivity becoming of lesser importance above about 3 GHz. The dielectric loss factor  $\epsilon''$  due to conduction decreases with increasing frequency as shown in (4.4). The overall, effective ac conductivity of a biological material is then given by:

$$\sigma(f) = \sigma_0 + \omega\epsilon_0\epsilon'' \quad (4.5)$$

where  $\sigma_0$  is the conductivity arising from the electric field induced motions of the various ions in the electrolyte. From this equation, it follows that, provided  $\sigma_0$  is not dominant, the conductivity and the relative permittivity of most tissues increase with increasing frequency in three major steps, corresponding to the  $\alpha$ ,  $\beta$ , and  $\gamma$  dispersions as first fully described by Schwan [105]. the complex permittivity of 0.9% sodium chloride solution corresponds to the ionic strength of cellular fluid [155]. The permittivity of tissue in the region  $10^8$  to  $10^9$  Hz is a little less than that of a 100% concentration of the aqueous cellular fluids due to the presence of the non-polar membrane materials and other chemicals of low polarizability.

In addition, higher than about 100 MHz, where electrical charging effects of the cell membranes begin to decrease rapidly with increasing frequency, the dielectric characteristics of tissues can be expected to reflect the properties of the inter- and intra-cellular electrolytes and, in particular, to exhibit a dielectric dispersion associated with the relaxation of water dipoles [155] and [156]. For frequencies greater than around 100 MHz, the dielectric properties of tissues are largely determined by their aqueous contents, together with the presence of ions and small molecules in the cellular fluids. As stated above, the water content and sodium concentration in tumour cells is higher than in normal cells [143]. To understand the essential physical and physiological processes that give rise to the tissue properties to be described later it will be of value to consider first the dielectric properties of electrolytes, which form the main constituents of tissue.

The concentration of ions in biological fluids can be large, as for example, average concentration (millimol/liter) of  $Na^+$  (i.e. sodium) and  $Cl^-$  (i.e. chloride) ions in biological fluids are 140-170 and 100-120 respectively [137]. The physical effects of such dissolved ions on the dielectric permittivity of biological fluids arise from more than just the volume effect of replacing polar water molecules by non-polar ionic particles. The strong local electric field about each dissolved ion has the effect of orientating the water molecules, thereby reducing the way they can rotate in response to an applied electric field.

An initial study on the microwave heating of water and electrolyte solutions and determination of their dielectric properties was reported a few decades ago by Hasted [150]. An equation of the form of (4.6) can be used to describe the permittivity  $\varepsilon$  of dilute electrolytes and that ( $\varepsilon_1$ ) of the pure aqueous solvent in terms of a dielectric decrement  $\delta$  and the concentration or molarity in moles/Kg of water as follows [150]:

$$\varepsilon = \varepsilon_1 - \delta c \quad (4.6)$$

where  $\delta$  is the sum of the decrements arising from the cation and anion and is given by:

$$\delta = \delta^+ - \delta^- \quad (4.7)$$

To estimate the extent to which, for example, NaCl will reduce the relative permittivity of pure water from 79 to 68 at room temperature [137], the accepted method of calculating the values of  $\varepsilon_s$  and  $\tau$  for salt solutions was set out by Stogryn [157], who used equations of the form:

$$\varepsilon_s(T, N) = \varepsilon_s(T, 0) a(N) \quad (4.8)$$

$$2\pi\tau(T, N) = 2\pi \tau(T, 0) b(N, T) \quad (4.9)$$

where  $\varepsilon_s(T, 0)$  is the static dielectric constant of water calculated from (4.2);  $\tau(T, 0)$  is a function which fits the experimental data gathered on the relaxation time of water as a function of temperature; and  $N$  is the normality of the solution. (For a NaCl solution, 1 Normal = 1 mole/litre.) The functions  $a(N)$  and  $b(N, T)$  are given by:

$$a(N) = 1.000 - 0.2551 N + 5.151 \cdot 10^{-2} N^2 - 6.889 \cdot 10^{-3} N^3 \quad (4.10)$$

$$b(N, T) = 0.1463 \cdot 10^{-2} NT + 1.000 - 0.04896 N - 0.02967 N^2 + 5.664 \cdot 10^{-3} N^3 \quad (4.11)$$

Experimental measurements reviewed in [150] show that any differences in conductivity between the different body electrolytes are mainly due to the different negative ions — largely  $Cl^-$  in plasma and interstitial water, and various proteins in intracellular water. Then, plasma and interstitial water may be treated as 0.9% NaCl solutions (physiological saline). For the purposes of modelling cancer tissues as a first approximation, tissue can be considered to take the form of an electrolyte containing densely packed cells; body electrolytes are assumed to be 0.9% NaCl solutions [33]. Using equations (4.8) to (4.11), values for  $\epsilon_s$  and  $\tau$  of physiological saline (0.9%) were calculated at room temperature. The relaxation time  $\tau$  was found to be almost identical to that of pure water over this range. The parameter  $\epsilon_\infty$  apparently is independent of salinity [157]. This is to be expected, because at the highest frequencies water molecules cannot be made to oscillate significantly, so that the tendency for ions to impede the oscillation is unimportant.

### 4.3.3 Needle-type probe measurement system

Open-ended coaxial probes have been the subject of active investigation, particularly in medical applications. While initial studies have demonstrated the potential use of needle-type probes for monitoring electrical properties, the effectiveness of the technique has yet to be determined *in vivo* for clinical purposes. Technically, measurements of the electrical property using a conventional (flat) coaxial probe require flat homogeneous surfaces and the probe cannot penetrate into tissues. Hence, a needle-shaped, open-ended probe was developed to improve the validity of this technique and was applied to investigate the permittivity and conductivity of normal and breast cancer tissues. The measurement set up comprises the same system as shown in section 3.4. Permittivity measurements at microwave frequencies are done using these probes as shown in Figure 3.21 attached to an Agilent PNA-L network analyser (N5232A). The dielectric data are obtained from a Labview program controls the PNA measurement, as shown in Figure 3.22. The data are investigated at 0.1 to 3 GHz for permittivity and conductivity measurements for breast tissues, and 50 MHz to 3 GHz for pure water and saline concentrations. Measurements at each frequency have been done three to seven times at each concentration with freshly prepared solutions as well as breast tissues, to assess standard errors.

#### 4.3.4 Examination of the sensing volume

Large variations exist in the experimental results for the relative permittivity and conductivity when examining healthy breast tissue and cancerous tissue samples as stated by [158]. This variation is due to the breast tissue non-homogeneity, whereby the reflected signal from the sampling volume is influenced by small-scale property heterogeneity. This is especially so for tissue samples, of which few are homogeneous. For example, non-fatty breast tissue consists of variable patterns and percentages of interwoven adipose and fibroglandular compositions [129] and [159], but this is rarely considered in detail. Hagl *et al.* [160] investigated the sampling volume question and deduced a sensing volume of 1.5 mm (in depth) by 5 mm (in width) for a 2.2 mm diameter open-ended coaxial probe. This approach was subsequently utilized to find a sensing volume of 3 mm (in depth) by 7 mm (in width) for a 3 mm diameter dielectric probe which was applied in two large breast tissue specimen studies [158].

However, the experiments considered by [160] were based on homogeneous liquids in which probe tips were systematically moved to positions close to the base and side walls of a glass beaker to infer their concomitant sampling volumes. This assumes that the probe's sampling volume corresponded to the minimum volume of liquid that existed before the first evidence of signal change occurred, sufficient to alter the dielectric property estimates. Unfortunately, these experiments find the minimum volume of a homogeneous liquid that is required to measure its dielectric properties precisely. However, they do not determine the probe's sampling volume or, more importantly, how the probe's signals from the said sampling volume are influenced when the properties are not actually homogeneous. For example, if the experiments performed do approximate the sampling volume of the probe, then presumably the resultant probe property estimates from a heterogeneous sample would represent an effective average of the compositional percentages of those materials contained within the probe's sampling volume. These widely cited studies are often considered to be the definitive data on the electromagnetic properties of normal and tumour breast tissues, and while they do represent the largest and most systematic effort completed to date to probe the dielectric properties of breast surgical specimens, the results presented here suggest that those measurements are surface-property biased, and likely do not represent

the effective dielectric properties of the volume averaged tissue that could, for example, be recovered on a cm-scale through non-invasive microwave imaging methods [161].

In section 3.2.2.1.4 simulations results for needle probes are presented for a distance sweep across a composite, two-layer material consisting of muscle and fat tissues layers. Thereby, the sensitivity of each needle probe can be examined to distinguish between different dielectric tissues at frequencies of 0.1, 0.3, 1, and 3 GHz. The two layered properties are used to investigate the influence of heterogeneity on the probe's dielectric property estimates when the layers are in close proximity to the tip of the probe. The interface line was translated to predetermined distances away from the probe tip to assess the degree to which the probe produced strong contrast in reflection coefficient, representative of the compositional averages of the dielectric properties of the two materials resident within a small sensing volume around the tip of the probe. The probe tip was moved in equal steps of  $10\ \mu\text{m}$ , and away by  $2\text{mm}$  from the interface line. While layered structures offer only one class of the infinite number of heterogeneous property distributions that could be considered, they are easily controlled and simplify the problem by eliminating effects from heterogeneity in the lateral directions. When exposed to microwaves, the high water content of malignant breast tumours or muscle tissues cause significantly larger microwave scattering than normal fatty breast tissues with low water content. A feature that can be deduced from Figure 3.11 to Figure 3.18 is that the dielectric properties of tissues are influenced by their tissue water content. Muscle, for example, which in humans can have water contents ranging from 73 to 77.6 wt% [162], exhibits a much lower reflection as result of high permittivity and conductivity compared to that for fat whose water content can range from 5 to 20 wt%, as illustrated in Figure 3.11 to Figure 3.18 for both magnitude and phase of reflection coefficient  $S_{11}$ .

For a probe angle  $\varphi = 0^\circ$  (i.e. a flat probe), the results in Figure 3.11 to Figure 3.18 show that the magnitude and phase of  $S_{11}$  are influenced proportionately by the material resident within the first  $\sim 50$  to  $200$  microns in depth of distance from the probe tip at 0.1 to 3 GHz, respectively. However, as the probe's tip becomes more needle-like, the sensing distance increases dramatically, hence the electric field becomes non-uniformly distributed around the aperture. As the needle moves from fat towards muscle in  $10\ \mu\text{m}$  steps, the probe behaves as having a much larger sensing volume in which the resultant reflection coefficient estimates represent a compositional average of the dielectric

properties of the materials within the sensing volume. Both  $|S_{11}|$  and phase curves are proportional to needle angle and forming its slope.

#### 4.4 Simulation results

A microwave needle coaxial probe measurement system has been simulated in EMPro and tested in its use for detecting normal versus cancerous breast tissues. A simulation of our probe on normal and cancerous breast tissues by Debye model shows its potential in accurate detection of the difference in complex reflection coefficient and permittivity. Numerical results for the all needle probes were obtained for cancerous tissue, as show in Figure 4.6.

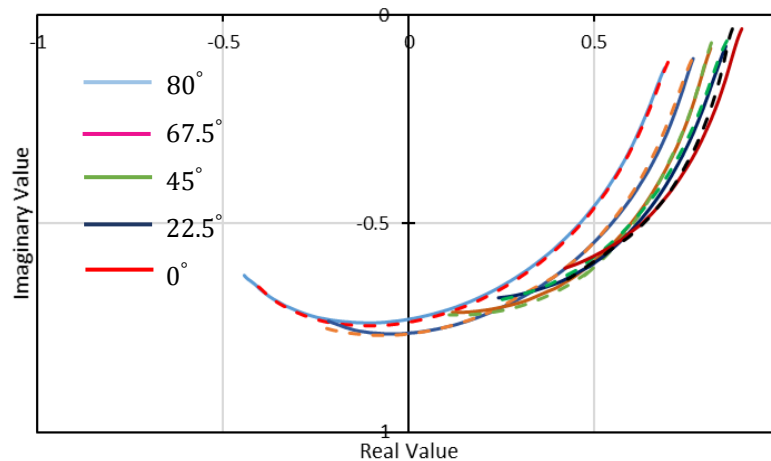


Figure 4.6: Simulated (dashed line) and measured (solid line) relative complex reflection coefficients resulting for different probe apertures at 0.1 to 3 GHz of rat breast cancer tissues.

#### 4.5 Experimental results

The open-ended needle probe measurement system was tested on both pure water with different saline concentrations, normal and cancer rat breast tissues. Rat tissues were obtained with permission from the European Cancer Stem Cell Research Institute at the University of Cardiff, breast tissues were obtained via a dissection of a rat. Measured tissues were directly extracted from a rat just an hour before the measurement, whose cells remain as fresh as living ones before degeneration. Figure 4.5 shows the needle

coaxial probe injected into a breast tumour of a rat. Results for both normal and cancerous breast tissues were compared to the data from [129], [131], [140], [141]. Results for the dielectric loss of pure water with different saline concentrations are shown in Figure 4.7.

A Debye model was used to convert complex  $S_{11}$  data into complex permittivity. Both normal and cancerous tissues were simulated from 0.1 to 3 GHz using complex permittivity values obtained from [134]. As shown in Figure 4.8 both materials were successfully detected, and it is possible to see a clear difference between the normal versus cancerous breast tissue, which is needed for the detection via dielectric properties.

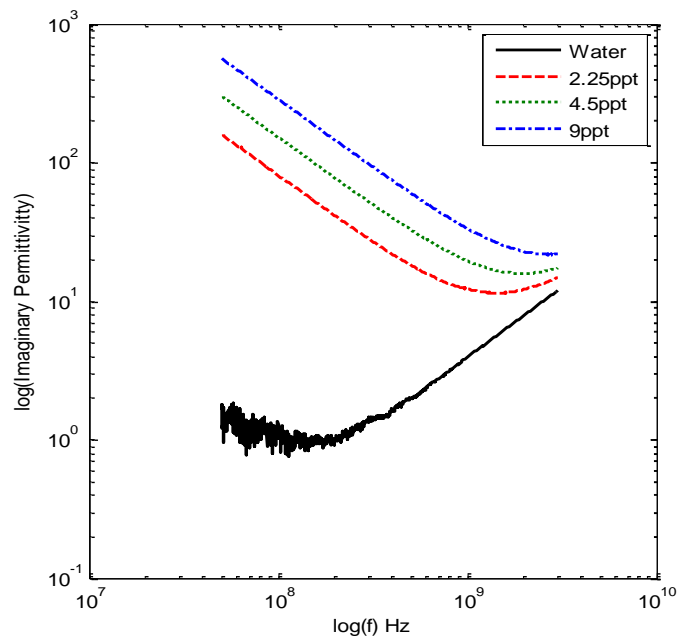


Figure 4.7: Frequency dependence of dielectric loss factor ( $\epsilon''$ ) of pure water and different saline concentrations in the frequency range 50 MHz to 3 GHz, measured by our needle probes.

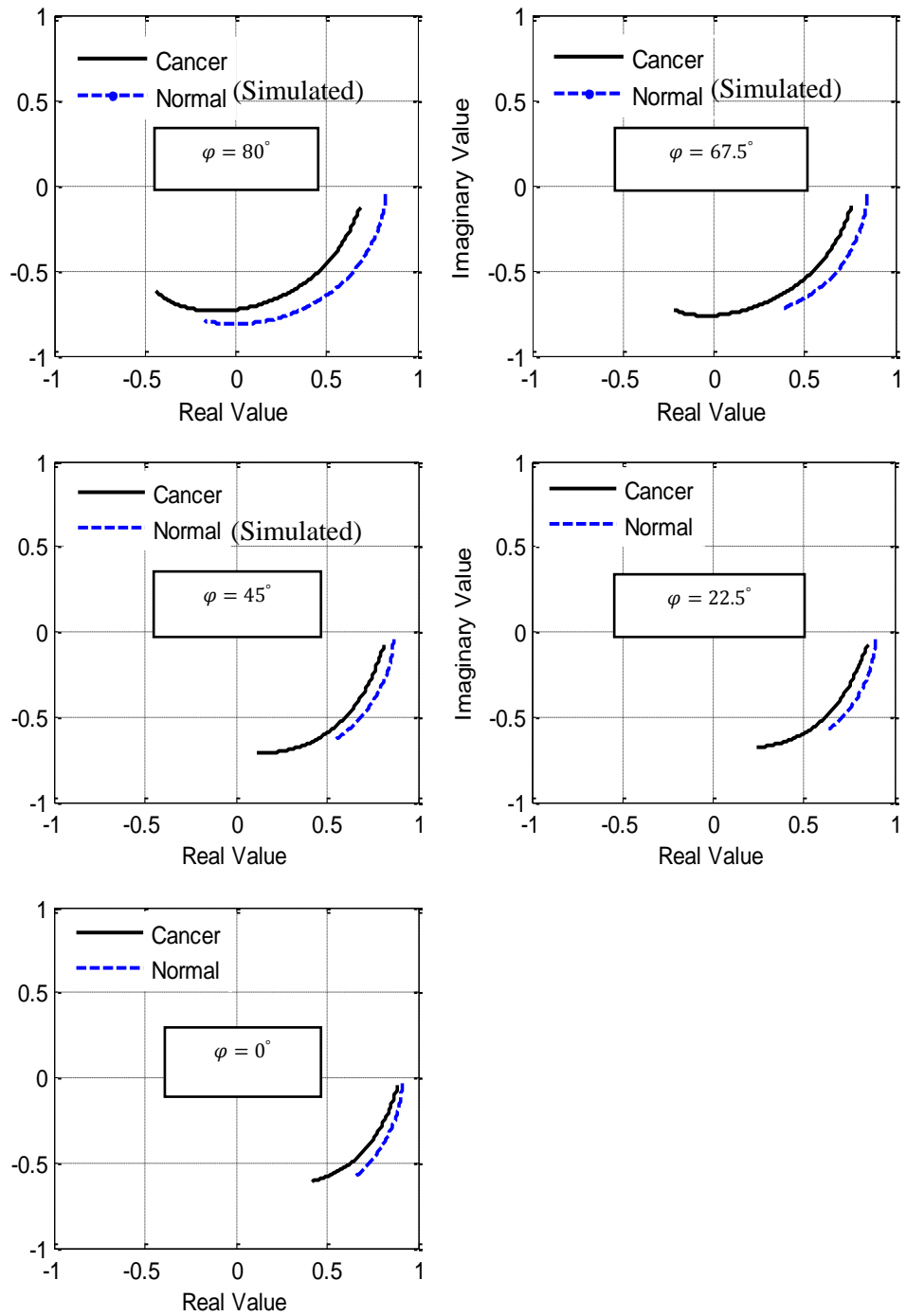


Figure 4.8: Simulated and measured relative complex reflection coefficient resulting by different probe apertures at 0.1 to 3 GHz of rat breast normal and cancer tissues by needle probes.

## 4.6 Discussion

Using this technique *in vitro* dielectric measurements were made on rat breast tissues. A large number of data were gathered on normal and tumorous breast tissues. Each data

set was parameterised using the Debye equation. Comparisons were made on the dielectric properties of breast tissues with values calculated from previous studies. Figure 4.9 shows the comparison of the relative complex reflection coefficient between the physiological saline and cancer tissues resulting from the use of different probe apertures over the bandwidth 0.1 to 3 GHz. It is clear that high contrast is attained between cancerous tissue and saline, especially so for the  $\varphi = 80^\circ$  (i.e. sharp).

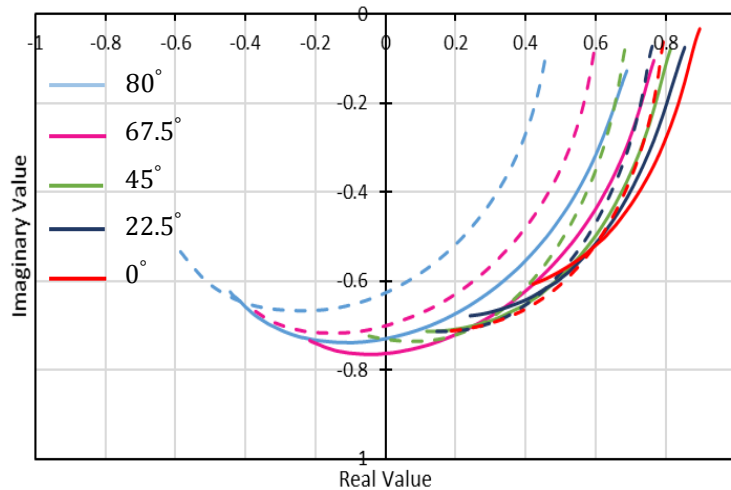


Figure 4.9: Measured normal saline (dashed line) and breast cancer (solid line) relative complex reflection coefficients resulting by different probe apertures at 0.1 to 3 GHz.

This may imply that physiological saline is not a good approximation to tissue fluid; or it may imply that another relaxation process is occurring in addition to the dipolar relaxation of saline. To characterize salinity effects in water, the dielectric constant as a function of frequency and salinity must be determined. This has been examined further by measuring saline samples of varying concentration, prepared by diluting normal saline with deionised water, with dissolved NaCl of various concentrations, over the frequency range 50 MHz to 3 GHz and performed at room temperature  $25^\circ\text{C}$ ; the resulting data are illustrated in Figure 4.10.

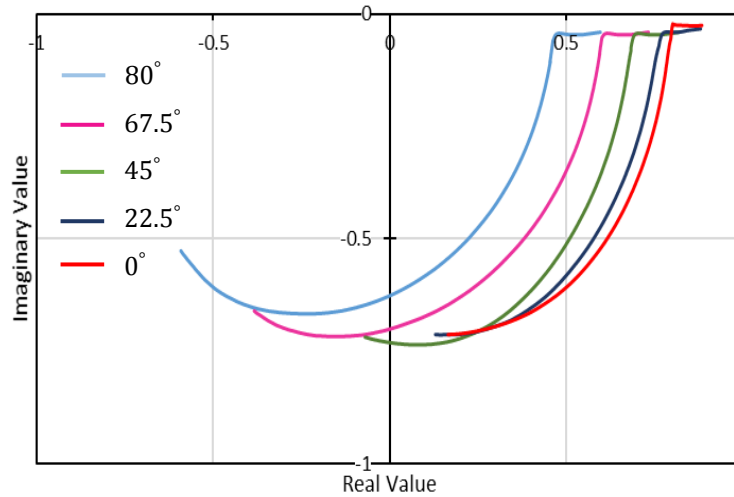


Figure 4.10: Measured relative complex reflection coefficient of normal saline, using needle probes of varying angles, from 50 MHz to 3 GHz.

The dielectric losses  $\epsilon''$  for normal saline at low microwave frequency was greater than that for pure water, which was attributed to the presence of various ions in saline water, as evidenced by the higher electrical conductivity of 1.5 S/m versus  $5.7 \times 10^{-6}$  S/m for pure water. The dielectric loss of physiological saline at 50 MHz was about  $\times 570$  greater than that for the pure water, whereas at 3 GHz, the value was only  $\times 9.9$ . Evidently, the presence of the electrolyte in the saline solution had a larger influence at the lower frequencies.

The dielectric constant of aqueous NaCl electrolytes in the range 50 MHz to 3 GHz are displayed in Figure 4.10. Single molecules of water can easily follow the frequency of the microwaves. The presence of ions in water can cause the cluster structure of water to be broken, such that the water molecules that solvate the ions may be rotationally more rigid than the remaining water molecules, thereby causing the relaxation times to become higher.

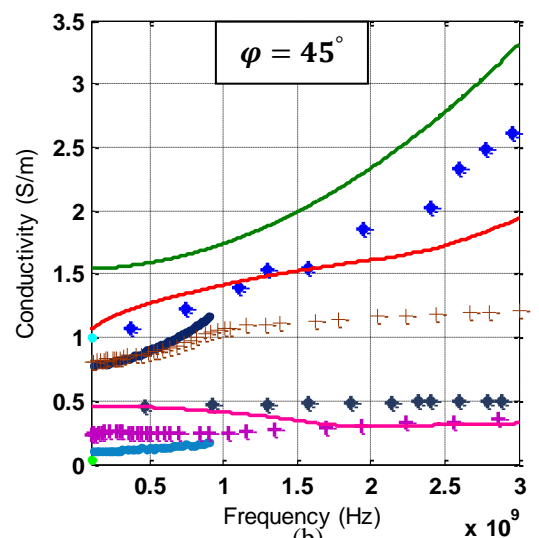
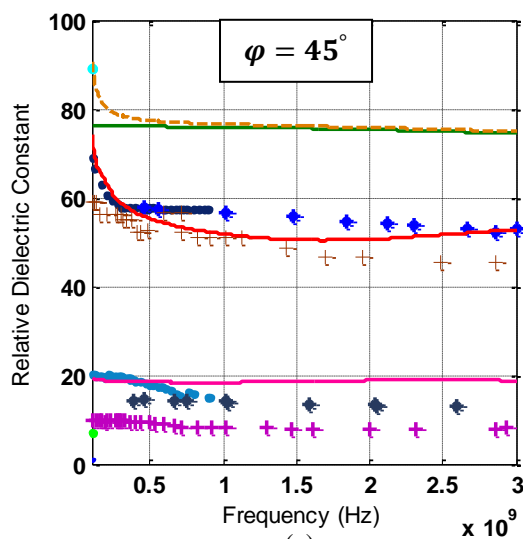
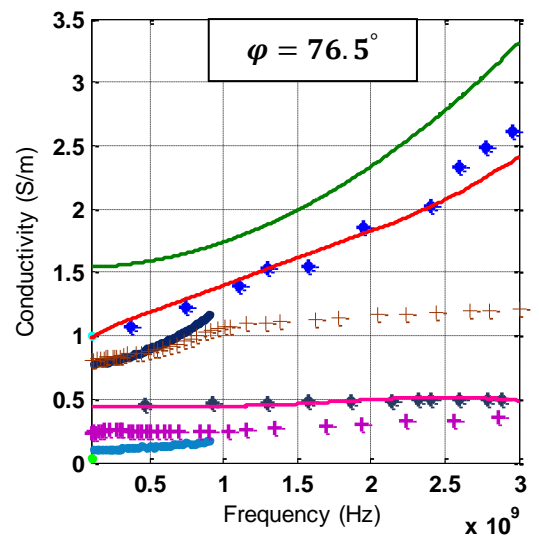
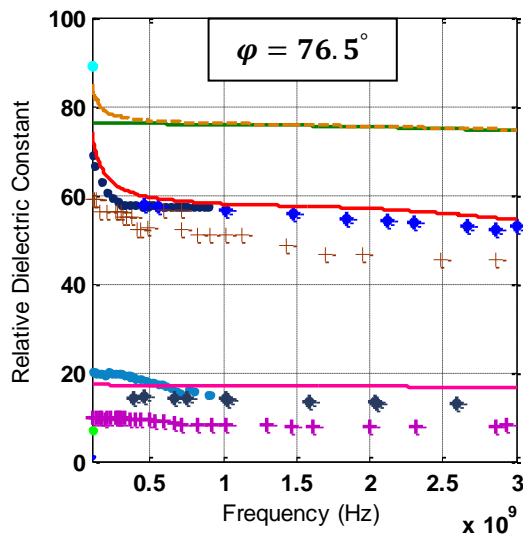
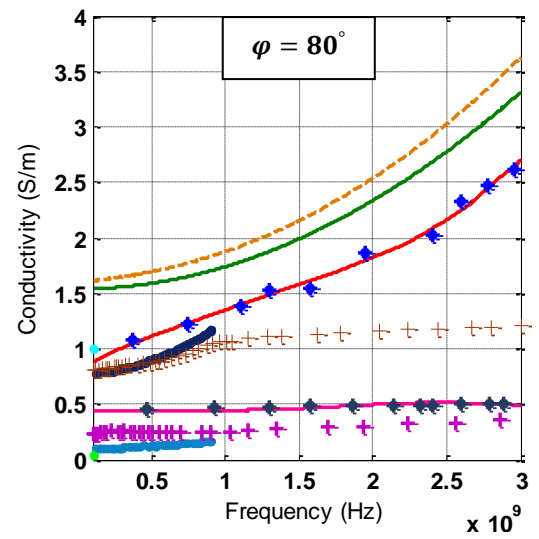
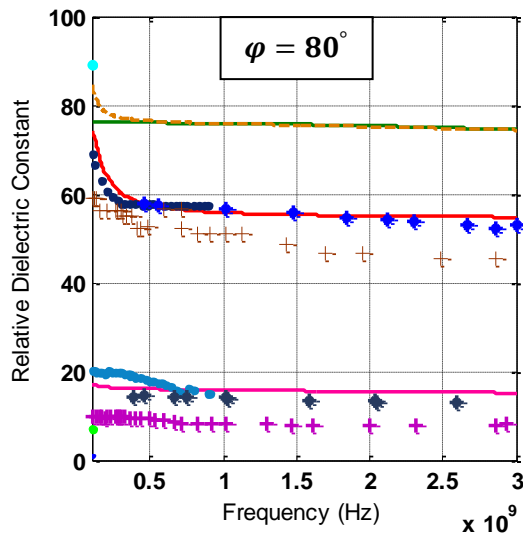
The cancerous and normal rat tissues were examined by different needle probes to measure the complex reflection coefficient, which is illustrated in Figure 4.8. This experiment is included to demonstrate how the sensitivity to dielectric contrast increases with needle angle. The contrast sensitivity of the reflection coefficient for a probe with  $\varphi = 80^\circ$  at 0.1GHz has increased around 14% in magnitude compared with  $\varphi = 0^\circ$ . Twenty measurements of the dielectric properties of normal and tumorous rat breast tissues were made, on six samples. The relative permittivity was found to range from 18

to 22, the conductivity from 0.43 to 0.5 S/m, at 0.1GHz for normal tissues. In cancer tissues, the corresponding values were 69 to 80 for the real part of the complex permittivity, and from 0.86 to 0.79 S/m for the conductivity. In Table 4-1, the data collected on tumours and normal tissues are presented for contrast examination: this table includes  $|S_{11}|$  and the phase contrast at 0.1 GHz for all needle probes.

Table 4-1 Contrast percentage of normal versus cancerous tissues with different needle probes at 0.1GHz.

<b>Relative Change of Normal Vs. Cancer breast tissues</b>		
<b>0.1GHz</b>	<b><math> S_{11} </math> %</b>	<b>Phase %</b>
$\varphi = 0^\circ$	1.65	5.17
$\varphi = 22.5^\circ$	4.11	86.08
$\varphi = 45^\circ$	5.52	115.12
$\varphi = 67.5^\circ$	8.6	140.77
$\varphi = 80^\circ$	15.49	168.49

From the large variation of data presented in [158], breast carcinomas are tissues with a large range of water contents. The dielectric properties of normal, benign and malignant breast tissues were further addressed in this study [158]. The measured dielectric curves in both the permittivity and conductivity for normal and cancerous tissues agreed well with literature [129], [131], [140], [141], as shown in Figure 4.11. However, the data of Surowiec *et al.* [129] at 0.1 GHz seem very much lower than the collected normal tissue data. Adjusting for adipose content, Lazebnik *et al.* [158] found only a 10% difference between the conductivity of normal tissue and malignant tissue, and an approximate 8% difference in permittivity at 5 GHz. However, adjusting for adipose and fibroconnective tissue, they found no statistical differences between normal glandular and malignant glandular tissues in the breast.



(a)

(b)

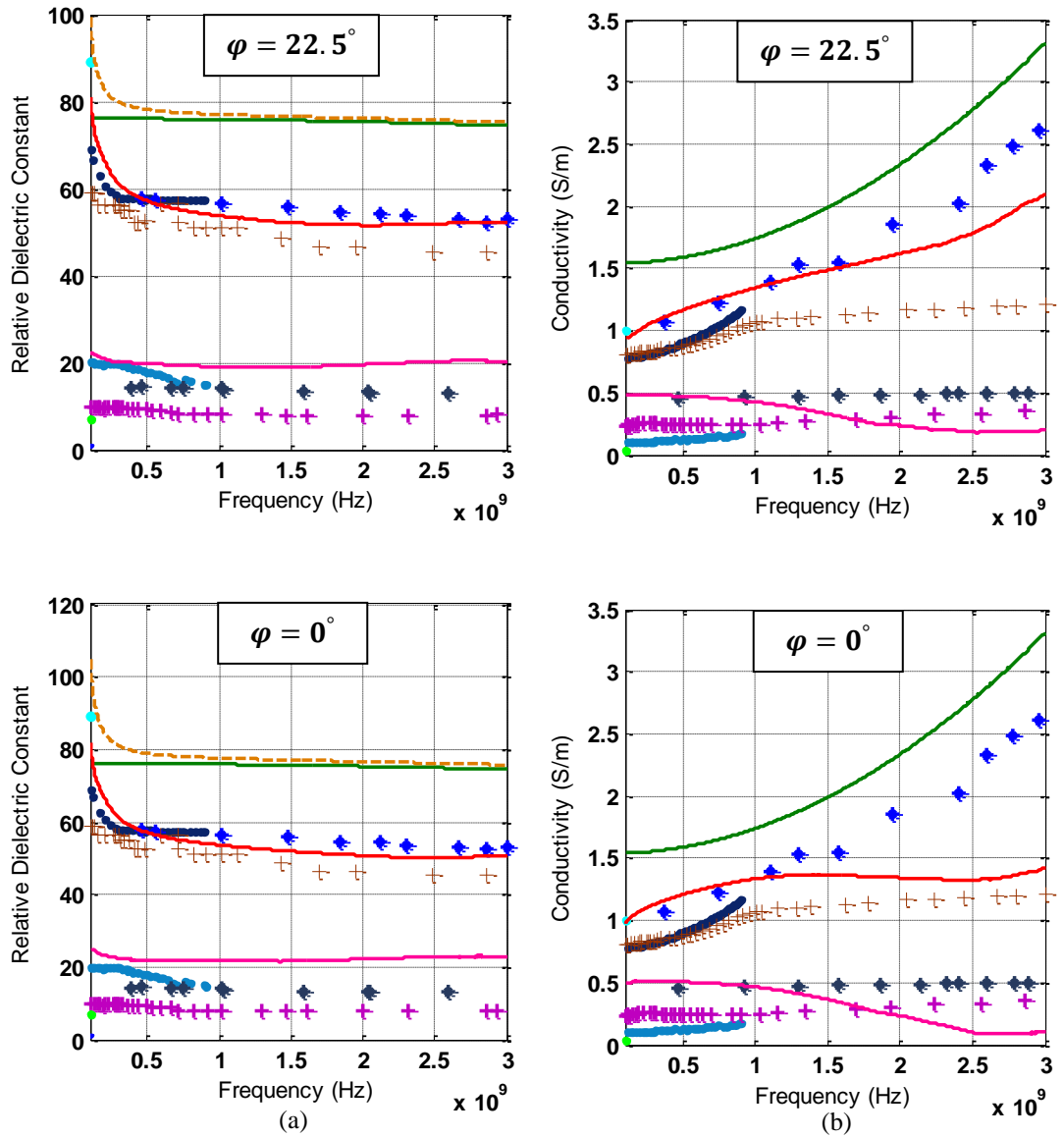
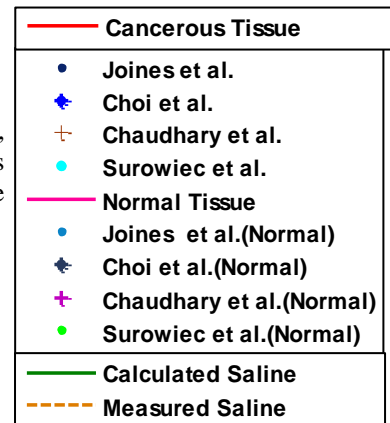


Figure 4.11: The variation of (a) the relative permittivity, and (b) the conductivity of normal and cancer tissues between 100 MHz and 3GHz measured using our needle probes compared with values from the literature.



In general, the probe method is used to measure the dielectric parameters. However, it is difficult to decide on the absolute value for each material because the measurement is

highly sensitive. In addition, the dielectric parameters depend greatly on the temperature of the sample. Therefore, in comparison with data obtained by others, there are some for which the value of the dielectric properties may be different.

When the saline solutions were measured, it was noticed that as the probe becomes more flat the dielectric constant significantly increases at low frequency, with an increase in the dielectric loss factor. We believe that this discrepancy was caused by a small interfacial air layer forming between the probe's end and the solution. To investigate this idea, a very thin air layer (i.e. 50 $\mu$ m thick) was used in an EMPro simulation to cover the probe aperture in the presence of saline solution. Comparison results of the saline solution measurements with and without the air layer are illustrated in Figure 4.12 and confirm our interpretation. In practice, these effects may be negated by surface treatment of the Teflon spacer at the probe's end to reduce its hydrophobicity.

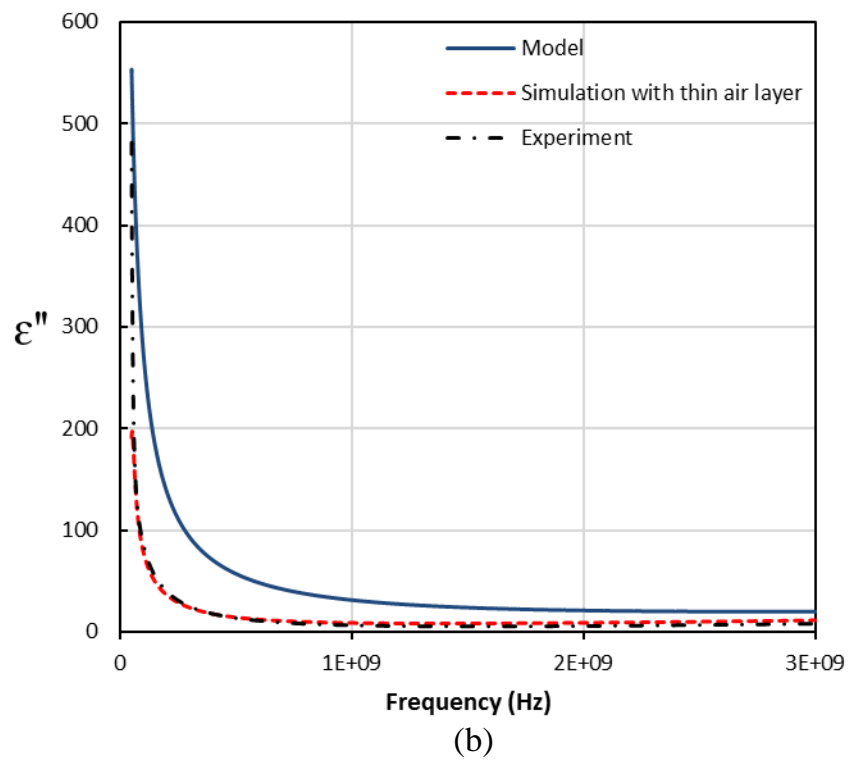
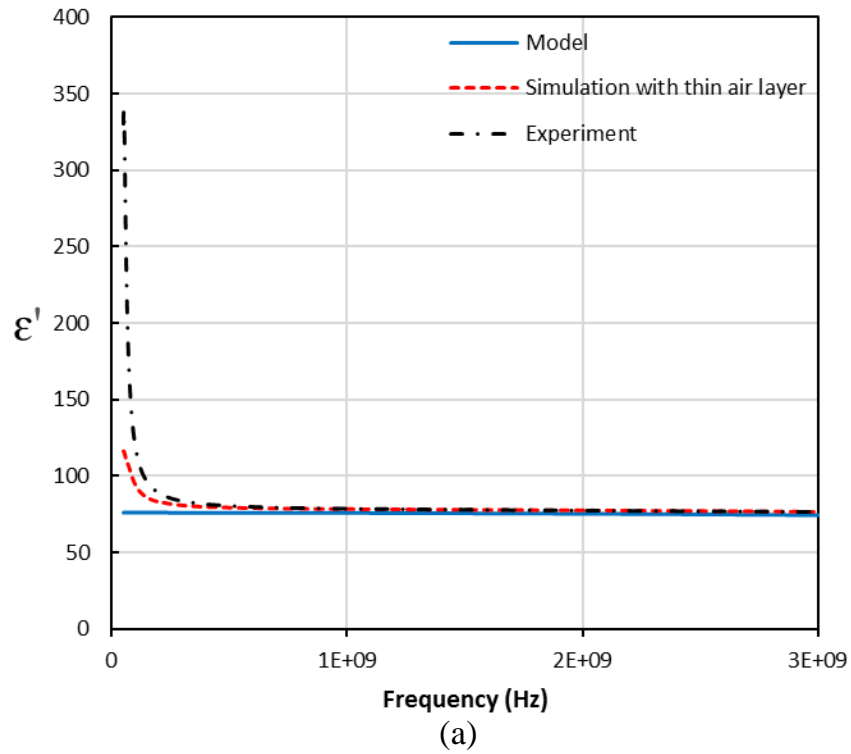


Figure 4.12: The variation of, (a) the dielectric constant ( $\epsilon'$ ), and (b)- the dielectric loss factor ( $\epsilon''$ ), of saline solution between 50 MHz and 3GHz for a  $\varphi = 0^\circ$  probe compared with simulation and calculated values.

In summary, the capability of microwave needle probes to measure the dielectric properties of cancer and normal tissue *in vitro* was demonstrated in this chapter, with high dielectric contrast and sensitivity achieved, especially at low microwave frequencies. Simulations confirm consistency between the model and measurements. This method has the advantage of its non-invasive nature, especially for cancer tissue diagnosis. The measurements with mouse breast cancer and normal tissues demonstrate that cancer breast tissues have much higher water content than the healthy tissue. Subsequently, one would expect the magnitude of the reflection coefficient to be higher for normal tissue, as is observed. This is due to the dielectric relaxation of the bulk water in the tissue, which behaves in a similar manner to pure water. This is clearly evident from the results presented, and it can be concluded that probes with higher aperture angle result in a more sensitivity measurement than for the flat aperture probe. Significantly higher permittivity and conductivity values for the tumour breast tissues are measured compared with normal tissue. Our results are in very good agreement with previous studies reported in the literature, only in our case using a needle probe which lends itself better to a practical diagnostic device compared with a flat probe (often with a broad flange).

Additionally, it was confirmed that physiological saline cannot be used to model the cancer tissues. Further studies of this effect would be of relevance to further developments of the clinical use of radiofrequency and microwave needle diagnostic probes. The use of a needle probe in the final decision-making process completes the ability of this system to accurately diagnose healthy and cancerous breast tissue. Future work includes real-time experimental testing of breast tissues with the needle microwave providing the final diagnosis. We also plan to use the same needle type probes for therapeutic treatment of tumours, such that the interesting possibility opens up of tumour detection at low powers (i.e. the 1 mW level used in our characterizations here), switched to much higher powers (10's W) when tumour treatment is required.

## **CHAPTER 5 MICROWAVE NON-THERMAL IRRADIATION FOR CANCER THERAPY**

In this chapter, a novel microwave sensor technique is developed that has been proved to be successful in treating cancerous cells utilising microwave irradiation without a strong thermal effect. The current efforts in the development of the technique are analysed, which include underlying sensor principles, microwave treatment technologies and infrastructure, as well as hardware, software, and validation procedures. This study demonstrates the beneficial uses of open-ended coaxial probes with microwave non-thermal high power irradiation techniques to enable penetration of electromagnetic energy into cancer tissue. Key features in this technique will be presented, such as the use of pulsing modes to prevent any rise in temperature and the effects of delivered power level on cells in their culture medium, and the assessment of sensitivity to cell states.

To achieving this challenging aim, a literature review was conducted comparing three recent, alternative cancer treatments, collectively termed as “ablation”. Microwave ablation was found to be the most promising treatment for cancerous tumours. Much of the literature has emphasis on thermal ablation and consequently this effect has been explained, followed by further information regarding the impact of electric fields on cancerous tissue. Extensive simulations were carried out, from which it can be observed that the electric field distribution is sufficient to propagate through the entire sample being tested at the power levels and operational frequency being used.

A number of probes were fabricated, which underwent a series of experimental tests to evaluate their performance and to test whether cell death could be achieved without any thermal effect by implementing a range of pulsing modes, varying between duty cycles

of 5 – 25%. Coaxial applicators based on open-circuit RG402 and RG405 cables were used to deliver microwave radiation at the proposed duty cycles to cancerous cell cultures and *in vivo* tissues. A measurement interface has been created in LabVIEW to control a range of parameters including temperature, reflected power,  $S_{11}$ , and power dissipated. The results of the experiments show a high success in accomplishing complete cell death, in an applied power range from 10W to 50W with duty cycles of 5 and 10%, at both 2.2 GHz and 5.8 GHz, with no significant temperature rise. The mechanism of cell death has been termed electroporation [163], in which the cell membrane breaks down as a result of the high content of polar molecules being agitated under the high applied microwave electric field.

In order to achieve this distinction between cell death caused by thermal effects and cell death caused by irradiation (i.e. high electric field), cancerous cell cultures and *in vivo* tissues were provided by the European Cancer Stem Cell Research Institute at Cardiff University, and University Hospital of Wales (from both Heath and Llandough sites). These cells will be utilised with a range of experiments developed, ensuring that temperature rise is minimal whilst achieving cell death.

In general, the treatment part of this thesis will be arranged in main sections as follows: firstly, a literature review will be conducted assessing the various treatment options of cancer, with a particular focus on ablation methods. Then, a comparison of ablation techniques will be conducted considering the advantages of each. A detailed review of microwave ablation will be conducted, considering the theory and a distinction between thermal and non-thermal effects will be attempted. Following on from this, a range of simulations will be conducted to assess the potential electric field generated by probe, at different power levels in cancerous tissue. These simulations will be created by using COMSOL Multiphysics to ensure that accurate outcomes will be obtained.

In chapter 6, the equipment used to generate both the continuous and pulsed wave microwave radiation has been explored in detail, with each element being detailed. A LabVIEW programme has been created and developed that will control the measurement and recording a range of important parameters including temperature, dissipated power and  $S_{11}$ , allowing for information to be gathered about the experiments being conducted. In addition, these devices will be used to conduct experiments in which both continuous wave and pulsed signals are used to irradiate a cancerous tissue sample. It is anticipated that the pulsing method will reduce the heating effect, allowing

for heating and non-heating effects to be distinguished by careful monitoring of temperature rises.

In chapter 7, the experiments and results will be analysed using various methods, including high power optical microscopy to generate images before, immediately after and 24 hours after the experiments, allowing for comparisons to be drawn between the samples. Trypan blue staining was used to investigate the condition of the irradiated cells. Also, to expand on the investigation, a scan was conducted on 945 cell proteins immediately after the microwave irradiation and after a waiting period of few hours. Finally, the results will be discussed using available literature and theory, and the next steps proposed to confirm and validate the technique, via animal studies.

## **5.1 Literature Review**

Cancer is a leading cause of mortality across the world with an estimated 8.2 million deaths being attributed to cancer in 2012. Furthermore, the rates of mortality and new cases of cancer are projected to increase rapidly by 2030, with an estimated 21.7 million new cases of cancer and 13 million deaths as a result of cancer [164]. This increasing rate of cancer is largely due to a growing and ageing population, which is further exacerbated through an increasing adoption of the ‘Western Lifestyle’, typified by a number of traits including poor diet, lack of physical inactivity and smoking [164].

Breast cancer has been selected as the focus of this study. This has been done for a number of reasons. Firstly, it is the most common form of cancer in the UK affecting 50,285 individuals in 2011 and posing a lifetime risk to women of one in eight [165]. In addition to the large numbers affected by breast cancer, it is also very prevalent in the elderly, with over 50s accounting for 80% of diagnoses [166]. This age group is particularly vulnerable to conventional treatment methods and are often unable to undergo these treatments. This can lead to an ‘under-treatment’ scenario in which the tumour may not be fully treated, leading to the affected individual being susceptible to further harm from the cancer. Additionally, as awareness of breast cancer is increased and greater numbers of women are undergoing breast cancer screening, cancers are being detected at earlier stages in their development, leading to smaller tumours being detected. The leading cause of concern in treating small tumours is termed ‘*over-*

*treatment*' and can result in patients undergoing very serious procedures, surgery under general anaesthetic for example, for a relatively minor tumour. This can result in significant stress placed upon the patient, with lengthy treatment and recovery times, taking up considerable resources at great expense.

Consequently, it is critically important to have a wide range of treatment methods available, providing the optimal treatment for individual cases. Now, commonly used treatment approaches include surgery, radiotherapy, chemotherapy, hormone therapy and biological treatment [167]. Each of these approaches has their associated advantages and disadvantages but, typically, all are resource-intensive and introduce a significant stress on the patient. On other hand, there is the scope for additional treatment options to be developed, in particular for smaller tumours, which are critically both less resource intensive and less invasive.

### **5.1.1 Cancer Treatment Techniques**

The important treatment technique being considered within this research falls under the broad category of ablation. Ablation is defined as the removal of tissue through vaporisation and is currently used to treat a range of conditions such as heart arrhythmias and menorrhagia [168]. Recently, ablation is being stated as a method to treat various kinds of cancer and there are three main types within this context, which will be presented in the next section.

#### **5.1.1.1 Cryoablation Technique**

Cryoablation involves destroying tumour cells by extreme cold processing. A probe is injected into a tumour, through which cold gas (e.g. nitrogen) is pumped, causing the temperature of the surrounding tissue to decrease. Consequently, intracellular ice crystals will be formed by the cooling process which will eventually lead to disruption of the tumour cell function, causing damage to organelles within the cytoplasm. However, this requires a critical temperature between  $-19.4^{\circ}\text{C}$  and  $-40^{\circ}\text{C}$  to be reached to ensure that the cancerous tissue is successfully treated [169].

### **5.1.1.2 Radio Frequency Ablation Technique (RFA)**

This is the most broadly used ablation method for small to midsize tumours, up to 7cm across [170]. The mechanism of radio frequency ablation involves inserting a thin needle electrode into the tumour site, upon which radio frequency (RF) (typically 450 – 500 kHz [171]) current is applied from the electrode tip through the surrounding tissue to the grounding pads placed on the patient’s skin as shown in Figure 5.1. The RF 3000® Generator as an example provides up to 2 amps of current and can provide a power of up to 200 watts, which is typical of currently-used systems. The level of power delivered is controlled by the user. The power level is set low to start and is steadily increased to allow for a gradual heating of the tumour volume [172]. The death of the tumour cells is due to the passive heating conducted by the resistive current paths that radiate outwards from the electrode to the surrounding tissue. This process is mainly limited by the thermal conductivity of the surrounding cells and, as a result, the ablation efficiency is poor near efficient heat sinks, such as large blood vessels. The known issue with this method is that its reliance on passive heating results in the ablation margin being higher than in other techniques, in order to guarantee the tumour is completely destroyed, meaning that usually a greater volume of healthy tissue is harmed. RF ablation can also be limited by an increase in impedance resulting from tissue boiling and charring, as water vaporization and char act as electrical insulators [173]. Some of the challenges associated with the selective heating of deep-seated tumours without damaging surrounding tissue are:

- Control of heating power and spatial distribution.
- Design and placement of temperature sensors.

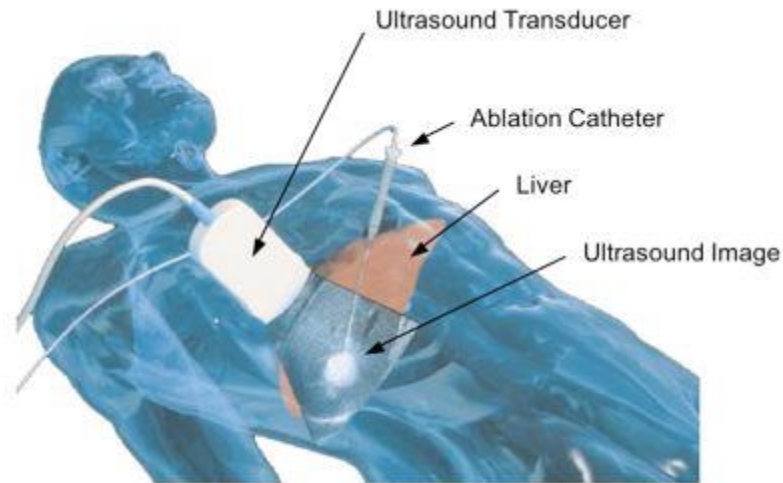


Figure 5.1: Schematic of minimally-invasive liver tumor RF ablation procedure. The ablation catheter is inserted through a small incision and steered into the tumor under ultrasound imaging guidance[171].

### 5.1.1.3 Microwave Ablation (MWA) Technique

Microwave ablation is the most relevant technique to this research. It involves delivering microwave radiation to the tumour at high frequency, typically at between 900 MHz and 2.45GHz [174], [175]. Also, the range 5.8 GHz - 10 GHz can produce shallow energy penetration that results in very precise ablations appropriate for cancer treatments [176], creating localised dielectric heating (diathermy) resulting in controlled tumour destruction. The critical temperatures within the treatment field are found to be greater than 60°C for instantaneous cell death, with temperatures from 42°C to 60°C requiring longer treatment time period to achieve cell necrosis [177]. Strickland *et al* used variable times and power outputs ranging from 36 to 200 W in an *in vivo* porcine liver model and demonstrated ablation zones ranging from 3 to 6 cm in diameter produced very rapidly, i.e. within three minutes [178]. A review of the efficacy of microwave ablation has been carried out by Martin *et al.* [174], in which 100 patients underwent ablations for hepatic malignancies, and concluded that microwave ablation is an effective and safe technique for treating this cancer type. The significant finding was that local recurrence of the tumour at the ablated site occurred in only 2% of patients. In addition, the main advantages over the previously mentioned RF ablation is active heating against RF ablations passive heating, which provides desiccation of tissue without the excessive charring and nerve damage associated with RF ablation. Active heating allows for more consistent tumour destruction near to blood vessels that act as

heat sinks, for ensuring consistent tumour destruction. This active heating effect can be best explained through the use of Debye model shown in Figure 5.2.

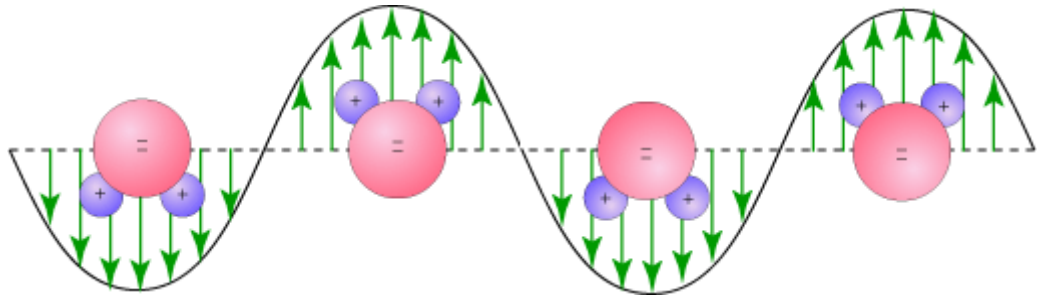


Figure 5.2: A diagram illustrating the impact an electric field has upon polar molecules [179].

Figure 5.2 illustrates a biologically important situation arises when water molecules are irradiated with microwaves of appropriate frequency to excite their rotational motion depending on the polarity of the applied electric field [180]. At high frequencies, the rotational kinetic energy increases, consequently, the polar water molecules cannot rotate at the same angular frequency as the applied microwave frequency and this leads to the molecules generated. These oscillations generate heat due to the frictional forces involved which eventually leads to the temperature of the surrounding body increasing. In regards to tissue, the combined effect of all the polar molecules oscillating leads to a temperature rise, triggering cell death through coagulative necrosis [181].

### 5.1.2 Comparison of Ablation Techniques

All three techniques previously described create some form of heat transfer in order to destroy the cells of the tumour; both RF ablation (RFA) and cryoablation depend on passive heat transfer, whereas microwave ablation (MWA) achieves an active heat transfer. Active heat transfer is a significant merit over passive heat transfer due to its ability to overcome heat sinks, a significant problem when trying to treat uniform lesion area. Moreover, it has the capability to treat large tumour regions compared with a passive heat transfer method as shown in Figure 5.3. It can be noted that the larger ablation zones (arrows) at each time point in the microwave panel. The zones generated using microwaves were 25% larger in mean diameter, significantly more circular and developed faster than those achieved with RF energy [175]. Unlike RFA, MWA and its active heating mechanism do not rely on electrical conduction. When tissue is charred

(often a result of the RFA procedure) it acts as an electrical insulator, further reducing RFA's ability to transfer heat, which is not relevant for MWA. However, all three techniques are still reported to have high degrees of success in treating small tumours [182] with all showing well-defined lesions. Although it should be noted that MWA showed the most clearly defined ablation regions with no viable tissue. A final important point to mention is that, in spite of all three methods being minimally invasive, being delivered laparoscopically (i.e. "keyhole" surgery), MA tends to be the best treatment option, delivering all the benefits of the alternatives whilst creating additional advantages due to its active heating.

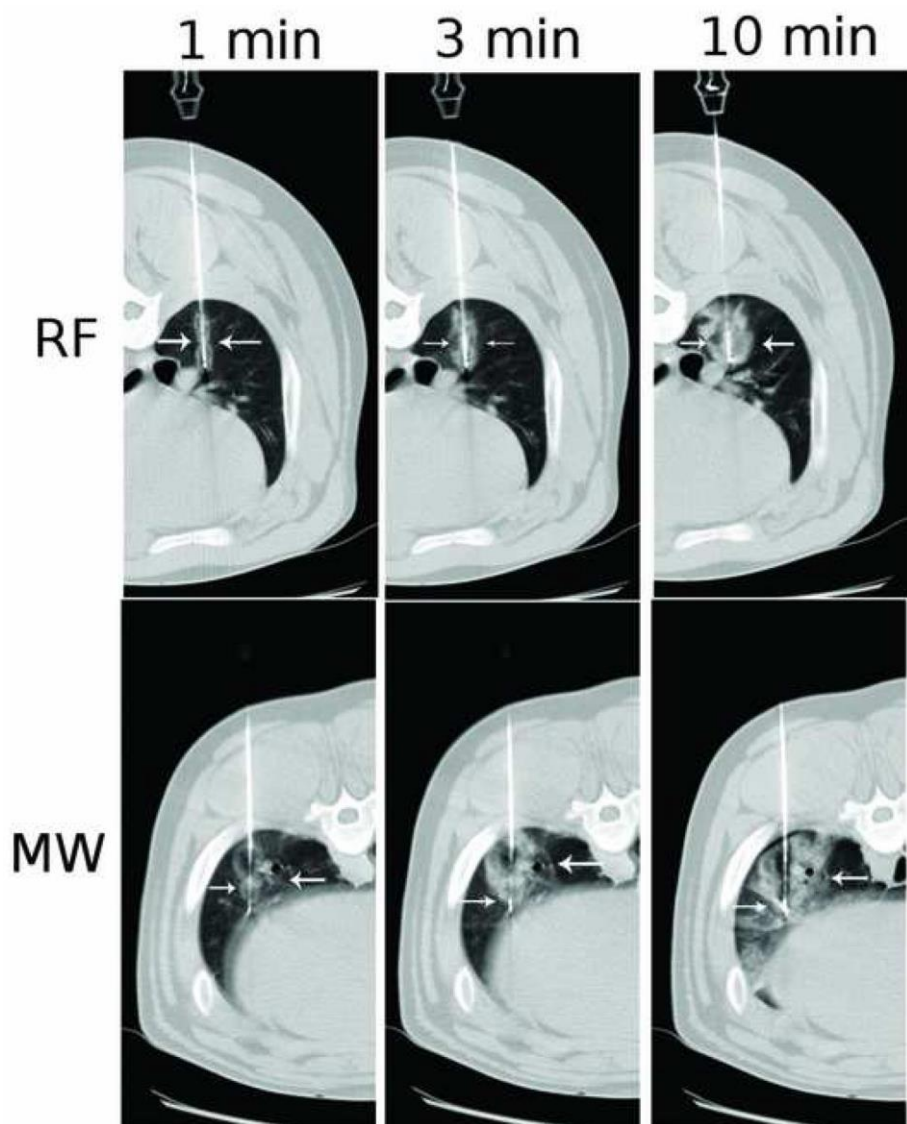


Figure 5.3: Sequential CT images obtained during RF vs MW ablation in *in vivo* porcine lungs. Note the larger ablation zones (arrows) at each time point in the microwave panel [175]

### 5.1.3 Microwave Ablation – Previous Studies

A number of studies have been conducted that seek to exploit a range of parameters in order to advance the treatment. A study by Yoon *et al.*, [183] has carried out extensive research into application of high frequency, low power microwave ablation. It has stated that at higher frequencies, 18 GHz being the most effective, there is a high degree of material selectivity in which the dielectric loss factor is at its peak between 10 - 24 GHz, and it is the dielectric loss factor that dictates the level of energy dissipation through heat. Subsequently, as the loss factor increases the temperature in the tissue also increases, which can lead to lower power levels being used that increase the efficiency whilst lowering the collateral damage. It has reported that nude mice xenografted with human breast tissue treated at 18 GHz with a 1W dose of microwave radiation demonstrates complete cessation in tumour growth and 100% survival at day 100 [183]. A further study by Jones, *et al.*, [184] has also presented that high frequency MWA is effective in destroying cancerous tissue. The study by Yoon, *et al.*, [183] has performed the procedure at higher power levels, 50W. These higher power levels generate larger ablation regions, a result that is to be expected on thermal grounds, in spite of the apparent lack of determining the optimum frequency. Consequently, whilst it can be seen that frequency can have an impact on improving the efficiency of the treatment, the microwave power levels are also a significant factor.

Jones, *et al.*, [184] also raises another interesting point in that whilst the impact of microwave heating is a well-established and understood phenomenon, there may be additional effects that are impacting on the cells. Determining the precise nature of these changes and the fundamental biology behind them are outside the scope of this thesis. On the other hand, the resulting impact of these other processes could be important in determining the viability of the cancerous tissue. Presently, there are two known impacts of MWA; these include microwave fixation and coagulative necrosis. Microwave fixed cells tend to maintain their structure but establish complete subcellular disruption and are no longer viable. This region is found in the area closest to microwave probe. Coagulative necrosis is found in cells further from the tip of the probe and again leads to death of cells [185].

A potentially very important result is shown in a study by Dwivedi, *et al.*, [186] which was concerned with low intensity microwave radiation and its impact on liver cells. The

significant finding of this study is that under low intensity microwave radiation there was significant disruption to cell membranes. This raises an interesting discussion point around the exact mechanism of this damage, since almost all studies previously focused on the heating effect, which is apparently contradictory to this research. The low power microwaves utilised would be expected to lead to only minor increases in the temperature, which is not sufficient to cause the damage quoted in other studies.

Obviously, several assumptions have been made leading up to this conclusion, as there is no temperature quoted by the study author, and it can only be assumed this power level would not lead to a huge temperature rise. Furthermore, the cells used are not cancerous cells that have previously investigated. However, this observation, in combination with the unknown causes of microwave fixation, warrant further investigation and will form the focus of the remainder of this thesis.

#### **5.1.4 Microwave Ablation – Theory**

The basics behind microwave ablation are that electromagnetic radiation is delivered from an antenna into a tissue sample, with the fields involved being governed by Maxwell's equations. The most influential part of this radiation is the electric field as a result of its interaction with polar molecules, such as water, and it is expected that it is the electric field that will still be the main factor behind cell necrosis. However, the more fundamental part is the requirement for energy to be delivered to the tissue in order to see the effect. The energy delivered is a function of the power delivered, which is best described in (5.1) [187].

$$SAR = \frac{\sigma}{2\rho} E^2 \quad (5.1)$$

where  $\sigma$  is the conductivity of the tissue (S/m),  $E$  is the electric field amplitude (V/m),  $\rho$  is tissue mass density ( $\text{kg/m}^3$ ) and  $SAR$  is the rms specific absorption rate (W/kg).  $SAR$  is effectively a measure of the rate of power deposition in the tissue and will determine the power transferred to the tissue, consequently governing the damage inflicted to the tissue. Due to the  $SAR$ 's high dependence on electric field, more consideration to this aspect will be given in next section.

#### **5.1.4.1 Electric Field Cellular Impact**

The microwave electric field is anticipated to interact with all the polar molecules within a cell and it is this interaction that is sought to be exploited for the purposes of this investigation. COMSOL simulations of ideal applicator geometries are considered in the next section.

In order to optimize the coaxial applicator design, a number of parameters were investigated and varied. The primary parameters studied were: the geometry of the aperture, the radius of the tip of the open-ended coaxial probe; and the axial position of the probe. The models were optimized to fulfill the requirements of the treatment process, in particular maximum delivered power to the cells at an operational frequency of 5.8 GHz.

## **5.2 Probe modelling in COMSOL**

As a result of a comprehensive search of information obtained through the literature review, a range of simulations have been generated to better understand the electric field distribution within the tissue sample. FEM software was utilised, allowing for a range of models to be created with varying parameters, with the information being used to provide evaluation for the practical experiments. The software selected is COMSOL Multiphysics, which utilises advanced numerical methods for modelling and simulating physics based problems. This software has been chosen (ahead of EMPro) because of its ability to couple EM and thermal problems, utilising its “Multiphysics” approach and using its specialist RF Module.

### **5.2.1 Determination of the model parameters**

One of the important parameters utilised is the frequency. The frequency selected is 5.8 GHz, which has been selected for a number of reasons. Firstly, based on the literature, higher frequencies tended to generate the best results. Additionally, there are equipment limitations, in that the signal generator available for the experiments has a maximum output frequency of 6 GHz, so that 5.8GHz is in the nearest ISM (Industrial-Scientific-Medical) band. Secondly, as mentioned previously, the microwave power levels dictate

the electric field levels (with  $E \propto \sqrt{P}$ ) and consequently a range of power levels will be tested, this is again being limited by the available equipment and safety concerns to 50W. Hence, a range of input power levels from 10W to 50W will be simulated. The dielectric properties of the materials being subjected to microwave radiation are required to be set, to guarantee accurate results will be generated. Three different materials have been simulated: water, normal breast tissue, and cancerous breast tissue. The dielectric properties of water are well known with relative permittivity being adjusted for temperature through equation (5.2) [188].

$$\begin{aligned} \epsilon_s(T') = & 78.54(1 - 4.579 \times 10^{-3}T' + 1.17 \times 10^{-5}T'^2 - 2.8 \\ & \times 10^{-8}T'^3) \end{aligned} \quad (5.2)$$

where  $\epsilon_s$  is the relative permittivity and  $T'$  is  $T - T_0$ , where  $T$  is temperature and  $T_0$  is the ambient temperature, set to 25°C such that the relative permittivity was found to be 78.54. The conductivity of water was set to  $5.5 \times 10^{-6} S/m$ . The normal and cancerous breast tissue dielectric properties were found in a large scale study conducted by Lazebnik, *et al.*, [134] and are summarised in Table 5-1.

Table 5-1 Dielectric properties of normal and cancerous breast tissues.

Parameter	Normal Breast Tissue	Cancerous Breast Tissue
Relative Permittivity	4.5	57
Conductivity (S/m)	0.2	5

The properties shown in Table 5-1 are measured at 5.8 GHz and will be utilised within the simulations. Finally, the other factor in the design of these simulations is the various geometries used; these reflect the available materials and have been created to the exact specifications to ensure the results of the simulation are accurate.

## 5.2.2 Geometry and Mesh Creation

COMSOL Multiphysics® 4.4 was used to design a new open-ended coaxial probe by attempting different geometric configurations based on different apertures. Then, different levels of excitation powers were applied to evaluate the electrical field distribution through different samples. The design was based on a drive frequency of 5.8 GHz. To create the models COMSOL requires a number of steps to be followed.

This process will be described for one of the models and will be repeated in exactly the same manner for all remaining models. The geometry is created which reflects the shape and size of the probe used. The method of creating the object shown in Figure 5.4 is known as translational geometry, which is a method of representing 3D objects in 2D. It relies upon there being a constant cross-sectional shape which can be translated in a fixed direction, as is the case for Figure 5.4 and for all future models.

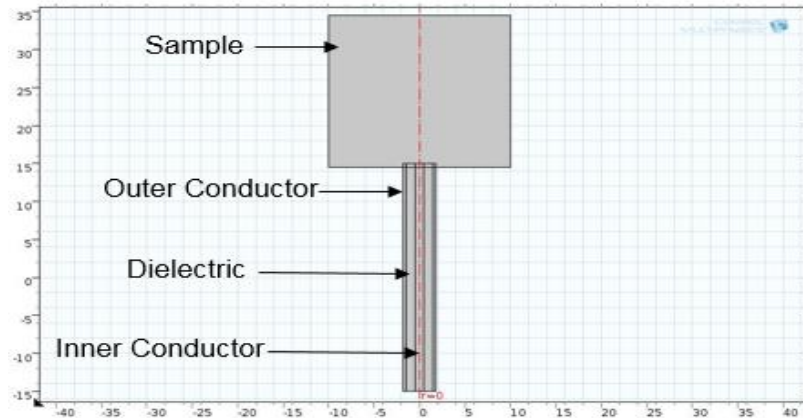


Figure 5.4: Labelled diagram of the RG402 microwave probe and sample as generated by COMSOL.

It shows the geometry of a simple open ended coaxial cable, which is acting as the antenna for the microwave radiation, as generated in COMSOL. It has been immersed into a water sample in this particular example. The model shown is an accurate representation of the probe that is expected to be utilized for the real experiments. Having created the geometry, material properties, frequency (5.8 GHz), and power level (initially 10W), are required to be entered and then the suitable mesh can be generated, as shown in Figure 5.5. This model contains one plane of symmetry. By using symmetry, only one-half of the structure, as shown in Figure, needs to be modelled by applying the symmetric boundary condition at the plane of symmetry to simplify their modelling process.

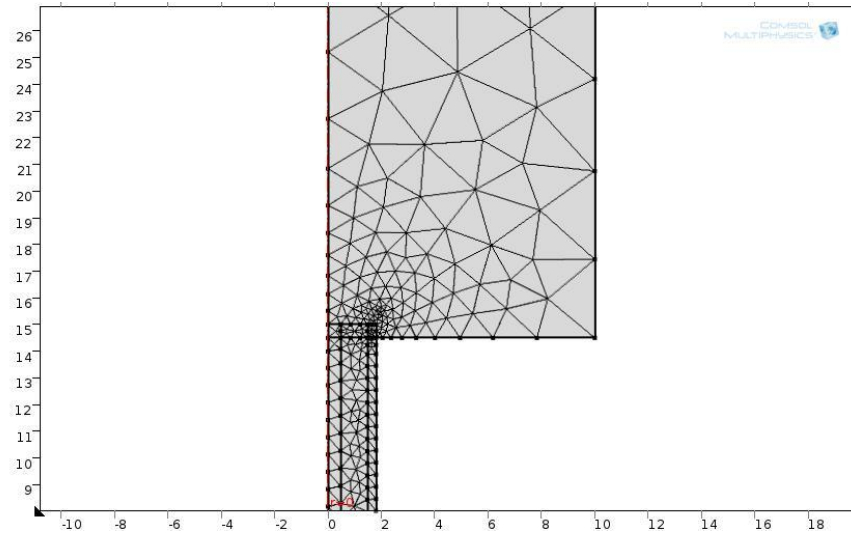


Figure 5.5: The mesh generated by COMSOL.

The accuracy level of this mesh can be increased by changing the element size; this was deemed unnecessary due to the already detailed mesh, with little benefit being gained through increased refinement, given the increased computation time. Having completed these steps the model can now be solved.

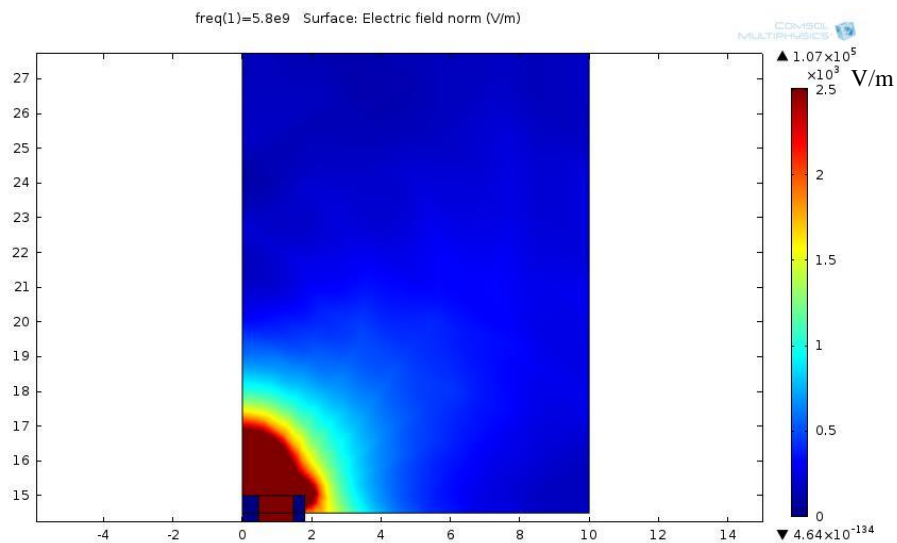


Figure 5.6: The solved model for 10W of radiation delivered into a water sample as generated by COMSOL.

Figure 5.6 displays the electric field distribution for the previously created model, with the red regions displaying higher levels of electric field, which as expected can be seen to be concentrated near to the tip of the probe.

Scattered electric field effects were investigated using an open-ended coaxial sensor, as the maxima of field is localized at the open-ended applicator aperture as demonstrated by:

$$2V_o^+ = V_{open-ended} \quad (5.3)$$

$V_o^+$  is the input voltage and  $V_{open-ended}$  is the voltage at the open-end of the applicator.

$$2V_o^+ = 2\sqrt{2P_{in}z_o} \quad (5.4)$$

where  $P_{in}$  is the input power, and  $z_o$  is the characteristic impedance. The electric field at the applicator aperture is given by:

$$E \cong \frac{V_{open-ended}}{a \ln(b/a)} \quad (5.5)$$

$$E \cong \frac{2\sqrt{2P_{in}z_o}}{a \ln(b/a)} \quad (5.6)$$

where  $a$  and  $b$  are the inner and outer radius of the applicator respectively.

### 5.3 Simulation results

Using the methodology set out above a range of simulations has been conducted in order to generate reliable information upon which the experiments can be conducted.

#### - Power Level Effect

The impact of different power levels on the electric field distribution has been assessed, the results of which are shown in Figure 5.7.

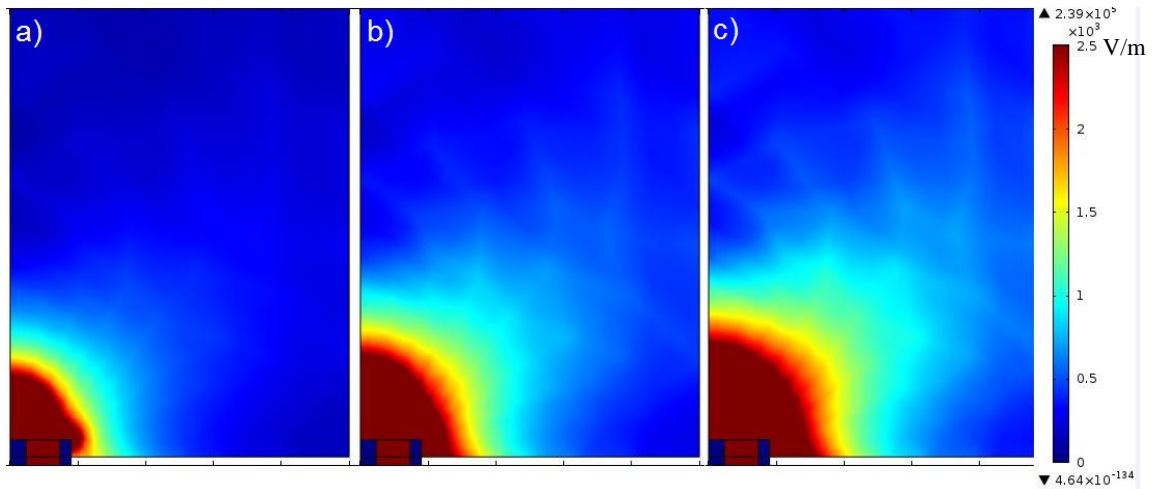


Figure 5.7: The electric field distribution at different power levels. a) 10W, b) 30W & c) 50W.

The electric field strength efficiency can be seen to increase as the power level is increased. When increasing the microwave power level, it can be seen from the COMSOL plot that the electric field magnitude everywhere increases, according to  $\propto \sqrt{P}$ . Owing to the deficiencies in using contour plots to illustrate electric field, it is not immediately apparent from Figure 5.7 that the field magnitude increases at the probe end (though it does), but the increases in the space around the probe is clear.

#### - Sample container effect

Having developed a general understanding of the electric field propagation characteristics in water, a range of realistic simulations can be produced to better reflect the sample containers that are expected to be used. These sample containers were provided by the European Cancer Stem Cell Research Institute and are commonly used for experimental procedures being carried out on cancerous cells. The first sample container is shown in. Figure 5.8.

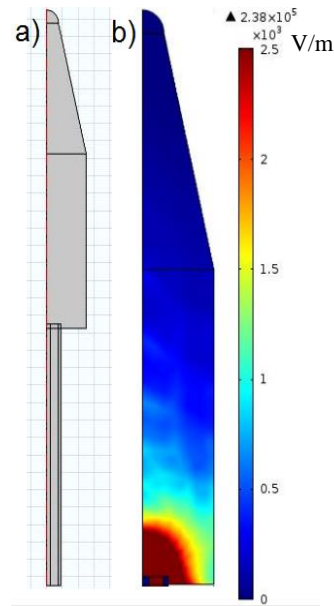


Figure 5.8: The geometry, a), and results of a simulation, b), at 50W for water in the sample container.

It shows poor field distribution with the electric not propagating the full length of the container. Consequently the decision was made to use only a partially full container with the results of this shown in Figure 5.9 This shows the results of placing the probe into the middle of container that is only partially of water, the remainder being air. The electric field does not propagate the whole length of this container at the highest available power level of 50W. In spite of this, this container was used for the initial water based experiments.

Finally, the experiments to be carried out with the cancer cells will be done in a different container. This final container was used for several reasons; it maximises the number of experiments that can be carried out and additionally it allows for a more uniform electric exposure field to be generated.

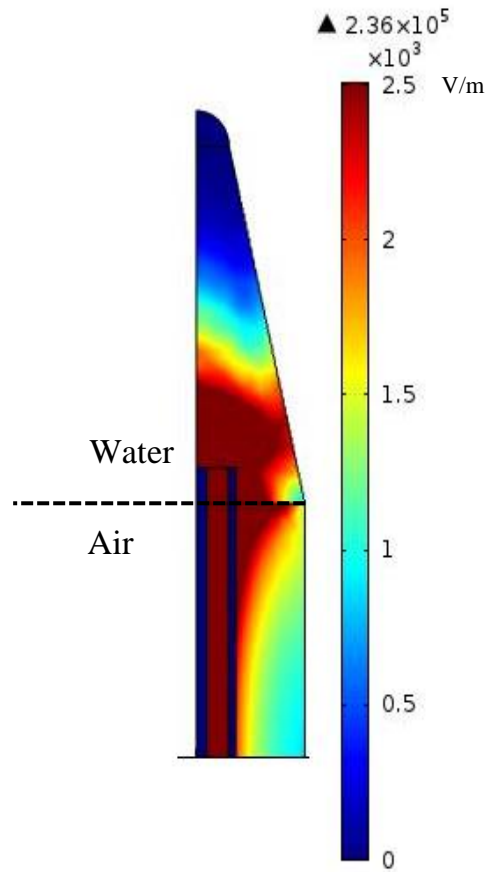


Figure 5.9: Electric field distribution of sample container filled with water and air at 50W.

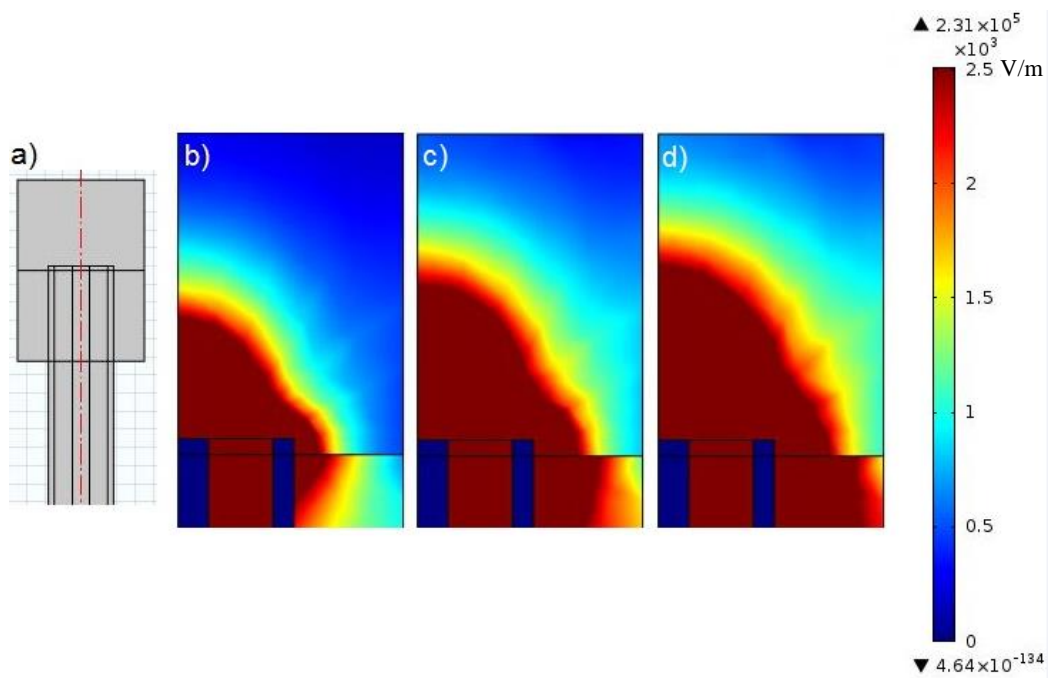


Figure 5.10: Simulated model of the cancerous sample in the container to be used experimentally, a) the geometry of the container, b) electric field at 10W, c) electric field at 30W & d) electric field at 50W.

Figure 5.10 shows the electric field distribution for the cancerous breast tissue with the parameters set out earlier. The electric field strength increases as the power level increases. It should also be noted that the  $S_{11}$  parameter for this tissue sample is much lower, recorded as 0.79, than was found for water, around 0.95 depending on the geometry. This is consistent with equation (5.1), which shows that as the conductivity increases so too does the SAR. However, the increased conductivity has negative implications for the electric field, reducing the depth of propagation due to greater number of free electrons opposing the electric field; this is again shown in Figure 5.10, with the electric field propagation depth being reduced when compared to water.

#### - **Simulation Limitations**

These simulations are not going to be completely accurate for the experiments that will be carried out. The biggest potential issue is a result of the unknown dielectric properties of the cancerous samples being provided. The samples provided are glioblastoma cells which will have different properties to those of the breast tissue modelled. Consequently, for the experiments to be carried out the simulations will not be a completely accurate representation. These will need to be improved by providing practical information of the cells under test.

# CHAPTER 6 EXPERIMENTAL SETUP FOR MICROWAVE IRRADIATION OF CANCER CELLS

## 6.1 System overview

Experimental implementation of high power microwave devices, as described herein, is challenging. This requires a complex setup, in which every aspect of the system must be carefully designed and constructed. A conceptual diagram of the nonthermal microwave system and its supporting/auxiliary systems, based on the information from the literature review, is seen in Figure 6.1.

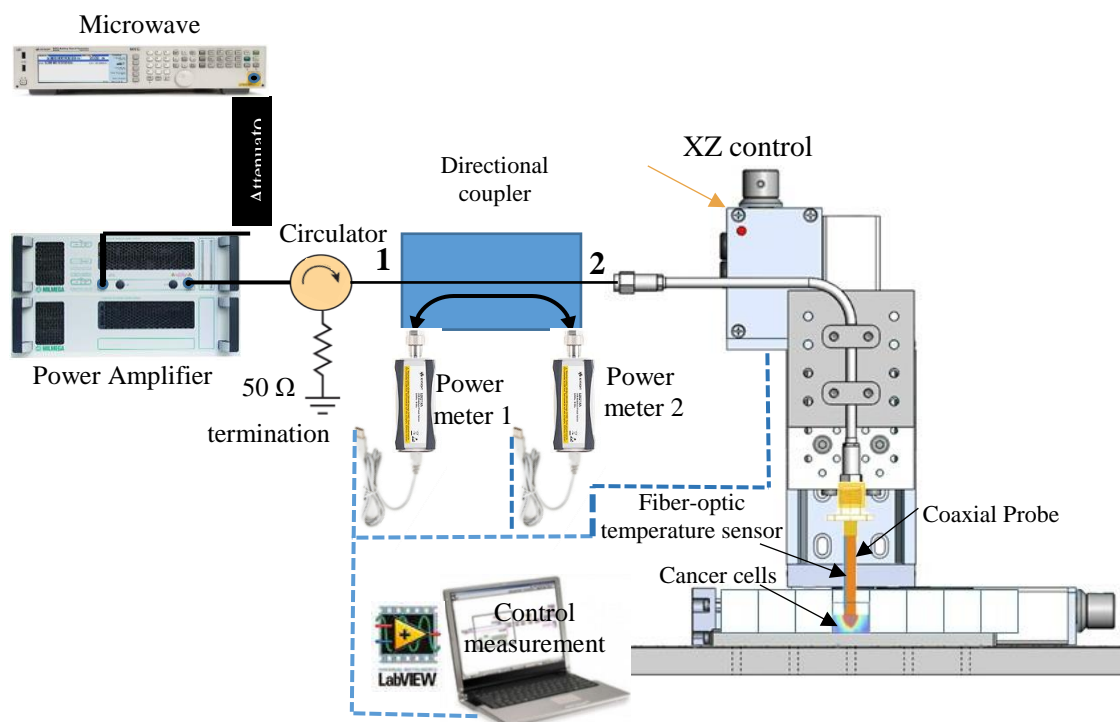


Figure 6.1: Schematic of the high power microwave system from source to probe (applicator).

The fundamental components necessary for the operation of this technique are:

- a) Signal generator
- b) High power amplifier
- c) Circulator
- d) Directional coupler
- e) Power meters
- f) Microwave applicator
- g) Temperature sensor

An overview of this entire system is warranted so as to demonstrate how these various components are integrated into a whole. This chapter aims to contribute towards an understanding of the components shown in Figure 6.1 and their function within the system. The signal generator is the source of microwave signal for the open-ended coaxial applicator; it produces a microwave pulse with the appropriate period, width and duration, fed to a high power amplifier, at the output of which an amplified microwave signal is produced. The high power signal then travels through the circulator. Simultaneously, the directional coupler drives a signal to the applicator which is injected into the cancer tissue. The coupler allows the transmitted and reflected powers to be measured by the power meters. Now, a more detailed description of these major subsystems components of the experiment will be presented.

### **6.1.1 Signal Generator**

An RF signal generator was used to generate the 5.8 GHz in the study, although there are many different types of RF signal generator designs available, the building blocks are essentially the same. For the purpose of this investigation the MXG 9 kHz – 6 GHz signal generator was used [189], which is ideal for the study. The generator had many useful inbuilt features: as well as continuous waves it offers a range of different modulation schemes such pulse modulation (PM), frequency modulation (FM), and amplitude modulation (AM) operation; it has built in software limiters of frequency and amplitude; the ability to generate several different periodic waveforms from built in standard libraries or user defined input; and built in VISA and GPIB interface to provide easy automation. The MXG signal generator has a maximum power output of 19 dBm (0.0794 W) and was unable to output the powers required for our research. A

dedicated power amplifier was used to boost signals from the signal generator to useful levels.

### 6.1.2 High Power Amplifier

The power amplifier is at the center of all of our experiments. This device is the source of the high-quality magnified microwave power signal that will be used for microwave cancer treatment. The amplifier used in this study was the Class A MILMEGA 1.8 GHz to 6 GHz solid state amplifier.

Class (A) is one of several different topologies of power amplifiers; the classification of amplifiers depends on several different factors such as: the configuration of the amplifier, how it processes input signals and the relationship between its input and output signals. Each classification has different advantages associated with it. For class (A) amplifiers the two main advantages are their ability for reproducing signals with low distortion and outputs that are directly proportional to the input, which are the two main criteria for this study.

A Class (A) amplifier is biased to operate within its active region and is usually not driven into its cut-off or saturation regions. In its simplest setup, a class (A) amplifier uses a single transistor connected in common emitter (CE) configuration, as seen in Figure 6.2, for both halves of its waveform.

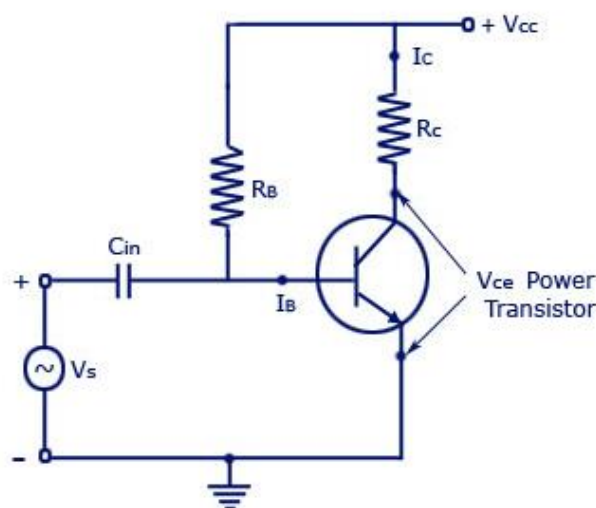


Figure 6.2: Simple diagram of class A amplifier circuit [190].

Since the transistor is always on and having current always flowing through it, it generates a lot of heat which can have an adverse effect on its self as well as other components within the amplifier, leading to varying performance and even temperature failure. The MILMEGA amplifier used in this research employs heat sinks and a fan system to help it shift this heat away from its casing. For high amplification a single transistor doesn't provide enough gain so most high power amplifiers adopt multi stage designs, where the gain is the product of the gains of all the transistor stages. Additionally the stages provide a certain level of isolation that contributes towards stable operation during mismatch condition [191].

### 6.1.2.1 MILMEGA AS1860 Amplifier

As a type (A) amplifier, the MILMEGA as1860 is perfect for the needs of this investigation; the signal generator will be driving the power amplifier towards the high end operational frequency limit (i.e. 5.8GHz), so it's ideal that it can maintain a high level of fidelity. An amplifier maintains a constant gain for low-level input signals. However, at higher input levels, the amplifier goes into saturation and its gain decreases. The linear input output characteristic of the amplifier simplifies the calibration process, discussed in Section 6.2. Table 6-1 below details some of the other features of the amplifier.

Table 6-1 Standard specification for MILMEGA amplifier taken from its datasheet [192].

<b>Specifications</b>	
( 1 dB Gain compression point) P1dB	50 dBm
Gain	46 dB
Gain Variation with frequency	$\pm 3.0$ dB
Operating Temperature range	0 to 40 °C
Maximum Input Power	15 dBm
VSWR (Input and output) for 50 $\Omega$ Impedance	2:1
RF connector style	Type N female

Despite its advantages, there are some limitations when using the amplifier:

- The maximum input power limitation means that an attenuator had to be placed between the signal generator feed and the input port of the amplifier, as a failsafe to limit the risk of damage to the power amplifier input port.
- A second limitation that was observed is a drift in the amplifier gain when it is initially turned on. Whilst it is true that the amplifier can be used from switch on, the circuits within the amplifier need time to become thermally stable for accurate power delivery. The drifting gain can have an important effect in system calibration, discussed in Section 6.2, especially at higher power levels where the deviation in delivered power can be as much as 10 W different from that expected. To compensate for this drift, the amplifier was left running over a long time period whilst its output power was monitored directly using a power meter. It was found that after a period of approximately 40 minutes of operation the amplifier gain typically settled on a value of around 46.1 dB.
- Looking at Table 6-1, the power amplifier is limited to a transmitted output power of 50 dBm. Gain compression occurs when the input power of an amplifier is increased to a level that reduces the gain of the amplifier by 1 dB; Figure 6.3 gives an example of the change in input and output powers when the power amplifier is driven into compression.

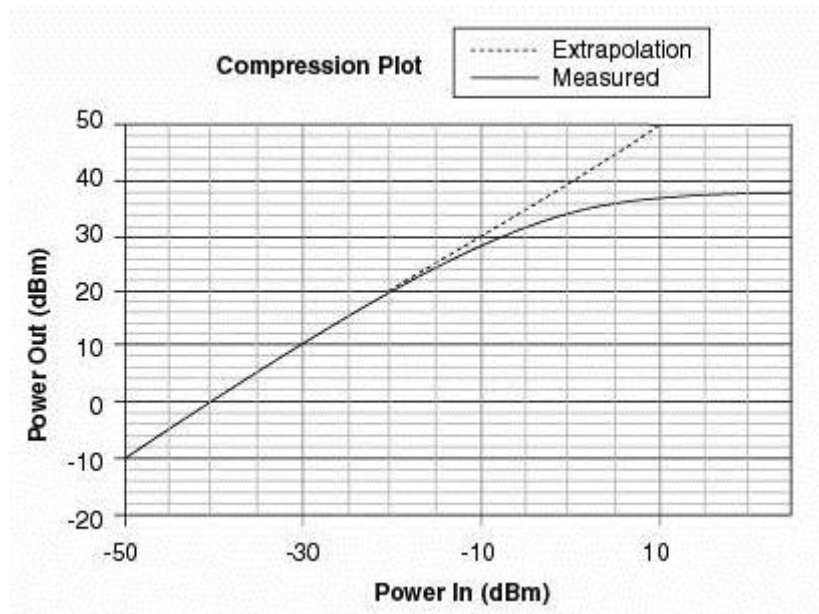


Figure 6.3: Example gain compression plot, in this case the P1dBm level is set at 20dBm output [193].

- As previously mentioned, power amplifiers have been known to fail due to excessive temperature rise caused by low impedance mismatch. To mitigate against this possibility the MILMEGA amplifier employed the use of fans to help keep operational temperatures at acceptable levels. In addition extra care was taken to make sure the components (i.e. wires, attenuators, devices etc.) connected to the input and output ports of the power amplifier are rated at 50  $\Omega$ , to minimise the chance of impedance mismatch and to use effectively the generated microwave power.

### **6.1.3 Circulator**

The primary function of the circulator within the experimental set up is to ensure that any reflections from the probe tip do not feed back into the power amplifier. The interaction with forward travelling waves propagating from the amplifier can lead the amplifier to see an apparent impedance mismatch; this can have a range of consequences such as: reduced power output, waveform distortion and the increased stress on the output transistors of a high power amplifier can lead to premature failure [191].

The circulator consists of a three port device formed by a y- junction strip line coupled to a magnetically biased ferrite material [194]. The output of the power amplifier travels through a circulator (which provides protection from large reflections coming from the open-ended applicator), and through a 30 dB dual-directional coupler. Both sampling ports of this coupler are fitted with power meters that allow us to measure the forward (towards the sensor) and reflected (back from the sensor) power. By this way, it's possible to make careful measurements of the power as well as scan the radial pattern of the microwave radiation.

When one of its ports is terminated, the circulator can act as an isolator for the incident and reflected signals. The HF signal propagates into the circulator at port 1 and exits at port 2. The returning reflected signal enters at port 2 and is terminated at port 3. Due to the bias magnetic field produced by the ferrite material there is minimum coupling between ports 1 and 3 (transmitted signal) and between ports 2 and 1 (reflected signal). Although in general circulators have very low losses and are capable of handling large

amounts of power, there are a few limitations concerning their operation: since reflected power can flow from port 3 back into port 1, a 50  $\Omega$  termination placed at port 3 needs enough dissipative capacity to ensure no residual signal is transferred back to port 1. A second limitation is the reliance on the resonance of the ferrite material, making the operation of a circulator very frequency specific; most circulators are designed only to operate within a narrow frequency band, outside of which there are increased losses and isolation cannot be guaranteed. For the purpose of this thesis the Altan Tec AS7122 circulator (5.4 to 6.6 GHz) was chosen, as illustrated in Figure 6.4.



Figure 6.4: Photograph of used circulator.

#### 6.1.4 Directional Coupler

Two of the key parameters of measurement within the study are the measurement of the reflection (Rx) and incident powers (Tx) at the probe. These measurements can be used to work out the power injected into samples, as well as scattering parameters; indeed, such measurements can be used to understand how the properties of the tissue sample change during microwave radiation exposure. Unfortunately the reflected and incident powers cannot be measured directly, but the directional coupler provides a way for the Rx and Tx signals to be sampled simultaneously without the need for adjustment.

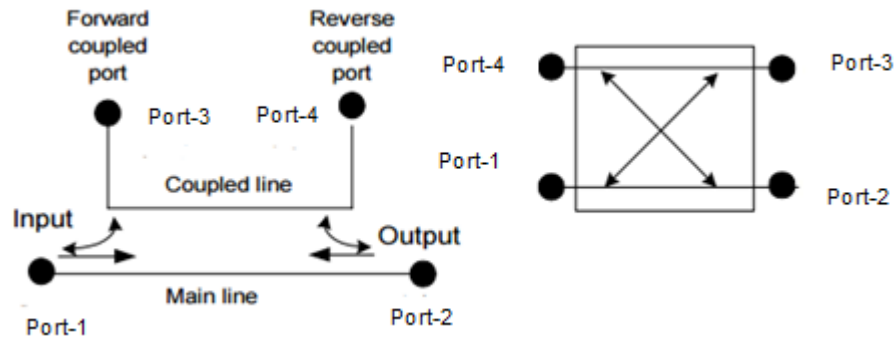


Figure 6.5: Four port directional coupler diagram [195].

The principle of how the directional coupler operates is quite simple; looking at the operational diagram presented in Figure 6.5, a signal is fed through port 1 in the mainline and outputs through port 2. A fraction of this signal appears in the coupled port. Reciprocal circuits within the coupler work to isolate the Tx and Rx so that when energy is injected from port 2 it will not be seen in the coupled port. In real life, however, there is always some Rx signal leaking into the coupled port. The directivity is a measure of the Tx and Rx coupling and is strongly affected by the impedance match provided by termination at the isolated port. During calibration it is essential to terminate the unused port otherwise a leaking Rx signal will cause inaccuracies to be introduced to the measurements taken from the coupled port.

The coupler used in the study is a four port bidirectional coupler with a rated coupling factor of 30dB between the main line and the coupled ports as shown in Figure 6.6. Since there are two coupling ports and no true isolation, the directivity of the coupler can be compromised, meaning that the signal seen from each of the coupled ports is likely to be slightly different from the rated value. Additionally the coupler is unlikely to have a flat performance level (not 30dB coupling) across its operational bandwidth; calibration of the system was used to determine the correct values of coupling factors with respect to the probe position. This point will be discussed further in the next section.



Figure 6.6: Photograph of used directional coupler.

### 6.1.5 Open-ended coaxial applicator

The primary treatment tool for cancer treatment experiments is the open-ended coaxial probe, only considered as an “applicator” at these high powers, as opposed to a “sensor” at low powers (chapters 2-4). Since this is an applicator problem, for these first experiments we decided to use the flat coaxial probe since its electric field distribution was more uniform compared with that of the needle probe. A view of the probe can be seen in Figure 6.7 This is RG402 open-ended coaxial cable with 5cm length, whose SMA female connector end is connected to high power microwave signal, and the other flat open end (*i. e.*  $\varphi = 0^\circ$ ) is immersed into suspension cancer cells or pressed into *in vivo* tissue. The design of the sensor aperture was later altered based on data from real experiment.



Figure 6.7: Photograph of used RG402 open-ended coaxial applicator.

Other instruments are of note here: attenuators and the thermocouple for temperature measurement. Additionally, a very sensitive fibre optic temperature probe and infrared thermo-camera were used in later experiments for precise temperature measurement.

## 6.2 System Calibration

To calibrate the power meters, a double ended probe was attached to the output of the coupler; its use allowed the reading from the Tx coupled port to be referenced to the probe tip. Additionally, using the double ended probe also meant the losses in the probe connector could be accounted for. To provide isolation and keep the coupler matched to

the system impedance a 50Ω terminator was attached to port 4. This configuration can be seen in Figure 6.8.

When power is injected through port 1, the calibration factor for port 3 is defined as:

$$K_1 = P_3 - P_2 \quad (6.1)$$

where  $P_2$  and  $P_3$  are the power meter readings (in dBm) at ports 2 and 3 respectively.

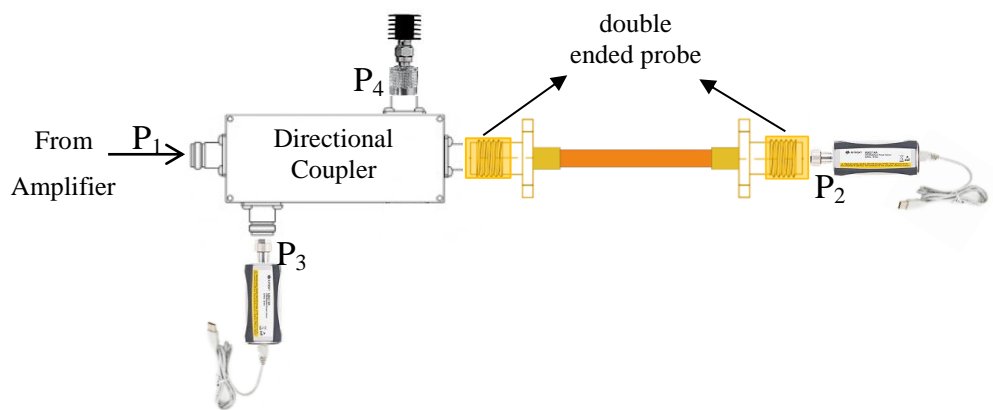


Figure 6.8: Diagram of forward signal calibration process.

In a similar fashion the calibration for the coupled reflection, shown in Figure 6.9, can be found this time with the power injected through the double ended probe and measurement taken from port 1 and the Rx coupled port.

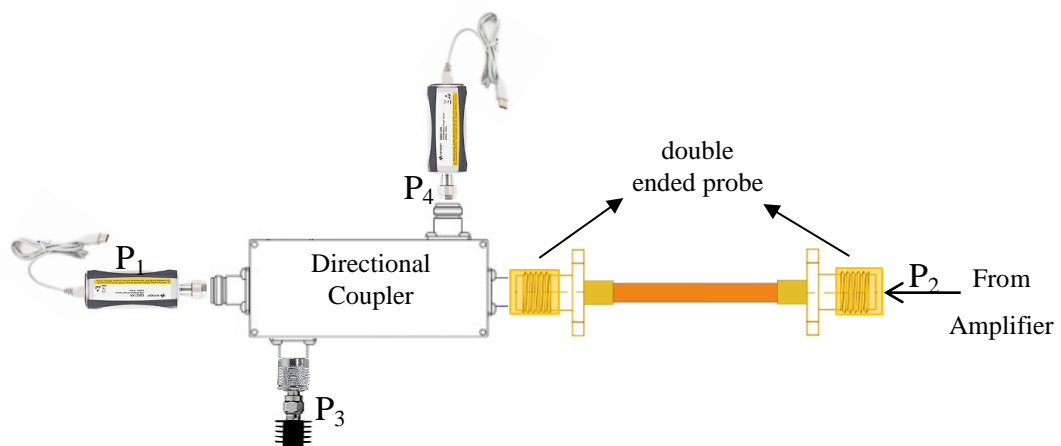


Figure 6.9: Diagram of reflection signal calibration process.

The calibration factor for port 4 is defined as:

$$K_2 = P_4 - P_1 \quad (6.2)$$

### - Calibration Limitations

The power meters used in the study are complex devices and have a limited level of direct power they can withstand (+23 dBm), however since the elements between the amplifier and the probe are assumed to be passive, the calibration process took place at lower output power levels than the levels used experimentally (40 dBm - 47 dBm); the assumption being that the coupling factors are constant and that there is a linear scaling when powers are increased.

After calibration is performed, two power meters were connected to the coupled ports  $P_3$  and  $P_4$  to allow simultaneous measurement of the Tx and Rx powers; the two power meters also act to provide isolation for each other, respectively. In general the power meters' impedance  $Z_L$  is not exactly equal to the system impedance  $Z_0$ , so the power meters have a non-reflection coefficient [196]. As a consequence some errors in readings could be introduced due to cross coupling between forward and reflected signals.

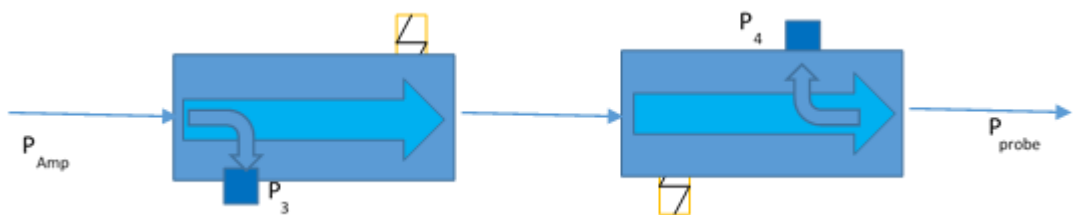


Figure 6.10: Cascade coupler setup for measuring Rx and Tx.

Bramall [197] suggests using a set-up of two directional couplers to mitigate mismatch in the power meters. In Figure 6.10 each coupler is dedicated to just measuring either the forward power or the reflected power. Good terminators (more closely matched to  $50\Omega$ ) are used to provide isolated ports with better impedance matching, so there is little to no cross coupling between the coupled ports.

Unfortunately for the investigation, we were unable to source an additional directional coupler that was fit for purpose (i.e. working well in range of 5.8 GHz), instead attenuators were added to the input of the coupled ports in series with the power meters; the attenuators were used to protect the power meters from damage in the event wrong amplitude selection at the signal generator but they also improve the termination of the coupler. Since the reflected signal had to travel through an attenuator its level becomes sufficiently low enough to prevent any cross coupling in the forward port and helps improve the calibration.

### 6.2.1 Electromagnetic Radiation Meter

During the experiment it is expected that the test sample will be exposed to microwave radiation up to 50W from the applicator. This radiation can propagate far beyond the samples., a HF meter was used and placed next to sensor to monitoring the risk of exposure. It is shown in Figure 6.11.



Figure 6.11: HF meter.

### 6.3 Measurements and Instrumentations

The measurements and instrumentation for this study consist of automation to detect and control the instruments and probes for measurement. Several parameters are needed to understand the properties of the tissue sample when they are exposed to microwaves radiation. These properties include the strength of the microwave signal, the transmission and reflection of the microwaves signal as well as the scattering

parameters. These parameters are important to be determined because they describe the propagation of the microwaves between the sample materials.

### 6.3.1 Peripheral Hardware

The additional hardware used for the measurement and detection of signals from the applicators consists of two identical power meters, temperature sensor and DAQ device.

- **Power meter**

The power meter shown in Figure 6.12, is a USB connected power meter that senses the strength of the microwave signal ranging from 50 MHz to 18 GHz [198]. The power meter reads either peak or average signal, depending on its triggering configuration. For peak signal detection, the power meter can be triggered from positive edge of each signal coming from the signal generator. This configuration is useful for the power measurement during microwave pulsing. On the other hand, the power meter can be set to take average measurement at interval sets of measurements, which is more convenient for our configuration. The Agilent U2021XA power meter has maximum input of +23 dBm, therefore, several precautions were made during direct measurement to ensure its protection. This precaution includes the use of low power microwaves (less than -10 dBm output from microwave signal generator) for equipment calibrations and additional 10 dB attenuator at Port 3 and Port 4 where the power meter reads the measurements from the coupler.



Figure 6.12: Agilent U2021XA Power Meter with USB connection.

- **Temperature sensor**

Figure 6.13 shows the temperature sensor that was used to measure the temperature changes within the tissue sample. It is a J-type thermocouple [199] with small temperature sensitive part at the tip, giving it the advantage of accessing the small space

within the container of the cancer cells culture. Also, the thermocouple is insulated with glass along the 2 m length of its two-wire connection. The range of temperature that this thermocouple can measure is between  $-40\text{ }^{\circ}\text{C}$  to  $400\text{ }^{\circ}\text{C}$ .



Figure 6.13: J-type thermocouple insulated with glass.

- **DAQ device**

A compact DAQ device NI 9219, manufactured by National Instruments, was chosen to sample and measure the current changes within the thermocouple and convert it into temperature measurement. The DAQ device is connected through USB and controlled by a LabVIEW program. Since the thermocouple required excitation current to determine the current and resistance along the wire with the change of temperature, this DAQ device has a built-in internal excitation current that is fed into the thermocouple wires. Also, the DAQ device has 4 input ports, which makes it suitable for the experiment that has been done with a water sample in a long container, where two thermocouples were used to measure temperature nearby and far from the probe.

### 6.3.2 Software

All the equipment and applicators are measured and monitored by using LabVIEW software.

**LabVIEW implementation:** All the instruments and measurement used in this study were controlled in a single LabVIEW program, which was written by help of Syed Muhammad Hilmi. LabVIEW or Laboratory Virtual Instrument Engineering Workstation is National Instrument's software for graphical programming to control and measure instruments. The software can take any input or output data and displays the measurements in any graphical form [200]. The software consists of Virtual

Instrument, or VI, that has a front panel and block diagram. Mihura [200] differentiates the front panel and block diagram of the VI by writing that the block diagram is used for the programmable flow of data acquired, while front panel is used for user interface for the program. The Agilent U2021XA power meter is configured within LabVIEW to perform specific functions during the measurement. Each setting for the power meter has been given in the LabVIEW library by Agilent in form of VI, however, further programming and reconstructing of the VI was made. Figure 6.14 and Figure 6.15 below show the flowchart and block diagram of the power meter configuration.

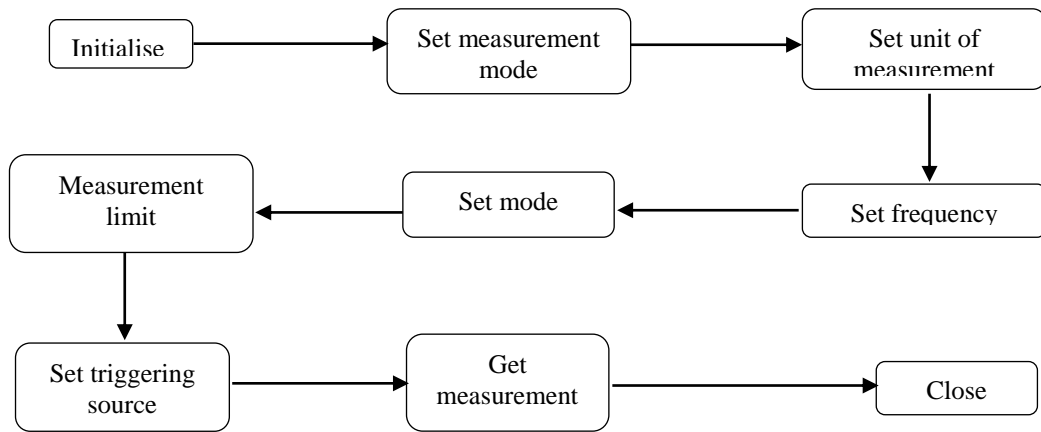


Figure 6.14: Flowchart of power meter's configuration in LabVIEW

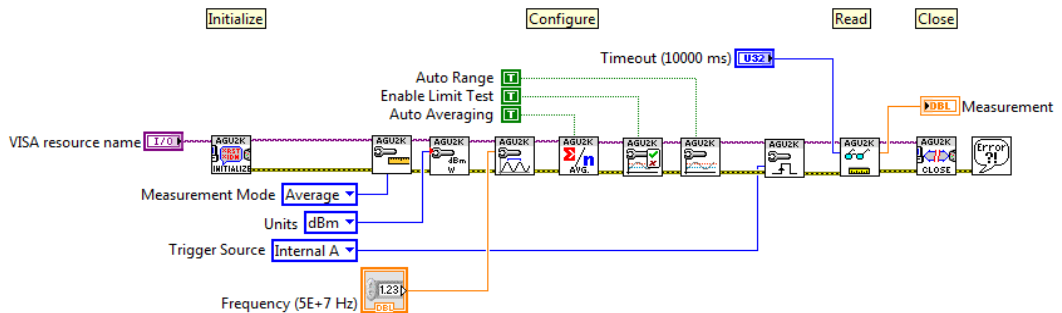


Figure 6.15: Block diagram of power meter's configurations in LabVIEW.

All the codes were written based on the programming manual given by Agilent [198] for this power meter. VISA or Virtual Instrument Software Architecture is a standard for configuring, programming and troubleshooting instrumental systems such as GPIB or USB interface [201]. The frequency of the measurement was configured by setting the frequency for the measurement at 5.8 GHz.

After all the configurations were made, the power meter was ready to take signal strength reading, and it was tested by connecting it directly to the RF signal generator.

**LabVIEW – Main VI:** After the configurations for the power meters were made, the measurement sub-VI was reconstructed within a ‘while loop’ for continuous measurement. Within this loop, continuous measurement from two power meters and thermocouple were made as well as manipulations of data taken from the power meter measurement to give reading of power dissipated into the sample, reflection coefficient and  $S_{11}$  parameter. The flowchart for the main VI for this research’s measurement and instrumentation are shown in Figure 6.16

One power meter measured at Port 3 while the other measured at port 4 of the coupler, and were given an offset value which was obtained from the calibration procedures mentioned in section 6.2 to give readings of transmission signal,  $T_x$  into the sample and reflection signal,  $R_x$  from the sample in dBm units.

$$T_x(dBm) = Power\ meter_{Port\ 3} + k_1(dBm) \quad (6.3)$$

$$R_x(dBm) = Power\ meter_{Port\ 4} + k_2(dBm) \quad (6.4)$$

Subtraction was made between transmission and reflection signal strength to give value of reflection coefficient  $|r|$ .

$$|r|(dB) = T_x - R_x (dBm) \quad (6.5)$$

Both values at Port 3 and Port 4 after corrected with offset values were converted into Watts by using the usual equation below:

$$Power\ watt = 0.001 \times \left(10^{\left(\frac{dBm}{10}\right)}\right) \quad (6.6)$$

The power dissipated (in Watts) into the sample was found from:

$$P_D (W) = T_x - R_x (W) \quad (6.7)$$

The  $S_{11}$  parameter of the travelling microwaves into the sample was measured by equation below

$$S_{11} = \frac{b}{a} \quad (6.8)$$

where  $a$  and  $b$  were calculated from the equations below:

$$T_x(W) = \frac{1}{2} |a^2| \quad (6.9)$$

$$R_x(W) = \frac{1}{2} |b^2| \quad (6.10)$$

Also, the temperature reading from thermocouples was configured by using the DAQ assist palette. Within Labview the palette recognised the DAQ device used and directly converts the measurement from the connected thermocouples into temperature reading, in units of degrees Celsius. The complete main panel for measurement is shown in the flowchart of Figure 6.16.

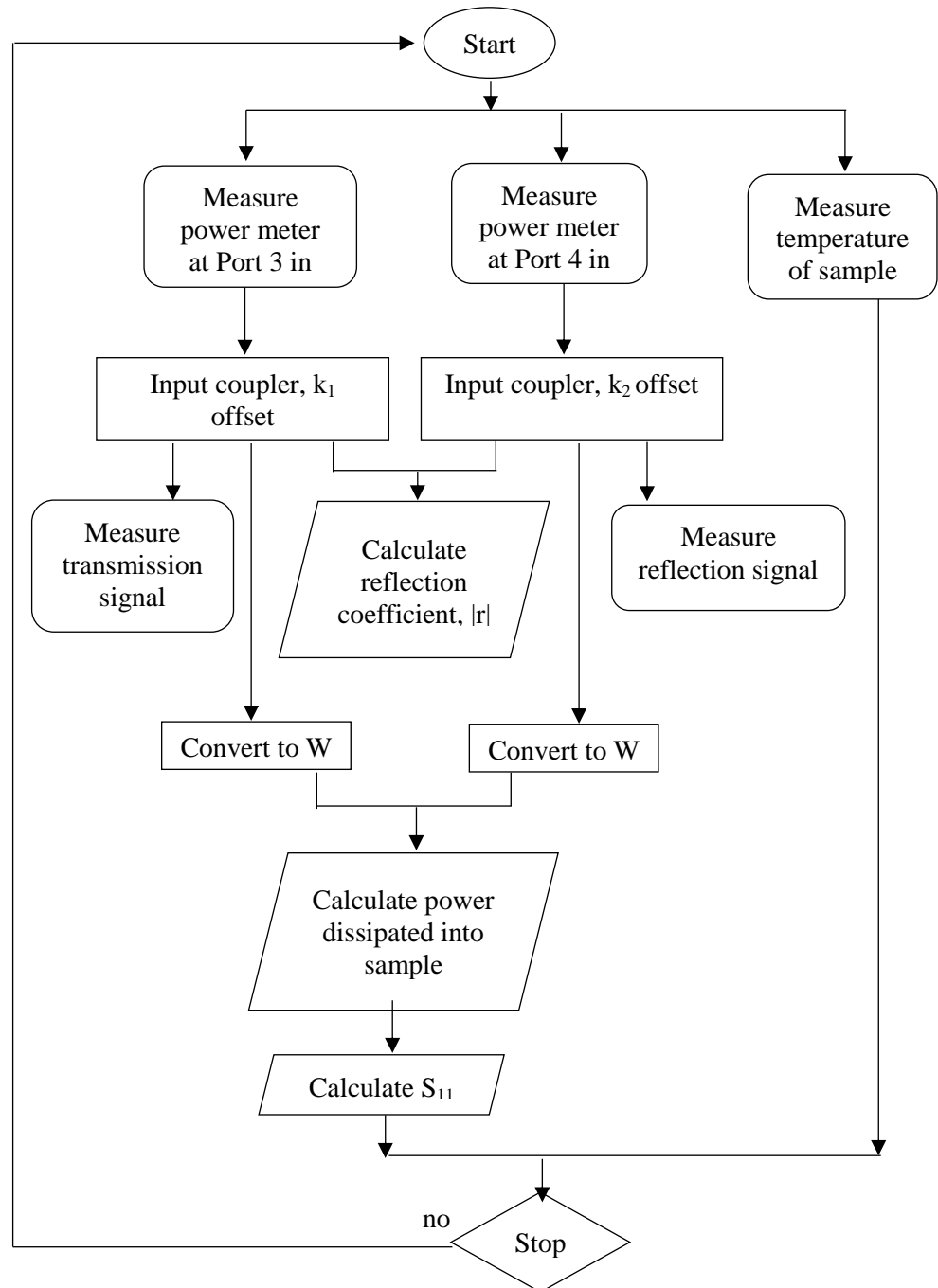


Figure 6.16: Flowchart of main measurement VI in LabVIEW.

The main panel VI shows the comparison of reflection coefficient, power dissipated into sample,  $S_{11}$  and the temperature within the sample, which is more interesting to look at for this research. Each measurement was divided into several tabs for easy access. Each power meter at Port 3 and Port 4 can be configured in the main panel, such as initialising the resource name as well as the offset at each port on the coupler. The temperature of the sample, both near the probe and far away from it, can be easily read at the thermometer or on digital view as shown in Figure 6.17. The actual reading of the power meters (in dBm units) are shown in main panel. These values are monitored for safety precaution in case it exceeds the maximum input rating (+23dBm).

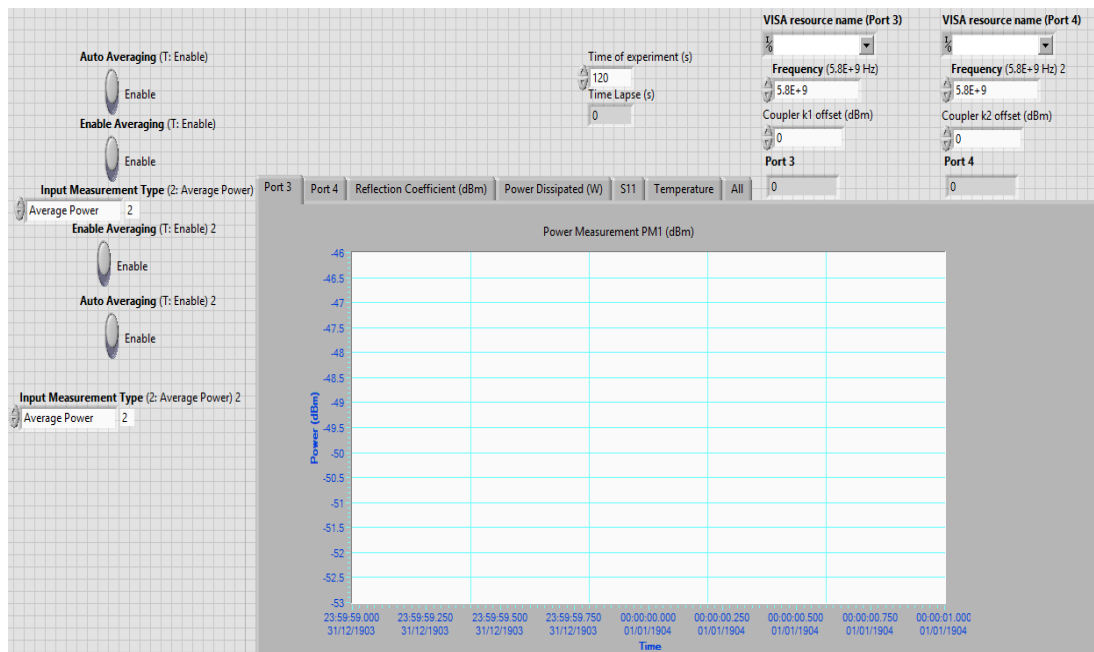


Figure 6.17: Main panel of the main measurement VI in LabVIEW.

## **CHAPTER 7 EXPERIMENTS AND RESULTS FOR MICROWAVE IRRADIATION OF CANCER CELLS**

The experimental setup and procedure for preliminary measurements have just been discussed in CHAPTER 6. A wide range of cancer cells samples have been tested in suspended medium and *in vivo* form, which will now be described here.

### **7.1 Equipment Calibration and Preliminary Measurement at 5.8 GHz**

For correct measurement of power meter readings a system calibration was performed based on the procedure described in Section 6.2, prior to the first experiment and after extended periods of equipment being idle; appropriate offsets were set in the user created LabVIEW program. The LabVIEW program was used to coordinate measurement, limit the experiment run time, log temperature, measure the power delivered to applicator probe and power reflected back from the probe. The calculations of the reflection coefficient and the dissipated power back have been implemented into the LabVIEW program.

### **7.2 Methodology**

An initial baseline test was carried out to determine the minimum energy needed to be delivered at the probe tip to achieve death in the cancerous cell cultures. A sample of 1 mL of water was placed in a container (an Eppendorf tube) of the dimensions defined in Figure 7.1. Water was used since the cancer cell samples were in solution (called 'N2 cell culture medium and it is water-based) and it provided a good first

approximation of what behaviour to expect with the cell cultures. The components list of this solution can be found in [202].

The initial experiment was done in the School of Engineering to test the full system performance. The microwave probe was immersed into the water sample and centred within the container, so the probe tip was just below the meniscus of the water sample. Two thermocouples were also inserted into the container to measure temperature difference: one was placed in close proximity to the probe tip and the other placed near the bottom of the container.

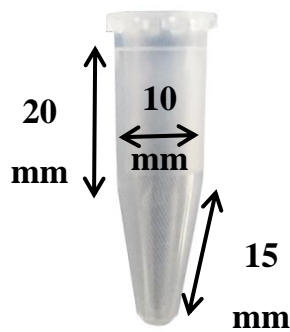


Figure 7.1: Dimensions for container used in preliminary experiment.

10 Watts of microwave radiation at 5.8 GHz was delivered to the applicator. The exposure time to cause a temperature rise in the water (i.e. measured by the thermocouple nearest to the applicator end) was recorded. The selection of 10 W and 55 °C is based on a literature review of conventional values of powers used in microwave treatment. It is understood that at temperatures above 42 °C the process of cell death begins [33], therefore 55 °C was taken as a good baseline temperature to expect complete cell death in the cell samples.

Based on the result from the baseline test, the energy being delivered at the applicator's tip was determined using (7.1):

$$Energy = Delivered Power * Duty Cycle * Exposure Time \quad (7.1)$$

A focus on the delivered energy was taken based on practicality; it was more simple to keep this as a constant than the power being injected into the sample, which is expected to change in line with the changes in the dielectric properties of the cancer cell culture as it is irradiated. The dielectric properties have a direct relationship to the ability of a sample to absorb microwave radiation.

The total energy delivered to the applicator and the temperature were kept as control variables; the other quantifiable variables such as the duty cycle, power delivered to the probe and exposure time were varied in order to maintain a constant energy and temperature profile. This decision to minimise the number of input variables was done in order to make the conclusions more manageable and allow the answering of the main questions posed in the research:

- 1) Is there a temperature independent mechanism of cell death?
- 2) What is the impact of EM field levels on cell death?

**Duty cycle effect:** The duty cycle was changed in accordance with Figure 7.2, the intention being to use short intervals of microwave radiation to reduce heat transfer into the sample, since the temperature change needs a period of time after continuous heat transfer to build up. By changing the power delivered to the probe tip, a change in the magnitude of EM field is demonstrated; this was discussed in the literature review and observed in simulation.

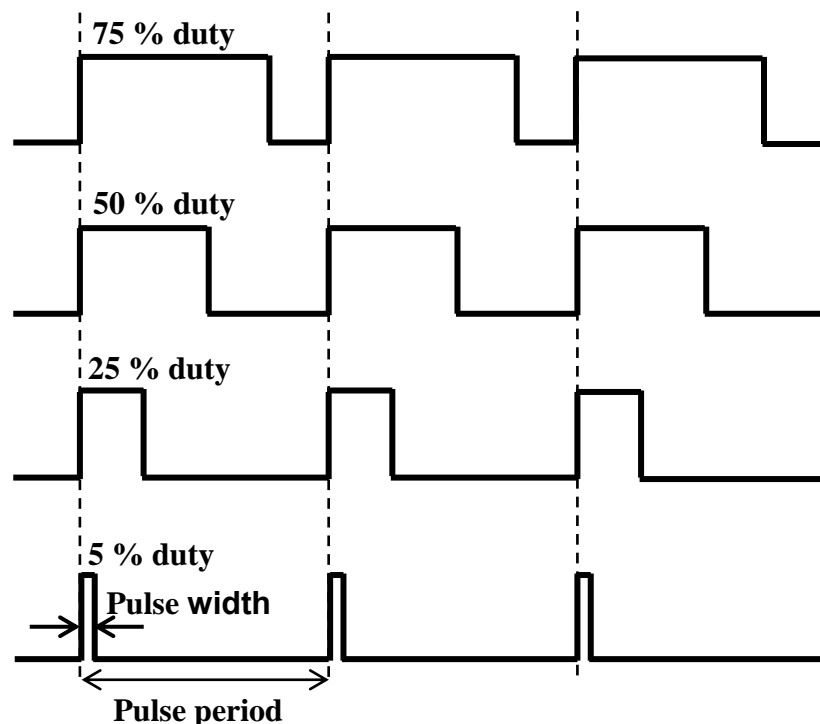


Figure 7.2: Pulse signal with different duty cycles.

Using the baseline result of 0.5Wh (i.e. 1.8 kJ) as the reference value of energy delivered, an iterative method was used for applying different duty cycles for different

power levels whilst maintaining a maximum temperature of 40°C over the course of the expected exposure time. A suitable pulse regime was achieved for use in the main experiment, as presented in Figure 7.3.

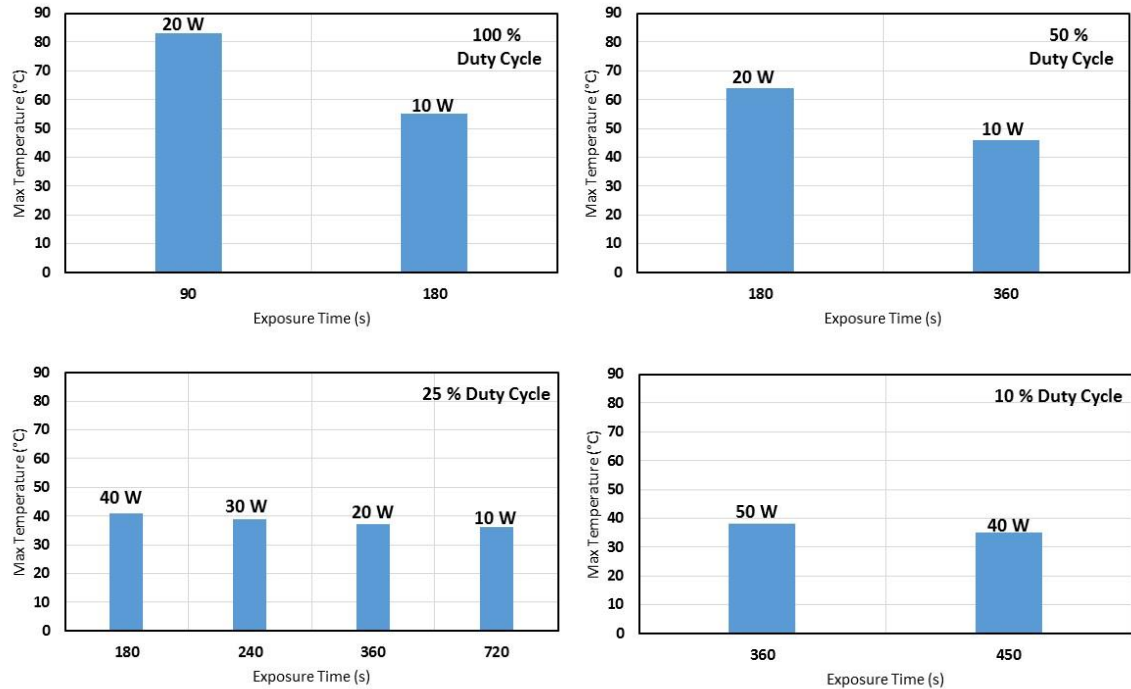
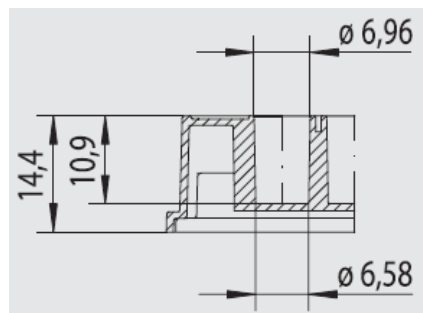


Figure 7.3: Different duty cycle and delivered power effects with temperature on a water sample.

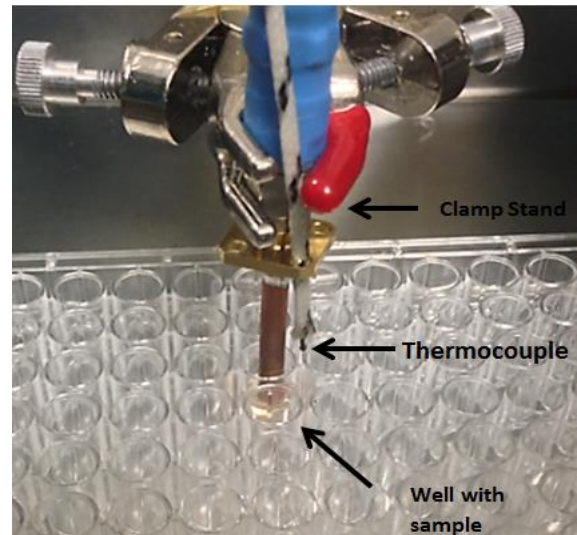
The range of powers was selected to give a wide spread of results in which to test our hypothesis about the relationship between power and electric field propagation. Chosen duty cycles were arrived at experimentally as a compromise between having a short duty cycle to minimise temperature changes and making sure the exposure time was not unduly long.

### 7.2.1 Lab Study 1 – RG402 applicator - Flat aperture

A smaller container of 10.9 mm depth and 7 mm diameter (i.e. it is called 96 well F-bottom / polystyrene) was used to carry out the experiments with cancer cell cultures. The plate containing the relevant sample was prepared and an RF power meter was used as a safety measure. The microwave probe was centred and immersed into the relevant well containing the cancerous cell culture, as shown in Figure 7.4. The well was filled with 50–100  $\mu\text{m}$  of cell culture.



(a)



(b)

Figure 7.4: (a) Dimensions of each well. (b) Showing the 96-F-bottom wells that are used for cell insertion.

**Limitations:** Since it was difficult in this set up to observe the meniscus and based on simulations the EM radiation was deemed large enough to envelope the container, care was taken to make sure the probe wasn't touching the sides or the bottom of the container and the probe was manually secured into position by means of a clamp stand. Also there wasn't enough space for the insertion of two thermocouple sensors, however, based on simulation profile for the propagation of EM Field it was deemed acceptable for the use of just one thermocouple in the sample. The experiments carried out were the ones identified in Figure 7.4. For each sample optical microscope images were recorded both before and after microwave treatment. For consideration of the possibility of latent effects, images 24 hours post treatment were also recorded.

The temperature profiles from the main experiment didn't accurately match the expected results based on the preliminary investigation. Whilst the energy transfer due to the incident microwave radiation stayed largely the same, due to the change in the container the volume of sample was reduced. Heat transfer is an extensive property and depends on volume of material [203], so for the same heat transfer the temperature change becomes greater for smaller volume. To compensate for the unintended temperature rises there was a deviation from the proposed experiments to using lower than predicted duty cycles. Table 7-1 below documents the experiments carried out during this stage of the investigation.

Table 7-1 Showing the experiments carried out on tissue sample during the study – 1.

No.	Power Delivered (W)	Duty Cycle (%)	Exposure Time (s)
1	10	100.00	180
2	10	25.00	720
3	20	100.00	90
4	20	25.00	360
5	30	10.00	600
6	30	5.00	1200
7	40	5.00	900

### 7.2.2 Lab Study 2 – RG402 applicator - Flat aperture

**Exposure time effect:** A secondary phase of the investigation involved applying 5% duty cycle and only allowing injection of microwave radiation into the sample until a temperature of 40°C was reached; the results from this part of the investigation were used to look at the effect of exposure time on cancer cell cultures (see Table 7-2). Since in this situation the control measurement was the temperature of the cell samples, two additional samples were placed in water baths at 40°C and 50°C, respectively. The 40°C sample provided a comparative temperature dependent only measure, for the other experiments carried out within this part of the study. The 55°C sample could be compared to the baseline results at 10W and 20W (100% duty cycle) from Figure 7.3. Both samples were placed in water baths for a period of 600s. It was assumed that after this time the average temperature in the samples should be the same as the water bath temperature.

Table 7-2 Showing experiments carried out on tissue samples during study – 2.

No.	Mode of Delivery	Power Delivered (W)	Duty Cycle (%)
8	Microwave	20	5
9	Microwave	30	5
10	Microwave	40	5
11	Water Bath @ 50°C	-	-
12	Water bath @ 40°C	-	-

**Tissue Sample Handling:** The cancer cell cultures used are very sensitive to environmental changes. Due to the operation of the amplifier, the ambient temperature in the laboratory was noticeably warmer than normal. To minimise any changes that could influence results, the time between each sample being introduced into the laboratory and being treated, and subsequent reassessment under the microscope before incubation, was reduced as much as possible; to this end our aim was for a turnover time of 3 minutes. Also to prevent cross contamination between tissues samples, an alcohol swab was used to wipe clean the probe tip and thermocouple between each experiment.

### 7.2.3 Results of Study 1 and Study 2

This section will summarise the results generated through the experimental procedure described in sections 7.2.1 and 7.2.2. The key values examined will include the power levels, duty cycle,  $S_{11}$  reflection coefficient, temperature of the cell culture and the visual impact observed on the cell culture. Microscopic images were recorded the viability of the cells determined.

#### 7.2.3.1 Experimental Results – Water Bath

The cell cultures were placed in water baths heated to 40°C and 50°C for 600s, to investigate the sole impact of temperature on the cells. The resulting images from this experiment can be shown in Figure 7.5 and Figure 7.6 for 40°C, Figure 7.7 and Figure 7.8 for 50°C

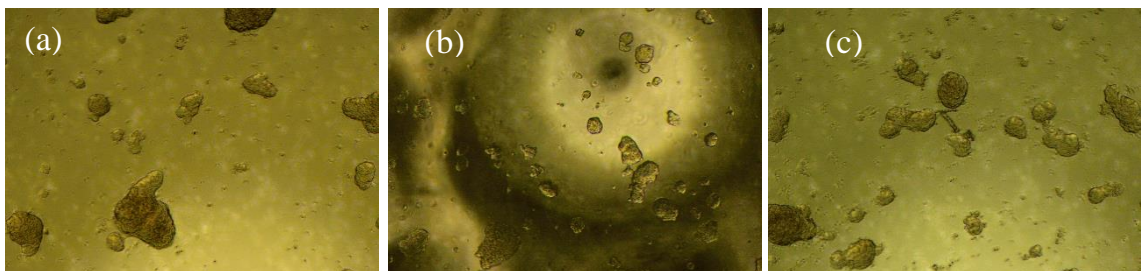


Figure 7.5: Microscopic view of the cancer cells at 5x optical zoom (a) before heating (b) immediately after heating & (c) 24 hours after heating in a water bath at 40°C, with no microwave irradiation.

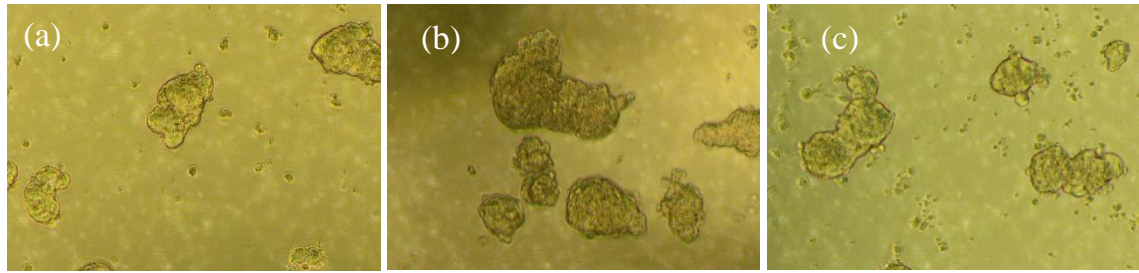


Figure 7.6: Microscopic view of the cancer cells at 10x optical zoom (a) before heating (b) immediately after heating and (c) 24 hours after heating in a water bath at 40°C, with no microwave irradiation.

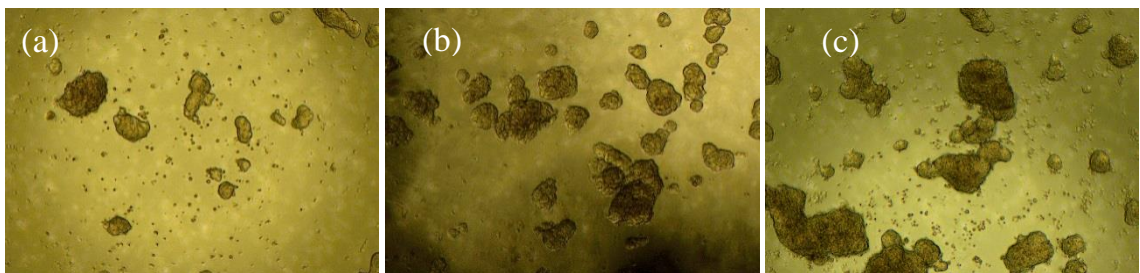


Figure 7.7: Microscopic view of the cancer cells at 5x optical zoom (a) before heating (b) immediately after heating & (c) 24 hours after heating in a water bath at 50°C, with no microwave irradiation.

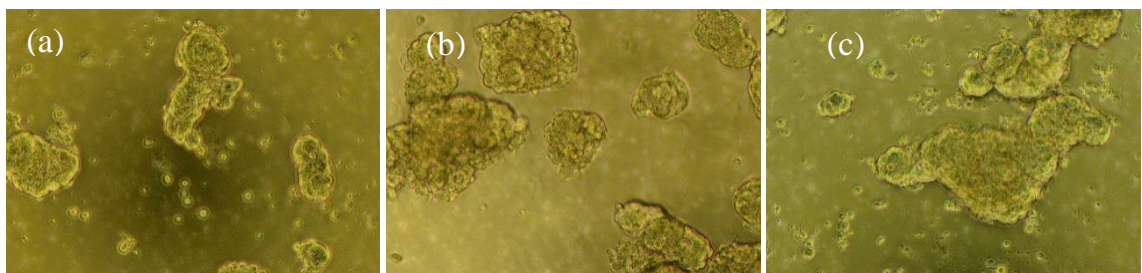


Figure 7.8: Microscopic view of the cancer cells at 10x optical zoom (a) before heating (b) immediately after heating and (c) 24 hours after heating in a water bath at 50°C , with no microwave irradiation.

The results of this initial test yielded no noticeable impact on the cell cultures, all of which remained viable.

### 7.2.3.2 Experimental Results – Successful Tests

Each of the following sets of the microscopic images is of the cell cultures that were deemed to be no longer viable 24 hours after the exposure to microwave radiation. In addition to the microscopic images, a graph has been created that shows the temperature rise during the exposure and the magnitude of  $S_{11}$ , from which the power dissipated can

be determined. The first result shown below is that of test No. 5 in which 30W was delivered using a 10% duty cycle.

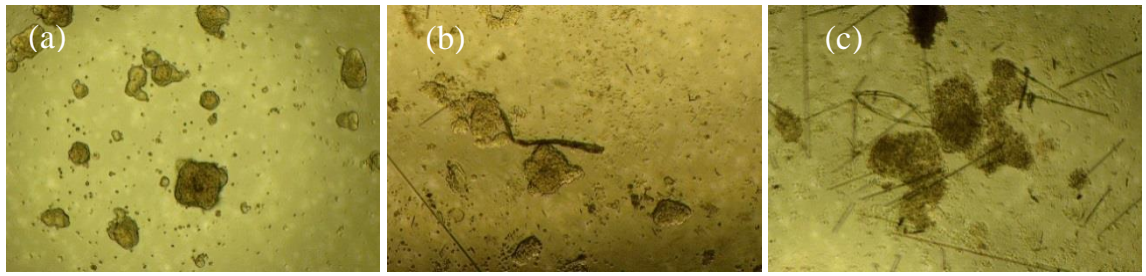


Figure 7.9: Microscopic view of the cancer cells at 5x optical zoom (a) before radiation (b) after radiation (c) 24 hours after radiation.

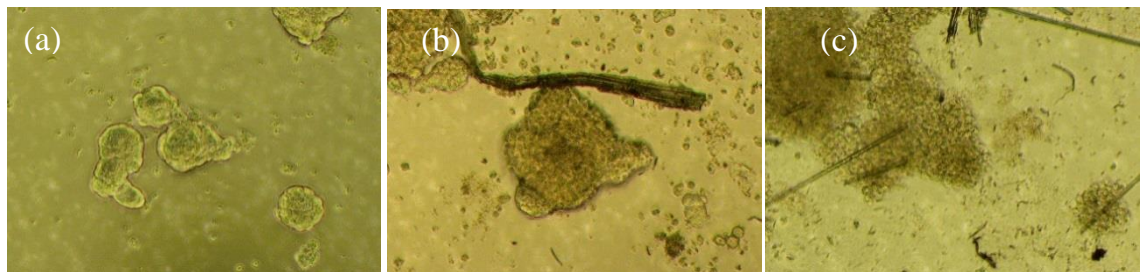


Figure 7.10: Microscopic view of the cancer cells at 10x optical zoom (a) before radiation (b) after radiation (c) 24 hours after radiation.

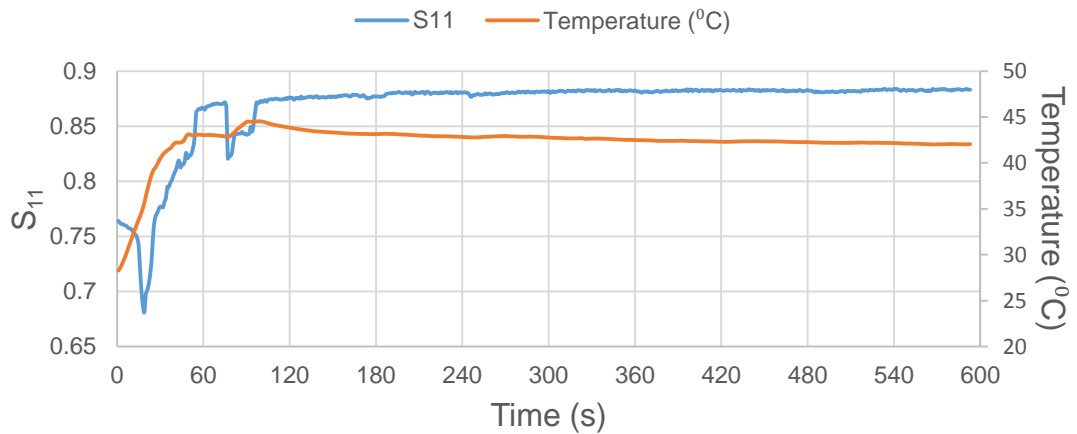


Figure 7.11: Temperature of the sample and  $S_{11}$  for 30 W microwave pulse radiation with 5% duty cycle.

The cells that were exposed to this particular radiation protocol were found to be completely unviable, having sustained significant damage as is shown in the images displayed in Figure 7.9 and Figure 7.10. Figure 7.11 displays the  $S_{11}$  and temperature parameters throughout the duration of the experiment, with the temperature hitting a

maximum of 45°C. A second successful test, test No. 7, is shown below, which was taken at 30W and a 5% duty cycle.

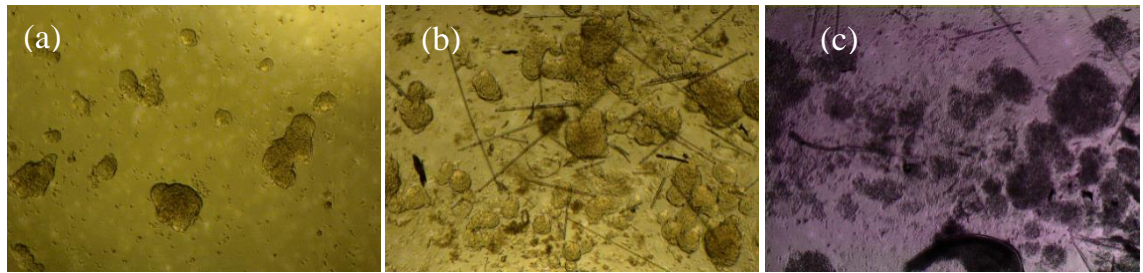


Figure 7.12: Microscopic view on the cancer cells at 5x optical zoom (a) before radiation (b) after radiation (c) 24 hours after radiation.

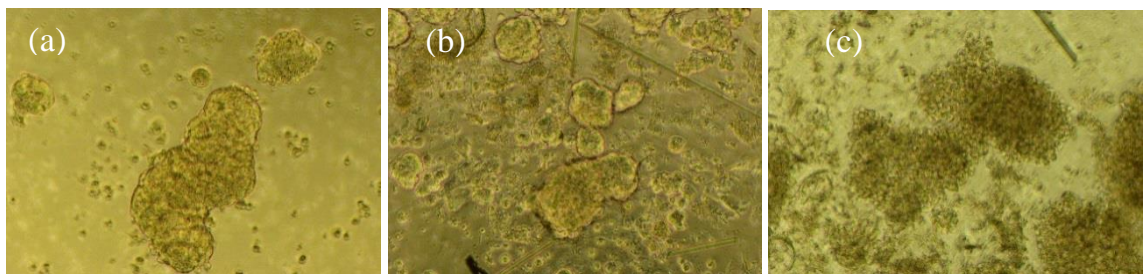


Figure 7.13: Microscopic view on the cancer cells at 10x optical zoom (a) before radiation (b) after radiation (c) 24 hours after radiation.

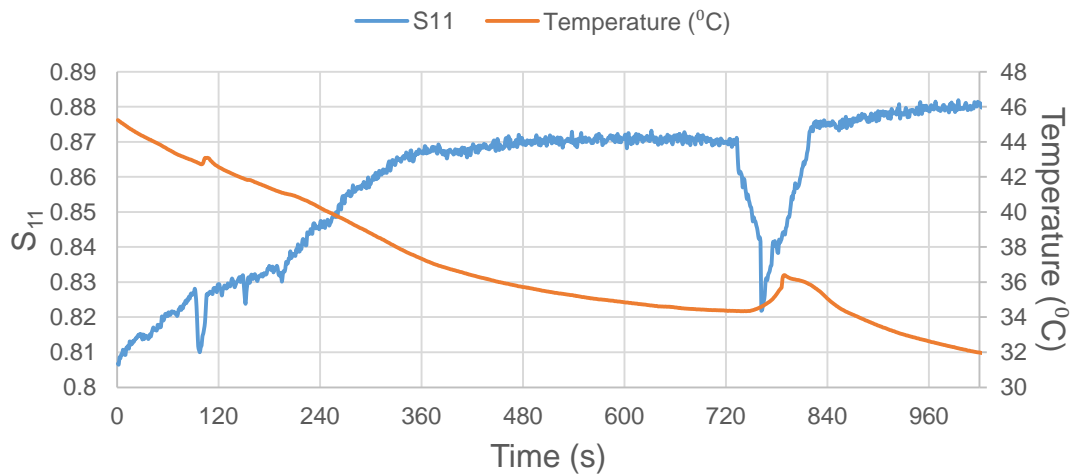


Figure 7.14: Temperature of the sample and the  $S_{11}$  for 30 W microwave pulse radiation with 5% duty cycles.

Figure 7.12 and Figure 7.13 display the results of the 30W, 5% duty cycle exposure and it can be seen that catastrophic damage has been done to the cells with a complete breakdown in their structure, which leads to the cells being no longer viable. Figure 7.14 details the temperature and  $S_{11}$  profile over the duration of the experiment, with

the temperature not increasing above 45°C. The final successful test, test No.10, was carried out under a different protocol in which the power delivered was turned off before a temperature of 43°C was reached. The regime used was 40W, 5% duty cycle and the results are shown below in Figure 7.15, Figure 7.16 and Figure 7.17.

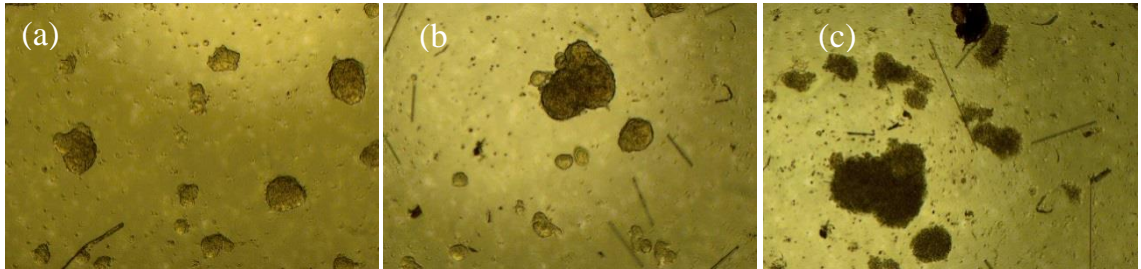


Figure 7.15: Microscopic view of the cancer cells at 5x optical zoom (a) before radiation (b) after radiation (c) 24 hours after radiation.



Figure 7.16: Microscopic view of the cancer cells at 10x optical zoom (a) before radiation (b) after radiation (c) 24 hours after radiation

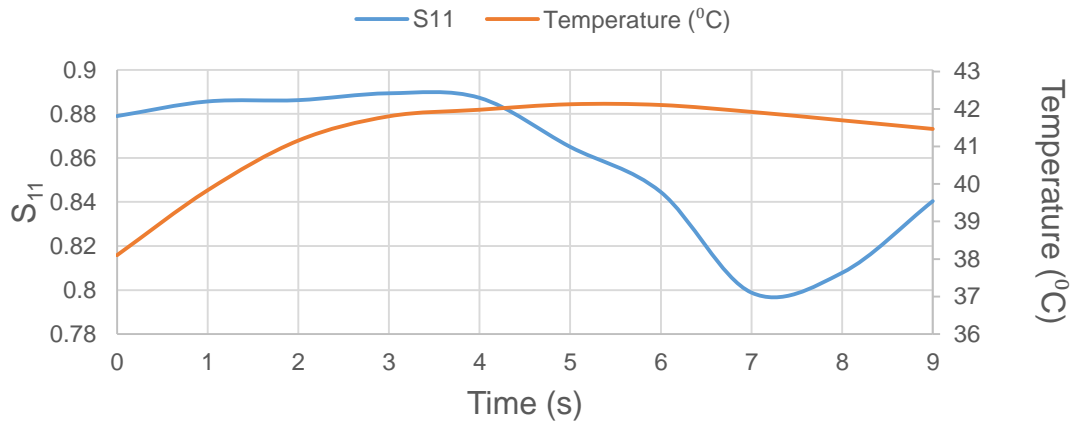


Figure 7.17: Temperature of the sample and S<sub>11</sub> for 40 W microwave pulse radiation with 5% duty cycles.

Figure 7.15 and Figure 7.16 show that after 24 hours significant damage has been done to the cells, resulting in complete cell death and, therefore, the cells are then found to be completely unviable. Figure 7.17 shows, critically, that the temperature never increases

above 43°C and that this sample was subject to a particularly short dose of radiation of 9 seconds.

### 7.2.3.3 Experimental Results – Unsuccessful Results

All of the experiments excluding tests No. 5, 7 and 10 yielded unsuccessful results in which the cell cultures were either completely unaffected or only partially affected. An example of an unsuccessful test, test No. 1, is shown below.

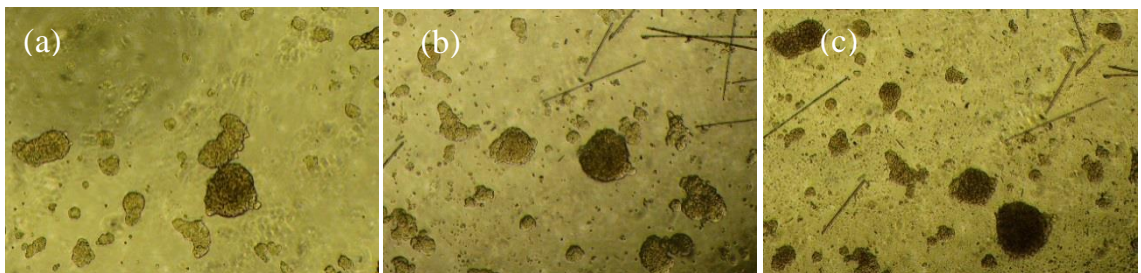


Figure 7.18: Microscopic view of the cancer cells at 5x optical zoom (a) before radiation (b) after radiation (c) 24 hours after radiation.

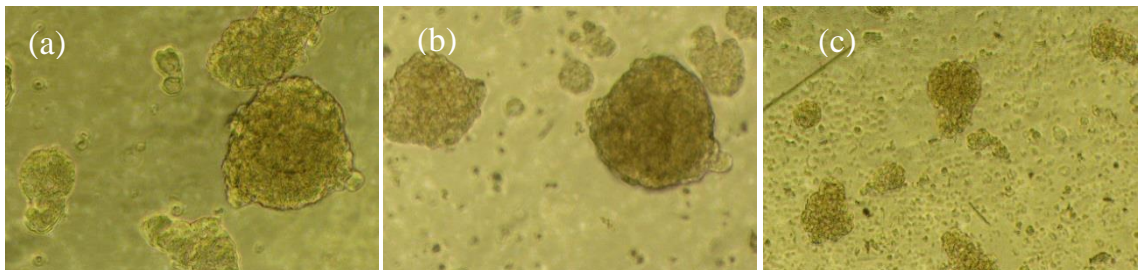


Figure 7.19: Microscopic view on the cancer cells at 10x optical zoom (a) before radiation (b) after radiation (c) 24 hours after radiation.

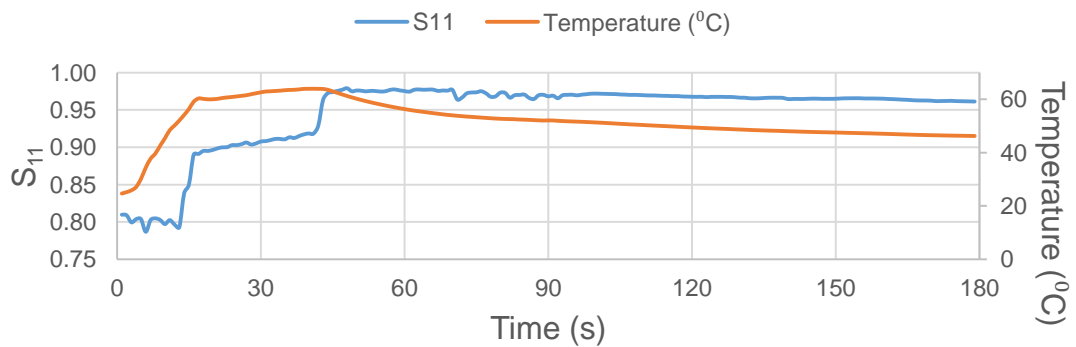


Figure 7.20: Temperature of the sample and S<sub>11</sub> for 40 W microwave pulse radiation with 5% duty cycles.

Figure 7.18 and Figure 7.19 show no obvious impact on the cell cultures with no impact on the viability of these cells. Figure 7.20, shows a significant temperature rise with values greater than 60°C being recorded.

A final piece of recorded data is that of the total energy delivered to the cancerous cell culture. This was calculated using the power dissipated into the sample and as such should reflect the total energy actually delivered into the sample. The results are presented in Table 7-3.

Table 7-3 Total energy delivered into the sample for each test.

<b>Test No.</b>	<b>Energy delivered into cancer cells culture (W/h)</b>
<b>1</b>	0.0478
<b>2</b>	0.0576
<b>3</b>	0.1247
<b>4</b>	0.1184
<b>5</b>	0.1017
<b>6</b>	0.1518
<b>7</b>	0.0911
<b>8</b>	0.0436
<b>9</b>	0.0182
<b>10</b>	0.0124

#### 7.2.3.4 Experimental Results – Summary

A summary of the results for all tests has been presented in Table 7-4.

Table 7-4 A summary of the results of all the conducted tests.

<b>Test no.</b>	<b>Power Level (W)</b>	<b>Duty Cycle (%)</b>	<b>Peak Temperature (°C)</b>	<b>Effect after 24hrs</b>
<b>40°C</b>	N/A	N/A	N/A	No effect on cell viability
<b>50°C</b>	N/A	N/A	N/A	No effect on cell viability
<b>#01</b>	10	100	65	No effect on cell viability
<b>#02</b>	10	25	N/A	Low effect: some cell death, but a large fraction of live cells remain

<b>#03</b>	20	100	49	Low effect: some cell death, but a large fraction of live cells remain
<b>#04</b>	20	25	75	No effect on cell viability
<b>#05</b>	30	10	45	Complete cell death
<b>#06</b>	40	5	60	Low-intermediate effect; live cells remain (both small and large spheres)
<b>#07</b>	30	5	46	Complete cell death
<b>#08</b>	20	5	34	Intermediate effect; live cells remain (small spheres only)
<b>#09</b>	30	5	41	Low effect: some cell death, but a large fraction of live cells remain
<b>#10</b>	40	5	42	Complete cell death

A summary of the results and the methodology used to obtain the results has been provided from a biological perspective by an expert in physiology and pathophysiology Dr. Florian Siebzehnruhl “Primary human glioblastoma cells were plated in single wells of 96-well plates in tumour sphere conditions. Once spheres had grown to 50-100  $\mu\text{m}$  diameter, the cultures were subjected to microwave irradiation. Immediately, before and after treatment, as well as 24 hours after treatment, glioblastoma spheres were imaged using low- and high-power light microscopy. No differences were noticed between individual cultures before treatment. Furthermore, no effects of treatment on cell viability or morphology were apparent immediately after treatment. At 24 hours post treatment, some cultures showed varying degrees of necrosis, which lead to complete eradication of tumour cells in three paradigms. No further changes were noted between 24 hours and 48 hours post treatment. Importantly, sphere cultures subjected to heat alone (40° or 50° C for 10 minutes) showed no signs of decreased viability, indicating that treatment effects were due to microwave radiation, rather than a transient increase in temperature”. The System set up measurement for the previous experiment is shown in Figure 7.21

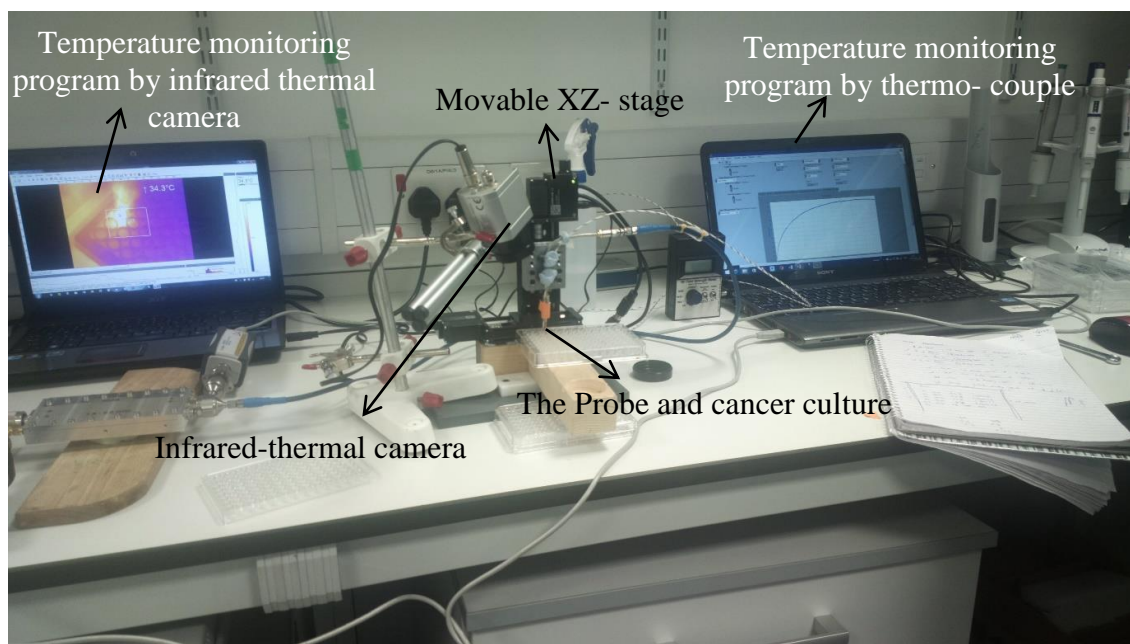


Figure 7.21: System set up measurement.

### 7.2.4 Study 3 – RG405 applicator – *in vivo* liver tissues

Two mouse liver samples were microwaved by pulsed microwave signals using the flat open-ended coaxial applicator made from RG405 cable. The applicator was placed in direct contact with the tissues, with the temperature during exposure not to exceed 40°C, with a minimum value of 30°C. The exposure protocols are as shown in Table 7-5. Some preliminary images of the irradiated and control liver samples are presented in Figure 7.22 and Figure 7.23.

Table 7-5 showing experiments carried out on liver tissues samples during study – 3.

Sample No.	Power Delivered (W)	Duty Cycle (%)	Exposure Time (s)
1	30	4%	1200
2	40	2.5%	900

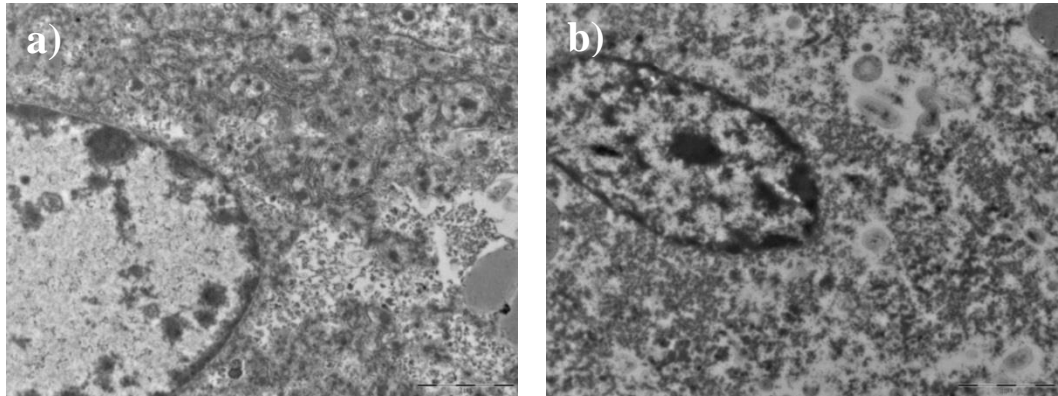


Figure 7.22: a) Liver - Control Area b) Liver - Microwave a

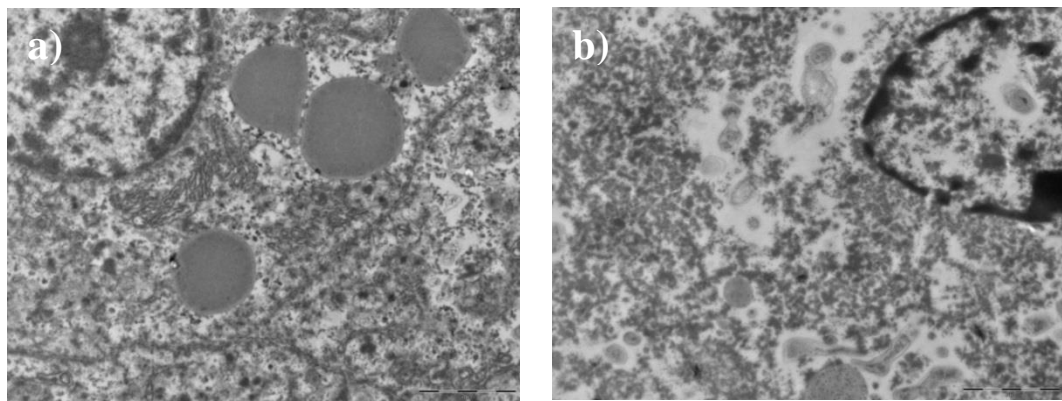


Figure 7.23: a) Liver - Control Area b) Liver - Microwave b

A consultant histopathologist at University Hospital of Wales Dr Fouad Alchami and Dr Florian Siebzehnrubl who is an expert within this field, have confirmed independently that the exposed cells are “clearly dead”. For the control tissues *a* and *b*, an area outside the zone where irradiation had occurred was selected; this could also be seen on the lower surface of the sample as a paler region of tissue. The structural preservation in the control tissue is not as good as preferred, but this probably represents autolysis, which is process of self-digestion caused by enzymes within the cells when the organism dies [204].

Also, it was suspected that mouse tissue is more prone to this, say, rat or sheep tissues. The outcomes certainly look encouraging. The comparison is striking between the preserved cytological structure, in the control tissue, and the disseminated structures, in the microwave exposed tissue. This gives a very good indication of cell death, associated with microwave exposure within the expected area.

Interestingly, some relevant changes that have occurred within the microwaved cells are related to 'larger' 3D electro-mechanical structures (e.g. organelles or nuclear membranes) and not some smaller molecules. Furthermore, it looks like a lot of cell organelles were ruptured during the microwave process. The big question here is why? Many individual questions have been considered, such as: does the cell membrane still look intact? Has the nuclear membrane been ruptured, as- it's a hard to tell in the images of microwaved tissue? Is the higher density around the nuclear edges more condensed heterochromatin? The recommendations by Dr Fouad Alchami (i.e. it is for future work) were suggested to repeat this all over again, once we are able to get surgical biopsy tissue with analysis at different regions (distances) from the probe centre, and compare with the anticipated calculated field of tissue response to microwave affects.

### 7.2.5 Study 4 – Use of Electric Cell-Substrate Impedance Sensing (ECIS) technique

**System improvement:** The mechnism of cancer cell death is still not clear, thus for more understanding, a number of system improvements were developed according to previous studies for improved investigation and analysis.

- a) The LabVIEW program was rebuilt, for more temperature measurement sensitivity by adding two new advanced sensors, i.e. fiber optic thermometry probes and infrared thermal camera. The two optical probes used are illustrated in Figure 7.24.

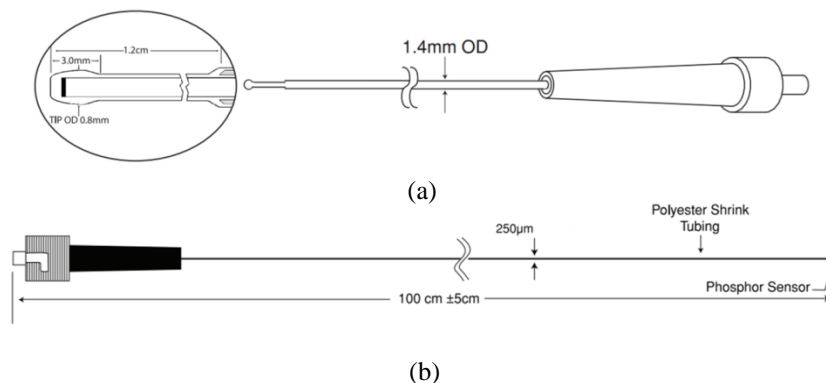


Figure 7.24: Two fiber optic thermometry probes, (a) STF Probe. (b) MicroProbe.

- b) New experiments were conducted with 1ms pulse period and 5% duty cycle.
- c) The experiment environment condition was changed, so that all of the new tests will be inside a special incubation chamber at 37 °C, as shown in Figure 7.25.



Figure 7.25: Incubation chamber at 37 °C.

- d) A small metal piece with a screw and two holes was made. One hole is for the sensor to control the depth of the sensor tip inside the walls by help of the screw. The second is for the fibre optic thermometry probe, as illustrated in Figure 7.26.

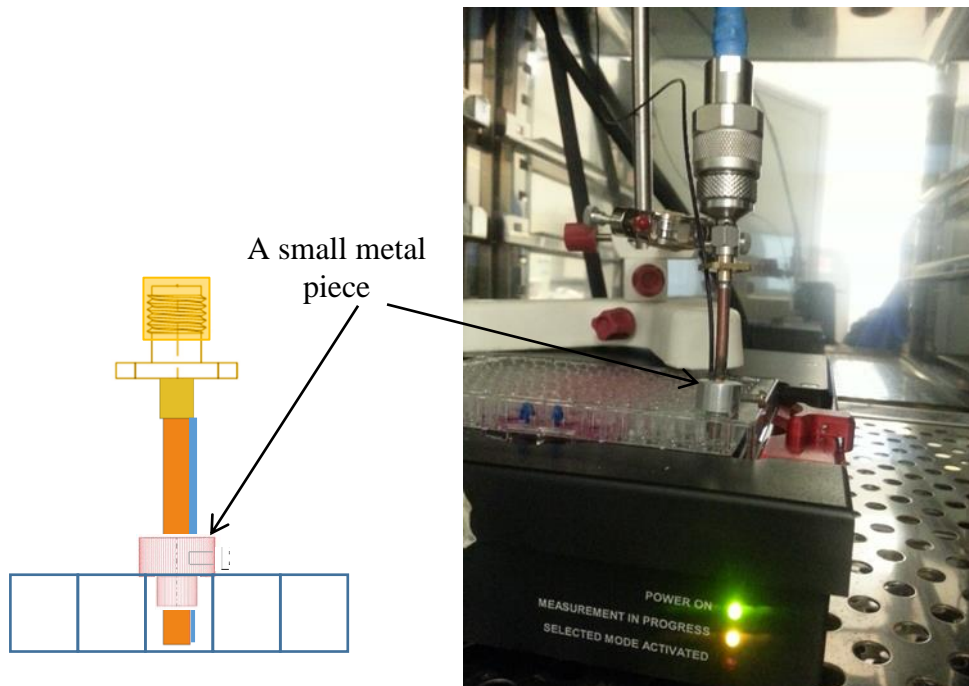


Figure 7.26: Small metal piece for temperature probe movement control.

The next section will provide a summary of the procedure used to prepare the cells for the new experiments.

### 7.2.5.1 Brief ECIS technique summary

ECIS is a technique designed and licensed by Applied Biophysics Inc (NY, USA) which monitors cell attachment and migration, on gold electrodes in 96 well arrays, using changes in resistance and impedance over time.

This study used 96W1E arrays (ECIS culture ware, Applied Biophysics Inc, NY, USA) which were stabilised by adding 200µl of stabilising solution (Applied Biophysics Inc, NY, USA) to each well and leaving them at room temperature for 20 minutes. This medium was aspirated off and replaced with  $12 \times 10^4$  cells/100µl of HEPES buffered medium and 100µl of media. The array was then placed in the ECIS incubator at 37°C connected to the Theta ECIS controller system (Applied Biophysics Inc, NY, USA). The software was configured so resistance of the current flow was measured at 4 kHz. Data was normalised using resistance from the first time point. Cells were left for 4 hours to adhere to the gold electrodes before exposure to microwaves.

**Media Replacement:** To assess the % kill rate using trypan blue, all the media from each well was removed either 12 hrs or 24 hrs after the event and diluted 1:2 with trypan blue. 200 µl of fresh media was added to each sample for the remainder of the experiment. A Countess™ II FL Automated Cell Counter was used to count the cell density of cell suspension by using a C-Chip disposable hemocytometer, as shown in Figure 7.27.

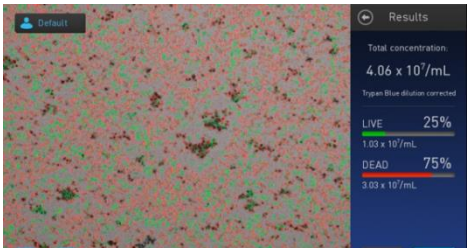


Figure 7.27: a) The Countess™ II FL Automated Cell Counter. b) C-Chip Disposable Hemocytometer

The supplier of the breast cancer cells provide all the details and images of what they look like under the microscope, and this is included as in Appendix I

### 7.2.5.2 Study 4 – Experiment 1 and Results

Table 7-6 A summary of the protocol and results of all tests of study 4 – experiment 1 after 24Hrs.

Test No.	Power Level (W)	Exposure Time (s)	Dead Cells rate – After 24Hrs	Notes
1	30	300	79%	
2	30	300	84%	
3	30	900	57%	
4	40	180	56%	
5	40	300	67%	
6	50	180	75%	Dead completely 
7	50	300	64%	
8	-	-	1%	Control sample

The exposure plan was followed as Table 7-6. The experiments were carried out inside the incubation chamber at 37 °C with the ECIS measurements running. All the samples were examined after approximately 24 hrs. The cell death rates were found to be both varied and high. Test No. 6 was clearly successful. Although the death rate was 75%, analysis using high resolution microscopy has shown that even the remaining live cells were not in good healthy state. A comparison between normal (i.e. No. 8) and irradiated (i.e. No. 6) cells was accomplished and is displayed in Figure 7.28.

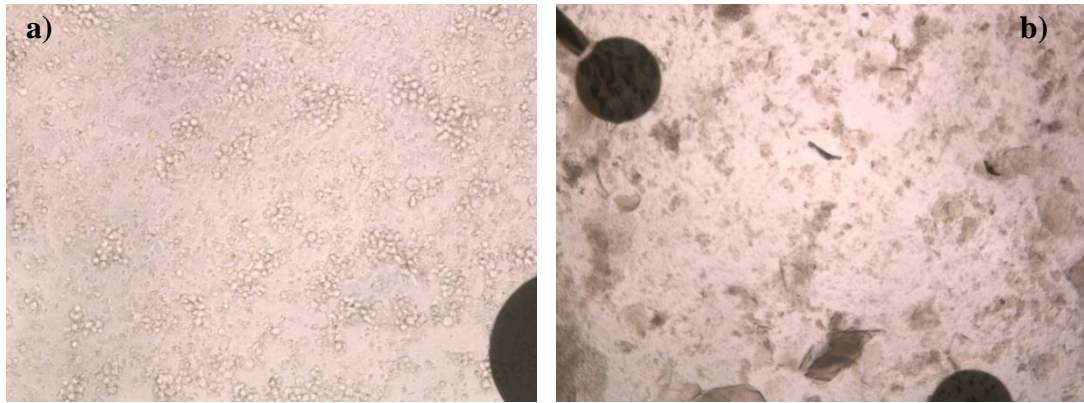


Figure 7.28: Microscopic view of the cancer cells after 24Hrs.a) Non radiated - Healthy cancer cells (No.8), b) First exposure- cancer cells (No.6).

The protocol used for test No. 6 was 50 W, 5% duty cycle for 180 s exposure time. The recorded measurements are shown below in Figure 7.29.

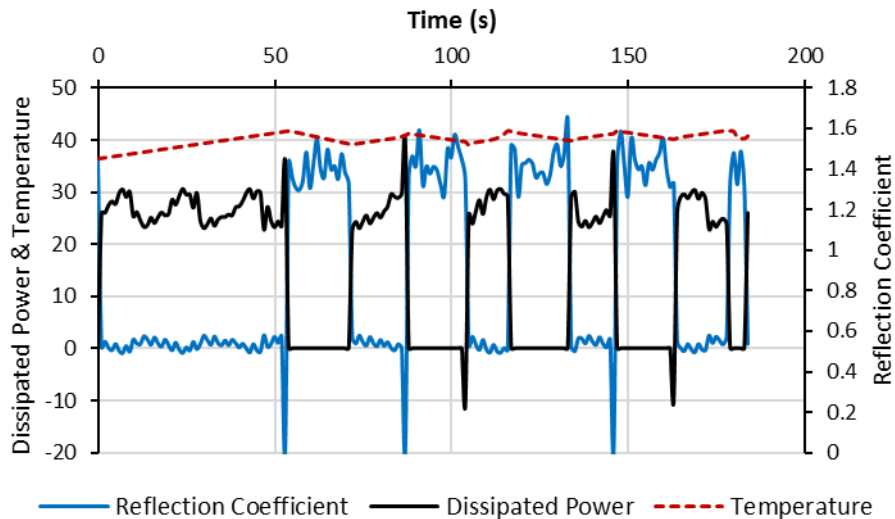


Figure 7.29: Temperature of the sample and  $S_{11}$  for 50 W microwave pulse radiation with 5% duty cycles, for 180 s exposure.

It is important to clarify that the measurement in off state when the reflection coefficient is  $> 1$ , which is noise measurement and should be ignore it.

The ECIS measurements for all tests were recorded. For example, Figure 7.30 shows the resistance values against time starting before and during microwave exposure. It can be noticed that, after a small period of the exposure, the resistance of all the cells increases suddenly then decreases for all test except for test No. 6.

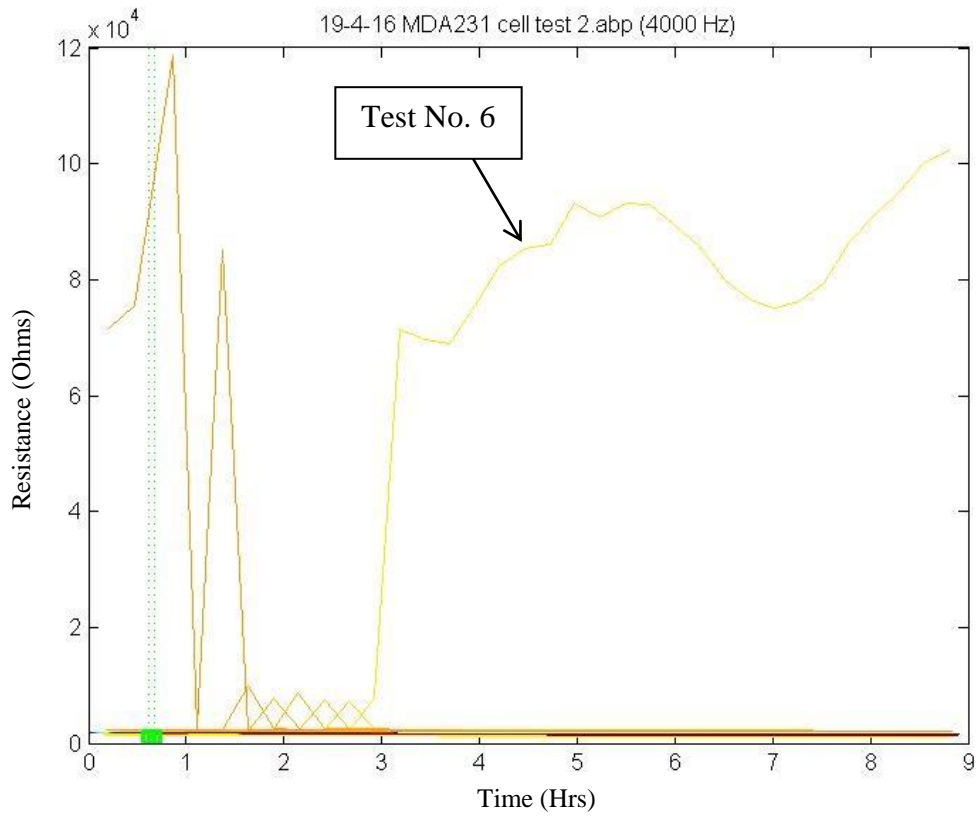


Figure 7.30: ECIS measurements

The cell medium was refreshed as shown in Figure 7.31, and then a second exposure followed after 24 hours.

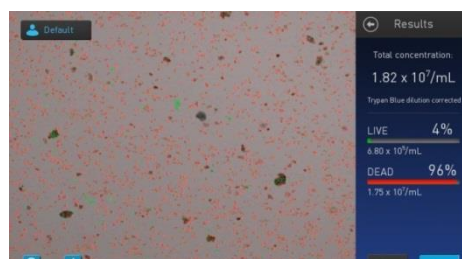


Figure 7.31: Cells medium refresh after 24 hrs.

### 7.2.5.3 Study 4 – Experiment 2 and Results

Table 7-7 A summary of the protocol and results of all tests of study 4 – experiment 2 after 24 hrs observation.

Test No.	Power Level (W)	Exposure Time (min)	Dead Cells – After 24Hrs	Notes
1	50	3	81%	
2	50	15	85%	
3	50	3	87%	
4	50	15	82%	
5	50	3	80%	
6	No exposure, refresh medium	-	96%	Dead completely
7	50	15	80%	
8	-	-	1%	Control sample



All the samples were examined after the second exposure and observed after 24 hrs, as shown in Table 7-7. The cell death rates were significantly increased, now in the range 80-87%. Test No. 6 was clearly now successful. Although the medium was refreshed with no exposure, the cell death rate was found to be 96%, i.e. the cells were destroyed completely and dead.

### 7.2.5.4 Study 4 – Experiment 3 and Results

The medium was refreshed again without new exposure. Then, observations were done after 24 hours as shown in Table 7-8.

Table 7-8 A summary of the protocol and results of all tests of study 4 – experiment 3 after 24Hrs.

Test No.	Power Level (W)	Exposure Time (s)	Dead Cells – After 24Hrs	Notes
1	Non	-	46%	
2	Non	-	41%	
3	Non	-	63%	
4	Non	-	49%	
5	Non	-	52%	
6	Non	-	100%	Dead
7	Non	-	57%	
8	-	-	1%	Control

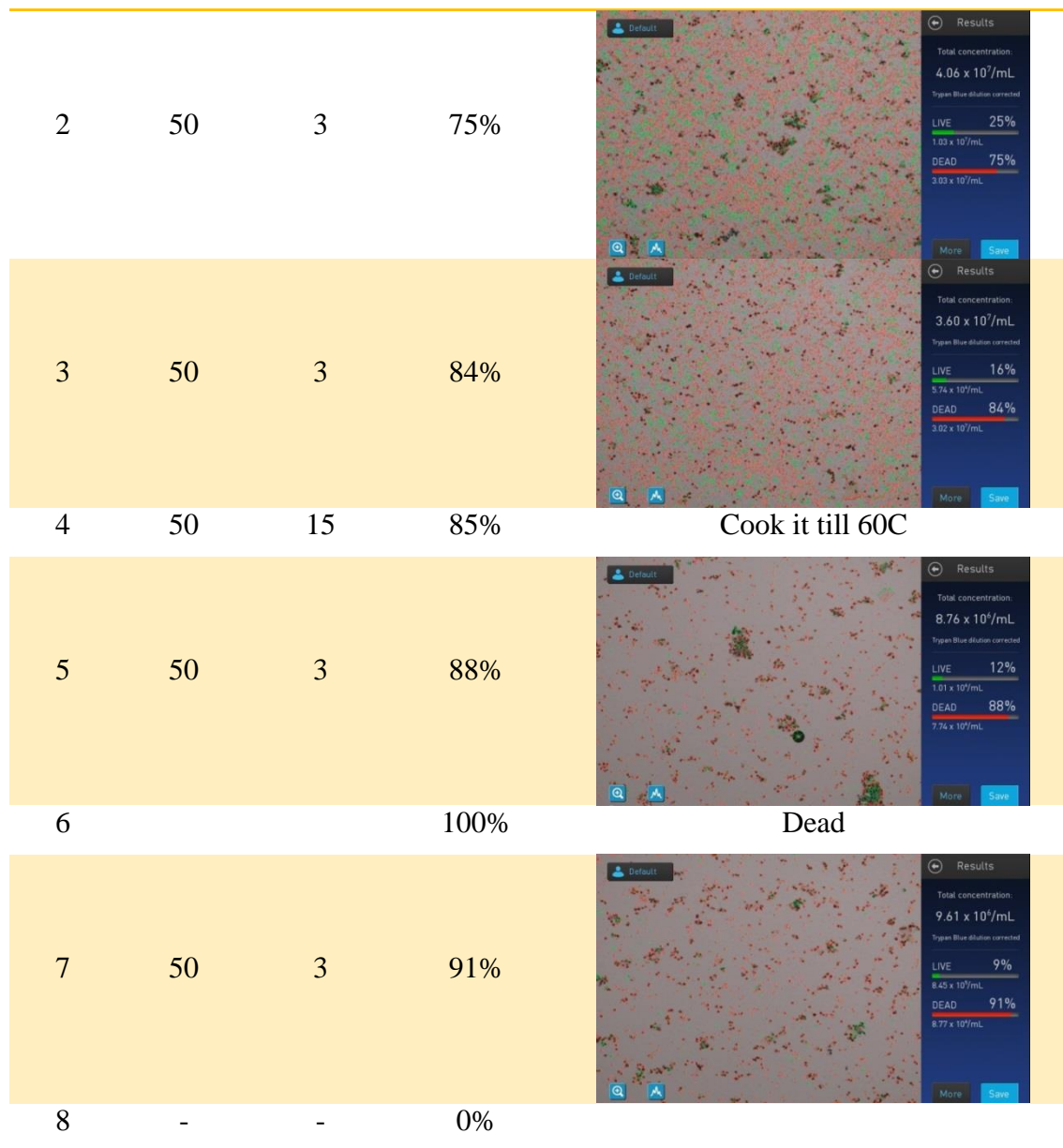
It was noticeable that the cell death rate decreased to a range of 41-63%. This means some cells were able to recover in the presence of the fresh medium, however, this recovery rate is very low. Test No. 6 was 100% dead.

#### 7.2.5.5 Study 4 – Experiment 4 and Results

Following on from the previous results, the experiment was repeated with the applicator located deeper in the sample holder, i.e. 1 mm above the base of the wall. Then, observations were done after 24 hours as shown in Table 7-9.

Table 7-9 A summary of the protocol and results of all tests of study 4 – experiment 4 after 24Hrs.

Test No.	Power Level (W)	Exposure Time (min)	Dead Cells After 24Hrs	Notes
1	50	3	72%	



Interestingly, all of the samples were destroyed and dead, and the death rate was significantly higher than before, with some interesting new observations. It was seen that clusters of cells have been formed, in which healthy cancer cells were surrounded by dead cancer cells. This new structure, in view of biology, will stop any new cells dividing. Eventually, this will lead to annihilation of the cancer completely. A comparison between the two exposure regimes was made to differentiate between thermal and non-thermal microwave mechanisms in terms of destroying cancer cells, as displayed in Figure 7.32.

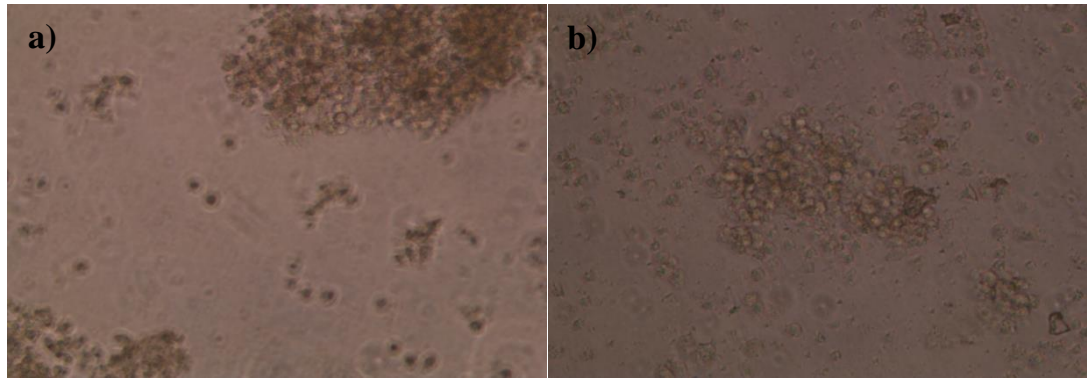


Figure 7.32: Microscopic view of the cancer cells for microwave thermal and non-thermal effects. a) Temperature – 42°C - (DEAD) b) Temperature – 60°C (DEAD).

In terms of biological analysis, the two microscope views are the same, with confirmation that all the cells were dead. Consequently, no difference can be noticed between the two, other the different treatments.

#### 7.2.5.6 Study 4 – Experiment 5 and Results

To increase the efficiency of the applicator probe in terms of delivering power, new experiments, with a new, “pointed” RG402 head (as shown in Figure 7.33) were carried out. , The centre conductor extends by 2 mm from the end of the outer conductor.

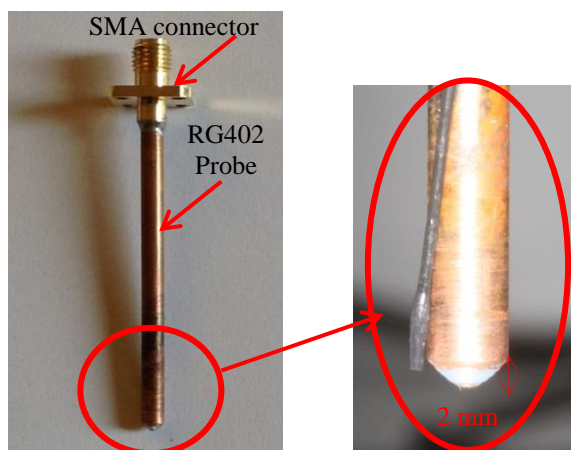


Figure 7.33: New RG402 pointed applicator with 2 mm distance from the outer conductor end.

A study by Hancock, *et al.*, [205] has suggested that improved performance of the probe could be achieved by using a pointed probe.

Table 7-10 A summary of the protocol and results of all tests for study 4 – experiment 5 after 48 hrs.

Test No.	Power Level (W)	Exposure Time (minute)	Dead Cells – after 48 hrs	Notes Left two days without refreshing
1	50	15	87%	DEAD – Cluster
2	50	15	87%	DEAD – Cluster
3	50	15	90%	DEAD – Cluster
4	50	15	88%	DEAD – Cluster
5	50	3	95%	DEAD – Cluster
6	50	3	93%	DEAD – Cluster
7	-	-	-	-
8			1%	Probe was left in sample without radiation for 24

Successfully experimental results were observed from the first exposure by using the pointed probe, as presented in Table 7-10. Test No. 8 confirms that there is no effect of the copper conductors on the cells. However, further investigations must be carried out to explore if there are any possible effects of metal ions released during the microwave exposure process.

### 7.2.5.7 Study 4 – Experiment 6 and Results

#### 7.2.5.7.1 Biological effect of microwaves on human cells

**Non-thermal Microwave Treatment of Breast Cancer:** Recent experiments in collaboration with University Hospital of Wales (both Heath and Llandough sites) and the School of Engineering at Cardiff University has uncovered evidence that microwave radiation can affect cancer cells, while maintaining low temperatures below 42 degrees Celsius.

The set-up consisted of a pulsed-microwave generator and a series of power amplifiers to provide pulsed MW signals with power levels up to 50W. The temperature control was established by pulsing the MW signal. In essence, the MW pulsed signal was only on for a short percentage during the experiment with significant off periods. The off periods allowed for any thermal heat to be dissipated through convection cooling.

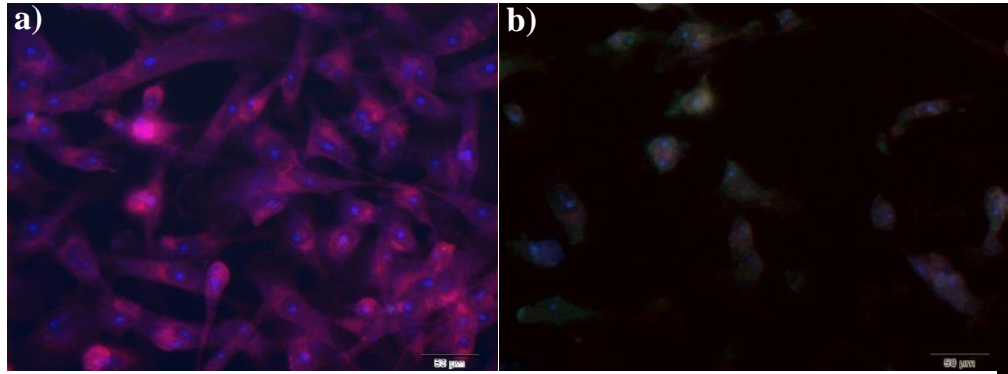
Initial experiments, involved the injection of microwave radiation into a liquid with suspended cancer cells within a well with around 5 mm diameter. Before irradiating the sample, a sufficient amount of time was given for the cells to 'settle down' and attached together. The microwave radiation was introduced using a standard RG402 microwave coaxial cable with an outer diameter of 2.97 mm with the probe tip being positioned a couple of millimeters above the bottom of the well. The set-up also included an optical sensor to monitor the temperature of the cell suspension to ensure temperatures below 42 degrees Celsius during the experiments. Typical duration of the MW irradiation was 4-10 mins.

**Trypan blue staining:** it can be used to discriminate between viable and non-viable cells, and was utilised to investigate the condition of the cells. It was found out that immediately after the microwave treatment the cancer cell looked relatively healthy, however, the cell death setting in only after a few hours. After about 24 hours the cell death rate typically increased to 60-80%. A number of experiments were conducted, showing consistent results. Control samples with the same cells suspended in the liquid didn't show any significant cell death rate.

**Effect of microwave treatment on peroxidase production:** A standard peroxidase assay was carried out. From the triplicate repeats of the positive controls we can clearly see that the peroxidase concentration decreases. Our results do not follow this trend and taking into account margin for error are consistent throughout the time period studied. Therefore it can be concluded that it is highly unlikely peroxidase is the main mechanism of causing these breast cancer cells to die.

**Investigation of 945 proteins of cells:** To expand on these investigations, a scan was conducted on about 945 proteins of cells immediately after the microwave irradiation and a waiting period of few hours. The scan has revealed a significant impact on the signal path within the cells affecting proteins within cell membranes and part of the cell cycles management and apoptosis process. The investigations show a completely new aspect of how microwaves can affect cancer cells and new methods to treat cancer tumours.

a) **Effect on distribution of membrane associated proteins:** To investigate the condition of the cells, the effect on the distribution of membrane associated proteins by non-thermal MW irradiation were analysed, as shown in Figure 7.34.



b) Figure 7.34: Effect on distribution of membrane associated proteins. (a) Staining of the control cells, (b) Staining of cells for 50W, 15 minute microwave exposure.

The two things that stand out here are:

- 1- The lack of any green in the control compared to the intense green seen after exposure. This green stain is representative of one of the key molecules for a common pathway which causes cells to die (Caspase 9).
- 2- The blue staining is redistributed between the two images and therefore may show why we are seeing a change in the cell shape.

c) **Changes in protein expression:** Matched protein was sent for analysis to *Kinexus* for microarray analysis from control and microwaved cells ( $n = 2$ ). The results showed interesting differences between the treated and control cells, particularly in regard to signalling and proteins involved in cell cycle control, as shown in Figure 7.35 and Table 7-11.



### 7.2.5.8 Study 4 – Experiment 7 and Results

Circles with diameter of 33 mm, which delivered in standard 6 well culture plates, were utilized in this new experiment, as shown in Figure 7.36.

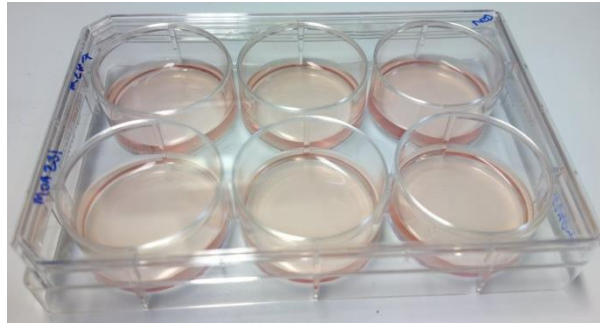


Figure 7.36: standard 6 well culture plate.

Two 6-well culture plates were treated by two different regimes in a bio-safety cabinet:-

- 1) The first protocol that uses a large diameter pointed probe, which was developed so that it was capable of handling higher total MW power over a larger radiation area, as displayed in Figure 7.37. This applicator was fabricated by using N-female connector with outer diameter of about 1.57 cm. It was divided in half and machined to be pointed. This probe was centred and immersed into the cancer cells for treatment. It was used to deliver 50W of MW power at 5% duty cycle and 15 minutes exposure time. This design requires large volume and therefore produced short pulse width and high peak power. This created minor sub-surface micro-cracking. Interestingly, this pulsing regime also led to the appearance of micro-cracks in the surface of each culture well, visible under an optical microscope. The origin of this effect is unclear. This may be related to the acoustic emissions also observed when high power pulses are applied.

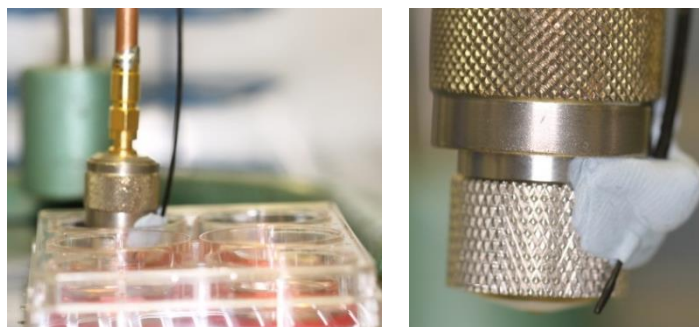


Figure 7.37: large diameter pointed probe.

- 2) The second protocol by using RG402 pointed sensor at different contacted areas in single well. Additionally, a circular area was created as wound to separate the cells for exploring the importance of cell contact, as demonstrated in Figure 7.38.

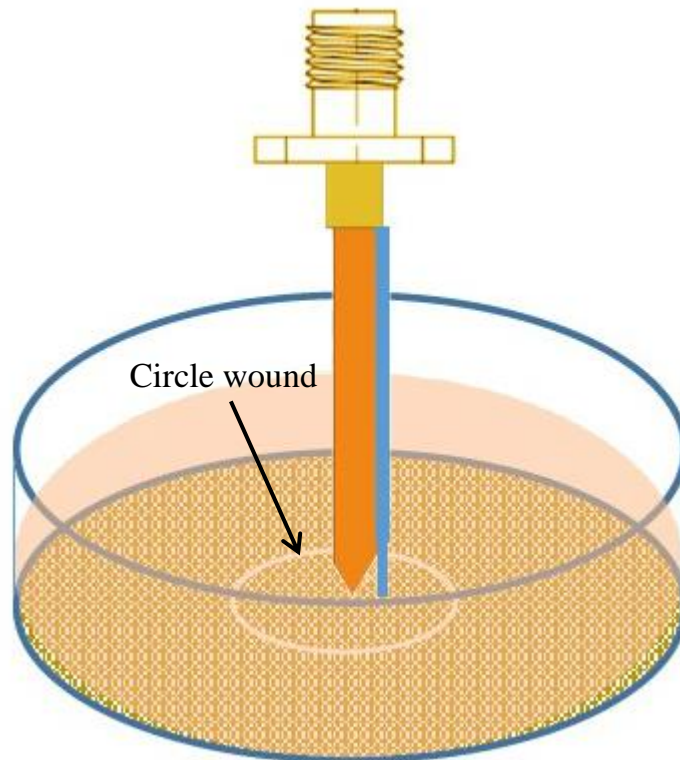


Figure 7.38: Pointed RG402 probe for exploring the importance of cell contact.

#### 7.2.5.8.1 Results from Study 4 – Experiment 7

##### Plate 1 – Assessment of larger probe and the effectiveness of multiple treatments

All wells were filled with 7 ml of medium:

- Wells were treated with the large probe at different powers (50W and 100W) respectively for 15 minutes. Initial viewing immediately after exposure showed that the cell morphology under 50 W exposure had changed, implying that cell death would occur over the next 24 hrs. For the 100 W exposure, the well area directly under the probe had no cells left attached, and their morphology was different, suggesting that this power had killed them in a different way. Some

morphological changes were seen in the cells beyond this area though they were not as evident as the 50W treated wells.

- Using the pointed RG402 probe, one well was treated twice in differing areas of the well, with the other being treated 4 times. Immediately after exposure both monolayers of cells showed morphological changes, as previously observed with the large probe. In the well with 4 treatment sites, clumps of suspended cells were already present.
- 24 hrs after treatment, in all the wells used with this probe, all attached cells (despite initial morphological changes) had recovered to restore a healthy cell monolayer. In the wells treated at multiple sites, cell death was evident as was the increasing number of suspended cell clumps. The rate was higher in the 4 times exposed well.

#### **Plate 2 – Exploring the importance of cell contact**

- The monolayer was artificially damaged differing differences from the probe site. A well was left undamaged as an active comparison.
- Wells where the created circle wound was far from the probe showed that the cells within the probe exposed area were clumping but complete detachment was yet to occur. Beyond the created circle wound edge no evidence of cellular damage was observed, and cells were found to be healthy.
- Wells where wound was imminent from the exposed area showed a higher rate of cellular damage within the exposed area, and some small potential sites where it had crossed beyond the wound edge. This was not consistent round the whole wound circumference.
- Wells exposed with no wound but for different times showed changes and cell death throughout the whole well. This indicates that cell to cell contact is one of the leading drivers in any subsequent cell death which occurs.

#### **7.2.5.9 Study 4 – Experiment 8 and Results**

**Frequency Effect on Non-thermal treatment process:** This experiment has been performed on two different cancer cells with two different microwave frequencies and different pointed probes as follows.

1- Suspension cell cultures in two 6-well plates were treated by two different regimes in a bio-safety cabinet, as shown in Figure 7.39.

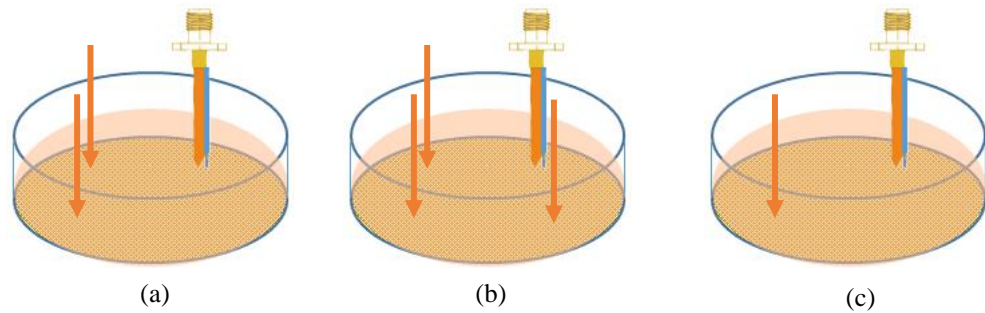


Figure 7.39: Different exposure regimes on suspensions of cancer cells.

The treatment protocol was demonstrated in Table 7 12:

Table 7-12 A summary of the protocol and results of all tests of study 4 – experiment 8, after 24Hrs.

Test No.	Power Level (w)	Exposure Time (minute)	Applicator Type-Frequency	Duty Cycle%
<b>Well – (a)</b>				
1-(a)	30	15	RG405-5.8GHz	5%
2-(a)	30	15	RG405-5.8GHz	7.5%
3-(a)	30	15	RG405-5.8GHz	5% ,7.5%,5%
<b>Well – (b)</b>				
1-(b)	40	15	RG405-2.2GHz	5%
2-(b)	20	15	RG405-2.2GHz	5%
3-(b)	10	15	RG405-2.2GHz	5%
4-(b)	20	15	RG405-2.2GHz	2.5%
<b>Well – (c)</b>				
1-(c)	30	15	RG405-2.2GHz	5%
2-(c)	20	15	RG405-2.2GHz	7.5%, @ 200s switch to 30W

The pointed RG405 was fabricated and utilized in this study as shown in Figure 7.40 , with zooming in for the tip as presented in Figure 7.41.

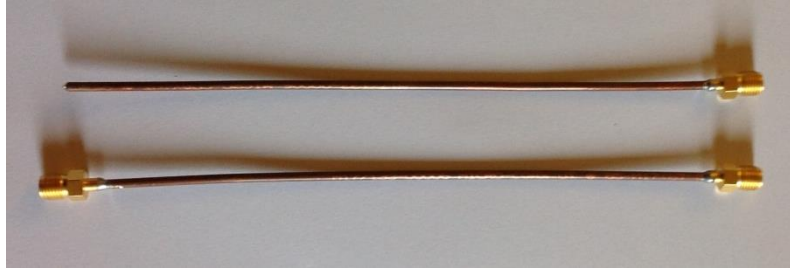


Figure 7.40: Pointed RG405 probe, with double-ended RG405 for calibration procedures.



Figure 7.41: Zooming in of the pointed RG405 tip.

#### 7.2.5.9.1 Results from Study 4 – Experiment 8

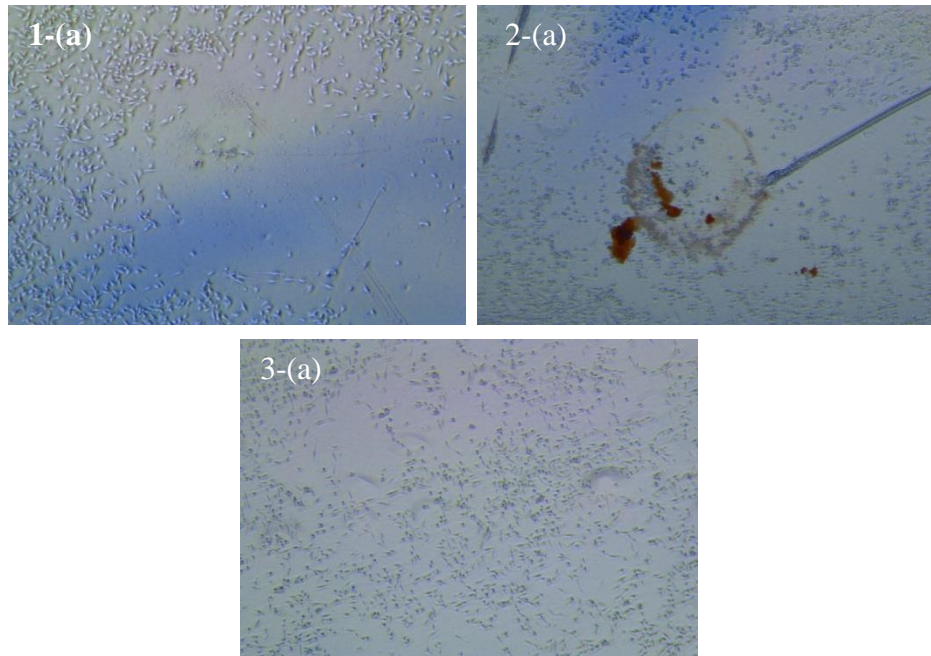


Figure 7.42: Microscope view for well – (a) of three exposure zones as demonstrated in Table 7-12 .

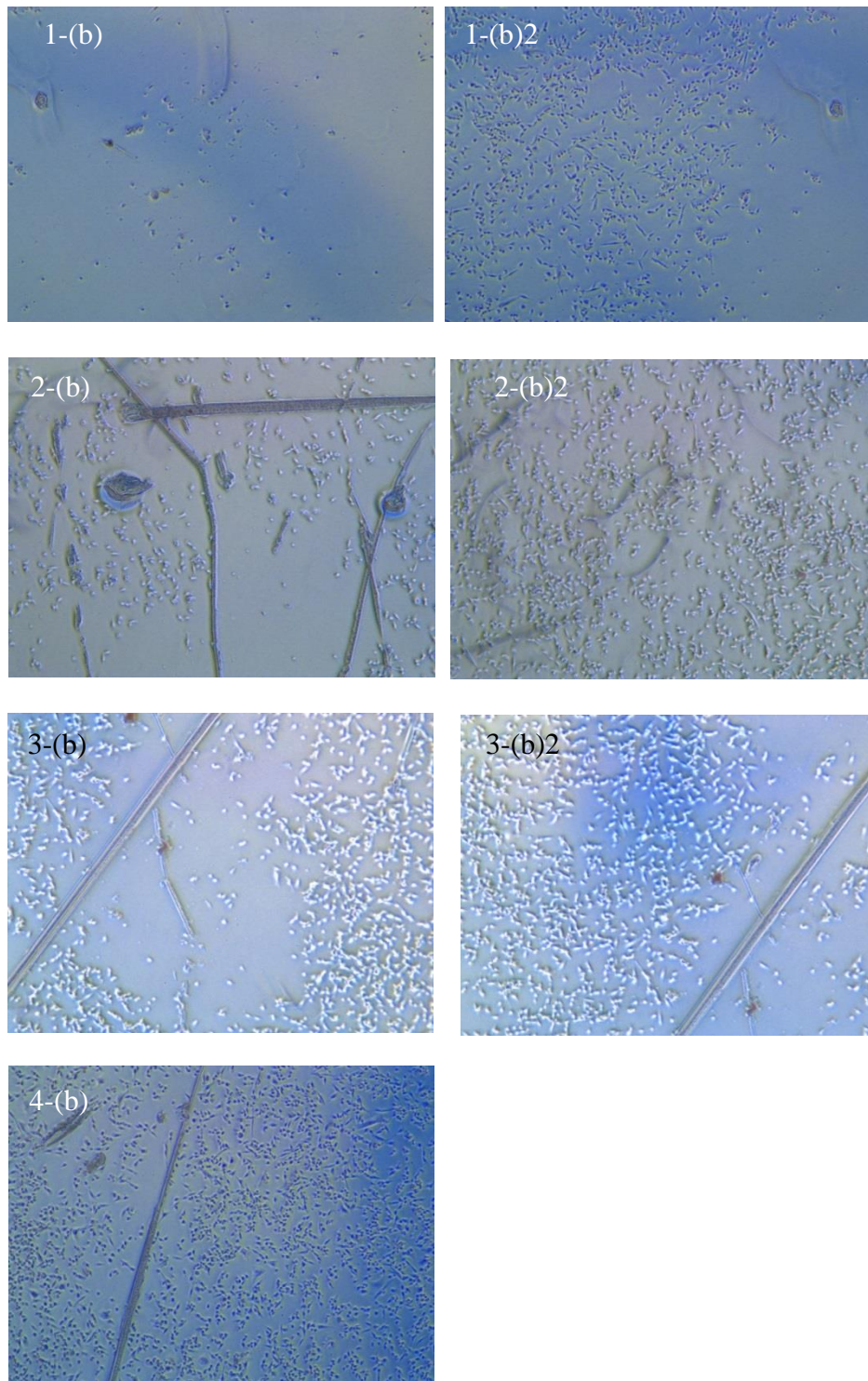


Figure 7.43: Microscope view for well – (b) of four exposure zones. Zones 1, 2, and 3 divided to two images due to the small view field of the microscope.

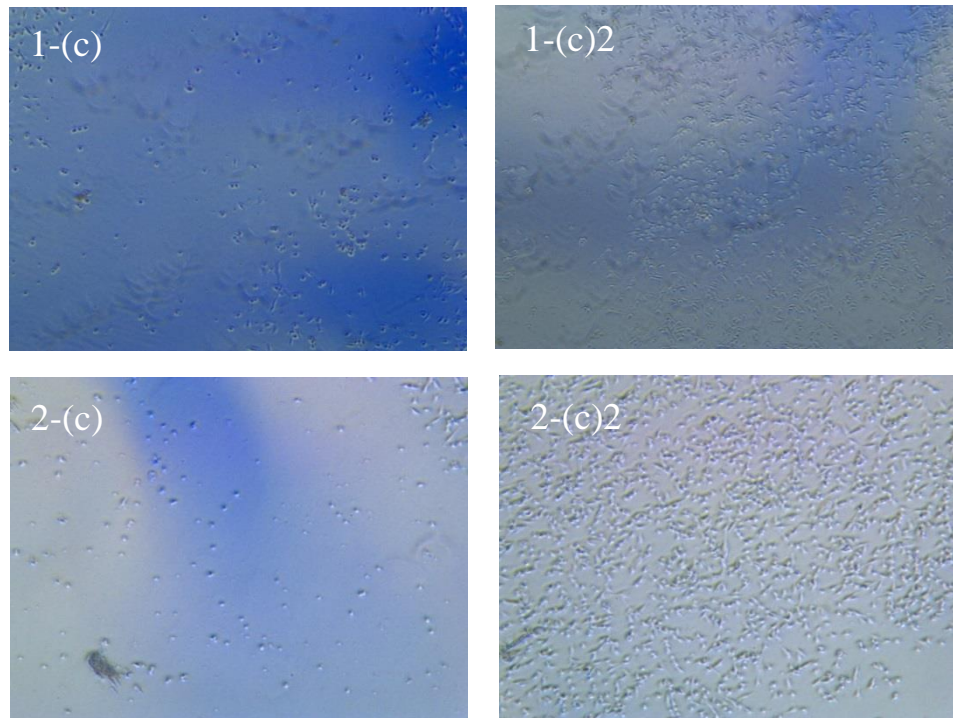


Figure 7.44: Microscope view for well – (c) of two exposure zones. Zones 1 and 2 divided to two images due to the small view field of the microscope.

- Two wells using 2.2 GHz MW exposure and one using 5.8 GHz MW exposure for comparison using the smaller probe were performed. It was observed that the 2.2 GHz exposure worked a bit differently. It produced most of the time an audible signal during the treatment. At 40W it was similar to the sound of ‘boiling water’ around the probe.
- In addition, there are two images for some as the field of view was too small to incorporate the killed clear area together with the healthy cells. The microscope images after 24hours were observed for all radiated zones of the three wells as shown in Figure 7.42, Figure 7.43, and Figure 7.44. In that case, the cleared area is for examples called 1-(c), the surrounding area with cells 1-(c)2. The kill area in well (b) and (c) were larger, apart from 4-(b) which was the same size as (a). This is explainable for 4-(b), owing to low level power 20W, 2.5% duty cycle and lower frequency 2.2 GHz.

### 7.3 Discussion

Comprehensive treatment studies have demonstrated the unique capability of non-thermal microwave irradiation for the annihilation of cancer cells. It is hoped that the results here will help pave the way for MWs to become a standard cancer treatment technique. The generic effect on organic molecules has been clearly illustrated. The cell molecules were radiated with 5.8 GHz and 2.2 GHz, different duty cycles and power levels (i.e. 10-50 W) with a limited peak temperature of 42°C that could be used to differentiate between thermal and non-thermal mechanisms of cell death. In order to create a full interpretation for the irradiation mechanism of cancer cell death, a search on irradiation effects has been conducted. A previous study by Porcellia *et.al.* [206] on the non-thermal effects of microwaves on proteins reported that with greater absorbance of radiation energy, the proteins lose more of their function (perhaps indicative of stronger changes in their structure). The effect is subtle for at least one of the enzymes that has been studied (no more than 50% activity loss at best), and takes more than an hour of radiation, for comparison, exposure times for our study are mostly in the 3-15 minutes range and, additionally, a delayed effect 24 hours and 48 hours after radiation was observed.

Figure 7.35 and Table 7 11 present results of study 4 – experiment 6 on changes in 945 protein expressions by our technique. The results showed interesting differences between the treated and control cells, particularly in regard to signalling and proteins involved in cell cycle control. The scan was conducted immediately after the microwave irradiation and also after a waiting period of few hours. Consequently, the protein conformation was changed significantly by microwave radiation. The dataset here is huge, so only limited proteins comparison graphs were presented in this thesis.

The unusual nonlinear responses that have been observed, both in terms of power and frequency dependences, often suggest non-thermal interaction of electromagnetic fields with biological rhythms in living tissue [207], cells in culture,[208] and also with components purified from cells (e.g. membranes,[209] and enzymes [210]).

The literature is focused solely on temperature rise in the cells as the cause of necrosis. First of these is that the cause of the cell death appears to be due to a complete breakdown of the cell membrane and intracellular organelles which were undergoing significant changes , observed in all microscopic images in this research. Generally, the

animal cell membrane is composed of approximately 50% lipids and 50% proteins by mass, with the most common lipid being a phospholipid. The phospholipid is particularly interesting for the purposes of this side due its hydrophilic element. The structure of the phospholipid is shown in Figure 7.45.

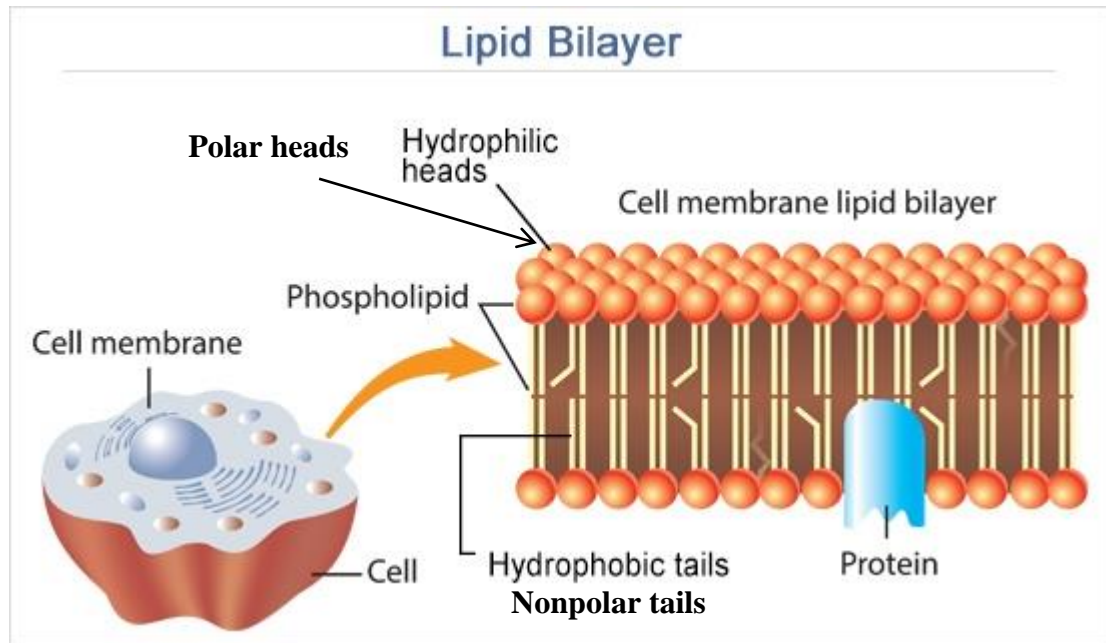


Figure 7.45: The lipid bilayer arrangement in a cell membrane [211].

Figure 7.45 shows an individual phospholipid, composed of a hydrophilic head and hydrophobic tail. The hydrophilic head is a polar molecule meaning that under an applied electric field it will subject force that will cause it to align in the direction of the field. The protein molecules will also contain charged amino acids, making these polar molecules, which again will be subject to a force from the applied electric field [212].

As a result of the significant amount of polar molecules forming the structure of the cell membrane, it is assumed that the energy provided by the electric field is sufficiently high to overcome the bonding energy holding these molecules together, resulting in the structure breaking down. Upon further investigation into the reported results it was discovered that the effect taking place as a direct result of the electric field has been termed electroporation and, as hypothesised above, directly impacts the cell membrane. A study published by Wang, *et al.* [213] has utilised electroporation to better deliver drugs to the cancerous tissue. This study also describes electroporation as the disorganisation of the lipids in the cell membrane much as set out above. In contrast to

this study, cell necrosis was achieved with much lower field levels than those described. The simulations provide a good approximation of the peak field levels which are around 2.5 kV/m. this study determines that field levels of a few kV/cm are required, an order higher than assumed to have been accomplished. Consequently, these results substantiate the claims made in this study that non-thermal irradiation is a viable alternative to thermal ablation and is capable of achieving cell death through a method that used in this research.

To provide further detail on electroporation, a brief review of this technique will be presented. The concept of irreversible electroporation was theorised in 2005 in a study by Davalos, *et al.* [214], and looked to exploit the ability to change the permeability of the cell membrane under an applied electric field. The electric field will generate a large number of nanopores within the membrane leading to apoptosis and permanent cell death. Irreversible electroporation, prior to this study has been completely ignored in cancer therapy. On the other hand, this study showed, through mathematical analysis, that large ablation regions can be achieved. A further review of this technique conducted by Lee, *et al.*[215] stated that irreversible electroporation is a viable and safe technique for tumour ablation. Finally, the study by Wang, *et al.* [213] gives rise to the alternative application of electroporation which is to increase the number of pores into the cancerous tissue, allowing for toxic drugs to be delivered more efficiently.

**Limitations in Lab Study 1 and 2:** As a result of the all findings after the unsuccessful experiments, it could be said that the reason of that is human error in setting the experiment up. In addition, there were significant limitations in Lab Study 1 and 2 which could account for the inconsistent results seen. Firstly, the most significant effect that has impacted the results can be seen in the microscopic images shown in Figure 7.18 and Figure 7.19 taken after the experiments, where a number of cracks can be seen. These micro fractures occurred throughout each experiment; whilst they were not visible an audible sound could be heard that corresponded with an increase in the  $S_{11}$  parameter significantly altering the power delivered to the sample. displays this most clearly in Figure 7.20, at 10 seconds there is a significant increase in the  $S_{11}$  followed by another increase at 40 seconds at which point the power dissipated within the sample was very small. This decrease in dissipated power is reflected through the declining temperature from 40 seconds, which before this cracking effect was increasing exponentially. The reasoning for this cracking is unknown and is expected to be as a

result of the interaction of the microwaves with the plastic used. In addition to the cracking, the power delivered to sample varied by a large a degree due to the changing  $S_{11}$  parameter, this results in the actual energy being delivered to the tissue varying significantly between each sample.

Another limitation is relates to the high degree of variability between the different samples used. This includes the lack of exact replication of the position of the probe and temperature sensor in the sample, as this was all carried out manually. This could lead to variations in the electric field profile dependent on the positioning and orientation of the probe, a lack of consistent temperature measurements as the thermocouples position was not the same between each sample.

The results may also not show the full extent of the damage due to the relatively low optical magnification used in Lab Study 1 and 2. The levels used do not show any intracellular components that could have been disrupted by the radiation and consequently in samples reported as “No effect on cell viability”, these cells could have undergone microwave fixation as described in Section 5.1.3 and be disrupted but not appear to have been.

A final limitation is in regards to the samples heated in the water bath. Whilst these were exposed to the higher temperatures for 10 minutes, the temperature the sample reached was not measured. This could result in the temperature not reaching the 50°C or only reaching that temperature for a short period of time not giving a perfect reflection of the heating effect, it could be argued that this is a closer representation of the results found within the experiments as the maximum temperature is only realised for a short period of time.

Briefly, the breast cancer cells gave reproducible death rate for non-thermal pulsed electric field exposure. In addition, the pointed probe constitutes a significant improvement over previous designs, increasing the cell death to reach 60-80% with first exposure.

## **CHAPTER 8 CONCLUSIONS AND FUTURE WORK**

This chapter summarises the main conclusions, discusses the pertinent challenges that have been faced during the research, and finally provides suggestions for future work and possible improvements that can be implemented. This thesis has been focused on two main studies, for cancer diagnosis and treatment, by using various open-ended coaxial sensor/applicator geometries.

### **8.1 Conclusions**

#### **8.1.1 Cancer detection**

In this thesis, it has been shown that it is possible to design, simulate and built small sized microwave sensors with high sensitivity for use on realistic cancer detection, as shown in chapters 3 and 4. Such microwave sensors are more sensitive for cancer detection at low microwave frequencies (i.e. between 0.1 to 3 GHz), and greater sensitivity enhancements can be achieved using a needle type probe with a sharp tip, which is also suitable for injecting into the tissue sample under test.

Chapter three gives a survey of the principles, theory, and simulation of open-ended coaxial sensors. The new, needle-type open-ended sensors are adopted here and are used to measure the dielectric permittivity of liquids, with the results showing significantly better sensitivity for the needle aperture compared to conventional flat sensor. The sensor was simulated by EMPro Software and optimized to improve its performance. Significant contrasts between various samples have been registered both in the simulations and experiments, with good agreement between the two. The dielectric

contrast is far greater when the angle of the aperture,  $\varphi$ , is stepped from  $0^\circ$  to  $80^\circ$ , meaning a sharper probe. The measured data for the amplitude of the reflection coefficient  $|S_{11}|$  are less precise than for the phase of  $S_{11}$  when measuring low loss materials. It is also observed that the data for  $|S_{11}|$  are less sensitive than the phase to the change of permittivity at low frequency. Therefore, it is suggested that the phase of the reflection coefficient is the most flexible and reliable parameter at low frequency, low permittivity, and low aperture angle. In general, as probes become more needle-like, the magnitude and phase both decrease significantly and as result the sensitivity increases since the sensing area increases distinctly for high angle probes, e.g.  $\varphi=80^\circ$ .

In chapter four, the needle-type sensors have been applied as diagnosis device with high spatial resolution at low frequency based on complex permittivity measurement of normal and cancerous tissues. Simulation results using EMPro software are provided here and demonstrated the potential of microwave needle probes for breast cancer diagnostics. Experimental results demonstrate their promising ability to detect breast cancer, making them adaptable and attractive tool for cancer diagnosis. Experimental results on normal and cancer tissues clarify the different nature of these tissues and also illuminate the dependence of complex reflection on operating frequency and sensor aperture geometry. The contrast in the sensitivity of the reflection coefficient for water-borne materials is found to increase with end angle. For example, compared with  $\varphi=0^\circ$ , simulations for  $\varphi=80^\circ$ , at the low frequency end (0.1 GHz) show that the magnitude increases by 13.8% and the phase increases by 163%.

### **8.1.2 Cancer treatment**

In chapter five, a novel microwave applicator technique based on non-thermal microwave irradiation was developed and tested for its application for cancer treatment. A number of high frequency treatment techniques have been considered in this work, including cryoablation, RF ablation and microwave ablation. All three methods are minimally invasive, with treatment being delivered laparoscopically. However, the microwave (MW) ablation method is preferable, mainly for its ability to achieve an active heat transfer. Active heat transfer is a significant merit over passive heat transfer due to its ability to overcome heat sinks, a significant problem when trying to treat uniform lesion areas. Moreover, its capability to treat larger tumour regions compared

with passive heat transfer methods. Hence, MW ablation is considered to be the best treatment option of the three ablation techniques. It should also be noted that MW ablation shows the most clearly defined ablation regions with no viable tissue.

Microwave ablation was found to be the most beneficial and with the most scope to be improved upon as detailed through several research papers that were looking to exploit various parameters in an attempt to improve radiation delivery. Much of the literature was found to focus on thermal ablation, which was explained through the Debye model and some theory was presented on the potential for electric field to interfere with cancerous tissue. Following from this a range of simulations was conducted using COMSOL Multiphysics, which aimed to understand the electric field profile generated from the probes selected for this study. Further to this, the simulations aided the understanding of the impact various parameters had on the electric field profile, such as MW input power and the material properties of cancerous and normal breast tissues.

Chapter six proposed equipment to build a complete system for non-thermal MW ablation. These include: the signal generator, power amplifier, circulator and directional coupler. Each piece of equipment has been explained in detail in order to fully understand how it has been utilised within the experimental set up. To obtain the measurements for this study a LabVIEW programme was built and utilised. The instruments and applicators were connected to LabVIEW via VISA and GPIB peripheral interface, allowing for additional control of the instrument when needed. The LabVIEW programme built in this research was able to provide an interface to the users allowing the parameters to be configured and provides an interface upon which a range of data could be presented. This flexibility in the control of the measurement gives us the ability to (a) control the level of the transmitted power, as well as (b) to adjust the exposure time. Control over these parameters helps us calculate and maximize the efficiency of the dissipated power. Also, it measures the sample temperature. These data were combined into a single graph shown in the main virtual instrument.

Chapter seven presented a range of novel experiments that have been carried out, including preliminary experiments conducted on water to obtain a reference case. This reference case was utilised in the planning of the experiments for MW ablation of cancer cells. The cancerous cells were subject to microwave radiation at a range of power levels and pulsing protocols and, additionally, a set of cancerous cells were heated up in a water bath to provide a purely thermally-treated example for comparison.

These experiments yielded repeatable, successful results from the microwave radiation in which the cells were completely destroyed with no major heating effect. The microscopic images showed that the cell membranes were completely broken down and this resulted in the cells being no longer viable. The reasoning behind the cell deaths were attributed to strong interactions between the polar molecules within the cell membranes with the applied MW electric field. Even more importantly, the experiments have shown that the technique was successfully used *in-vivo* with cancer tissues with 100% cancer destruction.

These results may lead to new important treatment methods for cancer, which could involve a mixed treatment process such as microwave irradiation, followed by more conventional drug treatment. In the field of cancer treatment, this technique now offers a new tool in the arsenal of weapons to fight cancer, providing new opportunities to save many lives.

## **8.2 Recommendations for Further Work**

Despite important developments in this research, there is still ample room for further improvements in theory and simulation of the two studied parts (i.e. diagnosis and treatment).

In terms of diagnosis, more breast cancer samples are needed for more needle-type sensor analysis. Also, it would be beneficial to test different types of cancer tissues. In addition, a hand-held, needle sensor based device has also been proposed and developed, which may prove useful for distinguishing skin cancers from healthy regions of skin for future work.

## **8.1 Microwave Handheld Skin Diagnostic Tool for clinic trail**

In order to try to develop a hand-held diagnostic based on the successful findings from the needle probe for the differentiation between cancerous and normal tissue, initial efforts were made on developing a prototype tool to investigate (and possibly diagnose) skin cancer, shown in Figure 8.1 The main objective is to be handheld diagnostic tool to simplify and expedite skin cancer detection, specifically in early stage.

The engineering idea behind creating this instrument is to measure the dielectric properties of a small area of skin.

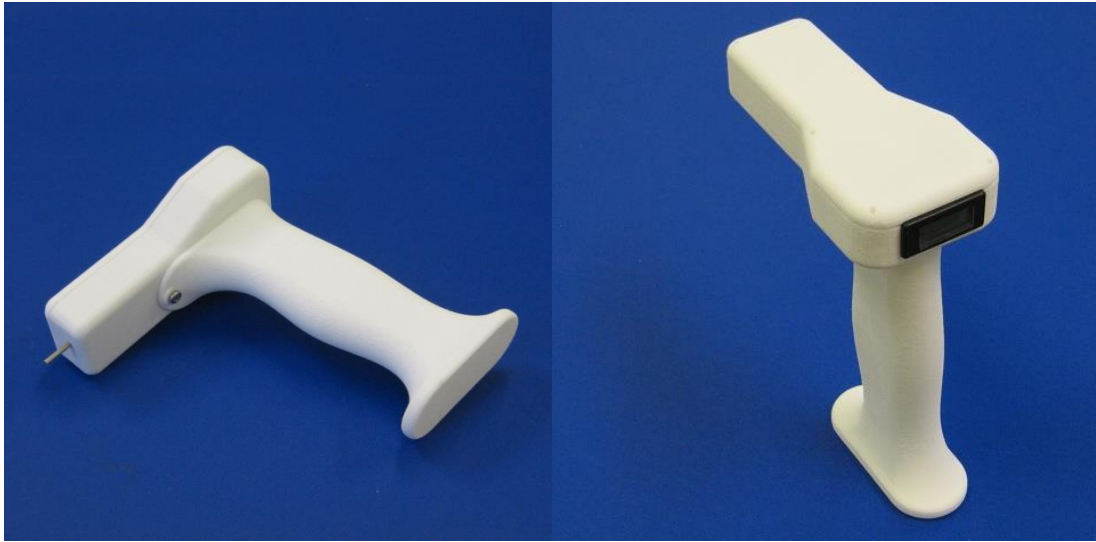


Figure 8.1: Prototype Microwave Handheld Skin Diagnostic Tool for clinic trial.

This proposed unit is collaboration between this research and Mr. Michael Casbon who is an expert in RF amplifier and system design and responsible for circuit design. The tool is still under development and improvement. This is an ongoing study for further work which considers the initial attempts to develop a microwave handheld skin diagnostic tool for future clinic trails. Diseased skin tissues, suspected of cancer, are irradiated and assessed by means of a coaxial probe with on-board microwave electronics.

In the treatment study, it will be important to devise a way which adequately describes the dielectric properties of cancer cells under test before and through treatment process to address the challenges of operating the current probes in real environments. This should be possible within the current set-up, using the dynamic measurement of  $S_{11}$  to characterise the tissue and so adjust the power delivery accordingly. Other challenges mainly include clinical effectiveness, robustness, accuracy, and power efficiency for increasing the reliability and accuracy of the experiments conducted.

The effects due to the change of dielectric properties of the cancer cells have not fully been explored in the treatment part of this thesis. Since the dielectric properties of cancer tissues vary considerably during treatment, it is suggested that the cavity

resonant applicator technique be used for this purpose, to enhance treatment reliability for the future investigation of non-thermal microwave treatments. Three cavities have already been designed for this purpose, at frequencies of 2.45, 4.2 and 5.8 GHz, and the finalised, fully tested structures are shown in Figure 8.2. Whilst time factors have not permitted their use within this thesis, they are ready for future work. Using these provides the opportunity to link the changes in the electrical properties of materials before the MW irradiation process to the changes in the properties during treatment. They also provided a much better-prescribed dose of MW irradiation since, rather than the electric field being high concentrated around the tip of the coaxial probe, since these cavities all operate in the  $TM_{010}$  mode there is a uniform electric field region along each of their axes. This gives a highly uniform, well-predicted MW electric field throughout the whole sample when placed in a standard Eppendorf tube on-axis.

Such cavities also allow the effect of MW magnetic field on cancer cells to be studied.

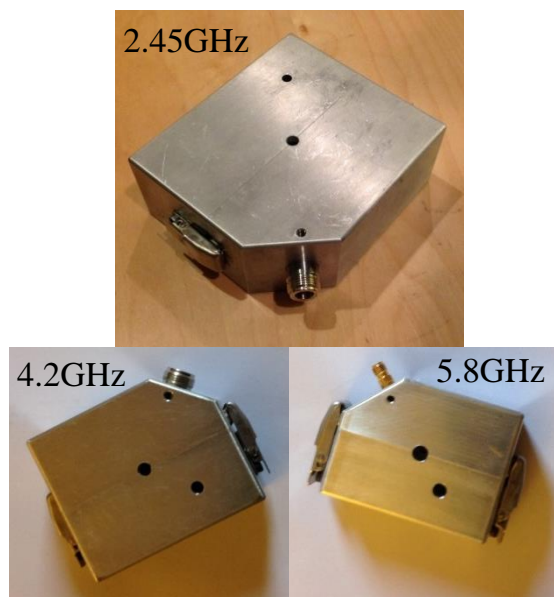


Figure 8.2: Three proposed cylindrical cavities with ability of separated electric and magnetic response for non-thermal cancer characterization applications.

This is not possible in the coaxial probe applicator since the sample necessarily has to sit within a region of high electric field owing to the open circuit condition at the end of the probe. However, there is a region of high magnetic field around the outer perimeter of each cavity when operating in the  $TM_{010}$  mode, which will allow magnetic field interactions to be compared and contrasted with the equivalent electric field interactions on-axis, similar to what has already been done on the MW excitation of photoluminescent bacteria [216].

Moreover, an investigation is required to be carried out into the probe design with additional probe geometries, in order to achieve better propagation characteristics. Furthermore, additional simulations could be conducted modelling the heat transfer characteristics of the sample. This will provide a much more detailed view of the heating and any potential local variations.

In addition, the measurement and instrumentation system for this research, utilised in LabVIEW could be improved through the use of a more robust controlling system. The main panel VI could be improved by creating an interface for the user's to input configurations for the power meters such as the frequency of measurement, and triggering source. This can be done by connecting the output of the signal generator to the input trigger of the power meter. The LabVIEW programme could also be improved by monitoring the actual value of power meter's reading, therefore, if it received a signal strength that is closed to its maximum power rating, the LabVIEW will automatically stop the measurement. This control practice will prevent the damaging of the power meter. It also can be implemented for the other equipment such as the RF power amplifier and signal generator by connecting LabVIEW with the equipment via number of different connections.

Furthermore, the experimental procedures that have been carried out in this research could be further improved by having a more robust technique to monitor the microwave radiation into the tissue sample more efficiently. The biological assessment from the cancer cells culture through radiated with microwaves could be monitoring at real time by using higher power microscopy such as an electron microscope. This would allow for the intracellular organelles changes and any damage being done to these could be observed at certain power levels, providing information around suitable power level and exposure times.

In addition, an array multiprobe topology is proposed that offers the ability to focusing on using microwaves for characterising cancer tissue, detecting cancer lesions, and treating a larger area of cancer.

Finally, due to previous results (i.e. change of the protein conformation), one of the biologists has suggested using non-thermal microwave technique with neurodegenerative diseases. These are frequently caused by build-up of misfolded

proteins that eventually interfere with nerve cell function. The challenge would be to change the molecules without damaging any brain cells in the vicinity.

A comprehensive microwave animal study currently underway at the University of Cardiff and the University Hospital of Wales involves applying the non-thermal microwave irradiation on animals (i.e. mice).

# APPENDIX I The supplier sheet of the breast cancer cells

BREAST

MDA-MB-231

arrived Aug 2014

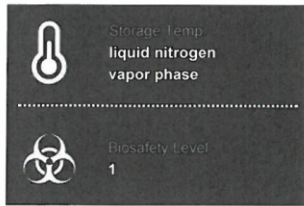


ATCC

Product Sheet

**MDA-MB-231 (ATCC® HTB-26™)**

Please read this FIRST



#### Intended Use

This product is intended for research use only. It is not intended for any animal or human therapeutic or diagnostic use.

#### Complete Growth Medium

The base medium for this cell line is ATCC-formulated Leibovitz's L-15 Medium, Catalog No. 30-2008. To make the complete growth medium, add the following components to the base medium: fetal bovine serum to a final concentration of 10%.  
(Note: The L-15 medium formulation was devised for use in a free gas exchange with atmospheric air. A CO<sub>2</sub> and air mixture is detrimental to cells when using this medium for cultivation.)

#### Citation of Strain

If use of this culture results in a scientific publication, it should be cited in that manuscript in the following manner: MDA-MB-231 (ATCC® HTB-26™)

American Type Culture Collection  
PO Box 1549  
Manassas, VA 20108 USA  
[www.atcc.org](http://www.atcc.org)

800.638.6597 or 703.365.2700  
Fax: 703.365.2750  
Email: [Tech@atcc.org](mailto:Tech@atcc.org)

Or contact your local distributor

Page 1 of 3

#### Description

**Organism:** *Homo sapiens*, human  
**Tissue:** mammary gland/breast; derived from metastatic site: pleural effusion  
**Disease:** adenocarcinoma  
**Cell Type:** epithelial  
**Age:** 51 years adult  
**Gender:** female  
**Morphology:** epithelial  
**Growth Properties:** adherent  
**Isoenzymes:**

AK-1, 1  
ES-D, 1  
G6PD, B  
GLO-1, 2  
Me-2, 1-2  
PGM1, 1-2  
PGM3, 1

#### DNA Profile:

Amelogenin: X  
CSF1PO: 12,13  
D13S317: 13  
D16S539: 12  
D5S818: 12  
D7S820: 8,9  
THO1: 7,9,3  
TPOX: 8,9  
vWA: 15,18

**Cytogenetic Analysis:** The cell line is aneuploid female (modal number = 64, range = 52 to 68), with chromosome counts in the near-triploid range. Normal chromosomes N8 and N15 were absent. Eleven stable rearranged marker chromosomes are noted as well as unassignable chromosomes in addition to the majority of autosomes that are trisomic. Many of the marker chromosomes are identical to those shown in the karyotype reported by K. L. Satya-Prakash, et al.

#### Batch-Specific Information

Refer to the Certificate of Analysis for batch-specific test results.

#### SAFETY PRECAUTION

ATCC highly recommends that protective gloves and clothing always be used and a full face mask always be worn when handling frozen vials. It is important to note that some vials leak when submerged in liquid nitrogen and will slowly fill with liquid nitrogen. Upon thawing, the conversion of the liquid nitrogen back to its gas phase may result in the vessel exploding or blowing off its cap with dangerous force creating flying debris.

#### Unpacking & Storage Instructions

1. Check all containers for leakage or breakage.
2. Remove the frozen cells from the dry ice packaging and immediately place the cells at a temperature below -130°C, preferably in liquid nitrogen vapor, until ready for use.

#### Handling Procedure for Frozen Cells

To insure the highest level of viability, thaw the vial and initiate the culture as soon as possible upon receipt. If upon arrival, continued storage of the frozen culture is necessary, it should be stored in liquid nitrogen vapor phase and not at -70°C. Storage at -70°C will result in loss of viability.

1. Thaw the vial by gentle agitation in a 37°C water bath. To reduce the possibility of contamination, keep the O-ring and cap out of the water. Thawing should be rapid (approximately 2 minutes).
2. Remove the vial from the water bath as soon as the contents are thawed, and decontaminate by dipping in or spraying with 70% ethanol. All of the operations from this point on should be carried out under strict aseptic conditions.
3. Transfer the vial contents to a centrifuge tube containing 9.0 mL complete culture medium and spin at approximately 125 x g for 5 to 7 minutes.



**ATCC**

Product Sheet

**MDA-MB-231 (ATCC® HTB-26™)**

Please read this **FIRST**

Storage Temp  
liquid nitrogen  
vapor phase

Biosafety Level  
1

**Intended Use**

This product is intended for research use only. It is not intended for any animal or human therapeutic or diagnostic use.

**Complete Growth Medium**

The base medium for this cell line is ATCC-formulated Leibovitz's L-15 Medium, Catalog No. 30-2008. To make the complete growth medium, add the following components to the base medium: fetal bovine serum to a final concentration of 10%.

(Note: The L-15 medium formulation was devised for use in a free gas exchange with atmospheric air. A CO<sub>2</sub> and air mixture is detrimental to cells when using this medium for cultivation)

**Citation of Strain**

If use of this culture results in a scientific publication, it should be cited in that manuscript in the following manner: MDA-MB-231 (ATCC® HTB-26™)

American Type Culture Collection  
PO Box 1549  
Manassas, VA 20108 USA  
[www.atcc.org](http://www.atcc.org)

800.638.6597 or 703.365.2700  
Fax: 703.365.2750  
Email: [Tech@atcc.org](mailto:Tech@atcc.org)

Or contact your local distributor

Page 2 of 3

4. Resuspend cell pellet with the recommended complete medium (see the specific batch information for the culture recommended dilution ratio) and dispense into a new culture flask.
5. Incubate the culture at 37°C in a suitable incubator. **(without CO<sub>2</sub>)**



**Handling Procedure for Flask Cultures**

The flask was seeded with cells (see specific batch information) grown and completely filled with medium at ATCC to prevent loss of cells during shipping.

1. Upon receipt visually examine the culture for macroscopic evidence of any microbial contamination. Using an inverted microscope (preferably equipped with phase-contrast optics), carefully check for any evidence of microbial contamination. Also check to determine if the majority of cells are still attached to the bottom of the flask; during shipping the cultures are sometimes handled roughly and many of the cells often detach and become suspended in the culture medium (but are still viable).
2. If the cells are still attached, aseptically remove all but 5 to 10 mL of the shipping medium. The shipping medium can be saved for reuse. Incubate the cells at 37°C in a free gas exchange with atmospheric air until they are ready to be subcultured.
3. If the cells are not attached, aseptically remove the entire contents of the flask and centrifuge at 125 x g for 5 to 10 minutes. Remove shipping medium and save. Resuspend the pelleted cells in 10 mL of this medium and add to 25 cm<sup>2</sup> flask. Incubate at 37° in a free gas exchange with atmospheric air until cells are ready to be subcultured.



**Subculturing Procedure**

Volumes are given for a 75 cm<sup>2</sup> flask. Increase or decrease the amount of dissociation medium needed proportionally for culture vessels of other sizes.

1. Remove and discard culture medium.
2. Briefly rinse the cell layer with 0.25% (w/v) Trypsin- 0.53 mM EDTA solution to remove all traces of serum that contains trypsin inhibitor.
3. Add 2.0 to 3.0 mL of Trypsin-EDTA solution to flask and observe cells under an inverted microscope until cell layer is dispersed (usually within 5 to 15 minutes).  
Note: To avoid clumping do not agitate the cells by hitting or shaking the flask while waiting for the cells to detach. Cells that are difficult to detach may be placed at 37°C to facilitate dispersal.
4. Add 6.0 to 8.0 mL of complete growth medium and aspirate cells by gently pipetting.
5. Add appropriate aliquots of the cell suspension to new culture vessels.
6. Incubate cultures at 37°C without CO<sub>2</sub>.

**Subcultivation Ratio:** A subcultivation ratio of 1:2 to 1:4 is recommended

**Medium Renewal:** 2 to 3 times per week



**Cryopreservation Medium**

Complete growth medium described above supplemented with 5% (v/v) DMSO. Cell culture tested DMSO is available as ATCC Catalog No. 4-X.



**References**

References and other information relating to this product are available online at [www.atcc.org](http://www.atcc.org).



**Biosafety Level: 1**

Appropriate safety procedures should always be used with this material. Laboratory safety is discussed in the current publication of the *Biosafety in Microbiological and Biomedical Laboratories* from the U.S. Department of Health and Human Services Centers for Disease Control and Prevention and National Institutes for Health.

**ATCC Warranty**

The viability of ATCC® products is warranted for 30 days from the date of shipment, and is valid only if the product is stored and cultured according to the information included on this product information sheet. ATCC lists the media formulation that has been found to be effective for this strain. While other, unspecified media may also produce satisfactory results, a change in media or the absence of an additive from the ATCC recommended media may affect recovery, growth and/or function of this strain. If an alternative medium formulation is used, the ATCC warranty for viability is no longer valid.

**Disclaimers**



**ATCC**

Product Sheet

**MDA-MB-231 (ATCC® HTB-26™)**

**Please read this FIRST**

The graphic contains two sections. The top section features a liquid nitrogen symbol (a flask with a drop) and the text: "Storage Temp: liquid nitrogen vapor phase". The bottom section features a biohazard symbol and the text: "Biosafety Level: 1".

**Intended Use**

This product is intended for research use only. It is not intended for any animal or human therapeutic or diagnostic use.

**Complete Growth Medium**

The base medium for this cell line is ATCC-formulated Leibovitz's L-15 Medium, Catalog No. 30-2008. To make the complete growth medium, add the following components to the base medium: fetal bovine serum to a final concentration of 10%.

(Note: The L-15 medium formulation was devised for use in a free gas exchange with atmospheric air. A CO<sub>2</sub> and air mixture is detrimental to cells when using this medium for cultivation)

**Citation of Strain**

If use of this culture results in a scientific publication, it should be cited in that manuscript in the following manner: MDA-MB-231 (ATCC® HTB-26™)

This product is intended for laboratory research purposes only. It is not intended for use in humans. While ATCC uses reasonable efforts to include accurate and up-to-date information on this product sheet, ATCC makes no warranties or representations as to its accuracy. Citations from scientific literature and patents are provided for informational purposes only. ATCC does not warrant that such information has been confirmed to be accurate.

This product is sent with the condition that you are responsible for its safe storage, handling, and use. ATCC is not liable for any damages or injuries arising from receipt and/or use of this product. While reasonable effort is made to insure authenticity and reliability of strains on deposit, ATCC is not liable for damages arising from the misidentification or misrepresentation of cultures.

Please see the enclosed Material Transfer Agreement (MTA) for further details regarding the use of this product. The MTA is also available on our Web site at [www.atcc.org](http://www.atcc.org)

Additional information on this culture is available on the ATCC web site at [www.atcc.org](http://www.atcc.org).

© ATCC 2014. All rights reserved. ATCC is a registered trademark of the American Type Culture Collection. [02/28]

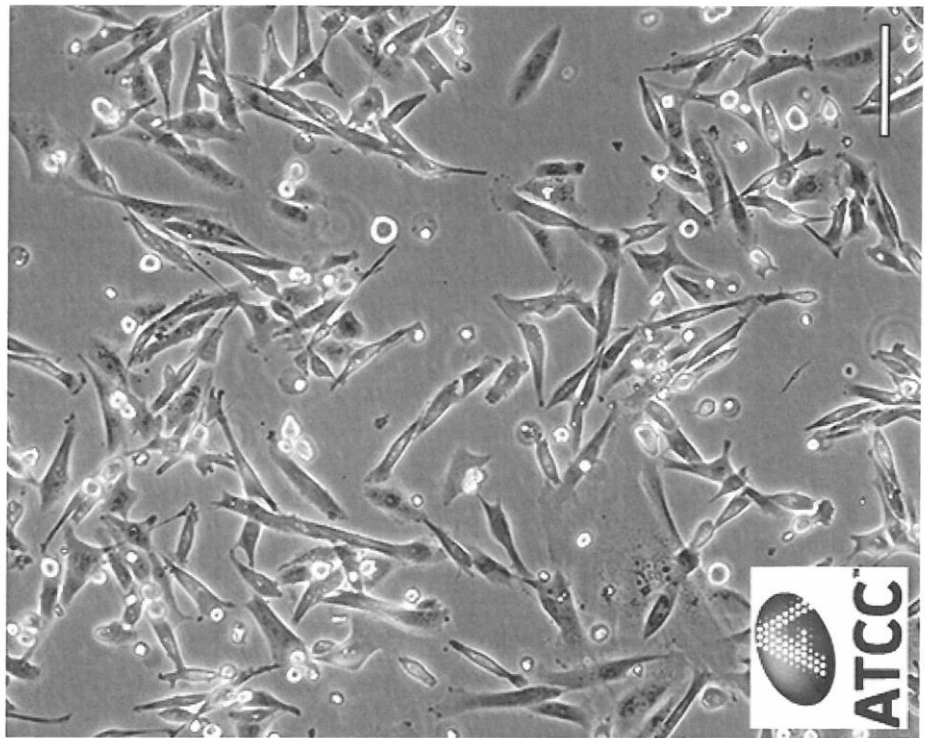
American Type Culture Collection  
PO Box 1549  
Manassas, VA 20108 USA  
[www.atcc.org](http://www.atcc.org)

800.638.6597 or 703.365.2700  
Fax: 703.365.2750  
Email: [Tech@atcc.org](mailto:Tech@atcc.org)

Or contact your local distributor

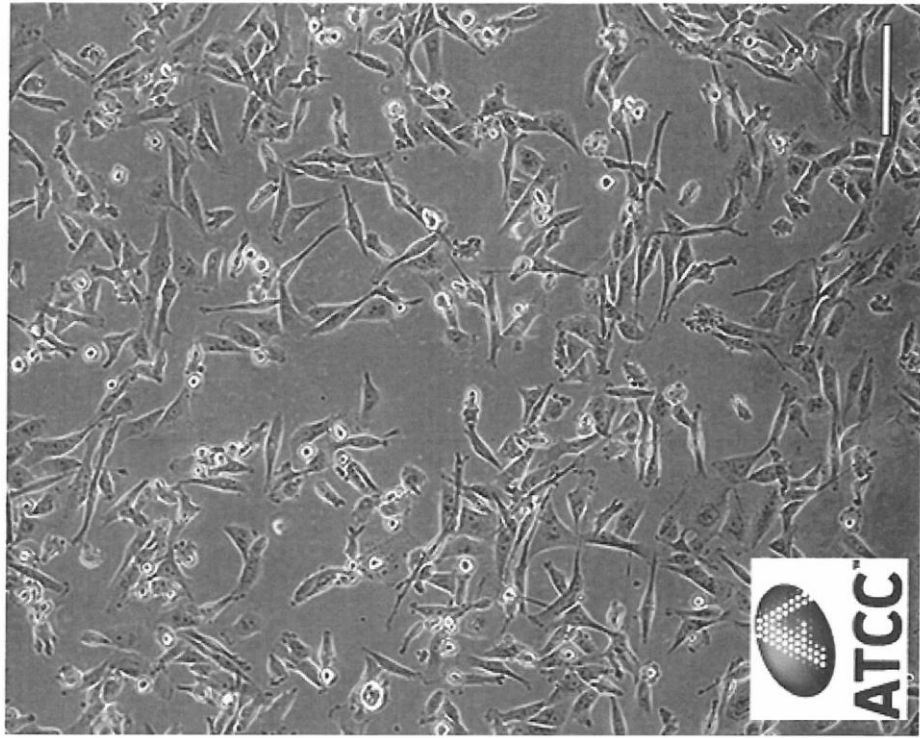
Page 3 of 3

ATCC Number: **HTB-26**<sup>™</sup>  
Designation: **MDA-MB-231**



Low Density

Scale Bar = 100µm



High Density

Scale Bar = 100µm

## BIBLIOGRAPHY

- [1] C. Gabriel, S. Gabriel, and E. Corthout, "The dielectric properties of biological tissues: I. Literature survey," *Physics in Medicine and Biology*, vol. 41, p. 2231, 1996.
- [2] R. Zoughi, *Microwave Non-Destructive Testing and Evaluation Principles*: Springer Netherlands, 2012.
- [3] C. K. O. L. F. Chen, C. P. Neo, V. V. Varadan, Vijay K. Varadan, *Microwave Electronics Measurement and Materials Characterization*. England: John Wiley & Sons Ltd, 2004.
- [4] M. B. B. M. F. S. Kashif Saeed, Ian C. and H. Ed., "Planar Microwave Sensors for Complex Permittivity Characterization of Materials and Their Applications," in *Applied Measurement Systems*, Z. Haq, Ed., ed: In-Tech, 24 Feb. 2012, pp. 319-350.
- [5] S. N. Jha, K. Narsaiah, A. L. Basediya, R. Sharma, P. Jaiswal, R. Kumar, *et al.*, "Measurement techniques and application of electrical properties for nondestructive quality evaluation of foods—a review," *Journal of Food Science and Technology*, vol. 48, pp. 387-411, 2011.
- [6] M. S. V. a. G. S. V. Raghavan, "An overview of dielectric properties measuring techniques," *The Journal of The Canadian Society for Bioengineering (CSBE)*, vol. 47, pp. 7.15-7.30, 2005.
- [7] O. V. Tereshchenko, F. J. K. Buesink, and F. B. J. Leferink, "An overview of the techniques for measuring the dielectric properties of materials," in *2011 XXXth URSI General Assembly and Scientific Symposium*, 2011, pp. 1-4.
- [8] F. H. Wee, P. J. Soh, A. H. M. Suhaizal, H. Nornikman, and A. A. M. Ezanuddin, "Free space measurement technique on dielectric properties of agricultural residues at microwave frequencies," in *2009 SBMO/IEEE MTT-S International Microwave and Optoelectronics Conference (IMOC)*, 2009, pp. 183-187.
- [9] W. F. Hoon, S. P. Jack, M. F. A. Malek, and N. Hasssan, "Alternatives for PCB Laminates: Dielectric Properties' Measurements at Microwave Frequencies," in *Dielectric Material*, ed Rijeka: InTech, 2012, p. Ch. 0.
- [10] A. P. Gregory and R. N. Clarke, "A review of RF and microwave techniques for dielectric measurements on polar liquids," *IEEE Transactions on Dielectrics and Electrical Insulation*, vol. 13, pp. 727-743, 2006.
- [11] Agilent, "Basics of Measuring the Dielectric Properties of Materials," Agilent2006.

- [12] K. Byoungjoong, C. Jaiwon, C. Changyul, and K. Youngwoo, "Nondestructive measurement of complex permittivity and permeability using multilayered coplanar waveguide structures," *IEEE Microwave and Wireless Components Letters*, vol. 15, pp. 381-383, 2005.
- [13] Z. W. A. Boughriet, H. Mccann, and L. E. Davis, "The measurement of dielectric properties of liquids at microwave frequencies using open-ended coaxial probes," in *1st World Congr. Ind. Process Tomogr.*, pp. 318-322, Apr. 1999.
- [14] Y. Xu, F. M. Ghannouchi, and R. G. Bosisio, "Theoretical and experimental study of measurement of microwave permittivity using open ended elliptical coaxial probes," *IEEE Transactions on Microwave Theory and Techniques*, vol. 40, pp. 143-150, 1992.
- [15] Y. Xu, R. G. Bosisio, A. Bonincontro, F. Pedone, and G. F. Mariutti, "On the measurement of microwave permittivity of biological samples using needle type coaxial probes," in *[1991] Conference Record. IEEE Instrumentation and Measurement Technology Conference*, 1991, pp. 546-550.
- [16] I. S. d. S. Dr. G. Mariutti, ed. Roma, Italia: private communication, Aug. 8. 1990.
- [17] M. A. Stuchly and S. S. Stuchly, "Dielectric Properties of Biological Substances — Tabulated," *Journal of Microwave Power*, vol. 15, pp. 19-25, 1980/01/01 1980.
- [18] R. N. Clarke, Gregory, A P, Cannell, D, Patrick, M, Wylie, S, Youngs, I, Hill, G, "A guide to the characterisation of dielectric materials at RF and microwave frequencies," Institute of Measurement and Control / National Physical Laboratory, London2003.
- [19] M. D. J. J. Baker-Jarvis, B. F. Riddle, R. T. Johnk, P. Kabos, C. and R. G. G. L. Holloway, C. A. Grosvenor, "Measuring the permittivity and permeability of lossy materials: Solids, liquids, metals, building materials and negative index materials," 2004.
- [20] U. K. a. Y. Feldman, "Broadband dielectric spectrometry of liquids and biosystems," *Meas. Sci. Tech.*, vol. 17, pp. R17-35, 2006.
- [21] G. W. a. D. K. Thomas, "Phenomenological and molecular theories of dielectric and electrical relaxation of materials," 1998.
- [22] J. P. Grant, R. N. Clarke, G. T. Symm, and N. M. Spyrou, "In vivo dielectric properties of human skin from 50 MHz to 2.0 GHz," *Phys Med Biol*, vol. 33, pp. 607-12, May 1988.
- [23] M. S. V. a. G. S. H. Raghavan, "An overview of dielectric properties measuring techniques," *Canadian Biosystems Engineering*, vol. 47, pp. 7.15-7.30, May 13 2005.
- [24] A. Technologies, "Agilent 85070E Dielectric Probe Kit 200 MHz to 50 GHz Technical Overview," Agilent TechnologiesNovember 6, 2003.
- [25] M. A. Stuchly and S. S. Stuchly, "Coaxial Line Reflection Methods for Measuring Dielectric Properties of Biological Substances at Radio and

- Microwave Frequencies-A Review," *IEEE Transactions on Instrumentation and Measurement*, vol. 29, pp. 176-183, 1980.
- [26] T. W. Athey, M. A. Stuchly, and S. S. Stuchly, "Measurement of Radio Frequency Permittivity of Biological Tissues with an Open-Ended Coaxial Line: Part I," *IEEE Transactions on Microwave Theory and Techniques*, vol. 30, pp. 82-86, 1982.
- [27] M. A. Stuchly, T. W. Athey, G. M. Samaras, and G. E. Taylor, "Measurement of Radio Frequency Permittivity of Biological Tissues with an Open-Ended Coaxial Line: Part II - Experimental Results," *IEEE Transactions on Microwave Theory and Techniques*, vol. 30, pp. 87-92, 1982.
- [28] D. Misra, M. Chhabra, B. R. Epstein, M. Microtznik, and K. R. Foster, "Noninvasive electrical characterization of materials at microwave frequencies using an open-ended coaxial line: test of an improved calibration technique," *IEEE Transactions on Microwave Theory and Techniques*, vol. 38, pp. 8-14, 1990.
- [29] H. Zheng and C. E. Smith, "Permittivity measurements using a short open-ended coaxial line probe," *IEEE Microwave and Guided Wave Letters*, vol. 1, pp. 337-339, 1991.
- [30] D. L. Gershon, J. P. Calame, Y. Carmel, T. M. Antonsen, and R. M. Hutcheon, "Open-ended coaxial probe for high-temperature and broad-band dielectric measurements," *IEEE Transactions on Microwave Theory and Techniques*, vol. 47, pp. 1640-1648, 1999.
- [31] E. C. Burdette, F. L. Cain, and J. Seals, "In Vivo Probe Measurement Technique for Determining Dielectric Properties at VHF through Microwave Frequencies," *IEEE Transactions on Microwave Theory and Techniques*, vol. 28, pp. 414-427, 1980.
- [32] G. Gajda and S. S. Stuchly, "An Equivalent Circuit of an Open-Ended Coaxial Line," *IEEE Transactions on Instrumentation and Measurement*, vol. 32, pp. 506-508, 1983.
- [33] A. M. Campbell, "Measurements and Analysis of the Microwave Dielectric Properties of Tissues," PhD, University of Glasgow, Oct. 1990.
- [34] D. Berube, F. M. Ghannouchi, and P. Savard, "A comparative study of four open-ended coaxial probe models for permittivity measurements of lossy dielectric/biological materials at microwave frequencies," *IEEE Transactions on Microwave Theory and Techniques*, vol. 44, pp. 1928-1934, 1996.
- [35] A. Cataldo, E. Piuze, G. Cannazza, E. De Benedetto, and L. Tarricone, "Quality and anti-adulteration control of vegetable oils through microwave dielectric spectroscopy," *Measurement*, vol. 43, pp. 1031-1039, 10// 2010.
- [36] M. M. Brady, S. A. Symons, and S. S. Stuchly, "Dielectric behavior of selected animal tissues in vitro at frequencies from 2 to 4 GHz," *IEEE Trans Biomed Eng*, vol. 28, pp. 305-7, Mar 1981.
- [37] F. M. Ghannouchi and R. G. Bosisio, "Measurement of microwave permittivity using a six-port reflectometer with an open-ended coaxial line," *IEEE Transactions on Instrumentation and Measurement*, vol. 38, pp. 505-508, 1989.

- [38] J. M. Anderson, C. L. Sibbald, and S. S. Stuchly, "Dielectric measurements using a rational function model," *IEEE Transactions on Microwave Theory and Techniques*, vol. 42, pp. 199-204, 1994.
- [39] J. M. Anderson, C. L. Sibbald, S. S. Stuchly, and K. Caputa, "Advances in dielectric measurements using an open-ended coaxial line sensor," in *Proceedings of Canadian Conference on Electrical and Computer Engineering*, 1993, pp. 916-919 vol.2.
- [40] S. S. Stuchly, C. L. Sibbald, and J. M. Anderson, "A new aperture admittance model for open-ended waveguides," *IEEE Transactions on Microwave Theory and Techniques*, vol. 42, pp. 192-198, 1994.
- [41] L. P. Christos and K. M. Devendra, "The co-axial aperture electromagnetic sensor and its application in material characterization," *Measurement Science and Technology*, vol. 8, p. 1191, 1997.
- [42] G. Deschamps, "Impedance of an antenna in a conducting medium," *IRE Transactions on Antennas and Propagation*, vol. 10, pp. 648-650, 1962.
- [43] K. F. Staebell and D. Misra, "An experimental technique for in vivo permittivity measurement of materials at microwave frequencies," *IEEE Transactions on Microwave Theory and Techniques*, vol. 38, pp. 337-339, 1990.
- [44] J. R. W. a. T. V. D. S. Ramo, *Fields and Waves in Communication Electronics*. New York: Wiley, 1965.
- [45] K. Technologies. (2016, February 22). *Using the Finite Element Method (FEM)*. Available: <http://edadocs.software.keysight.com/pages/viewpage.action?pageId=102948098>
- [46] J. R. M. M. Gex-Fabry, and F. E. Gardiol, "Reflection and radiation of an open-ended circular waveguide and application to nondestructive measurements of materials," *Arch. Elek. Übertragung*, vol. 33, pp. 473-478, 1979.
- [47] M. King and J. C. Wiltse, "Coaxial transmission lines of elliptical cross section," *Antennas and Propagation, IRE Transactions on*, vol. 9, pp. 116-118, 1961.
- [48] M. C. Decreton and F. E. Gardiol, "Simple Nondestructive Method for the Measurement of Complex Permittivity," *Instrumentation and Measurement, IEEE Transactions on*, vol. 23, pp. 434-438, 1974.
- [49] M. Decreton and M. S. Ramachandraiah, "Nondestructive Measurement of Complex Permittivity for Dielectric Slabs (Short Papers)," *Microwave Theory and Techniques, IEEE Transactions on*, vol. 23, pp. 1077-1080, 1975.
- [50] M. S. Ramachandraiah and M. C. Decreton, "A Resonant Cavity Approach for the Nondestructive Determination of Complex Permittivity at Microwave Frequencies," *Instrumentation and Measurement, IEEE Transactions on*, vol. 24, pp. 287-291, 1975.
- [51] H. Levine and C. H. Papas, "Theory of the Circular Diffraction Antenna," *Journal of Applied Physics*, vol. 22, pp. 29-43, 1951.
- [52] J. Galejs. New York: Pergamon, 1969.
- [53] A. Sommerfeld, *Partial Differential Equations*. New York, NY: Academic Press Inc., 1949.

- [54] N. Marcuvitz, *Waveguide Handbook*. New York, NY: McGraw, 1951.
- [55] J. R. Mosig, J. C. E. Besson, M. Gex-Fabry, and F. E. Gardiol, "Reflection of an open-ended coaxial line and application to nondestructive measurement of materials," *Instrumentation and Measurement, IEEE Transactions on*, vol. IM-30, pp. 46-51, 1981.
- [56] L. Ching-Lieh and Y. F. Chen, "Determination of electromagnetic properties of materials using flanged open-ended coaxial probe-full-wave analysis," *Instrumentation and Measurement, IEEE Transactions on*, vol. 44, pp. 19-27, 1995.
- [57] J. A. Stratton, *Electromagnetic Theory*. New York: McGraw-Hill, 1941.
- [58] F. M. Ghannouchi and R. G. Bosisio, "Measurement of microwave permittivity using a six-port reflectometer with an open-ended coaxial line," *Instrumentation and Measurement, IEEE Transactions on*, vol. 38, pp. 505-508, 1989.
- [59] F. M. Ghannouchi and R. G. Bosisio, "A comparative study on sensitivity analysis of various open-ended coaxial line geometries," in *Electrical Insulating Materials, 1988. Proceedings of the Twenty-First Symposium on*, 1988, pp. 103-107.
- [60] N. Marcuvitz, *Waveguide handbook*. Lexington, Mass.: Boston Technical Publishers, 1964.
- [61] M. Koshiha, K. Hayata, and M. Suzuki, "Finite-element method analysis of microwave and optical waveguides—trends in countermeasures to spurious solutions," *Electronics and Communications in Japan (Part II: Electronics)*, vol. 70, pp. 96-108, 1987.
- [62] B. M. A. Rahman, F. A. Fernandez, and B. J. Davies, "Review of finite element methods for microwave and optical waveguides," *Proceedings of the IEEE*, vol. 79, pp. 1442-1448, 1991.
- [63] C. Gabriel, "PERMITTIVITY PROBE MODELLING," King's College London November 1991.
- [64] B. M. A. Rahman, "Finite Element Analysis of Optical Waveguides," *PIER, Progress In Electromagnetics Research*, vol. 10, p. 29, 1995.
- [65] G. B. Gajda and S. S. Stuchly, "Numerical Analysis of Open-Ended Coaxial Lines," *Microwave Theory and Techniques, IEEE Transactions on*, vol. 31, pp. 380-384, 1983.
- [66] D. Blackham and R. Pollard, "Finite element analysis of open-ended coaxial lines," in *Microwave Symposium Digest, 1993., IEEE MTT-S International*, 1993, pp. 1247-1250 vol.3.
- [67] P. P. Silvester and R. L. Ferrari, *Finite Elements for Electrical Engineers*. England: Cambridge University Press, 1990.
- [68] E. Sumbar, F. E. Vermeulen, and F. S. Churte, "Implementation of radiation boundary conditions in the finite element analysis of electromagnetic wave propagation," *Microwave Theory and Techniques, IEEE Transactions on*, vol. 39, pp. 267-273, 1991.
- [69] J. P. Grant, R. N. Clarke, G. T. Symm, and N. M. Spyrou, "A critical study of the open-ended coaxial line sensor technique for RF and microwave complex

- permittivity measurements," *Journal of Physics E: Scientific Instruments*, vol. 22, p. 757, 1989.
- [70] a. C. R. B. D. S. Engelder, "Measuring dielectric properties of food products at microwave frequencies," *Microwave World*, vol. 12, pp. 6–15, 1991.
- [71] P. D. Langhe, K. Blomme, L. Martens, and D. D. Zutter, "Measurement of low-permittivity materials based on a spectral-domain analysis for the open-ended coaxial probe," *IEEE Transactions on Instrumentation and Measurement*, vol. 42, pp. 879-886, 1993.
- [72] A. Zulkifly, Y. You Kok, S. Abdul Halim, Z. Azmi, H. Jumiah, K. Kaida, *et al.*, "Fast and Accurate Technique for Determination of Moisture Content in Oil Palm Fruits using Open-Ended Coaxial Sensor," *Japanese Journal of Applied Physics*, vol. 44, p. 5272, 2005.
- [73] Y. Yeow, Z. Abbas, and K. Khalid, "Application of Microwave Moisture Sensor for Determination of Oil Palm Fruit Ripeness," in *Measurement Science Review* vol. 10, ed, 2010, p. 7.
- [74] F. Buckley and A. A. Maryott, *Tables of dielectric dispersion data for pure liquids and dilute solutions*. Washington, D.C.: U.S. Dept. of Commerce, National Bureau of Standards, 1958.
- [75] M. Xu, E. M. Eyring, and S. Petrucci, "Dielectric relaxation of chloroform and chloroform-cyclohexane mixtures at gigahertz and terahertz frequencies. The inertial term," *Journal of Molecular Liquids*, vol. 73, pp. 41-48, 1997/11/01 1997.
- [76] J. Barthel, K. Bachhuber, R. Buchner, and H. Hetzenauer, "Dielectric spectra of some common solvents in the microwave region. Water and lower alcohols," *Chemical Physics Letters*, vol. 165, pp. 369-373, 1990/01/19 1990.
- [77] O. N. Shaforost, "Microwave whispering-gallery resonators for nanolitre liquid sensing," Institut für Bio- und Nanosysteme Bioelektronik (IBN-2), 2009.
- [78] K. Venugopalan and N. Agrawal, "Applications of Microwave Sensors in Medicines," in *World Congress on Medical Physics and Biomedical Engineering, September 7 - 12, 2009, Munich, Germany: Vol. 25/11 Biomedical Engineering for Audiology, Ophthalmology, Emergency & Dental Medicine*, O. Dössel and W. C. Schlegel, Eds., ed Berlin, Heidelberg: Springer Berlin Heidelberg, 2009, pp. 6-8.
- [79] A. Rosen, M. A. Stuchly, and A. V. Vorst, "Applications of RF/microwaves in medicine," *IEEE Transactions on Microwave Theory and Techniques*, vol. 50, pp. 963-974, 2002.
- [80] B. Stec, A. Dobrowolski, and W. Susek, "Estimation of temperature distribution inside biological tissues by means of multifrequency microwave thermograph," in *2001 Conference Proceedings of the 23rd Annual International Conference of the IEEE Engineering in Medicine and Biology Society*, 2001, pp. 3901-3903 vol.4.
- [81] A. H. Barrett, P. C. Myers, and N. L. Sadowsky, "Microwave thermography in the detection of breast cancer," *American Journal of Roentgenology*, vol. 134, pp. 365-368, 1980/02/01 1980.

- [82] J. Edrich, "Centimeter- and Millimeter-Wave Thermography — A Survey on Tumor Detection," *Journal of Microwave Power*, vol. 14, pp. 95-104, 1979/01/01 1979.
- [83] D. V. Land, Fraser, S. and Shaw, R. , *A review of the clinical experience of microwave thermography*: Taylor & Francis, London, 1986.
- [84] M. M. Abdul-Razzak, B. A. Hardwick, G. L. Hey-Shipton, P. A. Matthews, J. R. T. Monson, and R. C. Kester, "Microwave thermography for medical applications," *IEE Proceedings A - Physical Science, Measurement and Instrumentation, Management and Education - Reviews*, vol. 134, pp. 171-174, 1987.
- [85] V. J. Brown, "Development of computer modelling techniques for microwave thermography," Ph.D. Thesis, University of Glasgow, 1989.
- [86] D. V. Land, "A clinical microwave thermography system," *IEE Proceedings A - Physical Science, Measurement and Instrumentation, Management and Education - Reviews*, vol. 134, pp. 193-200, 1987.
- [87] D. V. Land, *Subcutaneous temperature measurement by microwave thermography*. Martinus Nijhoff, Dordrecht: NATO ASI Series E: Applied Sciences, eds. , 1987.
- [88] P. F. e. a. Forrest, *Breast cancer screening*: Department of Health and Social Security, London, 1986.
- [89] E. C. Fear, X. Li, S. C. Hagness, and M. A. Stuchly, "Confocal microwave imaging for breast cancer detection: localization of tumors in three dimensions," *IEEE Transactions on Biomedical Engineering*, vol. 49, pp. 812-822, 2002.
- [90] C.-K. Chou, G.-W. Chen, A. W. Guy, and K. H. Luk, "Formulas for preparing phantom muscle tissue at various radiofrequencies," *Bioelectromagnetics*, vol. 5, pp. 435-441, 1984.
- [91] S. Gabriel, R. W. Lau, and C. Gabriel, "The dielectric properties of biological tissues: II. Measurements in the frequency range 10 Hz to 20 GHz," *Physics in Medicine and Biology*, vol. 41, p. 2251, 1996.
- [92] S. Gabriel, R. W. Lau, and C. Gabriel, "The dielectric properties of biological tissues: III. Parametric models for the dielectric spectrum of tissues," *Physics in Medicine and Biology*, vol. 41, p. 2271, 1996.
- [93] A. M. Campbell and D. V. Land, "Dielectric properties of female human breast tissue measured in vitro at 3.2 GHz," *Phys Med Biol*, vol. 37, pp. 193-210, Jan 1992.
- [94] L. Xu and S. C. Hagness, "A confocal microwave imaging algorithm for breast cancer detection," *IEEE Microwave and Wireless Components Letters*, vol. 11, pp. 130-132, 2001.
- [95] E. R. Atkinson, *Hyperthermia techniques and instrumentation*: Boston, 1983.
- [96] J. A. a. C. Dickson, S.K. , *Thermosensistivity of neoplastic tissues in vivo*. Boston, 1983.
- [97] A. W. a. C. Guy, C. -K. , *Physical aspects of localised heating by radiowaves and microwaves*. Boston: G.K. Hall, 1983.

- [98] J. W. Hand, "Hyperthermia: Challenging applications of physics in cancer therapy," *Physics Bulletin*, vol. 38, p. 111, 1987.
- [99] J. C. Bolomey, Jofre, L., Peronnet, G. and Pichot, C. , "Microwave tomography and its potential application to the control of hyperthermia treatments," presented at the TEE Colloquium on electromagnetic techniques for detection and treatment of malignant disease, 2 April 1984.
- [100] J. C. Bolomey, "Active and passive microwave imaging: complementary approaches to remote thermal sensing in hyperthermia treatments," presented at the IEE Colloquium on industrial and medical applications of microwaves, 9th May 1986.
- [101] R. Aitmedhi, Anderson, A.P. and Sali, S. , "Non-invasive measurement of volumetric loss distribution by microwave phase tomography," presented at the IEEE Colloquium on industrial and medical applications of microwaves, 9th May, 1986.
- [102] L. Jofre, A. Broquetas, and M. S. Hawley, "Active microwave imaging: a cylindrical system for biomedical applications," in *IEE Colloquium on Medical Applications of Microwaves*, 1988, pp. 12/1-12/4.
- [103] A. Y. Cheung and A. Neyzari, "Deep local hyperthermia for cancer therapy: external electromagnetic and ultrasound techniques," *Cancer Res*, vol. 44, pp. 4736s-4744s, Oct 1984.
- [104] S. K. S. a. H. V. T. N.K. Gupta, "Estimation of Emissivity Characteristics of Biological Tissues at Microwave Frequency," *IE(I) Journal-ID*, vol. 84, pp. 1-3, May 2004.
- [105] H. P. Schwan, "Electrical properties of tissue and cell suspensions," *Adv Biol Med Phys*, vol. 5, pp. 147-209, 1957.
- [106] K. R. F. a. H. P. Schwan, *Dielectric properties of tissues*. New York: CRC Press, 1995.
- [107] D. Miklavčič, N. Pavšelj, and F. X. Hart, "Electric Properties of Tissues," in *Wiley Encyclopedia of Biomedical Engineering*, ed: John Wiley & Sons, Inc., 2006.
- [108] W. D. Hurt, "Multiterm Debye dispersion relations for permittivity of muscle," *IEEE Trans Biomed Eng*, vol. 32, pp. 60-4, Jan 1985.
- [109] S. G. a. H. P. S. O.G. Martinsen, "Interface Phenomena and Dielectric Properties of Biological Tissue," *Encyclopedia of Surface and Colloid Science*, Marcel Dekker, Inc., pp. 2643-2652, 2002.
- [110] W. F. Windle, *Textbook of histology*, 5th ed. New York McGraw-Hill, 1976.
- [111] E. P. Charles Polk, *Handbook of Biological Effects of Electromagnetic Fields*, 2 ed.: CRC Press, 1995.
- [112] R. Rubino, "NUMERICAL MRI-BASED BREAST MODEL FOR MICROWAVE IMAGING," MSc MSc, Politècnica de Catalunya, Barcelona, 2012.
- [113] J. P. Grant, "Measurement, medical significance and applications of the dielectric properties of biological materials," Ph.D., Surrey University 1984.

- [114] P. Debye, *Polar Molecules*. New York: Chemical Catalogue Co., 1929.
- [115] J. Crawford, "Microwave measurements of dielectric properties of some polar liquids," MSc MSc, Phillips University, 1957.
- [116] Ø. G. M. Sverre Grimnes, *Bioimpedance and Bioelectricity Basics*. Oslo: Academic Press, 2000.
- [117] C. C. Johnson and A. W. Guy, "Nonionizing electromagnetic wave effects in biological materials and systems," *Proceedings of the IEEE*, vol. 60, pp. 692-718, 1972.
- [118] L. A. G. a. L. E. Baker, *Principles of Applied Biomedical Instrumentation*, 2nd ed. New York: Wiley, 1975.
- [119] R. J. S. a. S. P. S. E. H. Grant, "Dielectric behaviour of biological molecules in solution " 1978.
- [120] A. S. Presman, *Electromagnetic Fields and Life*. New York and London: England: Plenum, 1970.
- [121] H. P. Schwan and K. R. Foster, "RF-field interactions with biological systems: Electrical properties and biophysical mechanisms," *Proceedings of the IEEE*, vol. 68, pp. 104-113, 1980.
- [122] K. R. Foster, J. L. Schepps, and H. P. Schwan, "Microwave dielectric relaxation in muscle. A second look," *Biophys J*, vol. 29, pp. 271-81, Feb 1980.
- [123] M. A. Stuchly, "Interaction of radiofrequency and microwave radiation with living systems. A review of mechanisms," *Radiat Environ Biophys*, vol. 16, pp. 1-14, Feb 23 1979.
- [124] H. P. Schwan, "Dielectric Properties of Biological Tissue and Biophysical Mechanisms of Electromagnetic-Field Interaction," in *Biological Effects of Nonionizing Radiation*. vol. 157, ed: AMERICAN CHEMICAL SOCIETY, 1981, pp. 109-131.
- [125] H. P. Schwan and K. R. Foster, "Microwave dielectric properties of tissue. Some comments on the rotational mobility of tissue water," *Biophysical Journal*, vol. 17, pp. 193-197, 1977.
- [126] H. P. Schwan, "Interaction of Microwave and Radio Frequency Radiation with Biological Systems," *IEEE Transactions on Microwave Theory and Techniques*, vol. 19, pp. 146-152, 1971.
- [127] T. C. Williams, J. M. Sill, and E. C. Fear, "Breast Surface Estimation for Radar-Based Breast Imaging Systems," *IEEE Transactions on Biomedical Engineering*, vol. 55, pp. 1678-1686, 2008.
- [128] Y. Xing, E. C. Fear, and R. H. Johnston, "Compact Antenna for Radar-Based Breast Cancer Detection," *IEEE Transactions on Antennas and Propagation*, vol. 53, pp. 2374-2380, 2005.
- [129] A. J. Surowiec, S. S. Stuchly, J. R. Barr, and A. Swarup, "Dielectric properties of breast carcinoma and the surrounding tissues," *IEEE Transactions on Biomedical Engineering*, vol. 35, pp. 257-263, 1988.
- [130] S. J. H. A. Peyman, S. Watts, R. Perrott, C. Gabriel, "Dielectric properties of porcine cerebrospinal tissues at microwave frequencies: in vivo, in vitro and

systematic variation with age," *Phys. Med. Biol.* , vol. 52, pp. 2229–2245, Apr. 2007.

- [131] J. W. Choi, J. Cho, Y. Lee, J. Yim, B. Kang, K. K. Oh, *et al.*, "Microwave detection of metastasized breast cancer cells in the lymph node; potential application for sentinel lymphadenectomy," *Breast Cancer Res Treat*, vol. 86, pp. 107-15, Jul 2004.
- [132] D. Popovic, L. McCartney, C. Beasley, M. Lazebnik, M. Okoniewski, S. C. Hagness, *et al.*, "Precision open-ended coaxial probes for in vivo and ex vivo dielectric spectroscopy of biological tissues at microwave frequencies," *IEEE Transactions on Microwave Theory and Techniques*, vol. 53, pp. 1713-1722, 2005.
- [133] M. Lazebnik, L. McCartney, D. Popovic, C. B. Watkins, M. J. Lindstrom, J. Harter, *et al.*, "A large-scale study of the ultrawideband microwave dielectric properties of normal breast tissue obtained from reduction surgeries," *Phys Med Biol*, vol. 52, pp. 2637-56, May 21 2007.
- [134] M. Lazebnik, M. Okoniewski, J. H. Booske, and S. C. Hagness, "Highly Accurate Debye Models for Normal and Malignant Breast Tissue Dielectric Properties at Microwave Frequencies," *IEEE Microwave and Wireless Components Letters*, vol. 17, pp. 822-824, 2007.
- [135] X. Yansheng, F. M. Ghannouchi, and R. G. Bosisio, "Theoretical and experimental study of measurement of microwave permittivity using open ended elliptical coaxial probes," *Microwave Theory and Techniques, IEEE Transactions on*, vol. 40, pp. 143-150, 1992.
- [136] M. El-Shenawee, "Resonant spectra of Malignant breast cancer tumors using the three-dimensional Electromagnetic Fast multipole model," *IEEE Transactions on Biomedical Engineering*, vol. 51, pp. 35-44, 2004.
- [137] R. Pethig, "Dielectric Properties of Biological Materials: Biophysical and Medical Applications," *IEEE Transactions on Electrical Insulation*, vol. EI-19, pp. 453-474, 1984.
- [138] H. F. a. S. Morse, "The electric capacity of tumors of the breast," *J. Cancer Res.*, vol. 10, pp. 340-376, Oct. 1926.
- [139] K. R. Foster and J. L. Schepps, "Dielectric properties of tumor and normal tissues at radio through microwave frequencies," *J Microw Power*, vol. 16, pp. 107-19, Jun 1981.
- [140] W. T. Joines, Y. Zhang, C. Li, and R. L. Jirtle, "The measured electrical properties of normal and malignant human tissues from 50 to 900 MHz," *Medical Physics*, vol. 21, pp. 547-550, 1994.
- [141] S. S. Chaudhary, R. K. Mishra, A. Swarup, and J. M. Thomas, "Dielectric properties of normal & malignant human breast tissues at radiowave & microwave frequencies," *Indian J Biochem Biophys*, vol. 21, pp. 76-9, Feb 1984.
- [142] C. F. Hazlewood, D. C. Chang, B. L. Nichols, and D. E. Woessner, "Nuclear magnetic resonance transverse relaxation times of water protons in skeletal muscle," *Biophys J*, vol. 14, pp. 583-606, Aug 1974.

- [143] R. Damadian and F. W. Cope, "NMR in cancer. V. Electronic diagnosis of cancer by potassium (<sup>39</sup>K) nuclear magnetic resonance: spin signatures and T1 beat patterns," *Physiol Chem Phys*, vol. 6, pp. 309-22, 1974.
- [144] D. Colton and P. Monk, "A new approach to detecting leukemia: using computational electromagnetics," *IEEE Computational Science and Engineering*, vol. 2, pp. 46-52, 1995.
- [145] S. Bone, P. R. C. Gascoyne, and R. Pethig, "Dielectric properties of hydrated proteins at 9.9 GHz," *Journal of the Chemical Society, Faraday Transactions 1: Physical Chemistry in Condensed Phases*, vol. 73, pp. 1605-1611, 1977.
- [146] C. D. Cone, "Electroosmotic interactions accompanying mitosis initiation in sarcoma cells in vitro," *Trans. N.Y. Acad. Sci.*, vol. 31, pp. 404-427, Apr. 1969.
- [147] S. Liewei, E. R. Ward, and B. Stroy, "A review of dielectric properties of normal and malignant breast tissue," in *Proceedings IEEE SoutheastCon 2002 (Cat. No.02CH37283)*, 2002, pp. 457-462.
- [148] A. M. James, E. J. Ambrose, and J. H. Lowick, "Differences between the electrical charge carried by normal and homologous tumour cells," *Nature*, vol. 177, pp. 576-7, Mar 24 1956.
- [149] R. C. C. M. O'Halloran, D. Byrne, M. Glavin, and E. Jones, "FDTD modeling of the breast: a review," *Progress In Electromagnetics Research B*, vol. 18, pp. 1-24, 2009.
- [150] J. B. Hasted, *Aqueous dielectrics*. London: Chapman and Hall, 1973.
- [151] S. D. Logsdon, "Soil Dielectric Spectra from Vector Network Analyzer Data," *Soil Sci. Soc. Am. Journal*, vol. 69, pp. 983-989, 2005.
- [152] U. Kaatze, "Techniques for measuring the microwave dielectric properties of materials," *Metrologia*, vol. 47, pp. S91-S113, 2010.
- [153] U. Kaatze, "The dielectric properties of water in its different states of interaction," *Journal of solution chemistry*, vol. 26, pp. 1049-1112, 1997.
- [154] S. a. S. Horikoshi, N., *Microwave Frequency Effects in Organic Synthesis*: eds A. de la Hoz and A. Loupy, 2012.
- [155] H. P. S. a. K. Li, "Capacity and conductivity of body tissues at ultrahigh frequencies," *Proc. IRE 41*, pp. 1735-1740, 1953.
- [156] H. P. Schwan, R. J. Sheppard, and E. H. Grant, "Complex permittivity of water at 25 °C," *The Journal of Chemical Physics*, vol. 64, pp. 2257-2258, 1976.
- [157] A. Stogryn, "Equations for Calculating the Dielectric Constant of Saline Water (Correspondence)," *IEEE Transactions on Microwave Theory and Techniques*, vol. 19, pp. 733-736, 1971.
- [158] M. Lazebnik, D. Popovic, L. McCartney, C. B. Watkins, M. J. Lindstrom, J. Harter, *et al.*, "A large-scale study of the ultrawideband microwave dielectric properties of normal, benign and malignant breast tissues obtained from cancer surgeries," *Phys Med Biol*, vol. 52, pp. 6093-115, Oct 21 2007.
- [159] D. R. W. H. Q. Woodard, "The composition of body tissues," *Br J Radiol*, vol. 59, pp. 1209-1218, 1986.

- [160] D. M. Hagl, D. Popovic, S. C. Hagness, J. H. Booske, and M. Okoniewski, "Sensing volume of open-ended coaxial probes for dielectric characterization of breast tissue at microwave frequencies," *IEEE Transactions on Microwave Theory and Techniques*, vol. 51, pp. 1194-1206, 2003.
- [161] M. Klemm, I. Craddock, J. Leendertz, A. Preece, and R. Benjamin, "Experimental and clinical results of breast cancer detection using UWB microwave radar," in *2008 IEEE Antennas and Propagation Society International Symposium*, 2008, pp. 1-4.
- [162] P. L. A. a. D. S. Dittmer, *Biology Data Handbook* 2ed. vol. 1: Federation of American Societies for Experimental Biology, Bethesda, Md., 1972.
- [163] E. L. Hansen, E. B. Sozer, S. Romeo, S. K. Frandsen, P. T. Vernier, and J. Gehl, "Dose-Dependent ATP Depletion and Cancer Cell Death following Calcium Electroporation, Relative Effect of Calcium Concentration and Electric Field Strength," *PLOS ONE*, vol. 10, p. e0122973, 2015.
- [164] A. C. Society, "Global Cancer Facts & Figures ", Atlanta: American Cancer Society 2013.
- [165] n. d. NHS. (28 Nov 2016). *Breast Cancer (female)*. Available: <http://www.nhs.uk/Conditions/Cancer-of-the-breast-female/Pages/Introduction.aspx>
- [166] "Breast Cancer," Cancer Research UK, s.l.: Cancer Research UK 2014.
- [167] NHS. (2014). *Breast Cancer (female) - Treatment*. Available: <http://www.nhs.uk/Conditions/Cancer-of-the-breast-female/Pages/Treatment.aspx>
- [168] N. Heaton. (2012, 28 April 2015). *Endometrial Ablation*.
- [169] I. S. Gill, E. M. Remer, W. A. Hasan, B. Strzempkowski, M. Spaliviero, A. P. Steinberg, *et al.*, "Renal cryoablation: outcome at 3 years," *J Urol*, vol. 173, pp. 1903-7, Jun 2005.
- [170] T. C. T. A. Fund. (2014, 02 Dec 2014). *Cancer patients and ablation cancer treatment therapy (radio frequency ablation)*. Available: <http://www.rfablation.co.uk/patients.php>
- [171] D. Haemmerich, "Biophysics of radiofrequency ablation," *Crit Rev Biomed Eng*, vol. 38, pp. 53-63, 2010.
- [172] S. Tatli, U. Tapan, P. R. Morrison, and S. G. Silverman, "Radiofrequency ablation: technique and clinical applications," *Diagn Interv Radiol*, vol. 18, pp. 508-16, Sep-Oct 2012.
- [173] G. Carrafiello, D. Lagana, M. Mangini, F. Fontana, G. Dionigi, L. Boni, *et al.*, "Microwave tumors ablation: principles, clinical applications and review of preliminary experiences," *Int J Surg*, vol. 6 Suppl 1, pp. S65-9, 2008.
- [174] R. C. Martin, C. R. Scoggins, and K. M. McMasters, "Safety and efficacy of microwave ablation of hepatic tumors: a prospective review of a 5-year experience," *Ann Surg Oncol*, vol. 17, pp. 171-8, Jan 2010.
- [175] M. G. Lubner, C. L. Brace, J. L. Hinshaw, and F. T. Lee, "Microwave Tumor Ablation: Mechanism of Action, Clinical Results and Devices," *Journal of vascular and interventional radiology : JVIR*, vol. 21, pp. S192-S203, 2010.

- [176] E. S. a. R. C. V. Surducun, "Medical and scientific apparatus with microwave thermal and non-thermal effect," *Nonconventional Technology Review*, vol. 1, pp. 42-49, 2010.
- [177] E. M. Knavel and C. L. Brace, "Tumor Ablation: Common Modalities and General Practices," *Techniques in vascular and interventional radiology*, vol. 16, pp. 192-200, 2013.
- [178] A. D. Strickland, P. J. Clegg, N. J. Cronin, B. Swift, M. Festing, K. P. West, *et al.*, "Experimental study of large-volume microwave ablation in the liver," *Br J Surg*, vol. 89, pp. 1003-7, Aug 2002.
- [179] B. D. Beadle. (15 June 2016). *HEAT TRANSFER*. Available: <http://vhmsscience.weebly.com/heat.html>
- [180] B. H.-L. T. Mohorič, V. Vlachy, "Effects of translational and rotational degrees of freedom on the properties of model water," *Condensed Matter Physics*, vol. 18, pp. 1-9, 2015.
- [181] C. J. Simon, D. E. Dupuy, and W. W. Mayo-Smith, "Microwave ablation: principles and applications," *Radiographics*, vol. 25 Suppl 1, pp. S69-83, Oct 2005.
- [182] N. Bhardwaj, A. D. Strickland, F. Ahmad, L. Atanesyan, K. West, and D. M. Lloyd, "A comparative histological evaluation of the ablations produced by microwave, cryotherapy and radiofrequency in the liver," *Pathology*, vol. 41, pp. 168-72, Feb 2009.
- [183] J. Yoon, J. Cho, N. Kim, D. D. Kim, E. Lee, C. Cheon, *et al.*, "High-frequency microwave ablation method for enhanced cancer treatment with minimized collateral damage," *Int J Cancer*, vol. 129, pp. 1970-8, Oct 15 2011.
- [184] R. P. Jones, N. R. Kitteringham, M. Terlizzo, C. Hancock, D. Dunne, S. W. Fenwick, *et al.*, "Microwave ablation of ex vivo human liver and colorectal liver metastases with a novel 14.5 GHz generator," *Int J Hyperthermia*, vol. 28, pp. 43-54, 2012.
- [185] T. Yamaguchi, K.-i. Mukaisho, H. Yamamoto, H. Shiomi, Y. Kurumi, H. Sugihara, *et al.*, "Disruption of Erythrocytes Distinguishes Fixed Cells/Tissues from Viable Cells/Tissues Following Microwave Coagulation Therapy," *Digestive Diseases and Sciences*, vol. 50, pp. 1347-1355, 2005.
- [186] R. S. Dwivedi, U. Dwivedi, and B. Chiang, "Low intensity microwave radiation effects on the ultrastructure of chang liver cells," *Experimental Cell Research*, vol. 180, pp. 253-265, 1// 1989.
- [187] J. Chiang, P. Wang, and C. L. Brace, "'Computational Modelling of Microwave Tumour Ablations'," *International journal of hyperthermia : the official journal of European Society for Hyperthermic Oncology, North American Hyperthermia Group*, vol. 29, pp. 308-317, 2013.
- [188] M. Zahn, Y. Ohki, D. B. Fenneman, R. J. Gripshover, and V. H. Gehman, "Dielectric properties of water and water/ethylene glycol mixtures for use in pulsed power system design," *Proceedings of the IEEE*, vol. 74, pp. 1182-1221, 1986.

- [189] K. Technologies. *N5181B MXG X-Series RF Analog Signal Generator, 9 kHz to 6 GHz*. Available: <http://www.keysight.com/en/pdx-x201911-pn-N5181B/mxg-x-series-rf-analog-signal-generator-9-khz-to-6-ghz?cc=US&lc=eng&cmpid=zzfindn5181b&state=0>
- [190] circuitdiagramworld. (2015, 02 May 2015). *Class A power amplifier\_Circuit Diagram World*. Available: [http://www.circuitdiagramworld.com/amplifier\\_circuit\\_diagram/Class\\_A\\_power\\_amplifiers\\_12263.html](http://www.circuitdiagramworld.com/amplifier_circuit_diagram/Class_A_power_amplifiers_12263.html)
- [191] vectaawave. (2014, 28 April 2015). *ectawave.com*. Available: <http://vectawave.com/wp-content/uploads/2014/12/Application-Note-01-1214.pdf>
- [192] M. Technology. (2015, 15 April 2015). *AS1860 Broadband Amplifier 1.8 GHz - 6.0 Ghz, MILMEGA Series 2000*. Available: <http://www.mdltechnologies.co.uk/product/series-2000-1-8-ghz-6-0-ghz-as1860-30-30-watt/>
- [193] N. Instruments. (2016, 2015). Available: <http://www.ni.com/white-paper/2952/en/>
- [194] NovaMicrowave. (2014, 27 April 2015). *Understanding Circulators & Isolators*. Available: <http://www.novamicro.com/understanding-circulator-and-isolaters.php>
- [195] H. L. Matzner, S. (2002, 02 May 2015). *Basic RF Technic and Laboratory Manual*. Available: [http://www.hit.ac.il/upload/engineering/experiment\\_10\\_-\\_swpdirectionalcoupler.pdf](http://www.hit.ac.il/upload/engineering/experiment_10_-_swpdirectionalcoupler.pdf)
- [196] M. Hiebel, "Amplifier measurements," in *Handbook of RF and microwave power amplifiers* J. Walker, Ed., ed Cambridge ; New York Cambridge University Press, 2010, pp. 570-576.
- [197] K. E. Bramall, "Accurate Microwave High Power Measurements Using a Cascaded Coupler Method," *Research of the National Bureau of Standards*, vol. 75C, pp. 185-192, 1971.
- [198] K. Technologies. (2014). *Keysight U2020 X-Series USB Peak and Average Power Meter: Programming Guide*. Available: <http://literature.cdn.keysight.com/litweb/pdf/U2021-90003.pdf?id=834479>
- [199] R. Components. (2015). *Datasheet Cable Thermocouple*. Available: <http://docs-europe.electrocomponents.com/webdocs/12fd/0900766b812fde04.pdf>
- [200] B. Mihura, "LabVIEW for data acquisition," Prentice Hall PTR, United States of America 2001.
- [201] N. Instruments. (2014). *National Instruments VISA : What is VISA?* Available: <https://www.ni.com/visa/>
- [202] T. F. Scientific. (09-07-2015). *N-2 Supplement (100X) liquid*. Available: <http://www.lifetechnologies.com/uk/en/home/technical-resources/media-formulation.166.html>
- [203] P. K. Nag, *Basic and Applied Thermodynamics*, 2nd ed.: s.l.:Tata McGraw-Hill Education, 2010.

- [204] M. K. Miodrag Zdravković, Miroslav Stojanović, "Identification of postmortem autolytic changes on the kidney tissue using the pas stained method," *Medicine and Biology*, vol. 13, pp. 181-184, 2006.
- [205] C. P. Hancock, P. Burn, C. I. Duff, R. Sloan, M. White, J. Bishop, *et al.*, "A New Wave in Electrosurgery : A Review of Existing and Introduction to New Radio-Frequency and Microwave Therapeutic Systems," *IEEE Microwave Magazine*, vol. 16, pp. 14-30, 2015.
- [206] M. Porcelli, G. Cacciapuoti, S. Fusco, R. Massa, G. d'Ambrosio, C. Bertoldo, *et al.*, "Non-thermal effects of microwaves on proteins: thermophilic enzymes as model system," *FEBS Letters*, vol. 402, pp. 102-106, 1/27/ 1997.
- [207] Y. Feldman, A. Puzenko, P. Ben Ishai, A. Caduff, and A. J. Agranat, "Human Skin as Arrays of Helical Antennas in the Millimeter and Submillimeter Wave Range," *Physical Review Letters*, vol. 100, p. 128102, 03/27/ 2008.
- [208] S. Franzellitti, P. Valbonesi, N. Ciancaglini, C. Biondi, A. Contin, F. Bersani, *et al.*, "Transient DNA damage induced by high-frequency electromagnetic fields (GSM 1.8 GHz) in the human trophoblast HTR-8/SVneo cell line evaluated with the alkaline comet assay," *Mutat Res*, vol. 683, pp. 35-42, Jan 05 2010.
- [209] S. Gekle and R. R. Netz, "Nanometer-Resolved Radio-Frequency Absorption and Heating in Biomembrane Hydration Layers," *The Journal of Physical Chemistry B*, vol. 118, pp. 4963-4969, 2014/05/08 2014.
- [210] Z. Yang, X. Niu, X. Fang, G. Chen, H. Zhang, H. Yue, *et al.*, "Enantioselective Esterification of Ibuprofen under Microwave Irradiation," *Molecules*, vol. 18, p. 5472, 2013.
- [211] S. Pandit. (2016, September 20). *Difference Between Peripheral and Integral Membrane Proteins*. Available: <http://www.buzzle.com/articles/difference-between-peripheral-and-integral-membrane-proteins.html>
- [212] I. Gitlin, J. D. Carbeck, and G. M. Whitesides, "Why are proteins charged? Networks of charge-charge interactions in proteins measured by charge ladders and capillary electrophoresis," *Angew Chem Int Ed Engl*, vol. 45, pp. 3022-60, May 05 2006.
- [213] L. Wang, D. Liu, R. Zhou, Z. Wang, and A. Cuschieri, "Tumour Cell Membrane Poration and Ablation by Pulsed Low-Intensity Electric Field with Carbon Nanotubes," *International Journal of Molecular Sciences*, vol. 16, pp. 6890-6901, March 2015.
- [214] D. Davalos, J. Grutzendler, G. Yang, J. V. Kim, Y. Zuo, S. Jung, *et al.*, "ATP mediates rapid microglial response to local brain injury in vivo," *Nat Neurosci*, vol. 8, pp. 752-8, Jun 2005.
- [215] S. Lee, H. P. Liu, W. Y. Lin, H. Guo, and B. Lu, "LRRK2 kinase regulates synaptic morphology through distinct substrates at the presynaptic and postsynaptic compartments of the Drosophila neuromuscular junction," *J Neurosci*, vol. 30, pp. 16959-69, Dec 15 2010.
- [216] C. F. Williams, G. M. Geroni, A. Pirog, D. Lloyd, J. Lees, and A. Porch, "The separated electric and magnetic field responses of luminescent bacteria exposed to pulsed microwave irradiation," *Applied Physics Letters*, vol. 109, p. 093701, 2016.

